ABSTRACT

Title of dissertation: Fault Detection on a Full-Scale OH-58 A/C Helicopter Transmission

Adrian A. Hood, Doctor of Philosophy, 2010

Dissertation directed by: Darryll J. Pines, Chair
A. James Clark School of Engineering

Detecting seeded faults on a full-scale helicopter transmission is the focus of this work. Methods to isolate the dynamics of an individual sun gear, in an effort to assess its condition, are developed and validated on an OH-58 helicopter transmission's planetary reduction stage. This area has been shown to be challenging because the planetary system does not allow for direct measurements of the sun gear. Instead, special measurement and data processing techniques are needed to filter out the effects of the planet gears, bearings, input spiral bevel stage, and other components in and around the gearbox. Planetary indexing is used to geometrically synchronize dynamic measurements with the meshing tooth's position along its pressure line. This provides the opportunity for source/signal mapping that can lead to increased sensitivity, allowing faults to be detected early and thus increasing the available time for corrective action.

Accelerometers mounted along the transmission housing, acoustic transducers distributed about the test cell, and an oil debris monitoring system are all used to analyze three seeded fault cases. Transmission components, (two sun gears and a single planet bearing), which were damaged in previous fatigue tests, serve as the

focus of this current work. Two vibration separation (VS) algorithms, tailored to the three planet OH-58A, and the four planet, non-sequential OH-58C transmissions, were developed and their resulting signals analyzed. In addition, a geometrically synchronized measurement method to transmission diagnostics is also developed. This non-VS based method uses only the time synchronously averaged data and takes advantage of signal/source mapping required for VS. Eleven commonly used condition indicators are used on both global and separated signals and their results tabulated.

All three damage detection algorithms were successful in identifying the damage on the sun gear with multiple faults. Sun gear damage was confirmed by the presence of sun mesh groups. Detecting the single tooth spall continues to be a challenge. Also demonstrated is the ability for the vibration separation methods developed to isolate components.

Safety and cost are the main motivators for helicopter Health Usage and Monitoring Systems (HUMS). During flight, critical components are subjected to sustained vibratory and impulsive loads requiring the need for frequent inspections. Methods that can reduce this time and effectively detect faults in their infancy are highly sought. Actively monitoring the transmission's health can provide the benefit of detecting damage early and possibly avoid catastrophe. In addition, active monitoring provides an updated assessment of a component's condition which can possibly increase its life when compared to scheduled replacement times. The methods proposed for gear tooth diagnostics can be integrated in an overall helicopter HUMS program with the main objective of cost-effectively improving the safety of both civil and military helicopters while reducing the cost of ownership.

Fault Detection on a Full-Scale OH-58 A/C Helicopter Transmission

by

Adrian A. Hood

Dissertation submitted to the Faculty of the Graduate School of the
University of Maryland, College Park in partial fulfillment
of the requirements for the degree of
Doctor of Philosophy
2010

Advisory Committee:
Professor Darryll J. Pines, Chair/Advisor
Professor Inderjit Chopra
Professor Norman M. Wereley
Professor Alison Flatau
Professor Amr Baz

Dedication
To Adrian Jr. and Donovan.
Tenacity, Always Tenacity.

Acknowledgments

So many generous and brilliant people have encouraged and supported me along this journey. First and foremost, I would like to thank my advisor, Dr. Darryll Pines, for taking me on as a graduate student and ensuring that I saw this research to completion. I appreciate the valuable discussions that helped me better understand these studies. I am forever grateful. I also thank my committee members, Dr. Norman Wereley, Dr. Alison Flatau, Dr. Inderjit Chopra, and Dr. Amr Baz., whose encouraging words throughout helped more than they will ever know. I would like to thank Dr. Horace Russell for encouraging me to pursue graduate studies.

I am extremely grateful for being able to participate in the NASA Graduate Student Researchers Program (GSRP) which allowed me to collect the data needed for this research. The program was one of the most important and formative experiences of my life. In particular, I would like to acknowledge Dr. David Lewicki, who served as my advisor at NASA. His immense knowledge of gearing and skills in testing have set the standard. I am also appreciative of the help I received from other members of the Tribology and Mechanical Components Branch, in particular Dr. James Zakrajsek, Dr. Paula Dempsey, Dr. Robert Handschuh, Dr. Tim Krantz, Dr. Erwin Zaretsky, Harry Decker and Fred Oswald. I am very grateful to John Veneziano, who was responsible for overhauling the test rig and making sure everything needed for testing was operating properly.

Thanks to Dr. Sandeep Vijayakar of Advanced Numerical Solutions for granting me a license to use their Planetary 2D software.

During my time at UMD, many members of Dr. Pines's research group have played a role in this work–none as much as Dr. Paul Samuel, who graciously devoted time on a regular basis to discussing this research with me. He has helped me clear so

many considerable hurdles through direct, simple conversation. I am forever grateful. I would also like to thank Dr. Joe Conroy and Joe Coker for all of their assistance in helping me advance this work.

I must also express my sincere gratitude to the Aerospace Engineering staff. Brian Hill and Rebecca Sarni were always a source of encouragement. Debora Chandler's assistance over the years was extremely helpful as she saw to it that I stayed on track.

Many friends and family have helped me stay sane and on track throughout these years. Their support and care helped me overcome setbacks and keep the goal foremost. I greatly value their friendship and I deeply appreciate their belief in me. Thanks to my father, Charles Hood, for encouraging me to always ask questions and to try and view everything from non obvious angles. My mentor, Dr. Ulysses Glee, has always been a strong supporter since my undergraduate years. Thanks to my Uncle Ron Hood for assisting me and helping me stay on track to pursue my dream. Thanks to friends Kevin Monroe, Kirk Queen, and Aaron Frazier, whose daily calls down the stretch were a great help.

I want to thank Ms. Marion Nowak for making the review of this dissertation a priority. You are a true blessing!

For their infinite support and patience, I particularly want to thank my family– especially my wife, Danielle, and our two boys, who had to endure my year-long stay in Cleveland while I was conducting testing at NASA Glenn Research Center. You will always be my rock.

Lastly, I'd like to thank my mother, Cynthia Hood, sister, Andrea Hood, and brother, Aaron Hood.

Table of Contents

List of Tables

List of Figures

Chapter 1

Introduction

1.1 Background

Maintenance and insurance can account for more than half of a helicopter's direct operating costs. [1–4] During flight, critical components are subject to sustained vibratory and impulsive loads, requiring the need for frequent inspections. Hence, methods that can reduce this downtime and effectively detect faults in their infancy are highly sought.

Currently, the maintenance strategy of most helicopters is schedule based, with component replacement depending on flight hours. The component's life cycles are based on reliability analysis and may not take into consideration possible manufacturing defects, instances of improper lubrication, overloading, or, for military aircraft, possible damage in combat. An improved method is based on the philosophy that system components are monitored and replaced when there is evidence that they can no longer operate as intended. This approach not only offers a means to avert catastrophic accidents but can also decrease maintenance time and increase the useful life of various helicopter components, thereby reducing direct operating costs.

One area covered in the National Transportation and Safety Board's Annual Re-

port on General Aviation is the accident rate of fixed-wing aircraft[1] and rotorcraft.[2] Figure 1.1 shows a comparison of accident rates between fixed-wing aircraft and rotorcraft between 1975 and 2005.[3]. It shows that, over the 30 years cited, helicopters

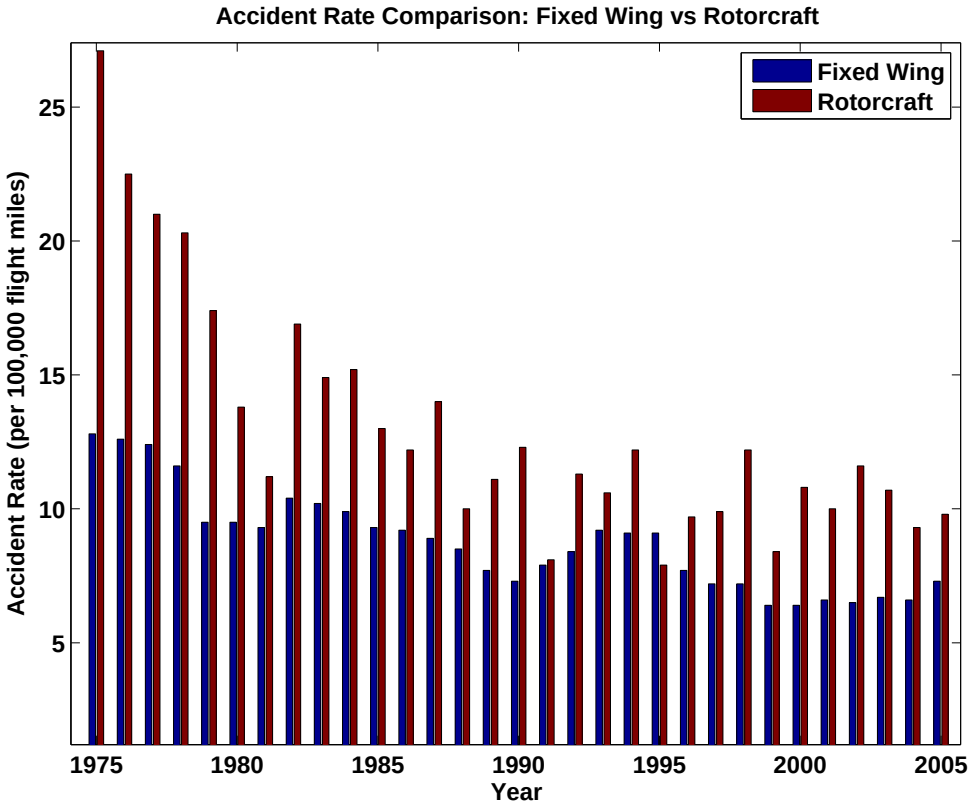

Figure 1.1: Accident Rate Comparison: Fixed Wing vs Rotorcraft (1975-2005)

are 48% more likely to be involved in an accident compared to fixed wing aircraft. For the period from 2000 to 2005, that number is 44%. Government aviation authorities are demanding that the safety record of civil helicopters match that of conventional fixed-wing turbojet aircraft. [5]

The integrity of a helicopter's transmission is extremely important. Its power

[1]Reciprocating engines, turboprops, and turbojets

[2]Reciprocating and turbine

[3]Tabulated in the Appendix

train is responsible for lift, propulsion, and maneuvering. In most helicopters, the transmission is non-redundant. Any failure has the potential to be catastrophic. A helicopter Health and Usage Monitoring System (**HUMS**), monitors the health of the helicopter during flight and attempts to detect the onset of damage. In addition, a **HUMS** collects usage data which is used to improve life models of system components.

A typical **HUMS** system consists of a collection of sensors, a data acquisition system, signal processing algorithms, and data interpretation methodologies for the purpose of improving safety, increasing reliability, increasing a component's usable life, and ultimately reducing operating costs. This work is concerned with **HUMS** applied to the helicopter's transmission.

Industry acceptance of **HUMS** was slow. In large part, this was due to the weight penalty associated with the often bulky support system. However, on-board information processing technology and avionics has evolved, making comprehensive **HUMS** more feasible. The first **HUMS** system to be certified was developed by GE Aviation Systems for offshore helicopters in the North Sea in 1991. Since then, many companies have surfaced offering **HUMS** , and some of these systems have become standard on certain aircraft. Table 1.1 highlights three providers and the helicopters that use their systems.

BF Goodrich	Honeywell	GE Aviation Systems
UH-60 Blackhawk	AH-64 Apache	CH-47 (British Military)
CH-47 Chinook	OH-58D Kiowa Warrior	Agusta Westland AW-139
CH-53E Super Stallion	MH-53	ERA Helicopters
S-76(R)	Bell 206L,212	Canadian Helicopter Corp.
S-92(R)	Bell 407,412,427,430	Bristow
	A109	Saudi Aramco
	AS-365N1/2/3 Aircraft	V22 - Osprey
		Eurocopter AS332 Super Puma
		Eurocopter AS532 Cougar

Table 1.1: HUMS Companies

1.2 Helicopter Gear Damage

Most helicopter designs utilize a single transmission to transfer the high speed power from the engine to the low speeds/high torque power required by the main rotor. The key components of the transmission are the gears, shafts, and bearings. All are susceptible to damage during normal operation. For gears, there are five general classes of gear tooth failure specified by the AGMA. The four main ones are wear, plastic flow, surface fatigue, and breakage. [6] This study focuses on the surface fatigue class of failure, which is characterized by the removal of metal and the formation of cavities. These may be small or large and may grow or go into remission. They occur when the gear material fails after repeated stresses that are beyond the endurance limits of the metal. Four surface fatigue class damage modes are discussed

below:

Micropitting: When this fault is viewed under magnification, the surface is seen as a field of very fine micropits, usually 0.0001 inches deep. This is often an indication of marginal lubrication. If the conditions persist, these micropits grow and merge with others, producing larger cavities called pits.

Pitting: This fault involves the removal of material with a diameter around 0.015 inches to 0.030 inches in diameter. Pits occur in localized parts of the gear teeth that are over-stressed. This phenomenon is sometimes called corrective pitting because it tends to redistribute the load by progressively removing high-contact spots and often stops once the load has been redistributed.

Spalling: This fault is an extreme case of pitting. The faults are larger, quite shallow, and usually irregularly shaped. A customary dividing line between spalling and pitting is a pit diameters of 0.030 inches [6] As a spalled tooth meshes, a portion of the tooth does not carry the load. This results in a rapid redistribution of load and a large stress concentration around the pit's edges. Left unfixed, this can lead to accelerated material removal, resulting in excessive spall. This is characterized by increased vibration levels because the impulsive effect can excite previously dormant modes of the transmission. There is also the possibility that the pit can go into remission.

Destructive Pitting: This fault appears as much larger pits than initial pitting, often in the dedendum section of the gear teeth. These larger craters usually are caused by more severe overload conditions and are characterized as spalls

whose size does not stabilize. As stress cycles build up, destructive pitting continues until the tooth profile is destroyed.

Figure 1.2 is an example of a spall on a spur gear. It has an irregular shape

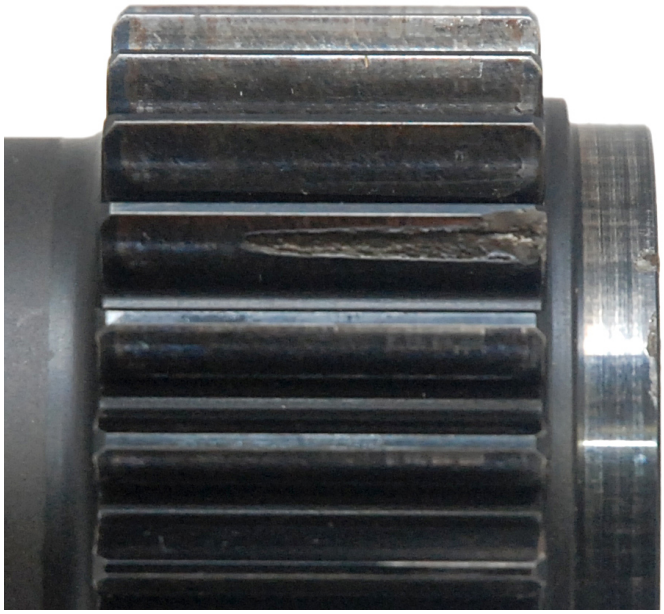

Figure 1.2: Spall Example

and takes up a considerable percentage of the tooth face. It is not possible, just from inspection, to determine if this fault is spall or destructive pitting. If the conditions that allowed the spall to develop and grow persist, it is possible that the fault would become destructive pitting, eventually leading to tooth breakage causing major damage to the aircraft. The prospect of tooth loss highlights the need for a reliable means to detect and assess damage in its infancy, granting adequate correction time to avert catastrophe, lower costs, and save lives.

1.3 Detecting Helicopter Gear Damage

In the last 30 years, researchers have attempted to develop qualitative and quantitative gear fault detection methods. [5, 7–22] Typically, a system is compared to a previous undamaged state over many flight hours and various tools are used to detect when the system deviates from the baseline. The effectiveness of the methodology is governed by its ability to discriminate between the changes due to operating conditions versus those truly due to damage. Decisions to abort a mission or to remove a helicopter from service for inspection or overhaul are based the output of this system. Thus, false alarms have the potential to be costly. In addition, the system should not be so insensitive that many faults are missed, leading to accidents and possibly the loss of lives. Thus, the number of false alarms, which can be as high as 1 per 1,000 flight hours, must be kept to a minimum. [23] In order to increase the probability of a correct diagnosis, it is best to learn as much about the system as possible. This is accomplished by understanding the gear system's fundamental properties and how 1.) they are affected by damage and 2.) how the damage manifests in measured signals.

1.4 Sensors

Damage can change how the system vibrates at different locations, produce changes in the system's acoustic spectrum, and modify the relative angular positions of the transmission's input/output shafts. In addition, damage can produce debris which can fall into the transmission oil supply. All these signals can be simultaneously measured and, when synchronized to the gear system's physical orientation, aid in the

pairing of dynamics measurements with possible sources and produce a higher level of interrogation than would be achieved by a single, un-synchronized sensor. This research collects data from multiple sensor modalities.

The bulk of the research in helicopter **HUMS** uses transmission mounted accelerometers to collect data. Microphones, including direct microphones, acoustic intensity probes, and acoustic arrays have also been used. [24, 25] In addition, transmission error sensors have been used to measure the differences between the rotation angles between the input and output shafts and provide an estimate of the relative tooth deflections during meshing. These can range from optical encoders to torsional accelerometers and are characterized by their maximum angular resolution, which is usually given in seconds of arc. Chip detectors serve as the means for damage detection in current helicopters. Such a device is incorporated into the oil line; if a piece of metal flows through it, the metal will short a circuit and initiate an action which may involve an alarm or simply an indicator light in the cabin. Oil debris sensors are more sophisticated versions of chip detectors and are capable of detecting both ferric and non-ferric materials in the oil as well as providing an estimate of the size of the debris. A running count as well as rate is used to assess the level of damage.

1.5 Gearbox Vibration Database

The body of full-scale seeded fault data for which to validate new damage detection methodologies is scarce. Conducting seeded fault tests in-flight is extremely dangerous and is not recommended. Thus, a researcher has to use data that was

either 1.) simulated, 2.) obtained from a known in-flight fault case, or 3.) obtained from seeded fault tests in the laboratory.

In 1996, a National HUMS Technology Road map was started with the goal of advancing the state of HUMS technology. The participating organizations included NASA, the FAA, the Department of Defense, and the Rotorcraft Industry Technology Association (RITA). [26] This road map defined the existing HUMS efforts, the state of HUMS technology, and technology needs. One of the needs identified as the result of this exercise was to enhance the effectiveness of diagnostics algorithms in the detection and isolation of faults in helicopter drive trains. The need for a central data repository for vibration data and existing diagnostics algorithms was identified. Sikorsky took the lead in developing a database storing the existing diagnostics algorithms and vibration data collected from multiple gearboxes for analysis. The database enables the user to apply different raw data to multiple algorithms and compare the results. [23] In this work, three seeded fault tests are conducted across two transmission platforms.

1.6 Scope and Contribution of Current Work

This work introduces three new tools to aid in sun gear fault detection and validates its use on a full-scale OH-58, models A and C, helicopter transmission. Test were conducted at NASA Glenn Research Center in Cleveland, Ohio, using various dynamics sensors. Planetary indexing is used to synchronize all measured signals with the transmission gear orientation allowing excitation sources to be isolated.

In 2005, Samuel successfully demonstrated planetary fault diagnostics using vibration separation techniques to locate seeded planet gear faults on a low-power transmission. This work is an extension of that research.

The specific damage modes of interest are pitting and spalling on two sun gears and a single planet bearing. To date, no other full-scale seeded fault tests with planetary geometry synchronized measurements of acoustics, vibration, and transmission error have been conducted. The seeded fault test conducted for this study are short duration, with the assumption that long time duration methods would be used to identify the possibility of damage, and the methodology developed in this research is used as a second-tier analysis to provide a higher degree of interrogation with the aim of reducing the number of false alarms.

The contributions of this work are:

- Development of three damage detection algorithms: two based on sun gear vibration separation and one based on measurements synchronized with the gear's planetary geometry .
- Demonstration of how the sun gear mesh group signature in vibration separation signatures is used to uniquely identify damage being attributed to the sun gear.
- Contribution to the damage detection database of carefully collected, geometrically synchronized, dynamic data for three damage cases of a full-scale helicopter transmission at full torque loads accelerometers, microphones, and torsional accelerometers.
- Demonstration that acoustic data can be used to detect damage using vibration

separation techniques.

1.7 Organization of Dissertation

Each of the following chapters is summarized below:

Chapter 2: **Literature Review:** This chapter highlights the work done by previous researchers in the field of helicopter transmission diagnostics. It also introduces many of the fundamental fault- detection techniques and condition indicators used in this current work.

Chapter 3: **Gearing:** This chapter provides some background information on gear dynamics needed to 1.) understand the measured signals, 2.) gain insight into the effects of damage on gear teeth, and 3.) develop the kinematic relationships needed for fault detection.

Chapter 4: **Vibration Separation:** This chapter discusses the vibration separation concept and introduces two new methods for sun gear vibration separation (**SGVS**). In addition, a geometrically synchronized measurement method of transmission diagnostics is also introduced, which exploits the correlation between measurements and planetary geometry as an alternative method to detect faults.

Chapter 5: **Experimental Setup:** This chapter discusses the experimental setup on the 500 HP OH-58 test rig at NASA GRC in Cleveland, Ohio.

Chapter 6: **Results:** This chapter gives the results for two seeded fault cases on the OH-58C and one on the OH-58A.

Chapter 7: **Summary, Conclusions, and Recommendations:** This chapter

summarizes the major findings and provides recommendations for future work.

Chapter 2

Literature Review

2.1 Early Work

The Helicopter HUMS concept has been around for four decades. In 1972, Houser and Drosjack started a program at Ohio State University in conjunction with NASA to investigate the many means of using vibration signals to detect the condition of mechanical components, with particular emphasis on gears and bearings in the helicopter power train. [27] Another early investigation into health monitoring of helicopter gears and bearings was conducted by the Royal Australian Navy in 1977. It established a vibration spectral analysis program to assist in the health assessment of the main rotor gearboxes on its fleet of Westland's Sea King and Wessex helicopters [28]

2.2 **HUMS**

HUMS is a subset of the larger Condition Based Maintenance (**CBM**) program, which also contains a Prognostics branch. An often cited architecture is the Open System Architecture for Condition Based Maintenance (OSA-CBM), which is illustrated in Figure 2.1. [29] The **HUMS** portion is divided into four modules: Data Acquisition, Data Manipulation, Condition Monitoring, and Health Assessment.

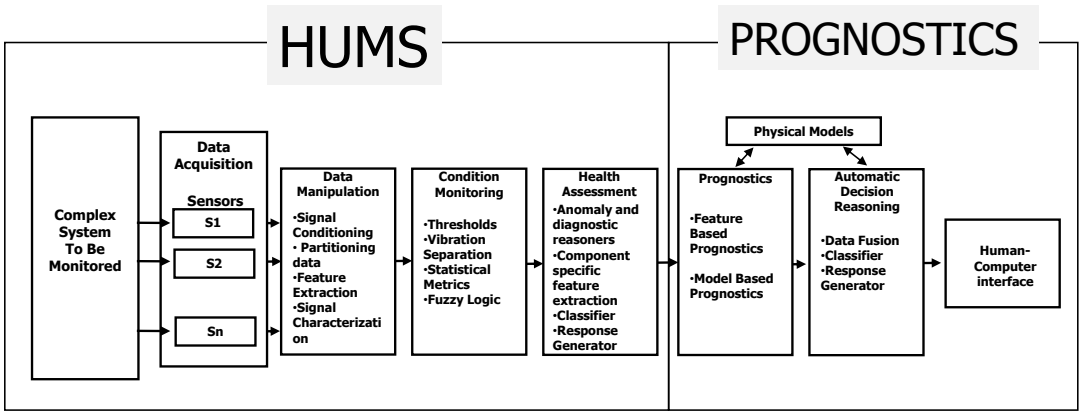

Figure 2.1: Condition-Based Maintenance

Data Acquisition: This module provides the **CBM** system with the sensor's signals used to monitor critical systems.

Data Manipulation: This stage conditions the data. This could include filtering unwanted signals, averaging, and partitioning based on known shaft cycles.

Condition Monitoring: This module uses various damage detection algorithms to create condition indicators that give a measure of a system's health.

Health Assessment: This is the decision-making module that weighs the calculated condition indicators against predetermined thresholds and, if necessary, prompts some corrective action.

The primary focus of the Prognostic branch is to calculate the future health of a system and/or component.

As a testimony to the importance of this modern maintenance philosophy, in 2007, CBM was mandated by the US Department of Defense. [30]

2.2.1 Helicopter **HUMS**

Helicopter **HUMS** is the advanced maintenance strategy applied to helicopters. It aims to ensure that the overall helicopter is operating safely and within specifications. It gives feedback to maintenance personnel to enable them to catch possible costly problems in their infancy. The key motivators for Helicopter **HUMS** are increased safety and reduced cost.

A typical helicopter **HUMS** system monitors the health of the rotor system, engines, airframe, and transmission. For the rotor system, the rotor's track and balance are monitored and reports of the necessary adjustments are made. In addition, the composite rotors are monitored to detect matrix cracking, delamination, and fiber breakage. [3, 31–33] For the engine, parameters such as takeoff power adequacy and degradation trends are monitored. The transmission is monitored to ensure that the gears, bearings, and shafts are not damaged. The structural health of the airframe is also constantly monitored.

In addition to monitoring the health, the helicopter's usage is also tracked. Information such as flight hours, engine starts, and exceedance is logged and collected. This information aids personnel in maintenance and procurement both in making repairs and properly stocking inventory. Before **HUMS**, vehicles were routinely taken out of service for unnecessary preventive maintenance, a costly practice.

2.2.2 Helicopter Transmission **HUMS**

This work focuses on the helicopter's transmission. Gears mesh with a characteristic vibration signature. As a system become damaged, this signature changes, producing abnormalities. The traditional approach to fault detection relies on human expertise to identify the abnormalities. However, it would be useful to develop reliable methods that allow inexperienced users to detect and characterize fault conditions. This is especially true in the military environment, which experiences a high turnover in maintenance personnel. Because of this, a means to process measured information, quantify the amount of damage, and use resulting values to produce an action item is essential for an effective fault-detection program. This is the the role of Condition Indicators (**CIs**). Traditional **CIs** deal with data distribution with the basic premise that measured signals have a deterministic structure based on operating conditions. Analysis tools look for statistically significant deviations from the baseline signatures and attempt to relate deviations to occurrences of damage.

Currently, vibration measurements are the main techniques for monitoring the health of a helicopter transmission. Signals from accelerometers mounted to a helicopter gearbox have a distinct frequency spectrum dependent on internal meshing dynamics. Since the transmission system is periodic, its spectrum contains components at shaft frequencies and their harmonics, as well as the fundamental gear mesh frequencies and their harmonics. These are considered the system's regular components.

In the late 1970's, Stewart investigated the changes in vibration signals of trans-

mission systems due to damage. [34] He observed that under no-fault conditions, a transmission's vibration signal tends to be dominated by the regular component and a generally Gaussian noise floor. This can be described as follows:

$$x_{perfect}(t) = \sum_{n=0}^{\infty} P_n \cos(2\pi f_m n t + \phi_n) + w(t) \tag{2.1}$$

where $x_{perfect}(t)$ is some idealized signal, P_n and ϕ_n are the amplitude and phase of the n^{th} harmonic respectively, f_m is the mesh frequency, and $w(t)$ is the noise which is assumed to have a normal distribution.

Errors in manufacturing, tooth spacing, tooth profile, alignment, and installation, as well as damage have been shown to manifest as modulating signals, thus producing sidebands in the measured signal. These modulating functions are also periodic with the shaft frequency and can be divided into two components: amplitude modulation, $a(t)$ and phase modulation, $b(t)$. These can be written as

$$a(t) = \sum_{n=0}^{\infty} A_n \cos(2\pi f_s n t + \alpha_n) \tag{2.2}$$

and

$$b(t) = \sum_{n=0}^{\infty} B_n \cos(2\pi f_s n t + \beta_n) \tag{2.3}$$

where A_n and B_n are the amplitudes of the n^{th} harmonic and α_n and β_n are the phase. The shaft frequency is given by f_s. For amplitude modulation, the sidebands represent scaled versions of the modulating function's frequency spectrum. Finding the FM sidebands is more complex and is dependent on the frequencies of a modulator function, $b(t)$, a modulation index value, and the solutions of Bessel functions. [35]

The equation representing the vibration signal is obtained by modulating $x_{perfect}$

with $a(t)$ and $b(t)$:

$$x(t) = \sum_{n=0}^{\infty} P_n(1 + a_n(t)) \cos(2\pi f_m n t + \phi_n + b_n(t)) + w(t) \tag{2.4}$$

Equation 2.4 demonstrates that detecting errors in the transmission system is possible by analyzing the sideband activity of the signal. For example, an eccentric shaft gives a slight change in center distance between gears every cycle. This manifests as a once-per-revolution fluctuation in mesh force producing an AM signal that results in sidebands spaced at the shaft frequency. Other contributors to amplitude modulation are tooth profile errors, tooth pitting, and spalling. In addition, the relative relationship between the gears and sensors also creates sidebands. The modulation can often be seen as a lobe pattern in the data associated with a planetary gear system.

If the teeth are manufactured such that the spacing on a tooth is incorrect, the engagement/disengagement schedule is disturbed, producing an FM signal. This effect can be caused by other factors, such as torsional vibration, pitch error, or the loss of tooth stiffness, possibly due to a root crack.

2.3 Statistical Condition Indicators

2.3.1 Time Synchronous Averaging

The periodicity of the measured signals can be exploited to isolate only the dynamics of interest. An effective means for minimizing the non-synchronous components in a measured periodic signal is the Time Synchronous Average (**TSA**). This is

the process of partitioning the data into individual shaft cycles and averaging across the cycles. As a consequence, the non-synchronous parts of the signal act as random components with zero mean and fall off at a rate of $1/\sqrt{N}$. McFadden calls this process the equivalent to passing the vibration signal through a comb filter which has pass bands at multiples of the rotation frequency of the gear of interest. Increased averaging has the effect of reducing the width of the comb teeth. [36]

For shafts rotating at a constant velocity and data acquired at a constant sampling rate, there is a 1:1 correspondence between the shaft's angular position and time. However, this is rarely the case because most shafts vary in speed, even slightly. Therefore, it is necessary to interpolate the data to pre-determined angular points so that the time synchronous averaging is conducted at like angles. A typical result for a vibration signal on the OH-58C is given in Figure 2.2. The x-axis is the frequency normalized by the gear mesh frequency. These are referred to as gear mesh orders and they make it easier to identify off-order components such as those due to the input pinion. The top plot is one cycle of data and the bottom is the result of 118 averages. The off-order components as well as the noise floor have been reduced significantly.

After **TSA**, waveform patterns associated with the meshing teeth often emerge. In some cases, it is possible to identify damage from inspection. However, if the damage is in its infancy, it may be difficult to isolate it from inspection. Thus, many techniques have been proposed to increase the detectability of damage in the **TSA** signal to make the early signs of gear failure easier to detect. The role of condition indicators is to provide a value that gives insight into the level of damage of a component.

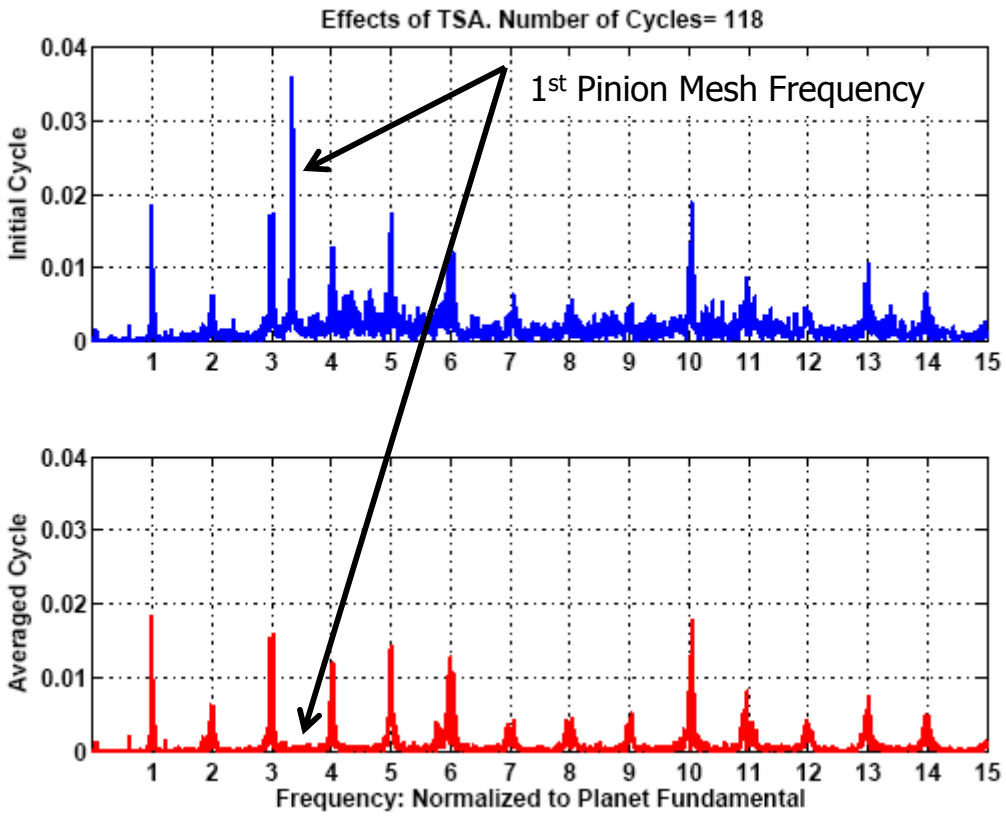

Figure 2.2: Effects Of TSA - Baseline Case

Stewart was the first to apply condition indicators to transmissions. [34] He observed that in a healthy transmission, the amplitude of the sidebands were small and were significantly increased in the presence of a fault. This was especially true for local defects, such as single tooth failure. In 1977, he introduced a set of algorithms to compute condition indicators, termed Figure of Merit. These had names like FM0, FM2, and FM4, and increased in complexity as the order increased. The most promising metric, FM4, works on the premise that the vibration signal for an undamaged system contains distinctive energy at known mesh and bearing frequencies. If a new signal, termed the difference signal, is synthesized that removes these non-random dynamics, then an assessment can be made on that resultant signal. Un-

der undamaged cases, all that should remain is Gaussian white noise characterized by a normal distribution. If the new signal contains distinctive components in the spectrum, then it is assumed that damage is the culprit.

The FM4 algorithm utilizes the kurtosis as a tool to test the "goodness of fit" of the difference signal to a normal distribution. The normalized kurtosis is described by:

$$\text{Kurtosis} = \frac{\frac{1}{n}\sum_{i=1}^{n}(x_i - \overline{x})^4}{\left(\frac{1}{n}\sum_{i=1}^{n}(x_i - \overline{x})^2\right)^2} \tag{2.5}$$

where x_i is each data point and $\bar{x}$ is the mean. The kurtosis value, relative to 3, gives an estimation of the amplitude distribution of the resultant signal, in particular its peakiness. Figure 2.3 shows three types of distributions. The first one is termed

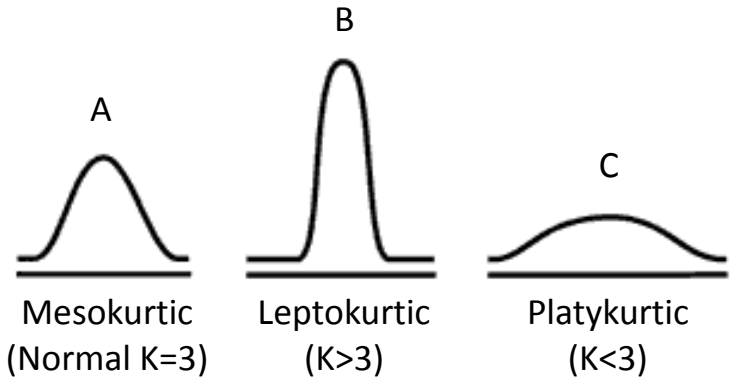

Figure 2.3: Possible Distribution Functions

mesokurtic and has the characteristic bell shape of a normal distribution. A normalized kurtosis value of 3 predicts Gaussian white noise. The other two distributions are discussed relative to the mesokurtic. The leptokurtic is characterized as having a standard deviation value less that that for the normal distribution and the opposite for the platykurtic. Figure 2.4 gives examples of distributions and their corresponding

kurtosis values. It shows the time plot, data distribution relative to a normal distribution, and computed kurtosis values for five different distributions. The normal distribution curve shares the same mean and standard deviation as the signal, but its amplitude is normalized to enable overlapping. The first plot is a normal distribution

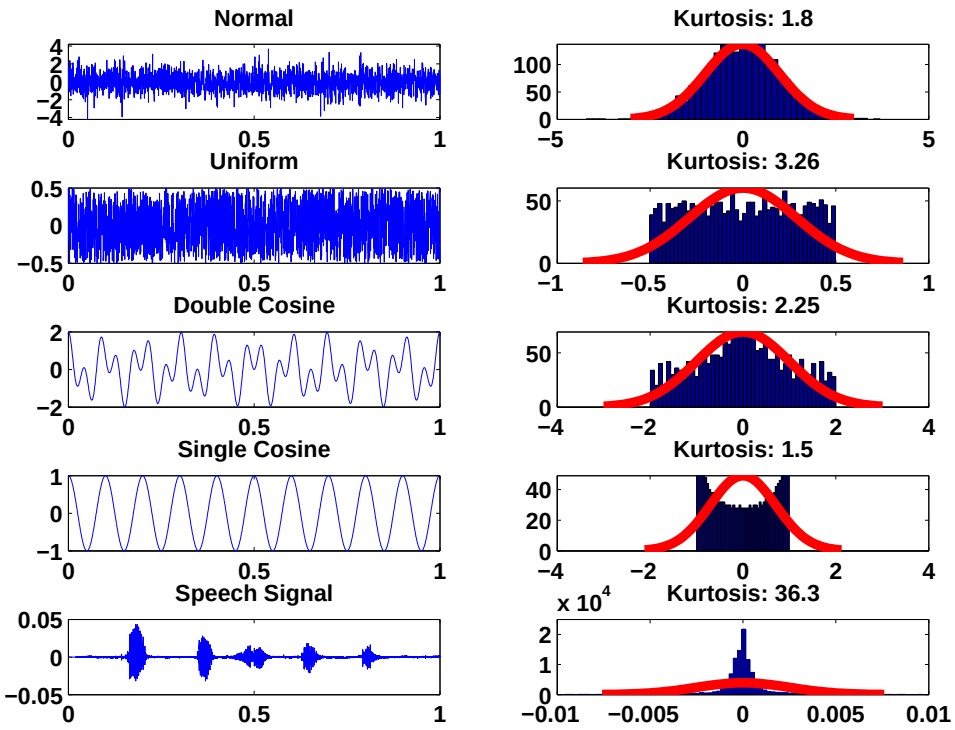

Figure 2.4: Distribution Examples and Kurtosis Values

and is used to provide a baseline for the others. The second distribution is uniform and produces a platykurtic profile because it is wider than the normal. The third and fourth signals were generated using only cosine functions. The third had two components and the fourth had a single component. The distributions becomes more platykurtic with an extreme case corresponding to the harmonic signal and a kurtosis value of 1.5. A leptokurtic signal is characterized as having spaced pulses which are indicative of speech signals. The signal used as an example was created by speaking

"A-B-C-D-E" into a microphone. However, in the case of gear damage, it could be produced with multiple gear tooth faults.

In 1985, McFadden amended the Royal Australian Navy's program (discussed earlier) to incorporate synchronous averaging, narrow-band enveloping, and FM4. [28,37] It was found that the fault in the input bevel pinion of the main rotor gearbox of an RAN Wessex WAK143 could have been diagnosed 100 hours prior to its crash into the Bering Strait in 1983 had this method been used. The data set from this tragic event has been used by subsequent researchers as a means to validate newly developed damage detection schemes. [28]

As discussed previously, the FM4 **CI** is the kurtosis of a modified signal called the difference signal. This is the original **TSA** signal with its gear mesh frequencies, harmonics, and first-order sidebands removed. Other condition indicators, namely M6A, and M8A, also operate on the difference signal; however, the **CI**, NA4, operates on a similar signal called the residual and differs in that the first-order sidebands are preserved. The next section gives additional insight into these two modified signals, how they are determined, and expectations when using synthesized signals.

2.3.2 The difference and residual signals

Many of the **CIs** investigated look at the statistical properties of either the difference signal, $d(t)$, or residual signal, $r(t)$. This section discuss how these signals are determined. If the signal to be tested represent a full shaft cycle, then $T_{cycle} = \overline{N}\Delta t$, where $\overline{N}$ is the number of points in a cycle, and Δt is the sampling rate. Therefore,

when taking a standard FFT, the frequency resolution, $\Delta f = f_{samp}/\bar{N} = 1/T_{cycle}$, is equal to the shaft frequency, f_{shaft}. This says that all Fourier coefficients are computed at integer multiples of the shaft frequency. This means, for example, if the first gear mesh frequency and its first-order sidebands are removed, this would involve modifying only three points. As an example, define an equally spaced frequency vector, f_{vec} that spans 0 to the Nyquist frequency and let the gear mesh frequency be $99 f_{shaft}$. Since f_{vec} starts at 0, the target frequency is simply $f_{vec}(100)$. Its sidebands are $f_{vec}(99)$ and $f_{vec}(101)$. In general, the gear mesh frequencies are at index values corresponding to $GMF = (1 : n-1) \cdot N_{teeth} + 1$ where $n = f_{Nyquist}/f_{shaft}$, and the left side band (LSB) and right side band (RSB) would correspond to $LSB = GMF - 1$ and $RSB = GMF + 1$ respectively. Again, this represents the case for which a full cycle is used, which is usually the case when testing a complete carrier cycle. However, when analyzing other signals, more general approaches are needed. The following are three ways to determine the difference and residual signals.

1.) Compute the FFT of the signal and then a.) for the residual signal, set to zero the values corresponding to GMF using a bandwidth of f_{shaft} and b.) for the difference signal; also set the values corresponding to LSB and RSB to zero, again, using a bandwidth of f_{shaft}. Both the positive and negative frequencies are handled. The new signal is then created by taking the inverse-FFT of the modified signal. If $T_{cycle} = \overline{N}\Delta t$, then the previous method can be used.

2.) Use a high Q comb filter. In this method, a second order digital notch filter is created based on the target frequency locations. The quality factor is $Q = f_{target}/BW$, where BW is the rejection bandwidth and is set to isolate just the components of

interest. For $BW = f_{shaft}$, $Q = N_{teeth}$ for $f_{target} = f_{mesh}$. The comb filter is developed by cascading the individual notch filters. The final difference signal is created by filtering the target signal. This approach is a more general one and does not provide any benefit in a case where there are no Fourier coefficients between f_{shaft} intervals.

3.) Re-construct directly from Fourier coefficients and subtract from original signal. This method isolates the Fourier components of the frequencies of interest and recreates a signal in the time domain. Given a frequency vector, f_{vec} and Fourier coefficients, FT, the following formula is used:

$$y_{regular}(t) = 2 \sum_{I} FT(I) \cos(2\pi f_{vec}(I)t + \angle(FT(I))) \tag{2.6}$$

where I are the index values in GMF, LSB, and, RSB when finding the difference signal and just GMF for finding the residual. The difference and residual signals are then obtained by subtracting $y_{regular}$ from the original signal. This method is slow when compared to Method 1.

Figure 2.5a shows an example of computing the FM4 for a **TSA** acceleration signal taken from a baseline OH-58C. The first row is one cycle of data partitioned into 99 individual **TMPs**. The second row shows the frequency response and its highly periodic nature. The third row shows the remaining signal after the planet mesh, harmonics, and its first-order sidebands are removed. This is shown at the same scale as Row 2 to emphasize the removal of regular components. Row 3 shows the same remaining signal at the noise scale where the rejected regions are noticeable. The fourth row represents the difference signal in the time domain obtained by taking the inverse-FFT. The FM4 calculates how normally distributed are the amplitudes

of the difference signal. This example produced a value of 2.95 and a plot of its distribution relative to normal is given in Figure 2.7a. Figure 2.5b is an example of a synthesized signal representing an individual planet gear taken from a baseline case of the OH-58C. It is made up of a collection of individual tooth mesh waveforms. These waveforms have a high degree of correlation. A look at the frequency response reveals that this signal is made up of only a few planet mesh components. The third row reveals what is left when the planet mesh and its sidebands are removed. The fourth row shows the same resulting signal at the noise floor scale. The remaining signal is then converted back to the time domain and its distribution of values determined. For this almost perfect case, a value of 5.11 was obtained, illustrating that when working with synthesized signals, the noise floor may not be as Gaussian as a real signal, resulting in higher than nominal FM4 values. The distribution is given in Figure 2.7b.

Damage is introduced by scaling an individual tooth mesh waveforms. Figure 2.6a shows an example in which the third **TMP** is scaled by a factor of 2. The resulting FM4 value jumps from 5.1 to 31.8. This is due to the increase in the sidebands producing a wider distribution of values when $d(t)$ is converted back to the time domain. Its histogram is also shown in Figure 2.6c. The effect of multiple tooth damage is demonstrated in Figure 2.7b. The FM4 value for this case drops to 11.4 and the distribution, shown in Figure 2.7d indicates that the FM4 values does not continuously increase as the level of damage increases.

This provides the background information when interpreting the **CI** values based on the difference and residual signals.

As shown in the next section, many condition indicators are very similar to the FM4. By understanding how the FM4 works, other **CIs** can often be predicted.

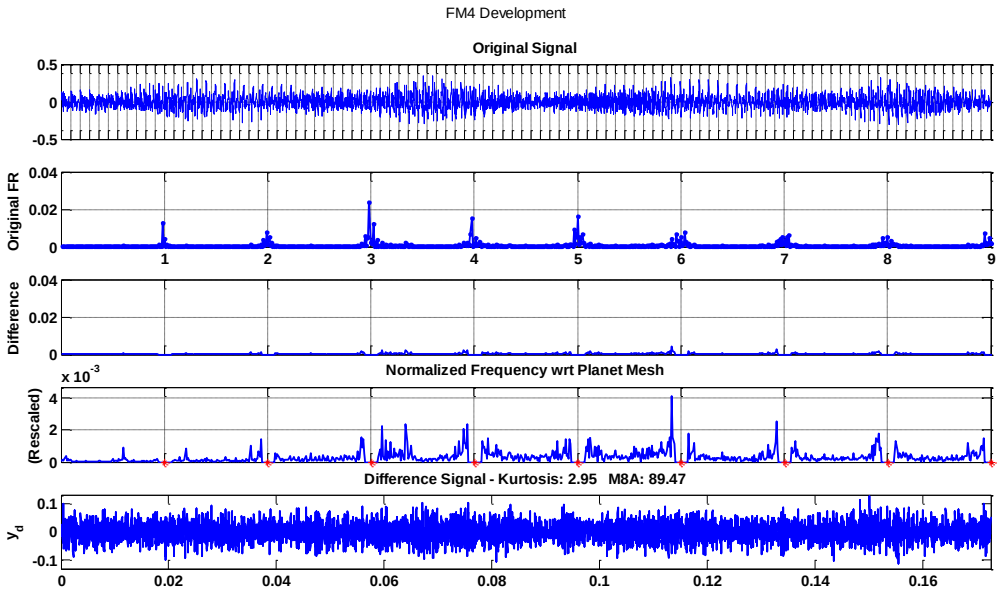

(a)

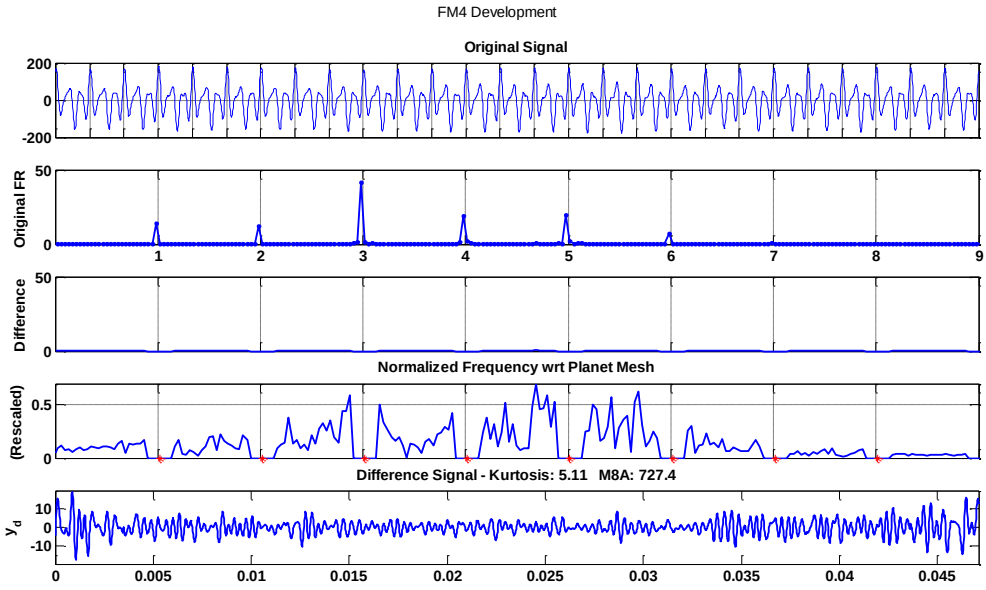

(b)

Figure 2.5: FM4 and Damage: TSA and Synthesized Signal

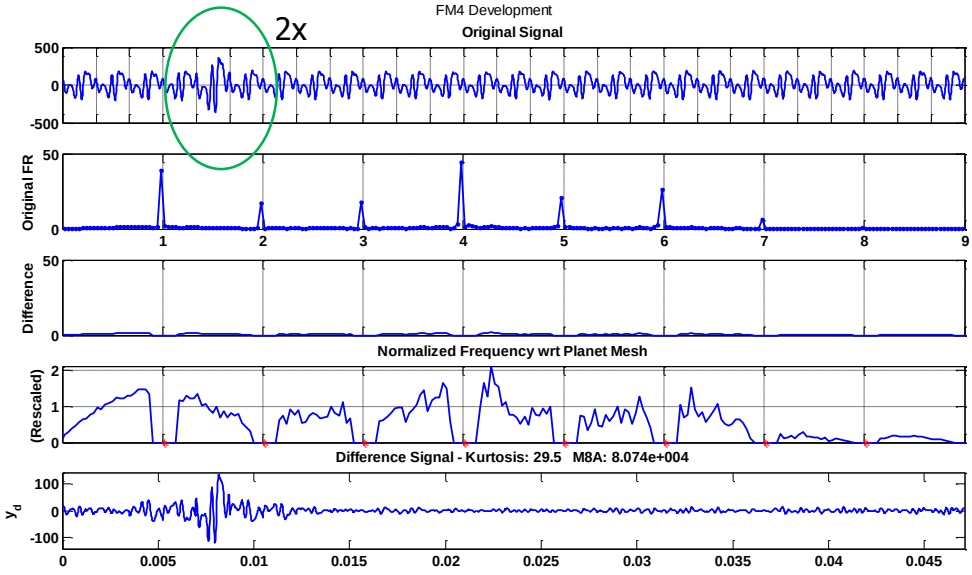

(a)

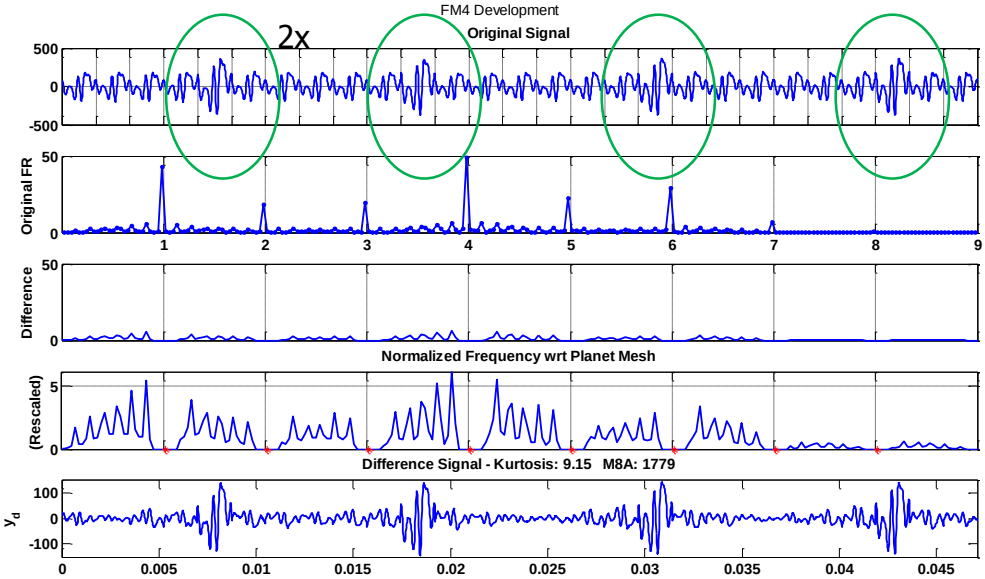

(b)

Figure 2.6: FM4 and Damage: Single Tooth and Multiple Tooth Damage

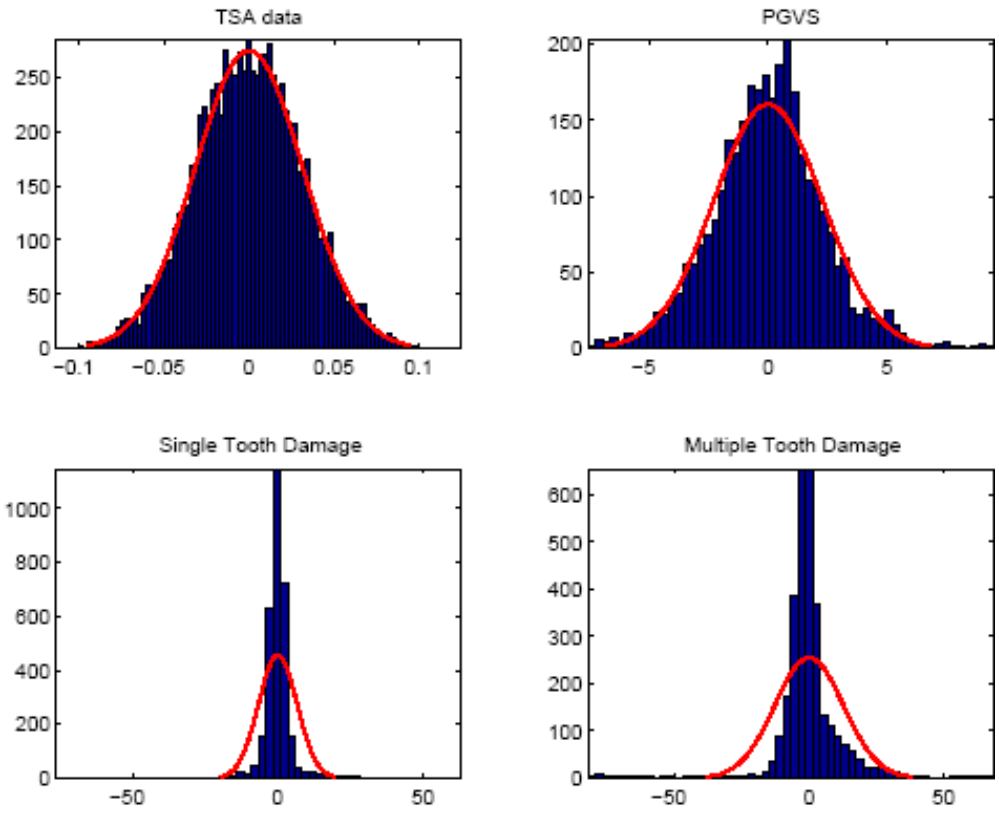

Figure 2.7: Effect of Damage on Difference Signal Distribution

2.3.3 Condition Indicators

The previous section discussed in detail the FM4 condition indicator. This next section discusses some of the other **CIs** used most often in the literature to analyze a measured signal $x(t)$: RMS, NA4, NP4, M6A, and M8A.

2.3.3.1 Root Mean Square (RMS)

The Root Mean Square (RMS) CI is given by:

$$CI_{RMS} = \sqrt{\frac{1}{\overline{N}} \sum_{i=1}^{\overline{N}} x^2(t_i)} \tag{2.7}$$

The main usage of this parameter is to monitor overall vibration levels. The RMS value does not increase with the isolated peaks in the signal; consequently, this parameter is not sensitive to incipient tooth failure. Nonetheless, it is still used in this work as a measure of intuition that a damaged system is expected to produce, on average, larger signals.

2.3.3.2 FM4 Parameter

The FM4 **CI** is a measure of the amplitude distribution the difference signal. This **CI** assumes that a gearbox in good condition has a difference signal with a Gaussian amplitude distribution, whereas a gearbox with defective teeth produces a difference signal with a major peak or a series of major peaks resulting in a less peaked amplitude distribution. If more then one tooth is defective, the data distribution

becomes flat and the kurtosis value decreases:

$$CI_{FM4} = \frac{\frac{1}{n}\sum_{i=1}^{n}(d_i - \overline{d})^4}{\left(\frac{1}{n}\sum_{i=1}^{n}(d_i - \overline{d})^2\right)^2} \tag{2.8}$$

where $d(t)$ is the difference signal described in Section (2.3.2).

2.3.3.3 NA4 Parameter

The NA4 CI was developed to improve the behavior of the FM4 parameter when more than one tooth is damaged. The first difference between NA4 and FM4 is that NA4 uses a residual signal to compute kurtosis which preserves the first-order sidebands. The second difference is the use of an average value of variance. Thus, if the gear damage spreads from one tooth to another tooth the value of the average variance increases slowly and allows the NA4 parameter to grow. The second reason why the NA4 parameter increases its value is that the residual signal contains the first-order sidebands, which increase when tooth damage occurs. The NA4 parameter is defined by:

$$CI_{NA4} = \frac{N\sum_{i=1}^{N}(\Delta r_i - \bar{r})^4}{(\frac{1}{M}\sum_{j=1}^{M}\sum_{i=1}^{N}(\Delta r_{ij} - \bar{r}_j)^2)^2} \tag{2.9}$$

where r_i is the i-th point in the time record of the residual signal, r_{ij} is the i-th point in the j-th time record of the residual signal, j is the current time record, i is the data point number per reading, M is the current time record in the run ensemble, and N is the number of points in the time record. When gear damage progresses, the averaged variance value increases rapidly, which results in a decrease of the NA4 parameter. To overcome this problem, the NA4* parameter was introduced. The fourth centralized moment of the residual signal is normalized with the average variance for a gearbox in

good condition. This allows the NA4* parameter to grow as the damage progresses.

$$CI_{NA4*} = \frac{N \sum_{i=1}^{N} (\Delta r_i - \bar{r})^4}{(\sigma(r_{OK}))^2} \tag{2.10}$$

The value $\sigma(r_{OK})$ is the variance for a gearbox in good condition.

Since this research only deals with short duration tests, only the NA4 **CI** is used and it will differ from the FM4 **CI** in that the residual signal also contains the 1st order sidebands.

2.3.3.4 M6A and M8A

These **CIs** were proposed by Martin to detect surface damage on machinery components. [38] Both of these features are applied to the difference signal. The theory behind M6A and M8A is the same as that for FM4, except that M6A and M8A are expected to be more sensitive to peaks in the difference signal because the higher exponents exaggerate the outliers in the signal. The equations for M6A and M8A are as follows:

$$CI_{M6A} = \frac{N^2 \sum_{i=1}^{N} (\Delta d_i - \bar{d})^6}{(\sum_{i=1}^{N} (\Delta d_i - \bar{d})^2)^3} \tag{2.11}$$

and

$$CI_{M8A} = \frac{N^3 \sum_{i=1}^{N} (\Delta d_i - \bar{d})^8}{(\sum_{i=1}^{N} (\Delta d_i - \bar{d})^2)^4} \tag{2.12}$$

2.3.3.5 NB4

This **CI** was developed in 1994 by Zakrajsek, Handschuh, and Decker as an indicator of localized gear tooth damage. [5] This **CI** is based on the Hilbert transform of a signal containing dynamics from only the region about the gear mesh frequency.

This is implemented by taking the FFT of the signal, doubling the left portion, selecting only the Fourier coefficients within a certain bandwidth of the mesh frequency for only the left half, and zeroing out the remainder, and then taking the inverse FFT. The kurtosis is then performed on the envelope of the signal. This is written as:

$$s(t) = |b(t) + iH(b(t))| \tag{2.13}$$

where b(t) is the signal band passed filtered about the mesh frequency.

2.3.3.6 NP4

Polyshchuk introduced the **CI** $NP4(n)$ which is the kurtosis applied to the signal's power [39]:

$$CI_{NP4}(n) = \frac{1}{N}\sum_{i=1}^{N}(\frac{P_n(t_i) - \overline{P_n}}{\sigma})^4 - 3 \tag{2.14}$$

where $P_n(t)$ is the signal power and n represents the number of gear mesh harmonics removed in the residual measured signal. [40] If the two parameters, $NP4(0)$ and $NP4(1)$ are greater that some positive threshold number, it would indicate damage.

2.3.3.7 CAL4

In 2003, Samuel conducted research on detecting damaged gear teeth of planetary systems [41] Due to the nature of the multiple teeth in mesh, a vibration separation scheme was used to reconstruct the vibration signature that would be generated if each gear was in a spur gear configuration. The **CIs** were then computed using the resultant signal. Using the diagnostic **CI** , CAL4, successful detection and location of damage in seeded fault cases was accomplished. This was one of the first studies

is which individual gear tooth meshes were investigated for damage detection. The CAL4 **CI** is based on the lifting scheme. Lifting is a time-domain prediction-error realization of the wavelet transform. It was developed as a method for creating new bi-orthogonal wavelets in settings where the Fourier transform could not be used, such as on bounded domains and on curves and surfaces. [1] For healthy gears, individual tooth mesh waveforms are divided into monotonic functions and approximated by low-order spline functions. Then, when this model is compared to a damaged system which may be incapable of being described by a low-order model, a high prediction errors results. A prediction error vector, created by concatenating individual prediction errors for each tooth on a given gear, is created and the kurtosis is computed. Denoting this vector as R:

$$CI_{CAL4} = \frac{N \sum_{i=1}^{N} (R_i - \overline{R})^4}{\left(\frac{1}{n} \sum_{i=1}^{N} (R_i - \overline{x})^2 \right)^2} \tag{2.15}$$

is weighted against 3.

A table of common condition indicators, along with descriptions, is found in Appendix B on page 221.

2.4 Damage Detection Analysis Tools

Determining effective methods to make condition indicators more sensitive to damage has been the subject of much research. Pulses, like those due to impacts, have their frequency content spread over a wide range in the frequency domain, making them non-distinct. However, this feature is often identifiable in the time domain. Thus, time domain methods would are more effective for such signals. Likewise, for

signals with strong harmonic content for the duration of the period studied, distinct features are identifiable in the frequency domain but may not be as noticeable in the time domain. For damage that manifests in this manner, a frequency-based method can be effective. Ideally, time-frequency methods aim to balance the benefits both domains have to offer.

One time domain techniques includes individual waveform analysis using cross-covariance. Some frequency domain techniques include FFT and Cepstrum. Some time-frequency domain techniques include short-time-Fourier-transforms, wavelets, and WVD, and some model-based approaches include system identification and neural networks. In 2005, Samuel and Pines conducted a state-of-the-art review of vibration based techniques, and additional information can be found at this reference [1].

2.5 Testing on the OH58 at NASA

The effect of RPM and torque levels influences the ability of damaged modes to be detected. Mosher, et al, conducted in-flight tests, demonstrating that current damage detection algorithms are dependent on torque levels, and proposed the ideal flight conditions to maximize damage sensitivity. [42, 43] Flight tests were conducted on an OH-58C Kiowa at NASA Ames Research Center (ARC). In these tests, acceleration, torque, RPM, aircraft positioning, and velocity was recorded. Eight standard flights were conducted and data was collected continuously throughout the flight of various maneuvers. The collected data provided 740 data records of 34 seconds each. It was found that for the flights, most of the data fell in the range of 40% to 80%

torque and 356 to 362 rotor RPM. For the planetary gear system, it was found that the amplitude and phase of the first gear mesh component showed a strong dependence upon torque and increased as the torque increased. An increase in phase as the torque increased was attributed to torsional strain in the shaft and the relative positioning between the tachometer sensor and the accelerometers.

Three uni-axial accelerometers and a single tri-axial accelerometer was used. Principle Component Analysis (PCA) was used analyze the vibration on three orthogonal axes into one single principle axis corresponding to the direction of maximum variance using a linear combination of the three accelerometer signals. [44] It was determined that the principle axes were consistent with the housing geometry, thus, only single axis accelerometers were used in this study.

Dempsey, et al, investigated the threshold of condition indicators using data from a spur gear fatigue rig at NASA GRC to set values for flight tests on an OH-58C conducted at NASA ARC. [45] The metrics investigated were FM4 and M8A. For the spur gear fatigue rig, run-to-failure test were conducted and the metrics were applied to data at different times during the test. This allowed metrics to be computed for baseline, onset of damage, and damage. The input spiral bevel pinion of the flight test data was the target of analysis. Values of 4.04 for the FM4 and 394 for the M8A was chosen as thresholds. For each maneuver, the **CIs** were computed and compared with these set thresholds. When applied to the flight test, which represents an undamaged case, only one maneuver would have produced a suspect waveform.

In 1997, Nachtsheim conducted tests seeded fault test on the OH-58A transmission on the 500 HP test stand at NASA GRC. [46] Seeded damage was introduced

using file marks cut on nine alternating teeth on the 19-tooth input spiral bevel pinion gear. The loading was increased monotonically and the tests were stopped when five of the seeded teeth were either fractured or a partially separated. Plots of the data shows increasing spectral activity in the lower frequency range. The analysis method chosen filters out frequencies above the pinion's first mesh frequency.

Lewicki, et al, conducted accelerated fatigue tests while testing advanced lubricants. [10]. Tests were conducted on the OH-58A and OH-58C transmissions with the goal of producing planet bearing and sun gear fatigue, mast-shaft ball bearing micropitting, and spiral bevel gear scoring. The test matrix used had different test durations (50-100 hours), input torque (100% to 117%) of design maximum, oil pressure (21% to 100%), inlet oil temperature (180^o to 275^o F), and mast radial loading (0%-100%) of design max. The resulting damage components serve as the test components in this current work.

Jammu, et al, ran accelerated fatigue tests on the OH-58A generating various component faults. The transmission ran from four to eight hours a day, from between nine and fifteen days. The transmission was periodically disassembled and inspected. A condition indicator based on the weighted sum of eight mounted accelerometers was compared to the same metric determined from a lumped parameter model of identified vibration paths. In addition, these values were used in a fuzzy logic algorithm called Structure Base Connectionist Network (SBCN). These test produced three planet bearing pitting fatigues, three sun gear pitting fatigue and five damaged components. Damage due to the sun and the bearing were detected in advanced stages.

2.6 Detecting Gear Tooth Damage using Alternatives Signal

2.6.1 Acoustic Sensors

Noise in helicopter gearboxes arises from both structure-borne and airborne sources as transmission elements make contact. Mesh-induced vibrations propagate throughout the gear drive system and produce sound from the components that radiate efficiently. Dominant spikes commonly found in noise spectra tests are typically a combination of gear and bearing characteristic frequencies, their harmonics and sidebands, as well as higher frequencies due to impact dynamics. The noise radiating from the complete gearbox comes from the mesh- induced vibrations propagating throughout the gear drive system, which includes the shafts, bearings, couplings, and housings, and is a function of the system's geometry as well as its excitation frequency. In the previous sections, accelerometers were the main signal collected and analyzed. While the use of vibration measurements has led to the development of several condition indicators, such techniques are susceptible to coupled structure-borne effects, thus complicating the acceleration signal with additional dynamics along the load path which often obscure gearbox faults. For example, roller bearings produce non-linear modulations to the generated vibration signal due to its rolling and sliding element which are difficult to quantify. Fortunately, gearbox faults also appear via other paths as a result of meshing dynamics. For example, sound radiation from gear contact offers an alternative method for detecting, classifying, and characterizing incipient failure modes of individual teeth.

Although there has been research on gear noise and its relationship to dam-

age, [47–50] no known, full-scale data sets incorporating geometrically synchronized, simultaneously acquired, acoustic and vibration measurements of healthy and faulty transmissions are known to the author to assess the merits of various damage detection algorithms. Most of the gear noise research found in the literature is from the standpoint of noise reduction and mainly focuses on the radiation of the entire gearbox and components connected to it. [47–52] There is not much work in the literature on using acoustic signals directly from meshing gears to detect and assess damage. This may be because the power of the sound at the source is insufficient to directly excite the gear housing. Thus, once the gears are enclosed, their contribution to the overall gearbox noise becomes negligible and difficult to measure. [53, 54] Another reason could be that since the environment for which measurements are taken is often noisy and complex, the acoustic signal will likely be contaminated, rendering the signal useless. [25] Fortunately, significant progress has been made in the capabilities of acoustic systems and signal processing making it possible to extract quality information from contaminated noise. [25] This current work presents one such technique. The direct noise from meshing gears is being re-investigated because the details of the signal's waveform are of interest in this research, more than overall sound pressure level (SPL) at the fundamental frequencies and harmonics which is what most gear noise papers explore.

As will be discussed in Chapter 3, transmission error is the main contributor to structure-borne noise in helicopter transmissions. Thus, methods of reducing the transmission error have been studied as a way to reduce noise. These studies can also be viewed in the framework of damage detection when the tooth profile is related

to noise generation. A study conducted by Lewicki, et al, showed the affects of profile modifications on gear noise on the OH-58 transmission. [51] In this work, acceleration as well as sound intensity measurements were taken simultaneously. The sound intensity was measured for various locations about the gearbox to obtain the global picture of the housing's radiation with the goal of finding a modification that provided an overall reduction is SPL. The average power spectrum was recorded for the test via an HP Spectrum Analyzer.

Shibata, et al, investigated using both microphones and accelerometers to monitor bearing damage. [55] They used Sound Dot Patterns as a means to visualize sound signals in a diagrammatic representation that maps the signal's autocorrelation to polar coordinates. They found that it was possible to distinguish differences between normal and faulty bearings.

Badi, et al, looked at using multiple sensors to detect damage in gears [56]. Both horizontal and vertical accelerometers as well as a microphone and stress wave sensor was used. The dynamics of the signals were more distinctive in both accelerometer signals and not quite a pronounced in the acoustic signal. The dynamics were non-distinctive in the spectrum of the SWS. Cross-spectrums of the different signals proved to provide more information than the sensors did individually. In this work, no attempt was made to interrogate the time domain signal.

Baydar and Ball researched the use of both acoustic and acceleration signals along with a pseudo-Wigner-Ville Distribution to detect progressing damage in a two-stage helical gearbox. [25] Three seeded faults conditions were tested: broken tooth, gear crack, and tooth wear. In this study, vibration and acoustic signals were

taken under similar conditions but not simultaneously. Baydar and Ball found that both signals were able to detect damage manifested as broadening of the frequency spectrum about the mesh frequencies due to modulation. In addition, they were able to locate the damage due to the dense location in the time-frequency plot. The acoustic signal was more sensitive to the early stages of crack development than the vibration signal. They explained this to occur because stiffness decreases and, thus, there is a smaller impact load producing a less pronounced signature. The vibration signal was more sensitive to a broken tooth. For the wear cases, when 25% and 50% of the tooth's face was removed, it was found that the spectrum of the acoustic signal concentrated to the fundamental of the meshing frequency.

2.6.2 Transmission Error

The main source of noise and vibration is the unsteady forces due to transmission error. Typically, in modeling gears behavior, the input / output relationships between a gear pair is $r_{in}\theta_{in} = r_{out}\theta_{out}$ where r_{in} and r_{out} represent characteristic gear radii and θ_{in} an θ_{out} are the rotation angles of two meshing gears. This relationship presents a good approximation at low speeds and low torques. However, at high speeds and torque, the relationship deviates. Transmission error represent changes in this relationship and is defined as:

$$TE = r_{out}\theta_{out} - r_{in}\theta_{in} \tag{2.16}$$

A constantly changing relationship between the input / output behavior be-

tween meshing gears provide the dynamic excitation that leads to vibrations and eventually structure-borne sound, thus providing an alternative dynamic signal to analyze. Li, et al, used transmission error measurements and an empirical model based approach to estimate the size of a gear tooth's root crack. [57] This was done by integrating a modulation profile into the dynamic stiffness used in a four-degree-of-freedom dynamic system with an output of transmission error when the resultant model was fitted to measured data and was found that the crack size estimates were in good agreement with the actual measurements.

2.6.3 Oil Debris Sensor

Analysis of wear particles can assist in determining the source of wear and the condition of the machine. In the aviation industry, this technique has been successfully employed for condition monitoring of rotation components prior to the introduction of vibration monitoring techniques. Today, it still serves as a complementary diagnostic tool for most aircraft/helicopter platforms.

Dempsey, et al, has conducted research on the use of oil debris sensors. [58] In this work, fuzzy logic was used to identify the damage level on each feature and to perform the decision level fusion process to the features.

2.7 Full-Scale Damaged Gear Datasets

The database of available full-scale data of a helicopter transmission system for both damaged and undamaged cases is fairly small. Already mentioned was the

case for Westland. This data was obtained as part of the Air Vehicle Diagnostics System project funded by the Office of Naval Research in 1993. [59] The data consist of eight accelerometer signals from each of 68 no-fault and seeded-fault runs on the aft transmission of a CH46E helicopter. Another source of experimental data is from NASA's in-flight tests and test rig tests on the OH-58A/C transmission. [60]. This test rig was developed to test various advanced lubricants and advanced gear designs and to conduct damage detection research. In-flight tests were collected at NASA Ames. [42, 44, 45, 61, 62] Data from the current research, also collected at NASA GRC, is designed to match cases of the NASA Ames flight tests and contributes to the database of publicly available measurements for full-scale seeded fault tests.

Being able to couple measurements to gear system dynamics is an invaluable tool for fault detection. The next section will discuss some of the work that has been done in the field of gear dynamics.

2.8 Gear Dynamics

The first systematic study of gear dynamics was started by Ross in 1927 and Buckingham in 1931. [63,64] Buckingham's results were based on studies on dynamics loads conducted by an ASME committee on gear dynamics. The committee's major finding was that dynamic loads were considered to result mostly from tooth errors that occur mainly as the load transfers from one tooth pair to the next. These errors are related to the stiffness of individual teeth. Original work on gear tooth stiffness was done by Walker in 1940, and Weber in 1949. [65] The first vibratory model for

gear dynamics was suggested by Tuplin. [66–68] Subsequent researchers investigated the effect of gear errors and excitation to time varying mesh stiffness on the dynamic loads. [66, 69–77] In 1959, Attia used strain gauges mounted directly to a gear tooth and instrumented through a slip ring to measure tooth strains during meshing. [78] A plot showing his results and the relative location of the meshing tooth is given in Figure 2.8. [78] This represented one of the first works in which strain gauges were

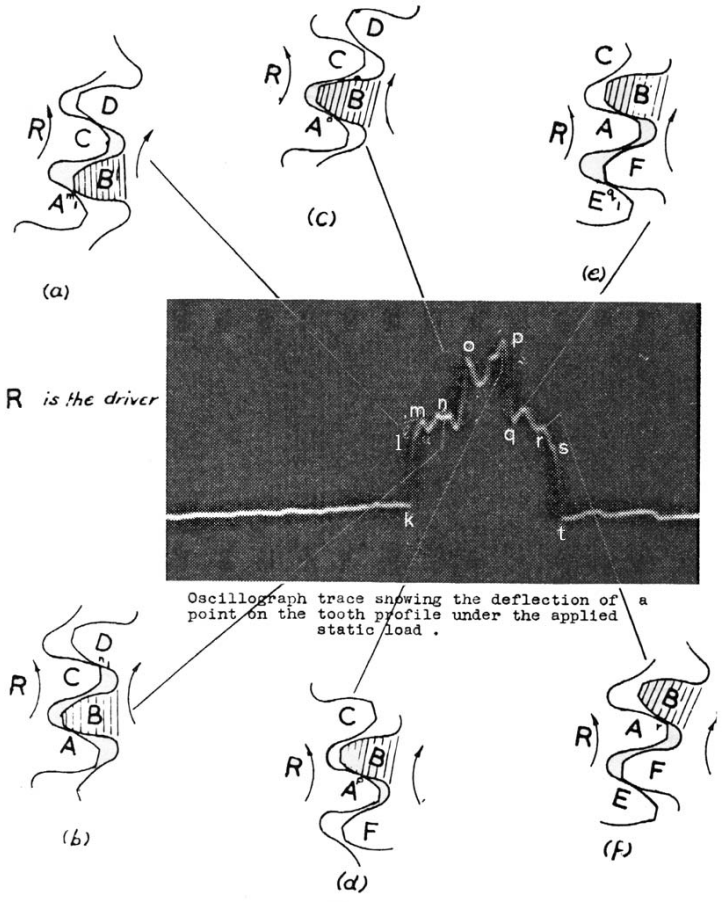

Figure 2.8: Measured Static Tooth Deflection (Attia 1959)

mounted directly to the tooth.

In 1968 and 1970, Munro looked at the effects of pitch errors and profile errors on the transmission error. [79] In 1970, Houser and Seireg developed a generalized

dynamic factor for spur and helical gears. [80] In 1972, Ichimaru and Hirano, investigated spur gear error under heavy load and showed that the change in tooth profile showed a characteristic trend to decrease dynamic load. [81] In 1978, Cornell and Westervelt presented a closed form solution for a dynamic model of a spur gear system and showed that tooth profile modification, system inertia, damping, and system critical speeds have significant effects on dynamic loads. In 1981, Cornell developed a meshing stiffness model for both low-contact ratio gears (LCRG) and high-contact ratio gears (HCRG). In this development, three contributors to tooth defection were taken into consideration: cantilevered beam deflection, deflection due to a flexible foundation, and Hertz contact stress. [82, 83] In 1988, Lin, et al, presented a governing non-linear dynamical model of spur gear transmission and studied the effects of each parameter on the dynamic factor. In these papers, an algorithm was introduced that was later used by NASA GRC in its Dynamic Analysis for Spur Transmissions (DANST) computer code. [84] This code, originally written in Fortran, was rewritten in Matlab™for use in this work. In 1999, Parker, et al, developed a lumped parameter model of a planetary system and showed that there are three types of modes for evenly spaced planets: rotational, translational, and planet modes. [85] Subsequent work showed that, for unequally spaced planets, the aforementioned mode structure is lost, except in the case of diametrically opposed planets. [86]

Chapter 3

Gearing

Gears are used to transmit power and change direction, speed, and torque while maintaining constant speed ratios. The most widely used are spur gears due to their ease of manufacture as well as their efficiency, which is typically on the order of 98% for well-designed gears. Spur gears are used on parallel axis systems and can be both external and internal.

Almost all of today's parallel axis gears (spur and helical) use involute tooth profiles. This is a tooth shape for which, at any given point along its face, the surface normal is tangent to the gear's base circle. Figure 3.1 is used to illustrate this concept.

Often this process is visualized as a string, $\overline{AA'}$, being unwrapped and held taut around a circle of radius r_b. The angle ϵ_{RA}, termed the roll angle, is measured from a point on the base circle and extends to the point of tangency between the profile's normal and the base circle at point A. The angle ϕ is the instantaneous pressure angle and varies with position along the tooth. The angle θ is measured from the start of the involute at the base circle and extends to the position vector of the involute profile r_{RA}. By nature of the involute, the length of $\overline{AA'}$ is the arc of the unwrapped portion of the base circle, therefore $\overline{AA'} = r_b\epsilon_{RA}$ and the following relationship is found

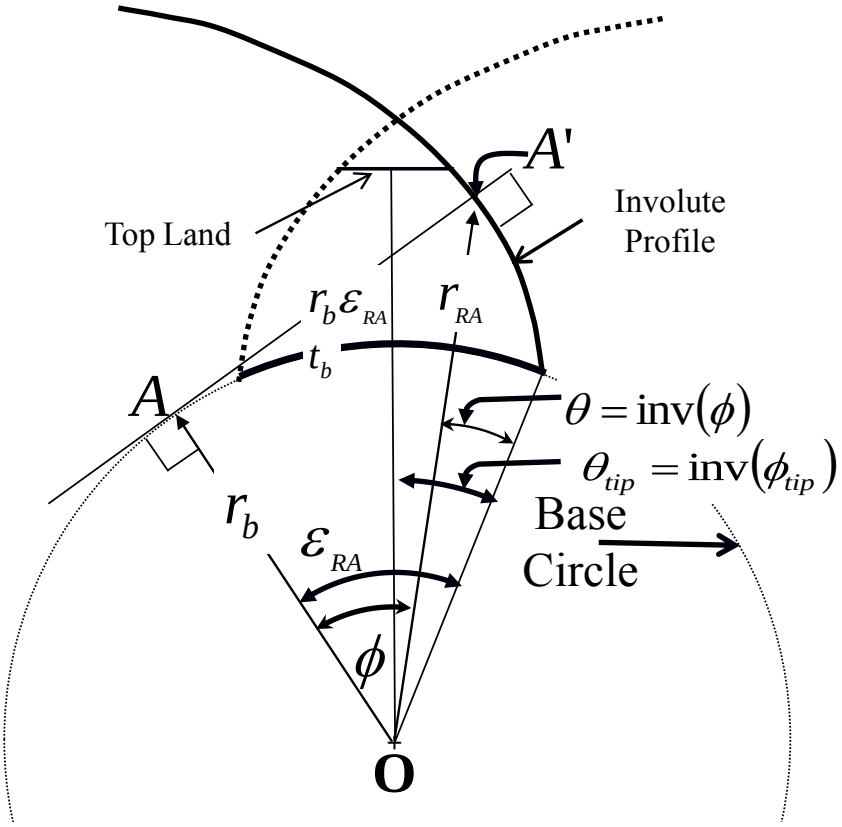

Figure 3.1: Involute Profile

$$\tan(\phi) = \frac{r_b \epsilon_{RA}}{r_b} = \epsilon_{RA} = \phi + \theta. \tag{3.1}$$

The angle, θ, is determined from Equation 3.1 by defining the involute function:

$$\text{inv}(\phi) \doteq \tan(\phi) - \phi = \theta \tag{3.2}$$

The position vector, r_{RA}, is now given by:

$$r_{RA} = \frac{r_b}{\cos(\phi)} = \frac{r_b}{\cos(\text{inv}^{-1}(\theta))} \tag{3.3}$$

where $\text{inv}^{-1}(\theta)$ give the value ϕ that satisfies Equation 3.2 and is solved iteratively. Points along the involute are often described in terms of the roll angle, $\epsilon_{RA} = tan(\phi)$.

The tooth shape is formed by mirroring the involute across the y-axis as shown by the dotted lines. The two involute merge at a point, but a practical tooth has a top land. The angle from the start of the involute to the point of intersection between the two involutes is θ_{tip}. The transverse circular base tooth thickness is given by t_b and is selected as a convenient datum thickness that can be determined experimentally by span measurements. It can also be calculated from the knowledge of any other thickness, t_i as:

$$\frac{t_b}{2r_b} = \theta_{tip} = \left(\frac{t_i}{2r_i} + \text{inv}\phi_i \right) \tag{3.4}$$

The polar angle, which is the angle between the position vector and the center-line is given by $\text{inv}(\phi_{tip}) - \text{inv}(\phi)$.

The pitch circle is an imaginary circle such that when the two gears are mated, their pitch circles are tangent. The point of tangency is termed the pitch point. Figure 3.2 shows the meshing region between two external spur gears. For each tooth, the normal to the surface is tangent to its base circle; therefore, when in mesh, the mutual normal is tangent to both base circles producing the pressure line. The pressure line, $\overline{AF}$, also passes through the pitch point. This geometry produces a stationary pitch point, which is the requirement for a pair of gears to maintain a constant gear ratio, termed conjugate tooth action. Additional benefits include insensitivity to small errors in center distance, ease in manufacturing, and interchangeability. When $r_{RA} = r_p$, the instantaneous pressure angle is equal to the shape cutter angle, α_c, of the cutting tool used to make the gear.

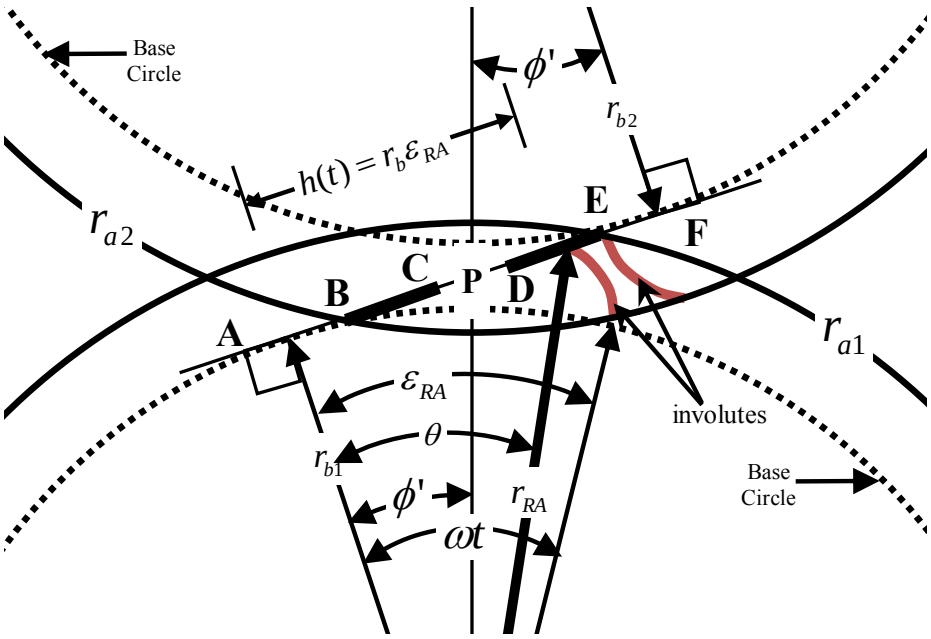

Figure 3.2: Detailed Gear Parameters

A fundamental condition for two gears to properly mesh is that they must share the same base circle pitch. When two gears are mated, the angle between the base circle tangent point (A or F) and the centerline is the operating pressure angle, ϕ'. This is the instantaneous pressure angle when $r_{RA} = r_p$. This angle is shared, therefore:

$$r_{p1} = r_{b1}\cos(\phi') = \frac{N_1}{N_2} r_{b2}\cos(\phi') \tag{3.5}$$

resulting in:

$$\frac{N_1}{2r_{p1}} = \frac{N_2}{2r_{p2}} = DP \tag{3.6}$$

where DP is termed the diametrical pitch of the gear. Therefore, if standard gears are used, compatibility is ensured if the mating gears share the same DP and cutter edge angle, α_c. Typical cutter edge angles are 20^o and 25^o. Larger pressure angles result in thicker teeth and increased root strength, thus higher load-carrying capacity;

however, smaller pressure angles provide higher contact ratios, the measure of the average number of teeth in contact, resulting in smoother and quieter operation.

For perfectly involute gears, the points of contact between the meshing gears occur along the pressure line. The addendum circle is the circle that the gear's top land sweeps out during rotation. Most gear standards defines this radius as $r_a = \frac{1}{DP}$ inches beyond the pitch circle, but this is often modified to improve performance. The dedendum is the distance from the pitch point to the bottom of the gear's fillet. The two main values usually used for the dedendum radius are $r_{root} = \frac{1.25}{DP}$ (AGMA 201.02) or $r_{root} = \frac{1.157}{DP}$ (ANSI B.6.1).

3.1 Gear Tooth Profile Generation

In gearing, small changes in tooth profiles can have a large effect on the system's vibration and noise signature. [50, 51, 87] In addition, being able to accurately determine the geometric coordinates of each gear in a planetary set is an invaluable tool when analyzing geometrically synchronized measurements. Because of this, a kinematic model is developed that incorporates accurate representations of gears. The previous section gave the equation for the involute portion of the tooth. Various methods are available that discuss the generation of the fillet region as well as techniques on determining the intersection point between the fillet and the involute which involves the solution to a non-linear equation. [6] This section describes the generation of the entire gear including the involute, top land, and fillet within a single framework which is more general in nature and lends itself to generating more

complex geometries.

3.1.1 Simulating the Manufacturing Process

The main methods to manufacture gears are rack generation, hob generation, and shaping. For rack generation, a rack cutter is reciprocated across the gear blank's face and its cutting edge generates the conjugate tooth profiles as the cutter and rack move in relative motion. Hob generation is similar to rack generation, except that the rack is in the form of a worm gear and, in effect, gives an infinitely long rack. Shaping uses a cutter with the same shape as the mating surface. Of these, hob generation is the most widely used method and usually results in accurate parts. [6] Internal gears are typically manufactured using shaping.

In deriving the gear's geometry, the rack cutting process is simulated and curves that satisfy the meshing equation produce the locus of points that define final gear's shape. [88] In Figure 3.3, there are two coordinate systems: S_1 and S_f.

The system S_1 is mapped to S_f using the following transformation matrix:

$$T_{f1}(\phi) = \begin{bmatrix} \cos\theta & -\sin\theta & x_f \\ \sin\theta & \cos\theta & y_f \\ 0 & 0 & 1 \end{bmatrix} \tag{3.7}$$

where $x_f = r\cos\phi$ and $y_f = r\cos\phi$. This ϕ should not be confused with the pressure angle. A mapping from S_f to S_1 is determined by taking the inverse of Equation 3.7, $T_{1f} = T_{f1}^{-1}$. If a coordinate system, S_2, exists, it too can be mapped to the S_f in a like

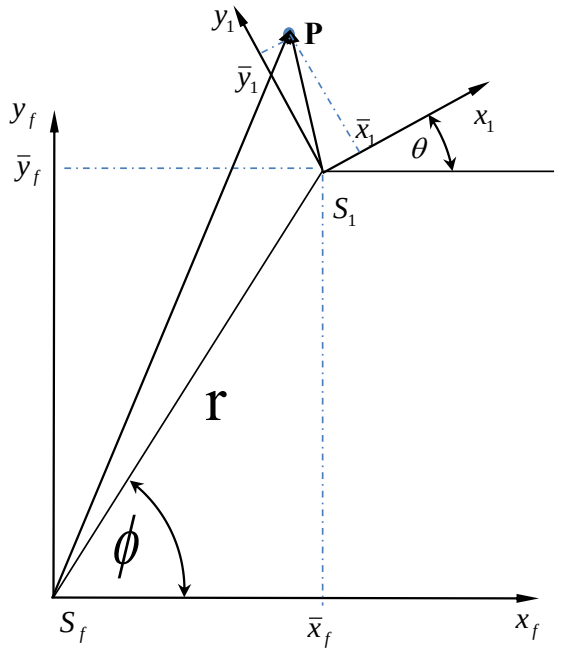

Figure 3.3: Coordinate Transformation

manner. In addition, a point in S_1 can be mapped to S_2 using the following identity:

$$T_{21} = T_{2f}T_{f1}. \tag{3.8}$$

where T_{2f} is the mapping from S_f to S_2.

Figure 3.4a shows the coordinate system used to generate external spur gears. It consists of three coordinate systems S_1, S_2, and S_f, representing the cutter, gear, and fixed coordinate systems respectively. In gear tooth generation, the generator (rack, hob, shaper), is described in S_1 and the goal is to create a gear in its own coordinate system, S_2. The generator is parametrically described in S_1 with surface coordinates (x(u), y(u)) as shown in Figure 3.4b.

The portion of the rack extending from A to C as well as from F to H generates the fillet region of the gear. The flat portion from A to B as well as from G to H

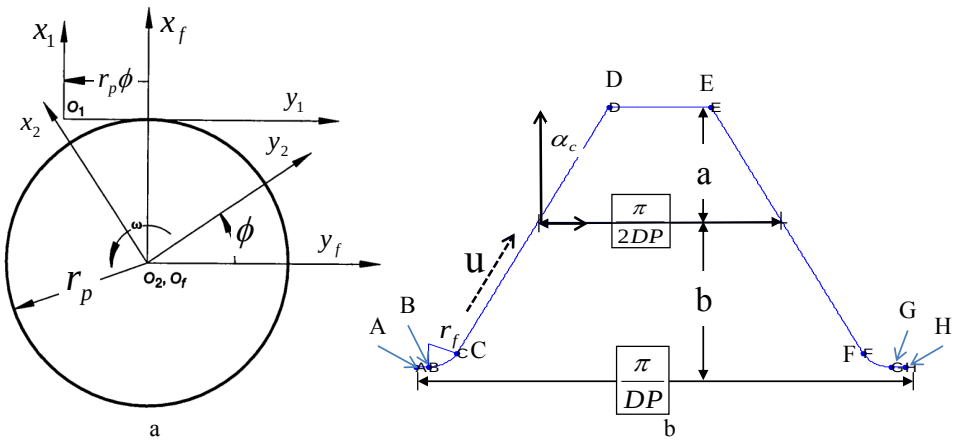

Figure 3.4: Cutting Rack Parameters

produces a flat region in the gear's fillet. If this length is zero, the rack will produce a fully rounded fillet. The edge regions, extending from C to D and from E to F, generate the involute tooth form. The region D to E generates the top land of the gear. The final gear has an addendum of $r_a = r + a$ and a dedendum of $r_{root} = r - b$. All important quantities are based on the diametrical pitchk, DP, and cutter pressure angle,α_c. A standard gear is cut when the depth of the cutter corresponds to the pitch radius of the blank. Deviation from the standard is obtained by changing the depth of the cutter by a predetermined hob offset value. This governs the addendum height as well as the tooth thickness. S_1 is shown in Figure 3.4a such that, as the blank, (S_2), rotates an angle ϕ, S_1 translates by $r_b\phi$. The mapping from the hob to the tooth is given by:

$$\vec{r}_2(\phi,u) = T_{21}(\phi)\vec{r}_1(u) = \begin{bmatrix} \cos\phi & -\sin\phi & 0 \\ \sin\phi & \cos\phi & 0 \\ 0 & 0 & 1 \end{bmatrix}^{-1} \begin{bmatrix} 1 & 0 & -r_p\phi \\ 0 & 1 & r_p \\ 0 & 0 & 1 \end{bmatrix} \begin{bmatrix} x(u) \\ y(u) \\ 1 \end{bmatrix} \tag{3.9}$$

The vector $\vec{r}_2$ is dependent on two parameters: the blank's angle, ϕ, and the cutter's surface parameter, u. In order for two surfaces to be considered in mesh, they must satisfy three conditions in the same reference frame. The frame chosen is arbitrary, but is usually the fixed frame:

1.) $\vec{r}_{1f}(\phi,u) = \vec{r}_{2f}(\phi,u)$

2.) Collinear Normals: $\vec{n}_{f1} = \vec{n}_{f2}$

3.) The mutual normal must pass through the center of rotation.

These conditions, when combined, form a system of equations termed the meshing equation and are given as:

$$f(\phi,u) = 0 \tag{3.10}$$

Figure 3.5 shows a family of curves for when ϕ is held constant and when u is held constant. The resultant gear tooth shape is determined when the family of curves $\vec{r}_f(\phi,\bar{u})$ and $\vec{r}_f(\bar{\phi},u)$ are tangent with each other. This is accomplished by solving the following meshing equation:

$$f = [\hat{k}\vec{r}_u\vec{r}_\phi] = \frac{\partial x}{\partial u}\frac{\partial y}{\partial \phi} - \frac{\partial y}{\partial u}\frac{\partial x}{\partial \phi} = 0 \tag{3.11}$$

for $\vec{r}_u = \frac{\partial x}{\partial u}\vec{i}_f + \frac{\partial y}{\partial u}\vec{i}_f$ and $\vec{r}_\phi = \frac{\partial x}{\partial \phi}\vec{i}_f + \frac{\partial y}{\partial \phi}\vec{i}_f$. This is generally implemented using a search algorithm to match each point surface coordinate (x(u),y(u)) with an admissible value ϕ. Theoretically, Equation 3.11 says that when two surfaces are in relative motion,

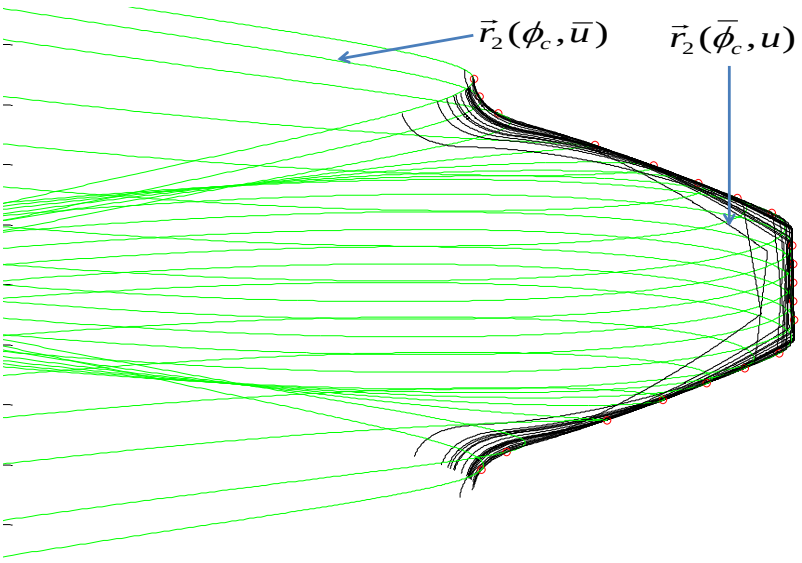

Figure 3.5: Solution Families used for Gear Generation

there exists a point along their line of centers for which the relative tangential velocity is zero. This point is termed the centrode. For spur gears, the centrode is the pitch point and since the coordinates for that point is known in the fixed frame, Equation 3.11 can be simplified. Referring again to Figure 3.4, the surface envelope is the surface for which the mutual normals between $\vec{r}_f(\phi, \bar{u})$ and $\vec{r}_f(\bar{\phi}, u)$ pass through this center of rotation at ($r\phi$,0). For this development, the meshing equation is given by:

$$f(\phi, u) = \frac{X(\phi) - x(u)}{N_y} + \frac{Y(\phi) - y(u)}{N_x} = 0 \tag{3.12}$$

where N_x and N_y are the components of the normal vector to the surface of the rack coordinates that lies in the same plane:

$$\vec{N_f} = (\frac{\partial y}{\partial u}\vec{i}_f - \frac{\partial x}{\partial u}\vec{j}_f) \tag{3.13}$$

For $X(\phi) = r\phi$ and $Y(\phi) = 0$:

$$\phi = \frac{1}{r}\left(y(u)\frac{y_u}{x_u} + x(u)\right) \quad x_u \neq 0 \tag{3.14}$$

which matches each point on the cutter, u, to a corresponding rotation angle, ϕ.

The rack coordinates are parameterized in its index value; therefore, $x_u = x(n+1) - x(n)$ and likewise $y_u = y(n+1) - y(n)$. Since x_u and y_u have only N-1 points, only N-1 points of $x(u)$ and $y(u)$ are used. If central difference is used to approximate the derivative, then only N-2 points are used. Once an admissible ϕ is matched to each surface parameter, u, the gear profile is generated in S_2 using Equation 3.9.

It should be noted that even though $x(u), y(u)$ may advance in one given direction, the value ϕ obtained from Equation 3.1.1 may not, thus the additional step of sorting the locus of points is needed to produce a continuous surface like those shown in Figure 3.6.

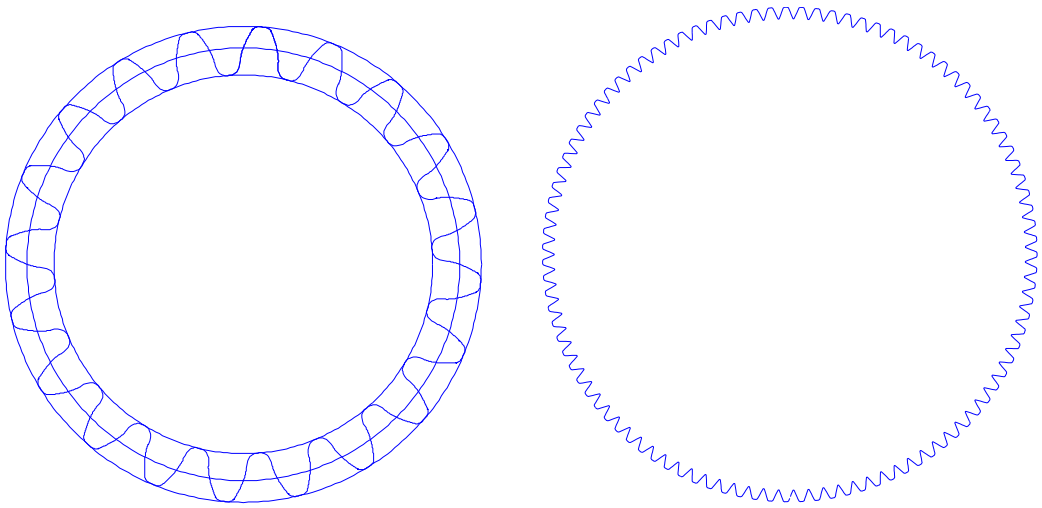

Figure 3.6: Generated Spur Gear: External and Internal

3.1.2 Ring Gear Generation

The ring gear is generated using the previously generated planet gear as a shaper. Describing it in S_1 with its origin at the center of the gear, it is mapped to the fixed frame using the following transformation matrix:

$$\vec{r}_2(\phi, u) = \begin{bmatrix} \cos\phi_p & -\sin\phi_p & rc\cos\phi \\ \sin\phi_p & \cos\phi_p & rc\sin\phi \\ 0 & 0 & 1 \end{bmatrix} \tag{3.15}$$

and the meshing equation is solved numerically. An example of a 99-tooth ring is given in Figure 3.6b.

3.2 Deviation from standard gears

The standards provided by the American Gear Manufacturers Association and the American Standards Association use rack parameters and are adequate if used within the specified limitations. Outside this region, the standards are often used as starting points for the final design. During operation, gears will deflect due to loading and the force vector will oscillate about the theoretical pitch point, resulting in a time-varying velocity ratio. The deviation from the constant velocity ratio is termed the transmission error and is the main contributor to gear vibration and acoustics. It can be corrected by tailoring the tooth's profile depending on expected loading. For gears that operate over a large range of loads, there are tradeoffs when deciding the operating load to target. The profile modification can be implemented in the cutting

stage by modifying the cutting tool or can be done after cutting using methods such as crowning. Other considerations are tip and edge relief as well as addendum length modification. Tip and edge relief is when the tips and/or side edges are rounded and used to avoid chipping due to a heightened stress concentration during meshing for the tip and misalignment for the edge. This has the effect of delaying mesh engagement and expediting tooth disengagement, with both resulting in a reduced contact ratio. A general rule of thumb is that if the gear carries more than 2,000 pounds per inch of facewidth for more than 10^6 cycles, it should have tip relief. [89] Figure 3.7 shows a typical profile modification chart where zero represents the involute and all modifications are done measured normal to the involute. [89]

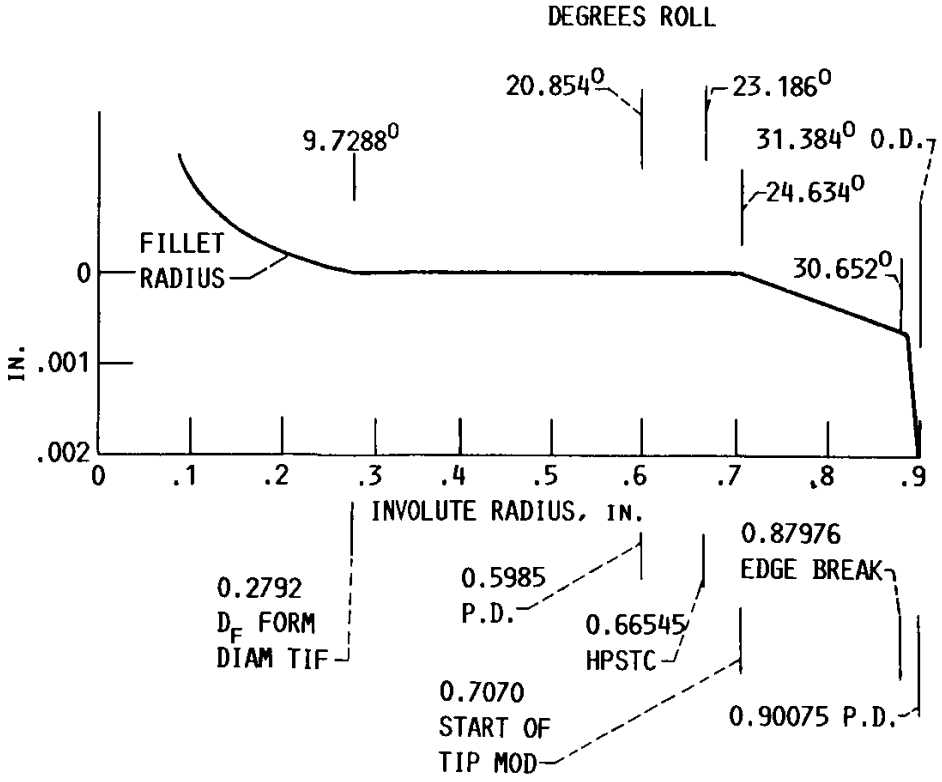

Figure 3.7: Profile Modification Chart (Townsend 1986)

Addendum length modifications are beneficial for gears of different radii by allowing a means to balance the shared load among such gears. As shown in Section 3.5.6, the gear tooth has a time-varying stiffness. When transmitting a force between two stiffnesses in parallel, the load sharing is based on the relative magnitudes of the stiffness. For equal stiffnesses, the load sharing is balanced; thus, the goal of addendum modification is to balance the load as much as possible throughout the entire mesh process. [90]

If the gears are mated such that their face widths are not parallel, then the load will not be distributed uniformly across the face and edge loading will result. This error often leads to damage and can be corrected by the use of crowning across the face making it thicker at center facewidth than at the ends. This produces a compromise between alignment errors and keeping the loads confined to the inner portions of the facewidth and as a result, reduces the load-carrying capability of the tooth since it acts to reduce the active facewidth. The crownings are not thick, on the order of .001" at the center. For spur and helical gears, this is done at finishing.

Modifications to the tooth profile, such as tooth wear, or chipped tip, also result in a deviation from the involute. However, these changes are considered damage. This highlights the importance of first developing a baseline for the undamaged case to account for these purposeful modifications.

3.3 Meshing Teeth

Gear tooth meshing can be separated into five stages: engagement, rolling / sliding contact, pure rolling contact, rolling sliding contact and disengagement as shown in Figure 3.8 along with a typical tooth mesh waveform. [41] The sliding

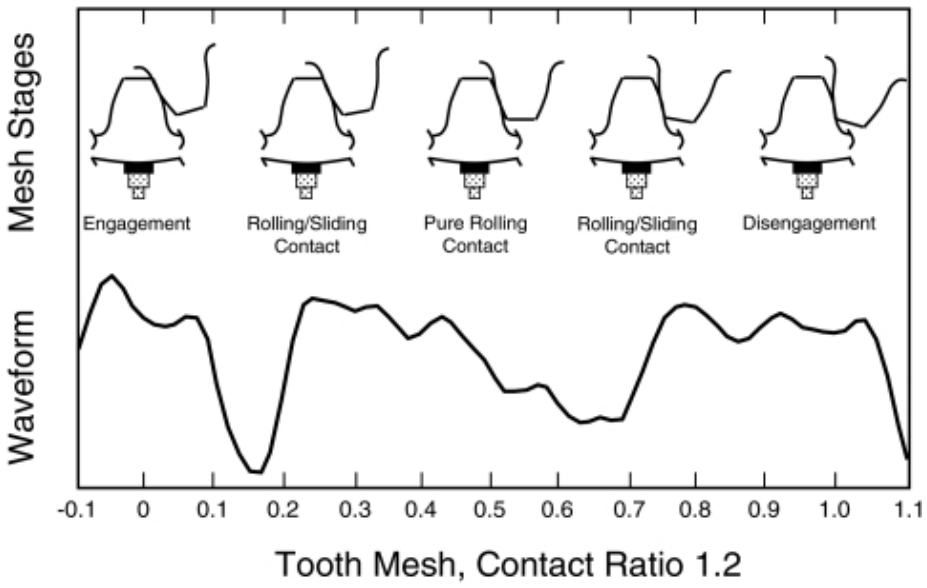

Figure 3.8: Meshing Stages (Samuel 2003)

occurs because, in general, the arc lengths between mating points along both teeth are different. The sliding speed, V_s, is expressed as:

$$V_s = r_{c1}\omega_1 - r_{c2}\omega_2 \tag{3.16}$$

where r_{c1} and r_{c2} are the tooth radii of curvature and ω_1 and ω_2 are the angular speeds of the gears. This reality manifests itself as a faint line along the gear tooth's face located at the pitch line, the location for which $r_{c1}\omega_1 = r_{c2}\omega_2$ and there is no relative sliding. Friction forces are produced as a result of this relative sliding; however, for

this research, it is assumed that this force has negligible contribution to sound and vibration, and the engagement and disengagement stages will be the focus.

Backlash between teeth must be sufficient to permit free action under the most severe combinations of manufacturing tolerances, alignment errors, and operating temperature variations. It can be introduced by thinning the teeth during manufacturing using a hob offset or by increasing the center distance. The recommended backlash for assembled spur gears is given in Table 3.1. [91]

DP (in^{-1})	1	1.5	2	2.5	3	4
ΔB ($in.$)	.025-.040	.018-.027	.014-.020	.011-.016	.009-.014	.007-.011
DP (in^{-1})	5	6	7	8-9	10-13	14-32
ΔB ($in.$)	.006-.009	.005-.008	.004-.007	.004-.006	.003-.005	.002-.004

Table 3.1: Recommended Backlash

An increase in center distance is accompanied by a change in the operating pressure angle due to an increase in the pitch radii:

$$\phi' = \cos^{-1}(\frac{r_{b1} + r_{b2}}{r_{p1} + r_{p2} + \Delta C}) \tag{3.17}$$

where the change in the center distance, ΔC, is determined from the backlash using the formula:

$$\Delta C = \frac{\Delta B}{2 \tan \phi}. \tag{3.18}$$

This pressure angle is different than α_c in Figure 3.4.

Figure 3.9 gives two diagrams showing the meshing of two spur gears and the key meshing points along the pressure line and the corresponding points along the tooth surface. In Figure 3.9a, the bold lines along the pressure line correspond to the region, within the mesh cycle, for which the two gears are in double tooth contact. The line segment, $\overline{AF}$, is the length along the pressure line from the two tangent

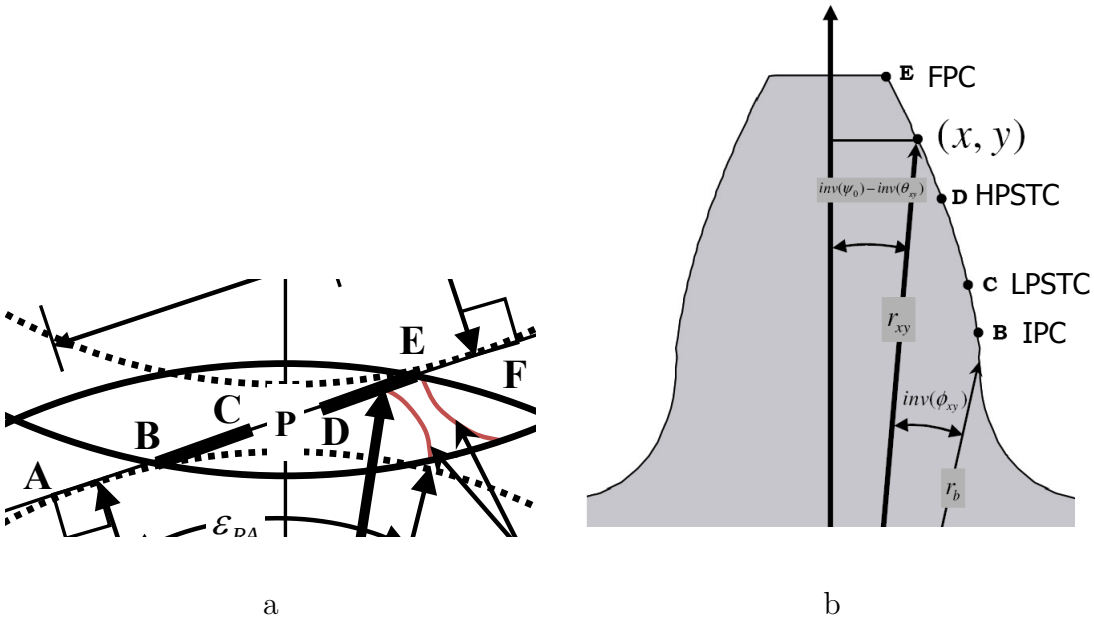

a b

Figure 3.9: Contact Points: a.) On the Pressure Line b.) On the Involute

points of each gear's base circle. The meshing period begins when the tail end of the effective addendum of the driven gear crosses the pressure line, point **B**. At this point, two teeth pairs are in contact, the current one and the previous one. This is characterized by reduced tooth forces due to the load sharing and is given the acronym IPC (initial point of contact). At point **C**, the driving gear's previous tooth is disengaging and the tooth is in single contact mode, characterized by a large increase in load on the current tooth. This position is the lowest point of single tooth contact

(LPSTC). This continues until point **D**, at which time the addendum of the driven gear's ensuing tooth passes the pressure line and the gears are in double contact mode again. Point **D** is termed the highest point of single tooth contact (HPSTC) and is significant in that it is usually the point along the tooth that experiences the highest load. The tooth engagement ends at point **E**, the final point of contact (FPC), when the effective addendum of the driving gear's current tooth passes the pressure line. The tooth mesh period (**TMP**) is represented by $\overline{BD}$. The contact ratio, C_r, is a measure of the average number of teeth in contact during a complete rotation. It is given by the ratio of the path of contact length, $\overline{BE}$ to the base tooth pitch P_b. For most spur gears, $1 < C_r < 2$. Gears with $C_r > 2$ are considered high contact ratio gears (HCRG) and are characterized by smooth and quieter operation. Contact ratios greater than 2 can be achieved by having an addendum larger than the standard $\frac{1}{DP}$ or by decreasing the pressure angle. Both modifications produce a tooth with more involute surface for which to mesh and will result in a narrower and weaker tooth-that

is, there are design tradeoffs. The relevant relations are:

$$\overline{AF} = (r_{b1} + r_{b2}) \tan \psi' \qquad \overline{BF} = \sqrt{r_{a2}^2 - r_{b2}^2}$$

$$\overline{AB} = \overline{AF} - \overline{BF} \qquad \overline{AE} = \sqrt{r_{a1}^2 - r_{b1}^2}$$

$$\overline{EF} = \overline{AF} - \overline{AE} \qquad \overline{BE} = \overline{BF} - \overline{EF}$$

$$\overline{AP} = r_{b1} \tan(\phi') \qquad \overline{BP} = \overline{AP} - \overline{AB}$$

$$\overline{FP} = r_{b2} \tan(\psi') \qquad \overline{EP} = \overline{FP} - \overline{EF}$$

$$\overline{BD} = \overline{CE} = \overline{AD} - \overline{AB} \qquad \overline{AD} = \overline{AB} + \overline{BD}$$

$$\overline{AC} = \overline{AD} - \overline{CD} \qquad \overline{BD} = \overline{CE} = P_b$$

$$\overline{CD} = 2\overline{P_b} - \overline{BE}$$

where the modified pressure angle due to backlash, ϕ', is used and $P_b = \frac{2\pi r_b}{N}$ is the base pitch for N teeth.

Since the initial contact is delayed due to backlash, the length of the path of contact is shortened, which results in a decrease in the contact ratio. However, the constant speed ratio is unaltered, which is one of the benefits of an involute tooth profile.

3.4 Planetary Gears

Planetary gears are a subset of parallel axis epicyclic gears for which the ring gear is fixed and the in/out members are the sun and carrier. This configuration provides the benefit of high load carrying capability in a compact design and is used throughout the helicopter and propeller-driven aircraft industry as well as in the

resurgent windmill industry.

A four planet example is given in Figure 3.10.

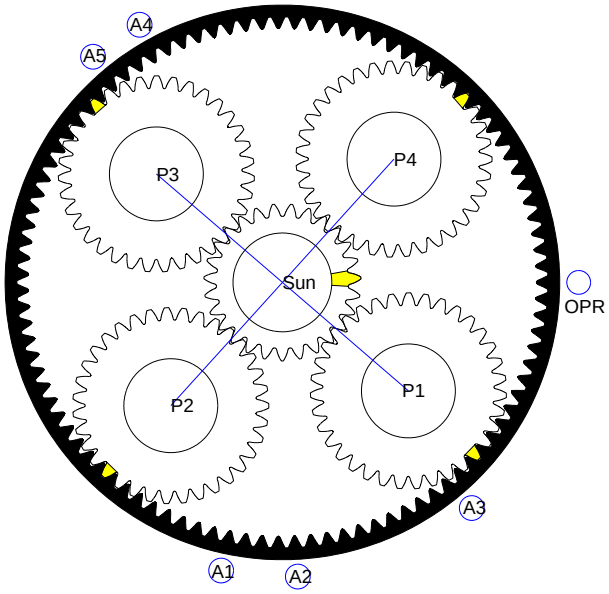

Figure 3.10: Planetary Gear Example

In this example, the sun gear, located in the middle, is surrounded by four planet gears. The planet gears mesh simultaneously with the sun gear and the outer ring gear. The planets serve idler roles; thus, they are not considered in the final gear ratio. The planet gears are all attached to a carrier plate that rotates in the same direction as the sun. In the helicopter reduction stage configuration, the sun gear provides the input and the helicopter's shaft is attached to carrier. The gear ratio is given by:

$$\frac{\theta_{sun}}{\theta_{carrier}} = \frac{N_r}{N_s} + 1 \tag{3.19}$$

and since they are the same sign, rotate in the direction. Although planetary gears are often used to produce different speed ratios, as in an automobile's automatic

transmission, their current use in helicopters maintains a constant speed ratio. There is, however, active research in the area of variable-speed helicopter transmissions. [92]

Analysis of planetary gear dynamics is complicated by the simultaneous meshing of multiple teeth. Figure 3.11 shows a typical baseline vibration spectrum for a two-stage helicopter transmission that is used in this study. The spectrum is

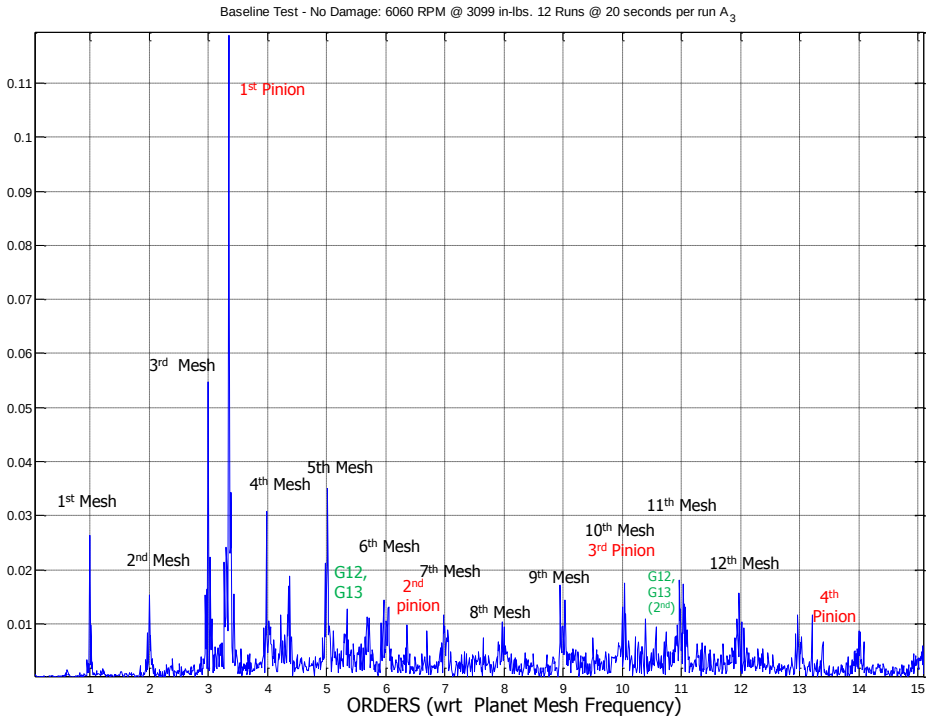

Figure 3.11: Typical Transmission Baseline Spectrum

rich with components due to the pinion/bevel gear mesh of the first stage and the sun/planet/ring gear mesh of the second stage. Also included are components due to surrounding structures.

3.4.1 Drop Tooth Design

The planet gears on the OH-58 A/C are not standard for the these planetary configuration. Ideally, all gears should share the same DP and cutter pressure angle. This would have the ring gear radius r_g equal to $2r_p + r_s$ resulting in:

$$N_p = \frac{N_r - N_s}{2} \tag{3.20}$$

For $N_r = 99$ and $N_s = 27$, the standard design would have $N_p = 36$. However, $N_p = 35$ and the system is referred to as a drop tooth design, since the planet is designed with one less tooth than the standard dictates. This drop tooth design provides two advantages: 1.) At 35 teeth, the hunting ratio becomes 35 instead of 3 allowing for more uniform wear across all teeth; 2.) Stronger tooth due to increased toothwidth. Because of this, the planet gear has a different DP with respect to the sun gear and ring gear. Had $N_p = 36$, **PGVS** would suffer the same limitation as **SGVS** with a hunting tooth ratio of 3 so another benefit of the drop tooth design is that it aids in vibration separation.

The ring gear's parameters need to be re-computed. Recall that in order for the planet gears to mesh properly with the ring gear, they must share the same base, radius resulting in their pitch radii being related by the gear teeth ratio. In addition, their center distance is given by CD, and the working pitch diameters of the ring and planet are calculated from:

$$r_{pp} = \frac{CD}{1 + \frac{N_r}{N_p}} \tag{3.21}$$

and $r_{pr} = CD - r_{pp}$, which is longer than the standard pitch radius. Unlike a gear's pitch radius, the base radius is an intrinsic property of the gear, so it can be used to

determine the working pressure angle. The planet's base circle radius is found from:

$$r_{bp} = \frac{N_p}{2DP}\cos(\phi) \tag{3.22}$$

The working pressure angle, ϕ' is found from:

$$\phi' = \cos^{-1}(\frac{r_{bp}}{r_{pp}}) \tag{3.23}$$

For a ring gear designed for this pressure angle and containing 99 teeth, its DP is equal to 9.14.

3.5 Dynamic Gear Models

Most dynamic gear models can be sorted into two classes: lumped parameter based and FEM based. The lumped parameters models treat the gear pair as rotating rigid inertias connected, along the pressure line, by a spring and damper system that represents the tooth stiffness and energy dissipation. Figure 3.12 is an example of a four degree-of- freedom model used in NASA's Dynamic Analysis of Spur Gear Transmission code (DANST) to represent a pair of spur gears in mesh. [84, 93, 94] This model takes into consideration shaft stiffness and damping (k_{s1}, k_{s2},c_{s1}, c_{s2}), the mass moments of inertias of the motor, (J_m), gears,(J_1 and J_2),and load,(J_L) and the local gear dynamic stiffness and dampening terms $k_g(t)$ and $c_g(t)$. Recall that the load acts along the pressure line; thus, for the model, the load direction stays constant. Therefore, Figure 3.12b can be used to represent the global dynamics of the meshing gears. As the gears mesh, the stiffness changes in time, and this time-varying stiffness acts as an excitation to the system. The system of equations can be written as:

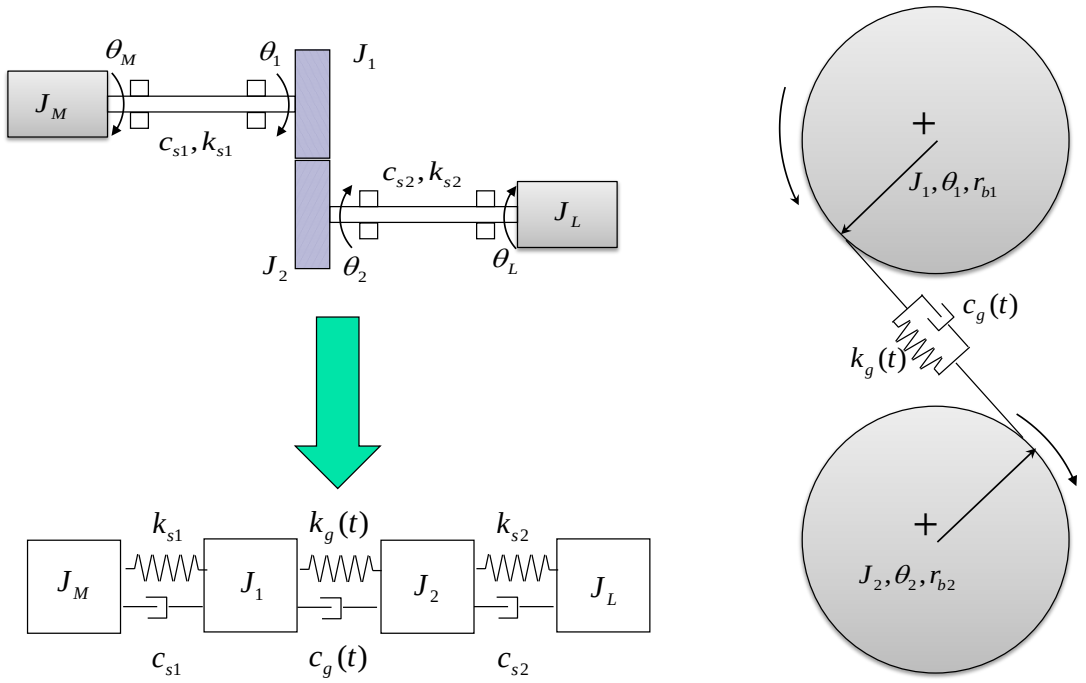

Figure 3.12: Four Degree-of-Freedom Gear Model

$$\begin{bmatrix} J_m & 0 & 0 & 0 \\ 0 & J_1 & 0 & 0 \\ 0 & 0 & J_2 & 0 \\ 0 & 0 & 0 & J_L \end{bmatrix} \begin{Bmatrix} \ddot{\theta}_M \\ \ddot{\theta}_1 \\ \ddot{\theta}_2 \\ \ddot{\theta_L} \end{Bmatrix} + \begin{bmatrix} c_{s1} & -c_{s1} & 0 & 0 \\ -c_{s1} & c_{s1} + c_g(t) r_{b1}^2 & -c_g(t) r_{b1} r_{b2} & 0 \\ 0 & -c_g(t) r_{b1} r_{b2} & c_{s2} + c_g(t) r_{b2}^2 & -c_{s2} \\ 0 & 0 & -c_{s2} & c_{s2} \end{bmatrix} \begin{Bmatrix} \dot{\theta}_M \\ \dot{\theta}_1 \\ \dot{\theta}_2 \\ \dot{\theta_L} \end{Bmatrix} +$$
$$\begin{bmatrix} k_{s1} & -k_{s1} & 0 & 0 \\ -k_{s1} & k_{s1} + k_g(t) r_{b1}^2 & -k_g(t) r_{b1} r_{b2} & 0 \\ 0 & -k_g(t) r_{b1} r_{b2} & k_{s2} + k_g(t) r_{b2}^2 & -k_{s2} \\ 0 & 0 & -k_{s2} & k_{s2} \end{bmatrix} \begin{Bmatrix} \theta_M \\ \theta_1 \\ \theta_2 \\ \theta_L \end{Bmatrix} = \begin{Bmatrix} T_m \\ T_{F1} \\ T_{F2} \\ -T_L \end{Bmatrix} \tag{3.24}$$

Rewriting Equation 3.24 in more condensed form:

$$J\bar{\ddot{\Theta}} + C\bar{\dot{\Theta}} + K\bar{\Theta} = T \tag{3.25}$$

and can be reduced to first order into the form by letting

$$y = \begin{Bmatrix} \dot{\bar{\Theta}} \\ \bar{\Theta} \end{Bmatrix} \tag{3.26}$$

$$\dot{y} = \begin{bmatrix} 0 & I \\ -J^{-1}K(t) & -J^{-1}C(t) \end{bmatrix} y + T \tag{3.27}$$

which can be solved with an ODE solver algorithm. The transmission error is given as

$$TE = r_{b1}y(7) - r_{b2}y(6) \tag{3.28}$$

Figure 3.13 is used to demonstrate the time-varying stiffness associated with gear meshing.

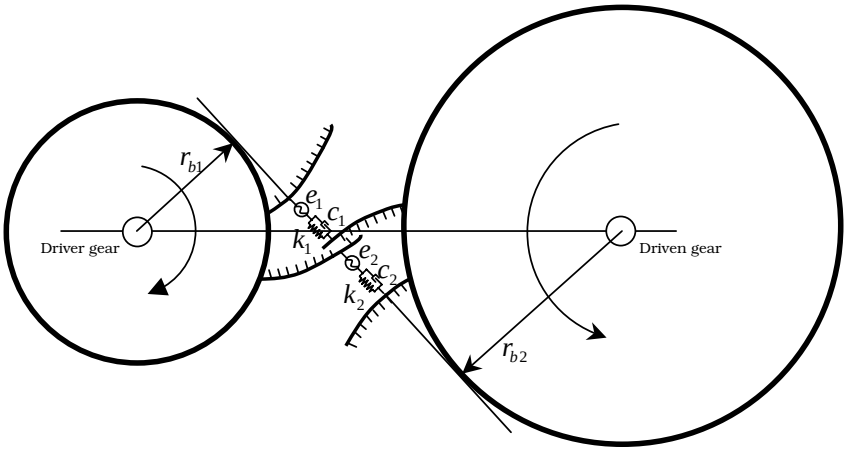

Figure 3.13: Spring Representation of Meshing Teeth

3.5.1 Damping

The damping in the shafts is due to material damping. This value is taken to be between .5% and .75% of critical damping. The effective damping of shafts is taken

to be:

$$C_{s1} = 2\xi_s \sqrt{\frac{K_{s1}}{1/J_D + 1/J_1}} \tag{3.29}$$

and:

$$C_{s2} = 2\xi_s \sqrt{\frac{K_{s2}}{1/J_L + 1/J_2}} \tag{3.30}$$

where ξ_s is the critical damping ratio of shafts with a value of .005. [95]

The effective damping of the gearmesh is given as:

$$C_g = 2\xi \sqrt{\frac{k_g r_{b1}^2 r_{b2}^2 J_1 J_2}{r_{b1}^2 J_1 + r_{b2}^2 J_2}} \tag{3.31}$$

where ξ is in the range between .03 and .17. [95] When the gears are in single tooth contact mode, the driving gear is pushing on the driven gear though a single spring-damper system. The stiffness for this mode is determined by:

$$K_{Total} = K_1 = \frac{P}{\delta_1} = \frac{P}{\delta_{1a} + \delta_{1b}} \tag{3.32}$$

where δ_{1a} and δ_{1b} is the deflection of the driving gear (a) and driven gear (b) in single contact mode (1) respectively. When two teeth are in contact, the driving gear is pushing through two springs that are in parallel. The total stiffness for this mode is determined by the combined displacements:

$$K_{Total} = K_1 + K_2 = \frac{P}{\delta_{1a} + \delta_{1b}} + \frac{P}{\delta_{2a} + \delta_{2b}} \tag{3.33}$$

The time dependent deflections, $\delta_{1a}, \delta_{1b}, \delta_{2a}, \delta_{2b}$ are derived in a quasi-static fashion. [78, 82, 94, 96, 97]

3.5.2 Derivation of the Stiffness Equation

This section derives the equations governing the stiffness between a pair of mating teeth. The static deflections are first determined and are assumed to be composed of the following components:

1.) Timoshenko beam deflection due to bending, shear, and compression.

2.) Deflections due to the flexibility of the tooth foundation.

3.) Hertzian contact deformation.

3.5.3 Beam Deflection

A number of researchers have modeled the static tooth deflection using non-uniform Timoshenko beam that that given in Figure 3.14. [82, 95, 96, 98]

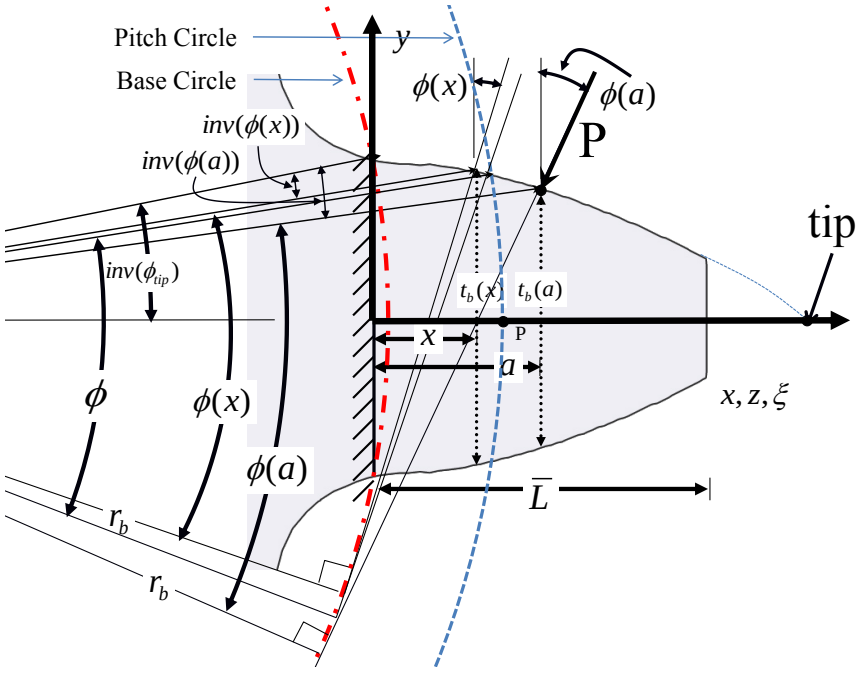

Figure 3.14: Cantilevered Gear Tooth

The deformations are due to bending, shear deformation, and axial compression.

As the two mating gears mesh, the load moves to and from the gear roots of each tooth. The effective deformations of the tooth per unit load increases, thus varying the effective stiffness between the gears.

The root is taken to the beginning of the fillet region producing an effective beam length of $\overline{L}$. A load of magnitude P is placed normal to the tooth profile at a position corresponding to $x = a$. This force is decomposed into a tangential force:

$$Q_P(x) = P\sin(\phi(x)), \tag{3.34}$$

and normal force:

$$N_P(x) = P\cos(\phi(x)). \tag{3.35}$$

The moment is given by:

$$M(x) = P\cos(\phi(x))[x - \frac{t_b(x)}{2}\tan(\phi(x))] \tag{3.36}$$

where $I(y) = b(x)^3/12$. The work done to deflect that point in the direction of the load must be equal to the strain energy in the tooth:

$$\frac{1}{2}\delta_b P = \frac{1}{2}\int \frac{M^2(x)}{E(x)I(x)} + \frac{\kappa Q_P(x)^2}{GA(x)} + \frac{N_p(x)^2}{EA(x)}dx \tag{3.37}$$

3.5.4 Deflection Due to a Flexible Foundation

Due to the stubbiness of the tooth, the flexibility of the foundation also needs to be considered. [82, 83] For plane stress:

$$\delta_{FF} = \frac{L\cos^2\phi_L}{PE}\left[\frac{16.67}{\pi}(\frac{l_F}{h_F})^2 + 2(1-\nu)(\frac{l_f}{h_F}) + 1.534(1 + \frac{\tan^2\phi_L}{2.4(1+\nu)}\right] \tag{3.38}$$

For plane strain:

$$\delta_{FF} = \frac{L\cos^2\phi_L}{PE}(1-\nu^2)\left[\frac{16.67}{\pi}(\frac{l_F}{h_F})^2 + 2\frac{1-\nu-2\nu^2}{1-\nu^2}(\frac{l_f}{h_F}) + 1.534(1+\frac{\tan^2\phi_L}{2.4(1+\nu)}\right] \tag{3.39}$$

3.5.5 Hertzian contact stress

The equation is given as:

$$\delta_{Hz} = \frac{1.275}{E12^{.9}F^{.8}P_j^{.1}} \tag{3.40}$$

where $E12 = (2E1E2)/(E1+E2)$. [94]

3.5.6 Stiffness Curve

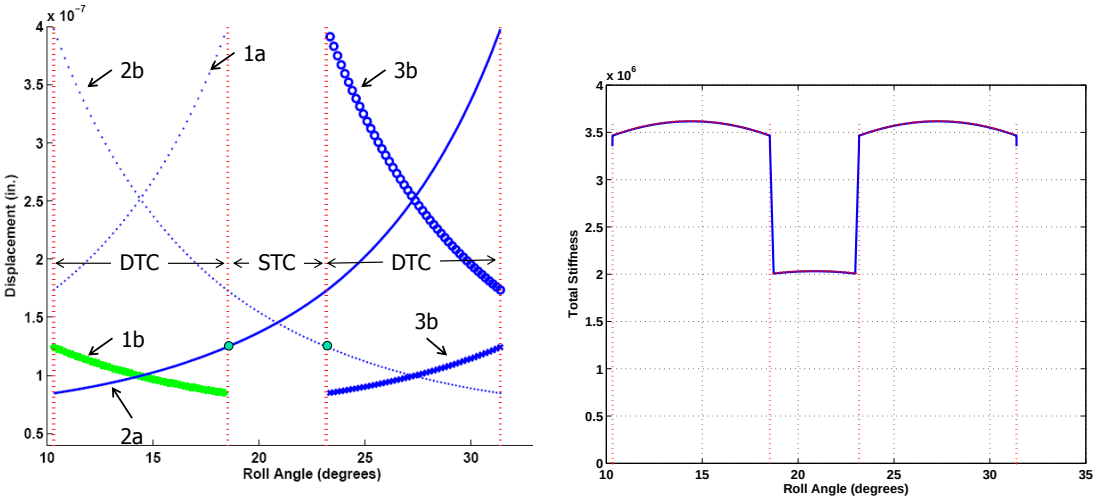

Figure 3.15: a.) Tooth Deflections b.) Total Stiffness (DP=12, N=28, $\Phi = 20^o$)

Figure 3.14 shows the variation in deflections and stiffness as a function of roll angle. Figure 3.15 represent the meshing of three pairs of teeth: pairs $T1$, $T2$, and $T3$, where a is the driving gear (pinion) and b is the driven gear (gear). The time

between the first vertical lines represent when the current tooth pair, $T2$, begins meshing. Tooth $T2b$ begins meshing at its tip, and its defection decreases as the gear rotates. The opposite is true of its mate. Also, in this interval is the tail end of the previous pair. This period between the markers represent a double tooth contact region, and the stiffness for this region is determined by Equation 3.33. A similar argument is made for the second double tooth contact region. In the center, where only tooth pair $T2$ is in mesh, the stiffness is computed using Equation 3.32. The stiffness function is given in Figure 3.15.

3.5.7 Effects of Damage on the Stiffness

Spall causes the contact area between meshing tooth pairs to decrease. This has the effect of modifying the area moment of inertia, contact width, and cross-sectional area. These changes ultimately change the stiffness equation. Chaari, et al, looked into the effect of spall on gear mesh stiffness. [99] Figure 3.17 shows their spalled tooth model. [99]

Two plots were created: 1.) The changes in the stiffness function as the spall width, w_s, changes; 2.) the changes in the stiffness as a function of height, a_s. [99]

3.5.8 Planetary Lumped Parameter Model

For a planetary system, for which there are many teeth pairs in mesh, the spur gear model is applied to each gear pair and combined producing a more complex lumped parameter model. A schematic is given in Figure 3.18. [85] The carrier, ring,

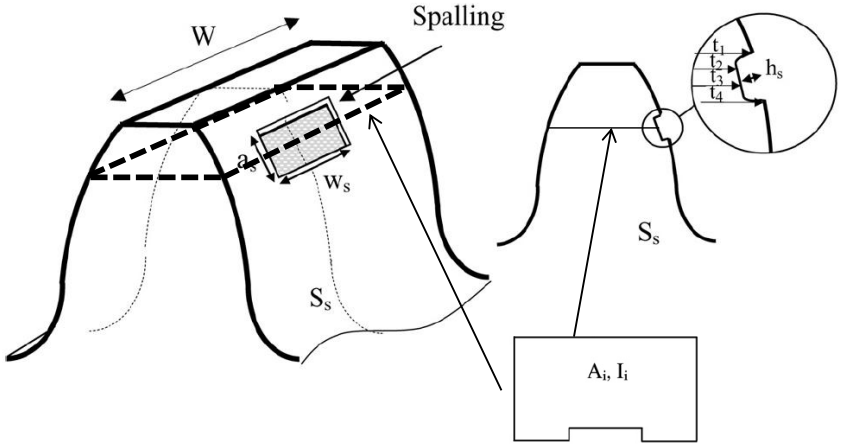

Figure 3.16: Spalled Tooth Model (Chaarie 2008)

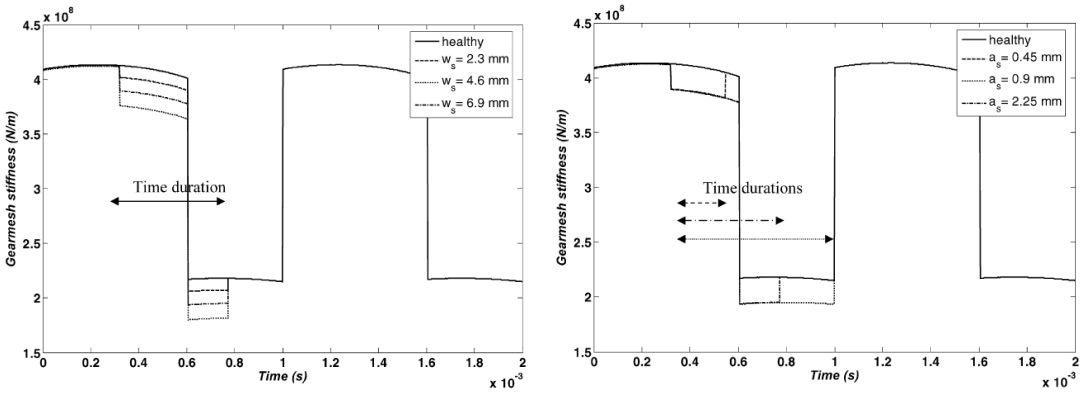

Figure 3.17: Typical Result of Spall on Stiffness Function (Chaarie 2008)

and sun gears share the same coordinate system with x_j,y_j with $j = c, r, s$. The planet gears' coordinate axis is given by ζ_n and η_n, where n ranges from 1 to the number of planets. It is assumed that the ζ_1 is aligned with x_j and all other axes, ζ_n, are separated by an angle ψ_n. Each component has three degrees of freedom, their translation components and a rotational component given by $u_j = r_j\theta_j$, where j represents the carrier, ring, sun, and each planet. The variable, r_j, represents the base circle of component j. Gear mesh interactions are represented by linear springs

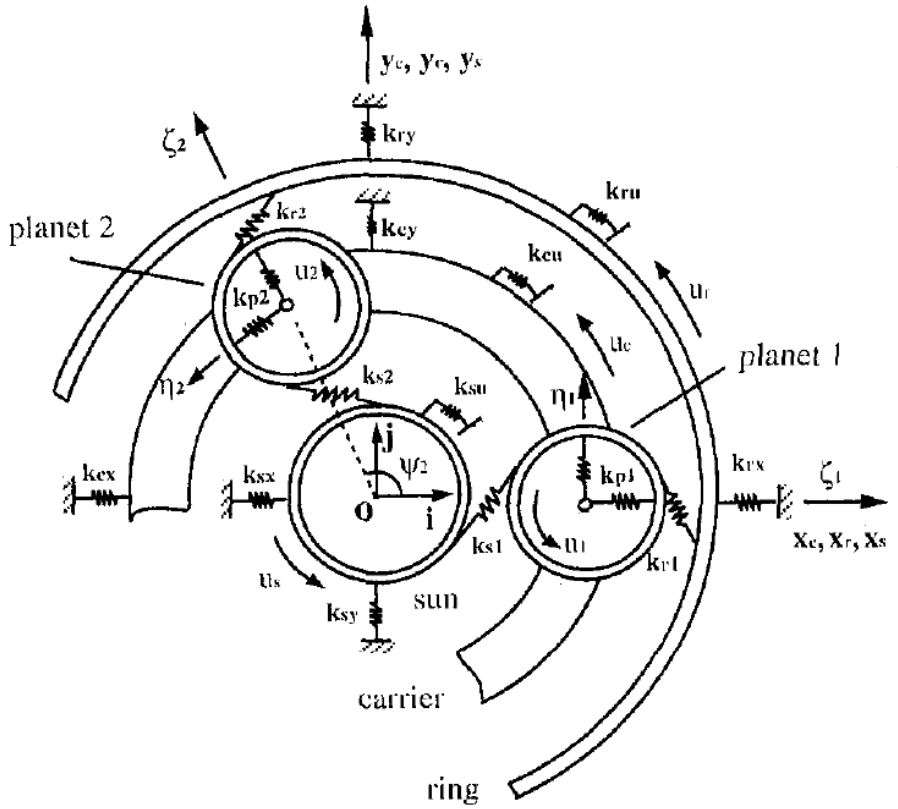

Figure 3.18: Lumped Parameter Model for a Planetary System (Lin 1999)

along the pressure line and component bearings are modeled by linear springs. For a state vector equal to:

$$q = [x_c, y_c, u_c, x_r, y_r, u_r, x_s, y_s, u_s, \zeta_1, \eta_1, u_1, \zeta_N, \eta_N, u_N] \tag{3.41}$$

and the assumption that all planets are equally spaced, all sun-planet mesh stiffnesses are the same, all planet-ring stiffnesses are the same, and all bearings are isotropic and the same value. Solving the problem:

$$M\ddot{q} + (K_b + K_m)q = 0 \tag{3.42}$$

where the parameters are defined in [85], yields, at most, 15 natural frequencies. There exist three classes of mode shapes: translational modes, rotational modes, and planet

modes. Six natural frequencies only occur once (multiplicity of 1) and are associated with rotational modes. These modes have rotational motion and no translation. There are six natural frequencies that occur in pairs (multiplicity 2) and are associated with translational modes. Translational modes are when the sun, carrier, and ring only have translational motion and no rotation. Finally, there exist (15-12=3) natural frequencies which occur in sets of (N-3) and are associated with planet modes. These refer to planet deflections with the sun, ring, and carrier fixed. [85]

In general, with the exception of the planet modes, the structure just discussed is lost when planets are arbitrarily spaced due to the coupling of the rotational and translational modes. [100] However, for a planetary system with diametrically opposing planets, the structure is preserved and the natural frequencies and mode shapes are the same as for equally spaced planets. [86]

3.5.9 Planet Spacing

The spacing between planet in a planetary configuration must be such that their separation angle, Ψ, must be an integer multiple of the least mesh angle given by

$$\lambda = \frac{2\pi}{N_s + N_r} \tag{3.43}$$

When all planets are equally spaced, they system has cyclic symmetry and its natural frequencies and modes have a well-defined structure.

The dynamic mesh force is periodic at the gear mesh frequency. For the planet gear designated as planet 1, it can be written as a Fourier series. [101, 102]

$$F_1(t) = \sum_{j=1}^{J} F_{ij} \cos(j2\pi N_r f_c t + \phi_j) \tag{3.44}$$

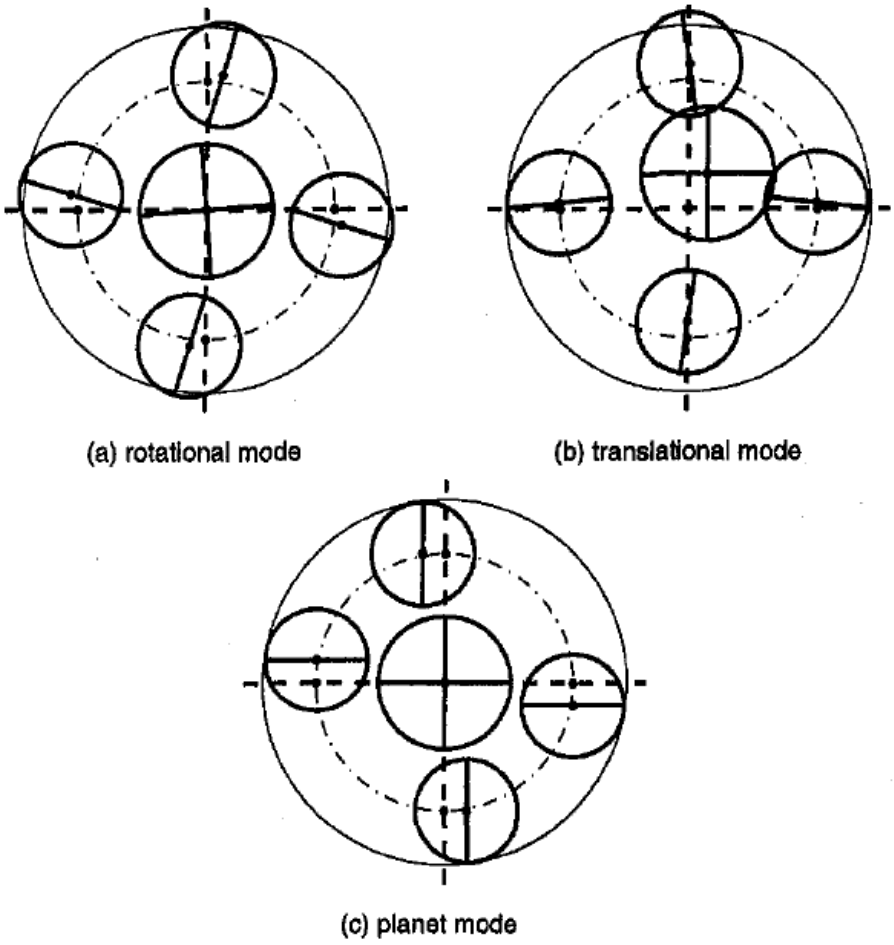

Figure 3.19: Planetary Gear Modes (Parker 2010)

where F_{ij} is the Fourier coefficient of j-th harmonic of the dynamic force of ring-planet i mesh, ϕ_j is the phase angle of the j-th harmonic component.

Assuming each planet has the same force profile given in Equation (3.44) but differs in phase, its forcing function will have the form:

$$F_1(t + \frac{\psi_i}{2\pi f_c}) = \sum_{j=1}^{J} F_{ij} \cos(j2\pi N_r f_c t + \phi_j + jN_r\psi_i) \tag{3.45}$$

where $jN_r\psi_i$ represents the phasing of the planets with respect to planet 1. If $jN_r\psi_i$ is an integer multiple of 2π, then the forcing functions for all planets are in phase. This means that the point along the tooth profile for each meshing tooth matches.

This would also suggest equal load sharing, since the effective stiffness at each tooth is the same.

If adjacent planets are out of phase by $\pi/2$ radians, then they are considered sequentially phased. This condition is tested using the following formula:

$$\sum_{i=1}^{N} N_r \psi_i = m\pi \tag{3.46}$$

where m is an integer value. This phasing has been shown to lower vibration and noise levels.

Another possibility is to have a system in which no planets are equally spaced and the phasing of the planet is neither in-phase nor sequential. For the OH-58A, with $N = 3$, $N_r = 99$, and $N_s = 27$, the system is both equally spaced, (ψ_i=[0 $\frac{2\pi}{3}$ $\frac{4\pi}{3}$]) and in phase ($\frac{2\pi 99}{2\pi 3} = 33$). For the OH-58C, with $N = 4$, $\lambda = \frac{\pi}{63}$. The spacing is unequal: [0,$\frac{31\pi}{63}$,180, $\frac{94\pi}{63}$]. Since $\frac{31\pi 99}{2\pi 63} = 341/14$, which is not an integer, the planets are not in phase. Finally, summing the individual phase angles, $(2 + 64/63)\pi \neq m\pi$, reveals that the OH-58C is also non-sequential.

This means that each planet is operating at a different point along the pressure line; thus, the sudden changes in stiffness occur at different times. [103]

3.6 Monitoring Sideband Activity

Planetary sidebands were investigated by Inalpolat and shown to have characteristics unique to the number of planets, planet spacing, and planet phasing. [101] At least two groups of sidebands exist for signals from mounted accelerometers. One set appear at integer shaft orders and the rest are non-integer shaft orders. The first

is due to the planet passing frequency. As a planet passes a fixed accelerometer, the signal experiences an increase in amplitude. Thus, an N planet system, one carrier rotation yields N lobes. This is like having $a(t)$ of Equation 2.2 with a frequency of Nf_g. Therefore, a sideband appears in the accelerometer's frequency response at $\pm N$ from each harmonic component of the shaft order. In this work, five planetary transmission categories were created and are given in Table 3.2

Case	Planet Relationship	Classification
1	$\Psi_i = \frac{2\pi(i-1)}{N}$ and $\frac{N_r \Psi_i}{2\pi} = n$	Equally spaced planet and in-phase gear meshes. Components at f_m and $f_m \pm N f_c$ (passing frequency)
2	$\Psi_i = \frac{2\pi(i-1)}{N}$ and $\frac{N_r \Psi_i}{2\pi} \neq n$ and $\sum_{i=1}^{N} N_r \Psi_i = m\pi$	Equally spaced planets and sequentially phased gear meshes. Zero amplitude at f_m. Components at $f_m \pm n f_c$ but not at each component (non-symmetric). Also not confined to passing frequency. Closest sideband to f_m is largest. If $\mathbf{rem}(\frac{N_r}{N}) = .5$, sidebands are equally spaced at some component an integer multiple of the f_c away from f_m
3	$\Psi_i \neq \frac{2\pi(i-1)}{N}$ and $\frac{N_r \Psi_i}{2\pi} = n$	Unequally spaced planets and in-phase gear meshes. Largest component at f_m. Largest sidebands at $f_m \pm N f_c$ (passing freq). If N and N_r are even, then significant sidebands at $f_m \pm 2n f_c$. If N is even and planets are diametrically opposed, $f_m \pm 2n f_c$ If N is odd, mainly at $f_m \pm n f_c$
4	$\Psi_i = \frac{2\pi(i-1)}{N}$ and $\frac{N_r \Phi_i}{2\pi} \neq n$ and $\sum_{i=1}^{N} N_r \Psi_i = m\pi$	Un-equally spaced planets and sequentially phased gear meshes. Sideband at several locations nf_c (not just passing order (Nf_c))
5	$\Psi_i \neq \frac{2\pi(i-1)}{N}$ and $\frac{N_r \Phi_i}{2\pi} \neq n$ and $\sum_{i=1}^{N} N_r \Psi_i \neq m\pi$	Un-equally spaced planets and arbitrarily phased gear meshes. Rich sideband activity at $f_m \pm n f_c$ Sidebands are non-symmetric

Table 3.2: Planetary Gear Planetary Phasing Classification

The OH-58A is considered a case 2 system, thus theoretically has a sideband

pattern that has a significant component at the first planet mesh frequency as well as two symmetric sidebands at half the amplitude. The sidebands are located at $(99+3)f_c$ and $(99-3)f_c$.

The OH-58C is considered a case 5 system, characterized by very rich sideband activity. The sideband orders are at $N_r \pm n$, which is non-sequential and unevenly spaced.

3.7 Finite Element / Contact Mechanics

Another model using a hybrid finite element /contact mechanics is now discussed. This method computes the dynamic responses of an assembled planetary system during meshing simulations. At each kinematic step, the system is scanned and candidate points are identified using a pre-described separation tolerance. At these candidate locations, the minimum distance within the region of points is identified and its normals and normal curvatures (curvatures in the two principle directions), are calculated. Using this information, the material properties, and the maximum expected load, the semi major and minor axis of the contact ellipse is approximated and then prescribed onto a tangent plane sized to encompasses the complete ellipse. This is illustrated in Figure 3.20a. [104]

This ellipse is then projected back onto each surface and the true surface points are identified. The Boussinesq solution and contact forces are integrated over the tooth contact region to accurately represent relative displacements in an inner region close to the tooth surface. [105] Outside this region, deformations are computed using

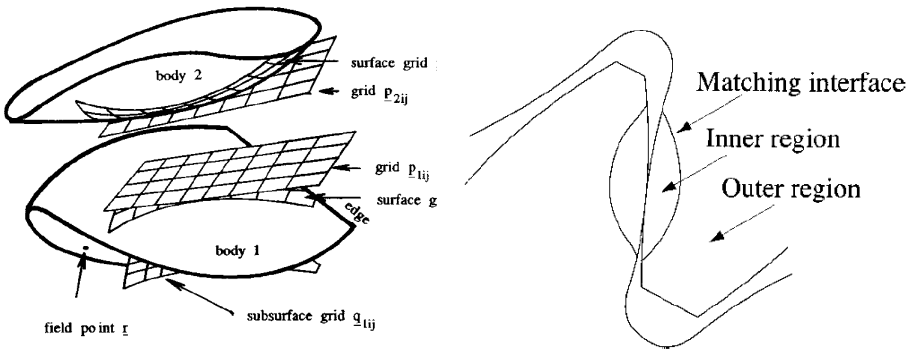

Figure 3.20: Contact Mechanics Diagrams (Vijayakar 1991)

finite elements. A matching interface separates the two solution regions and is determined by minimizing the least square difference between the two solutions at like points. The interface is shown in Figure 3.20b. [106] A significant advantage of this approach is that the interactions between all meshing teeth are evaluated internally, eliminating the need to supply a time-varying stiffness function for each gear mesh and later combining the results. Contact analysis at each time step determines the principle contact stresses and deformations of the gear bodies and housing. The input is a constant sun torque, and the Newmark method is used to conduct the dynamic analysis. This hybrid formulation significantly reduces the number of finite elements required, thus reducing the computation effort. Since the change in stiffness due to teeth going into and out of mesh as well as transmission error being a direct output, this model significantly reduces the number of assumptions needed to model the complex dynamic mesh forces. [107]

A sample output is given in Figure 3.21 using a commercial package called Planetary 2D [1] and shows that the structure of the path from the sun-planet mesh

[1]Provided by Dr. Vijayakar - Advanced Numerical Solutions

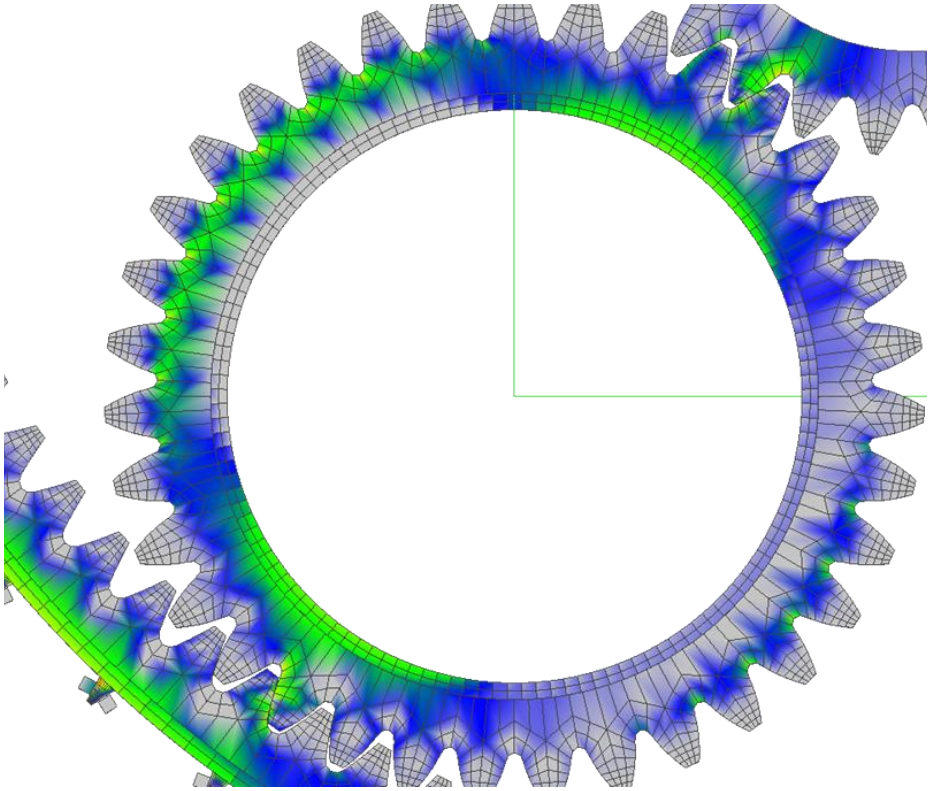

Figure 3.21: Close-up Sun-Planet-Ring Meshing Region

to the sun-ring mesh is complex.

Chapter 4

Vibration Separation

4.1 Introduction

Many of the condition indicators discussed here have performed well for gear pair configurations. However, they have shown to be ineffective on the individual components of a planetary system. [61] **TSA** has prove to be an effective tool to isolate non-commensurate dynamics. While this may be able to isolate the planetary system from others, it does not isolate the individual components of the planetary system. In 1990, McFadden introduced a method called vibration separation that allows for standard condition indicators to be applied directly to individual components of a planetary gear. Vibration separation is a signal processing technique used on planetary gear systems for the purpose of isolating dynamics associated with a single planet, sun, or ring gear. It involves extracting a subset of a measured acceleration signal at a time when a given planet is aligned with that ring-mounted accelerometer. This extraction is then used to synthesize a new signal that represents the dynamics of the target gear. The underlying assumption is that the extracted signals are dominated by the simultaneous meshing of the aligned planet's teeth with the ring and sun gears and that averaging can be used to expose the sought-after dynamics. The target gear's tooth engagement schedule is computed and is used to match extracted data with each of the target gear's teeth.

Detecting damage on planet gears using vibration separation has been shown to be successful. [41] However, detecting damage on the sun gear continues to be a challenge. This is because its dynamics need to be assessed through the planet gears introducing a higher degree of complexity.

Figure 4.1 gives a flowchart of the vibration separation processes used in this research. There are three stages: Acquisition/Interpolation, Extraction, and Assembly.

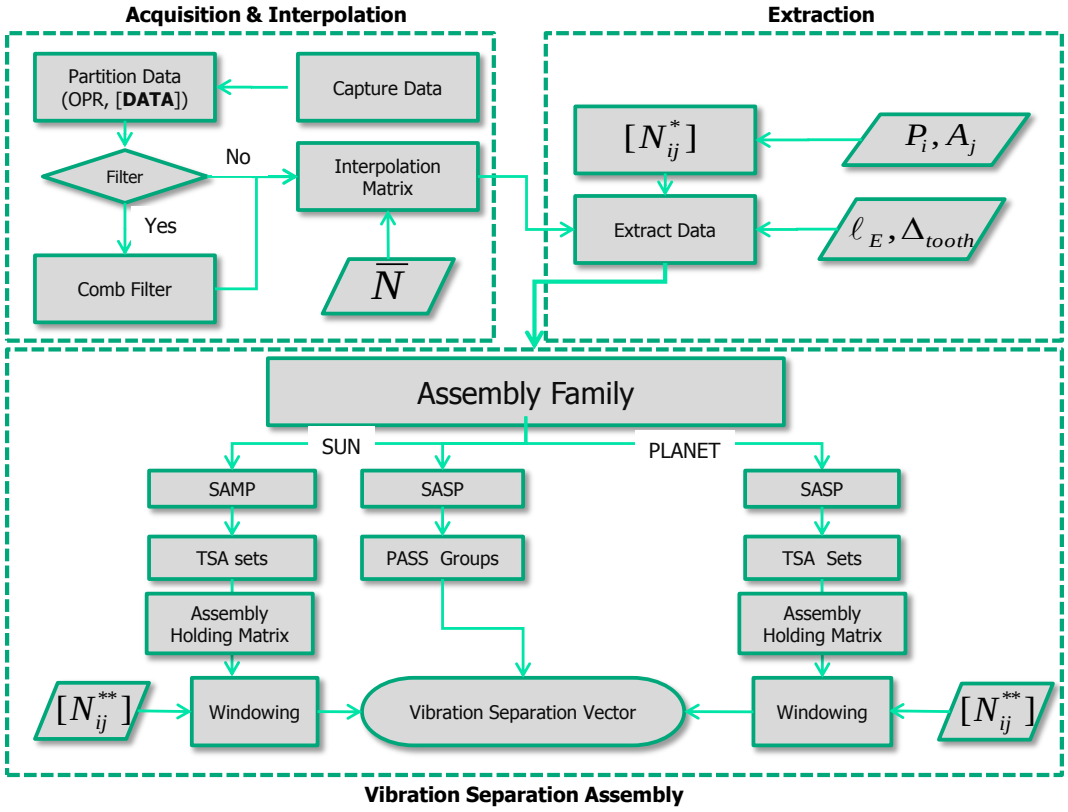

Figure 4.1: Vibration Separation FlowChart

The Acquisition/Interpolation stage encompasses the simultaneous data collection of the vibration and once-per-revolution (OPR) signal based on the output shaft's rotation. Using the OPR signal, the data is partitioned into individual cycles. Each cycle is optionally filtered and interpolated to $\overline{N}$ points and then stored as a column

in the **Interpolation Matrix**. This 2D matrix has length, $\overline{N}$ and width, $N_{extract}$, which depends on the number of complete cycles in the measured data.

The next step is the Extraction stage. Each column of the **Interpolation Matrix** represents a full carrier cycle and within each carrier cycle there is a point that represents when planet P_i and accelerometer A_j are aligned. This point, N_{ij}, is referred to as the extraction index. Given the extraction index, N_{ij}, a pre-determined number of point to extract, ℓ_E, and a delay factor, Δ_{tooth}, data is extracted and stored into a structured matrix called the **Assembly Family**. The **Assembly Family** is a 4-D variable which contains a field for each accelerometer where each field contains a 3D matrix. Each 3D matrix has layers corresponding to each planet and each column corresponding to a given carrier cycle.

The next stage is Vibration Separation Assembly where there are 2 options: planet gear vibration separation (**PGVS**) and sun gear vibration separation (**SGVS**). In this stage, the extracted data in the **Assembly Family** is assigned a mapping index, N_{ij}^{**}, that depends on the planet or sun tooth engaged at the time the data was extracted. This parameter governs the positioning in the final **Vibration Separation Vector** of that extracted data set. Different methods of assembly are used. For **PGVS**, the single accelerometer / single planet (**PGVS-SASP**) method is used to create the **Vibration Separation Vector** that corresponds to a given planet. For **SGVS**, either an **SGVS-SASP** method or an alternative single accelerometer / multiple planet (**SGVS-SAMP**) method is used to generate the final **Vibration Separation Vector** corresponding to the dynamics associated with the sun gear. The **SGVS-SASP** method allows the accelerometers to "'see"' the sun gear through

only one planet, and **SGVS-SAMP** allows them to "'see"' the sun through multiple planets. Damage detection **CIs** are then applied to the Vibration Separation Vector. The remainder of the chapter discuss the details associated with this flow chart.

4.2 Acquisition and Interpolation

This work looks at detecting faults on two different configurations of the OH-58's planetary stage. They are termed 'A' model and 'C' model and the two are shown in Figures (4.2) and (4.3) in their initial planetary orientation. The relative

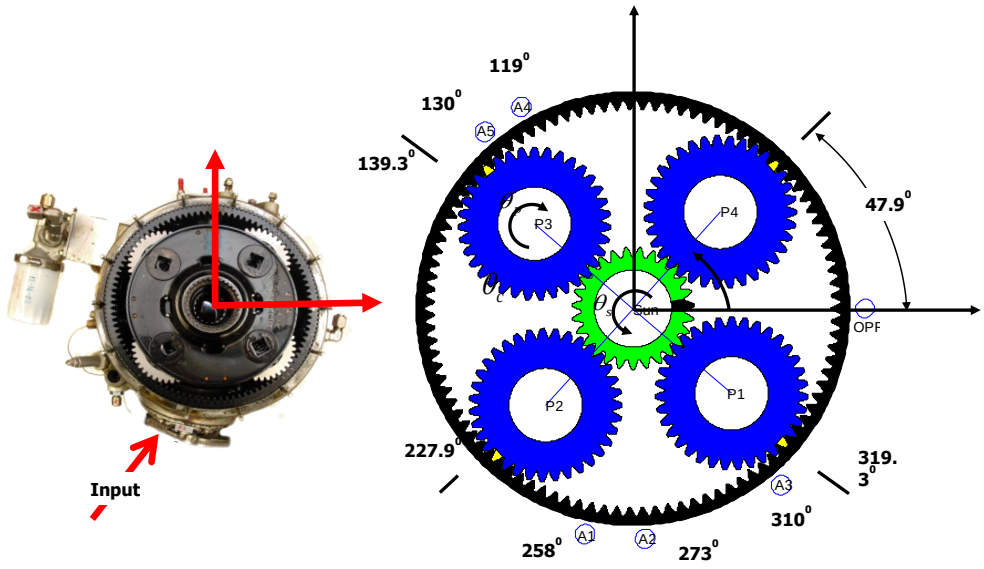

Figure 4.2: Initial Orientation of the OH-58C Planetary Stage

positions of accelerometers and the OPR sensor are also provided. For both systems, the output shaft is splined to the carrier so that one carrier cycle is the same as the output shaft cycle.

During testing, data is collected representing many carrier cycles. Figure 4.4

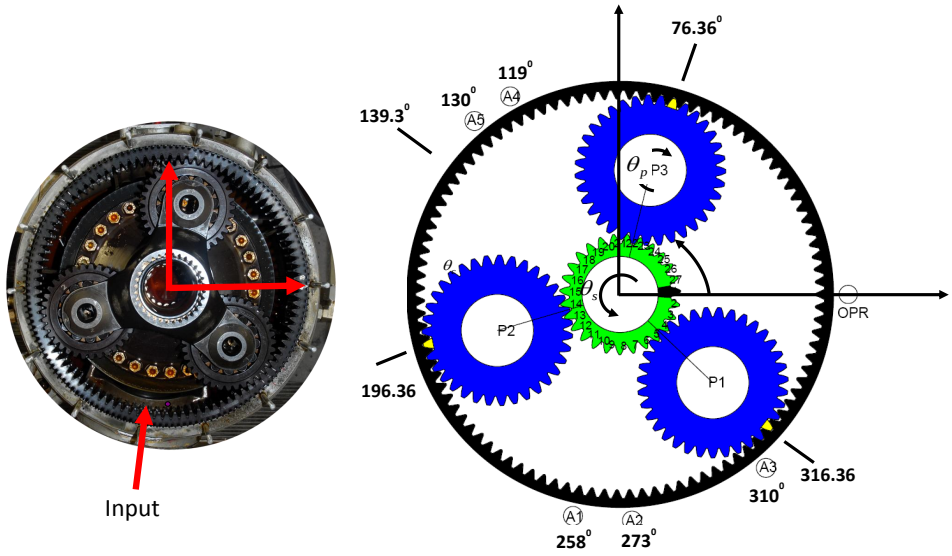

Figure 4.3: Initial Orientation of the OH-58A Planetary Stage

shows an example of a raw data set for a given accelerometer

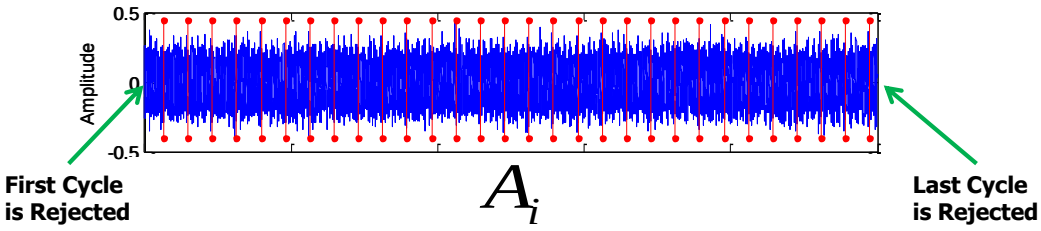

Figure 4.4: Aquisition and Interpolation: Partitioning the Raw Data

The output shaft's tachometer provides the OPR pulse used to parse these signals into the individual carrier cycles. Notice how the first cycle and last cycles are incomplete. Because of this, these two cycles are rejected.

Since data is needed from each carrier cycle, time synchronous averaging, which would average all cycles into one, is not performed prior to extraction but instead relegated to the point just before assembly. Because of this, non-synchronous dynam-

ics associated with other subsystems are included in every extraction. If the spectral information is known, frequency filtering can be used. As an example, the OH-58 is a two stage system for which the dynamics is dominated by the input spiral bevel pinion of the first stage. The frequencies associated with this pinion is identified from the OPR data and, using a narrow bandwidth IIR comb filter, filtered out. The comb filter is created by convolving a series of notch filters, each set to attenuate a pinion component and given by the equation:

$$H(z) = b\frac{1 - z^{-n}}{1 - az^{-n}} \tag{4.1}$$

The values a,b, and n govern the location, bandwidth, and attenuation of each filter. A typical result is given in Figure 4.5.

The benefit of using the filtered signal is that a high correlation between waveforms is expected from the onset making it possible that faults become apparent earlier in the processing.

4.2.1 Equally Spaced Tooth Mesh Periods

For every carrier cycle, there are N_r planet/ring tooth mesh periods, (**TMPs**). Thus, partitioning the carrier cycles at intervals representing a single **TMP**, should produce the same number of points in each partition. However, due to slight variation in shaft speeds, this is not always the case in practice. Therefore, in order to ensure this, interpolation is used. This reason is in addition to the one discussed in Section 2.3.1 for which interpolation is used to ensure that all cycles have measurement points at the same angular position which is necessary when doing time-synchronous

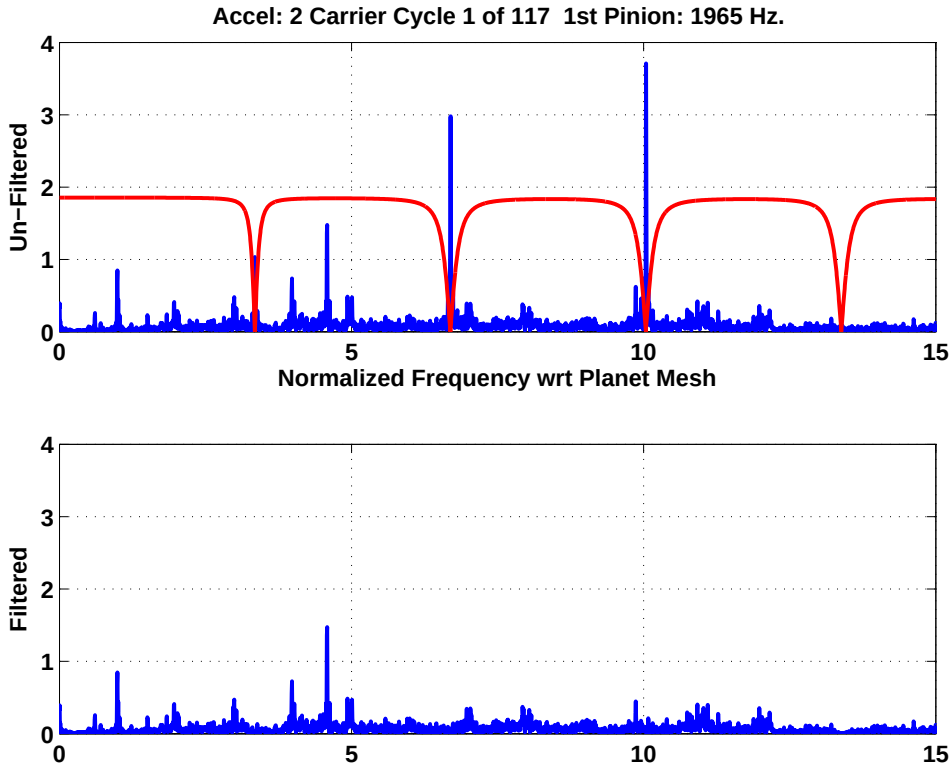

Figure 4.5: Effect of Filtering Before Interpolation

averaging. Interpolation makes the assumption that the rotation speed is either constant in between carrier cycles or that factors causing a non-uniform rotation are repeated every cycle. The number of interpolation points, $\bar{N}$, is chosen to satisfy two requirements:

1.) $\bar{N}$ is close to the original number of points.

2.) $\bar{N}$ can be divided into N_r equal sections, with each containing **NTP** points.

Designating the average number number of points per carrier cycle as $\bar{N}_{avg}$, then it is useful to find the smallest integer value, **NTP**, such that:

$$\underbrace{min}_{NTP}(|N_r(NTP-1)+1-\bar{N}_{avg}|) \tag{4.2}$$

Once NTP is solved, $\bar{N}$ is determined from:

$$\bar{N} = N_r(NTP - 1) + 1 \tag{4.3}$$

It is convenient to work in units associated with a single **TMP** consisting of **NTP** points. The **Vibration Separation Vector** consists of either N_p **TMPs** of an individual planet gear or N_s **TMPs** of the sun gear. The length of their corresponding **Vibration Separation Vector**, ℓ_v, is given by:

$$\ell_v = N_{p,s}(NTP - 1) + 1 \tag{4.4}$$

where $N_{p,s}$ is either N_p or N_s.

4.3 Extraction

The data extracted from each carrier cycle depends on four parameters: planet gear angle θ_P^i, accelerometer angle, θ_A^j, the number of data points to extract, ℓ_E, and a delay factor, Δ_{tooth}, which allows for slight adjustments on the extraction location.

Figure 4.4 illustrates why the 1st and last cycles are rejected. The first carrier cycle of the measured data is rejected due to the time delay in starting data acquisition, making the number of points in the first cycle inconsistent with those of subsequent cycles. This means that the analyzed portion of the data starts at $\theta_c = 2\pi$, as shown in Figure 4.6.

The last cycle also represents an incomplete cycle so it too is rejected.

The ordering of the planets starts with P_1. Since the carrier rotates counterclockwise, the planet numbering is clockwise, so that increasing planet number corresponds with the order in which they reach each accelerometer. The accelerometers are

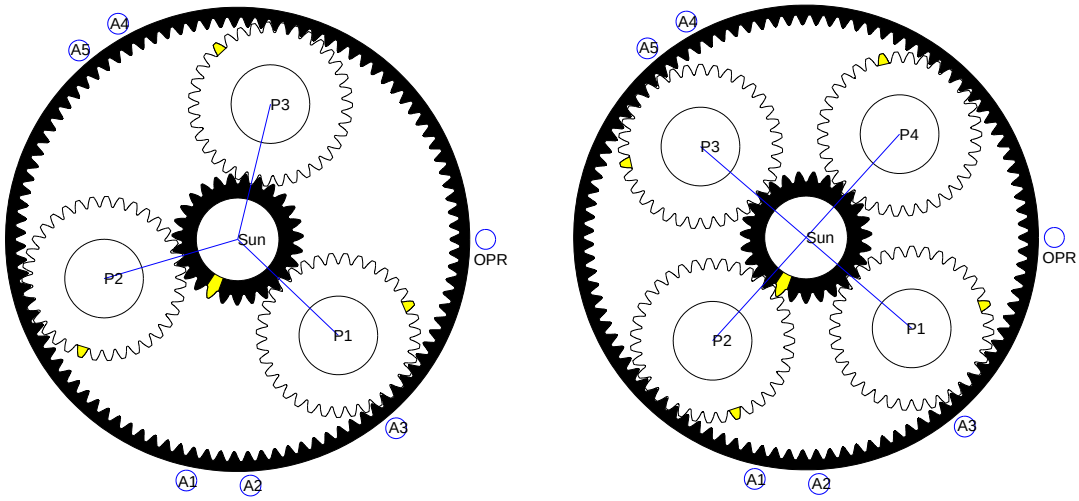

a *b*

Figure 4.6: Planetary Orientation at $\theta_c = 2\pi$ a.) OH-58A b.) OH-58C

numbered counter-clockwise from A_1 to A_5. Their angular accuracy is on the order of $\frac{1}{4}$ of the ring gear's tooth pitch ($\approx 1^o$). The convention used is such that, when the planetary system is in its initial orientation at $\theta_c = 0$, all planet teeth engaged with the ring gear are assigned Tooth ID 1 and increase in the direction opposite to the gear's rotation. In addition, the sun gear's tooth just above the origin is assigned Sun Tooth ID 1 and has an initial angle given as $\overline{\theta_s^1} = 3.8^o$. This value is the same for both configurations.

Recalling the discussion on planet spacing from Chapter 3 on Page 79, the OH-58C was shown to have unequal spacing. In particular, it has an **X** shape, so that a given planet is closer to one of its immediate neighbors. Because of this, the data extraction locations are dependent on which planet reaches the accelerometer of interest first. The sequence order is given in Table 4.1.

Model	Case	Angle Sequence
OH-58C	P_1 or P_3 reach target accelerometer first	$[0\ \frac{32\pi}{63}\ \pi\ \frac{95\pi}{63}]$
OH-58C	P_2 or P_4 reach target accelerometer first	$[0\ \frac{31\pi}{63}\ \pi\ \frac{94\pi}{63}]$
OH-58A	Angle sequence is equally spaced	$[0\ \frac{\pi}{3}\ \frac{2\pi}{3}]$

Table 4.1: Planet Arrival Sequence

4.3.1 Determining the extraction index, N^*_{ij}

For a given initial planet angle, θ^i_P, for planet P_i and accelerometer angle, θ^j_A, for accelerometer A_j, the initial carrier angle separating the two is given by:

$$\theta^{ij}_{sep} = \overline{\mathbf{mod}}(\theta^j_A - \theta^i_P, 2\pi), \tag{4.5}$$

where

$$\overline{\mathbf{mod}}(x, y) = \begin{cases} x - \mathbf{floor}(x/y) * y & \text{if } y \neq x \\ x & \text{if } y = x \end{cases} \tag{4.6}$$

where **floor** means to "round down to the next integer". This is done to ensure that the counter clockwise angle is used for θ^{ij}_{sep} which corresponds to the rotating direction of the carrier. Since the carrier cycle is interpolated to $\bar{N}$ equally spaced points, each spacing represents $\Delta\theta_c = \frac{2\pi}{\bar{N}-1}$. Therefore the closest index point corresponding to when P_i is aligned with A_j is given by:

$$N^*_{ij} = \mathbf{round}(\theta^{ij}_{sep} \cdot \Delta\theta_c) \tag{4.7}$$

The **round** function is to ensure the value used is the closest integer value. It is felt that this approximation has a minimal effect on the results since it is within a single

angular sampling. In addition, all extraction points are based on the same integer value.

Table 4.2 gives the values of θ_{sep}^{ij} for the OH-58A and OH-58C.

	OH-58A					**OH-58C**				
	A_1	A_2	A_3	A_4	A_5	A_1	A_2	A_3	A_4	A_5
P_1	301.6	316.6	353.6	162.6	173.6	298.7	313.7	350.7	159.7	170.7
P_2	61.6	76.6	113.6	282.6	293.6	30.1	45.2	82.2	251.2	262.2
P_3	181.6	196.6	233.6	42.6	53.6	118.7	133.7	170.7	339.7	350.7
P_4	210	225	262	71.1	82.1	210.1	225.2	262.2	71.2	82.2

Table 4.2: Separation Index Schedule (θ_{sep}^{ij}): OH-58A and OH-58C (degrees)

The extraction index, N_{ij}^{*}, is interpreted as the point for which the center of the planet tooth is aligned with the accelerometer. Although it serves as a convenient means to conceptualize the process, most likely this is not physically correct. As mentioned earlier, the accelerometer locations are approximate; thus, the exact location within the mesh cannot be determined. All that can be said is that each collection of **NTP** points in the **Vibration Separation Vector** represents a full mesh time period between a planet and a ring gear. If the partial dynamics associated with one tooth are captured in one extraction, the remainder is extracted in a subsequent extraction.

4.3.2 Choosing the Extraction Length, ℓ_E

One way to ensure that a tooth's full **TMP** is extracted from a single carrier cycle is to use additional data points corresponding to multiple **TMPs**. Setting M_v be an odd integer representing the number of **TMPs** of data desired, the corresponding number of points extracted is given by:

$$\ell_E = M_v(NTP - 1) + 1 \tag{4.8}$$

The constraint that M_v is an odd integer simplifies analysis in that it centers the waveform associated with N^*_{ij}.

The location of the first point extracted is given by:

$$\hat{N} = N^*_{i,j} - \text{floor}(\frac{\ell_E}{2}), \tag{4.9}$$

resulting in a range of points given by:

$$\textbf{RANGE} : \{\hat{N}, \hat{N} + 1, ..., \hat{N} + \ell_E - 1\} \tag{4.10}$$

With four planets and five accelerometers of the OH-58C, there are 20 extraction locations within each carrier cycle. Similarly, for the OH-58A, there are 15 extraction points.

4.3.3 Extraction Offset

The ability to adjust the extraction location adds versatility to the algorithm. This is accomplished by using Δ_{tooth}. It is given in units of **TMP** and written as:

$$\Delta_{tooth} = N_{offset}(NTP - 1) + 1 \tag{4.11}$$

where N_{offset} is the number of **TMPs** to adjust. A negative value will extract data prior to the planet reaching the accelerometer and a positive value will extract data after the planet has passed the accelerometer.

Equation 4.7 is then modified to:

$$N^*_{ij} = \mathbf{round}(\theta^{ij}_{sep} \cdot \Delta\theta + \Delta_{tooth}) \tag{4.12}$$

4.3.4 Assembly Families

The extraction process is illustrated in Figure 4.7. In this example, accelerometer A_1 is the signal under study for the 4 planet OH-58C. There are three cycles shown representing the first three columns of the **Interpolation Matrix**. Each of the four boxes in each cycle represent the extraction region, centered on N_{ij}, for a given ac-

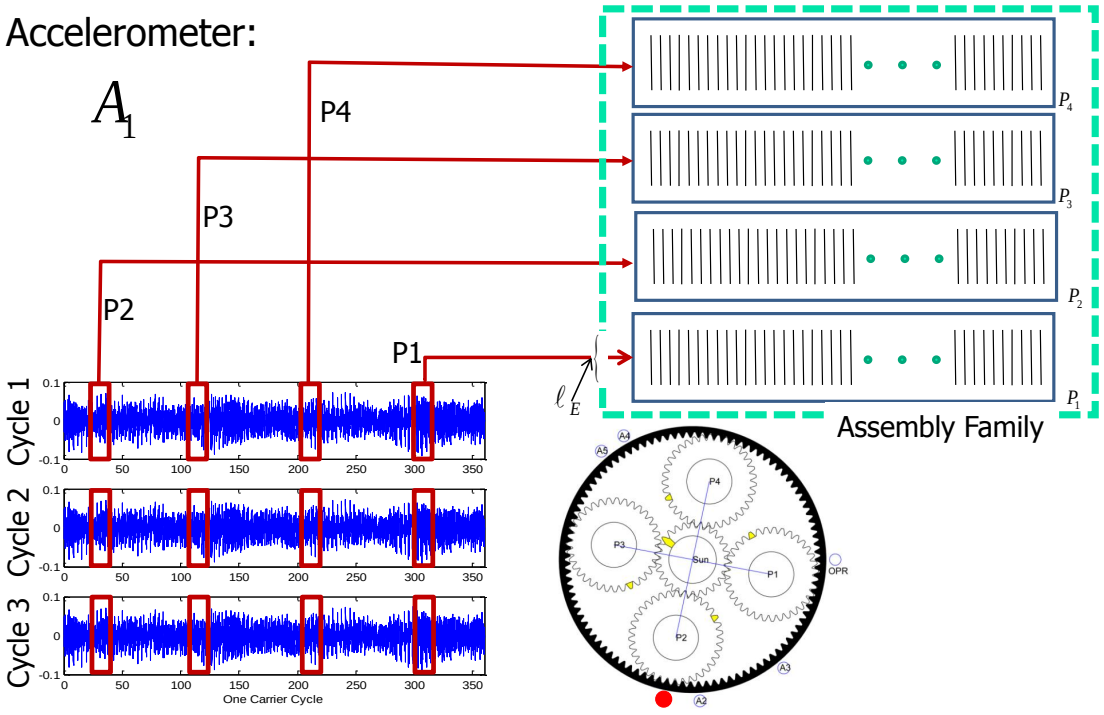

Figure 4.7: Vibration Separation Extraction Example. A_1

celerometer/planet pair. The ones shown are the ones associated with accelerometer A_1. The width of the box represents the length of data extracted, ℓ_E.

For this case, planet P_2 is the first planet to reach A_1 as shown by the gear schematic in the bottom right corner. So the first extraction in the first cycle corresponds to P_2 and occupies the first column in the P_2 layer of the **Assembly Family**. The next planet to arrive at A_1 is P_3. Its extracted values occupy the first column of layer P_3 in the **Assembly Family**. The extractions in cycle two are placed in their corresponding second columns of the **Assembly Family**. This continues until the last cycle. Thus, for A_1, the 3D **Assembly Family** sub-matrix has length ℓ_E, width $N_{extract}$, and four layers corresponding to P_1 through P_4 for the OH-58C or three layers corresponding to P_1 through P_3 for the OH-58A. This process is completed for all accelerometers and the collection of **Assembly Families** is stored in a structured variable given as:

AF(accelerometer).3D(Extracted Vector, Cycle, Planet)

4.4 Assembly

The 4D structured **Assembly Family** variable discussed in the previous section provides a convenient means to assemble the results into a **Vibration Separation Vector** for both **PGVS** and **SGVS** that can later be interrogated for damage.

As gears mesh, an important parameter comes into play governing the number of times a pair of gear teeth meet, called the hunting tooth ratio and is given by the least common, non-unity, factor between the number of teeth on a pair of gears. As

an example, for the systems under study, the hunting tooth ratio between the number of planet teeth, $N_p = 35$, and ring gear teeth, $N_r = 99$, is 35. This means that for a given ring gear tooth, it will take 35 carrier cycles before a given planet tooth is aligned with that ring tooth again. Likewise, the sun gear, $N_s = 27$, has a hunting tooth ratio of 3 with respect to the ring gear. This means that, for every 3 carrier cycles, a given sun gear tooth will align with a given ring gear tooth. Because of this discrepancy, fundamentally different vibration separation algorithms are needed for **PGVS** and **SGVS**. Two general methods are discussed: single accelerometer / single planet (**SASP**) for both **PGVS** and **SGVS** and single accelerometer / multiple planets (**SAMP**) for just **SGVS** .

4.5 Planet Gear Vibration Separation

This section discusses the isolation of dynamics associated with a single planet.

Figure 4.8 shows a single layer associated with a given planet and a given accelerometer of the **Assembly Family**.

The number of cycles available is $N_{extract}$ which depends on the amount of data. For example, a typical run under the current study collects data for 40 seconds. A transmission input of 6,060 RPM produces a carrier cycle of 5.79 Hz., resulting in $N_{extract} = 232$ complete cycles captured. Since the hunting tooth ratio is N_p, The first N_p cycles correspond to alignment of a different planet tooth with the accelerometer and constitute a set. Likewise, each additional set of N_p columns creates another set. There are **floor**$(\frac{N_{extract}}{N_p})$ sets available in the current **Assembly Family**, and, for the

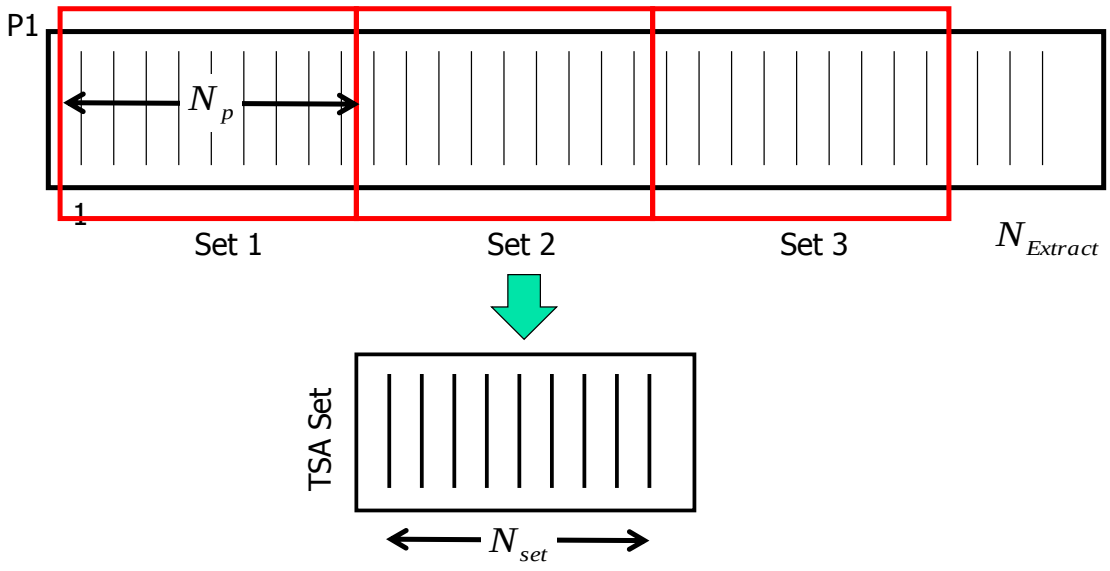

Figure 4.8: Planet Gear Vibration Separation Schematic

example provided, give 210 carrier cycles. Since, for each set, all columns represent the same tooth orientation, and the data was interpolated to correspond to the same angular position; they can be averaged into a single set of N_p columns and termed a time synchronously averaged set. The number of columns required in a **TSA set** is N_{set}, where, for the current case, $N_{set} = N_p$.

Figure 4.9, shows a detailed view of the **TSA set**, where each column of **TSA set** is now mapped to a row in the illustration. Recall from Section (4.3.2) the extraction index, N^*_{ij} only need to be determined once for each P_i/A_j pair, and data is extracted about this region for all subsequent cycles. The extracted data is placed at its corresponding position along the **Vibration Separation Vector** given by the mapping index, N^{**}_{ij}, which is governed by the planet's tooth mesh schedule. If $M_v > 1$, overlapping of data will occur and the amount of overlap is governed by the number of points extracted, ℓ_E. In addition, special windowing is required to merge

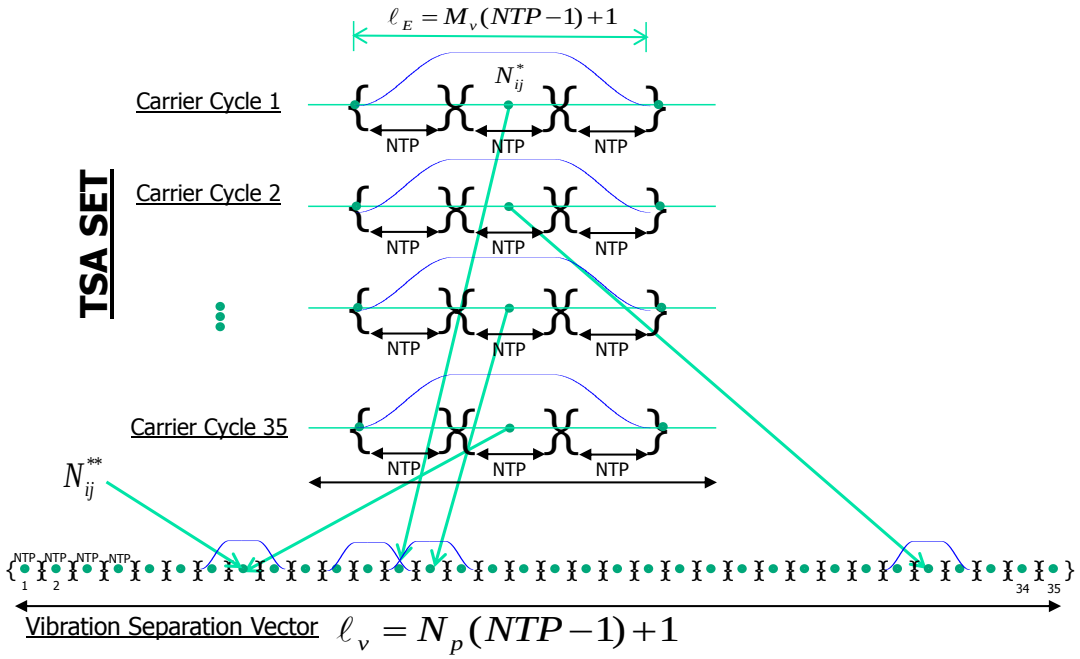

Figure 4.9: Planet Gear Vibration Separation Schematic ($N_{set} = 35$)

overlapping data without introducing distortion. Windowing is discussed in Section 4.5.3.

4.5.1 Determining the Mapping Index, N_{ij}^{**}: **PGVS**

As a planet meshes with each ring tooth, it advances one ring gear pitch. For a full carrier cycle, it will have rotated N_r ring gear pitches. For a planet containing N_p teeth, the next tooth to be in mesh one cycle later is determined from:

$$P_i^{k+1} = \overline{\mathbf{mod}}(P_i^k + \overline{\mathbf{mod}}(N_r, N_p), N_p) \tag{4.13}$$

where P_i^k is the kth Tooth ID on P_i. For a given planet P_i and accelerometer A_j, the local rotation angle of the planet gear is given by:

$$\theta_{pi}^j = (1 - \frac{N_r}{N_p})(\theta_{sep}^{ij} + m(2\pi) + \Delta_{tooth}) \tag{4.14}$$

where m is the number of carrier cycles from the initial orientation, $\theta_c = 0$, and the identity:

$$\theta_{pi} = (1 - \frac{N_r}{N_p})\theta_c \tag{4.15}$$

is used that relates a planet's local rotation to that of the carrier angle. Recall, m starts at 1 due to the rejection of the first carrier cycle in the data. Once θ_{pi}^{j} is determined, then:

$$N_{ij}^{**} = \mathbf{floor}(\overline{\mathbf{mod}}(\theta_{pi}^{i}, 2\pi)\frac{\ell_V - 1}{2\pi}) \tag{4.16}$$

In both the OH-58A and OH-58C, each planet gear has a different mapping index value.

4.5.2 Assembly Holding Matrix

To ease the assembly, handle special cases, and assess the individual contributions of each extracted waveform to the overall **Vibration Separation Vector** , an **Assembly Holding Matrix** is used. Figure 4.10 is a schematic of the **Assembly Holding Matrix**. Each column of the **TSA set** is windowed and assigned to a column within the **Assembly Holding Matrix** according to the target gear's mapping index N_{ij}^{**}.

This matrix has length ℓ_V and width N_{set}. Each column vector of the **TSA Set** is assigned a position within one of the columns in the **Assembly Holding Matrix** corresponding to the tooth numbers the data represents. This is given by

$$\mathbf{RANGE:}\{\hat{\hat{N}}_{ij}, \hat{\hat{N}}_{ij} + 1, \hat{\hat{N}}_{ij} + \ell_{vs} - 1\} \tag{4.17}$$

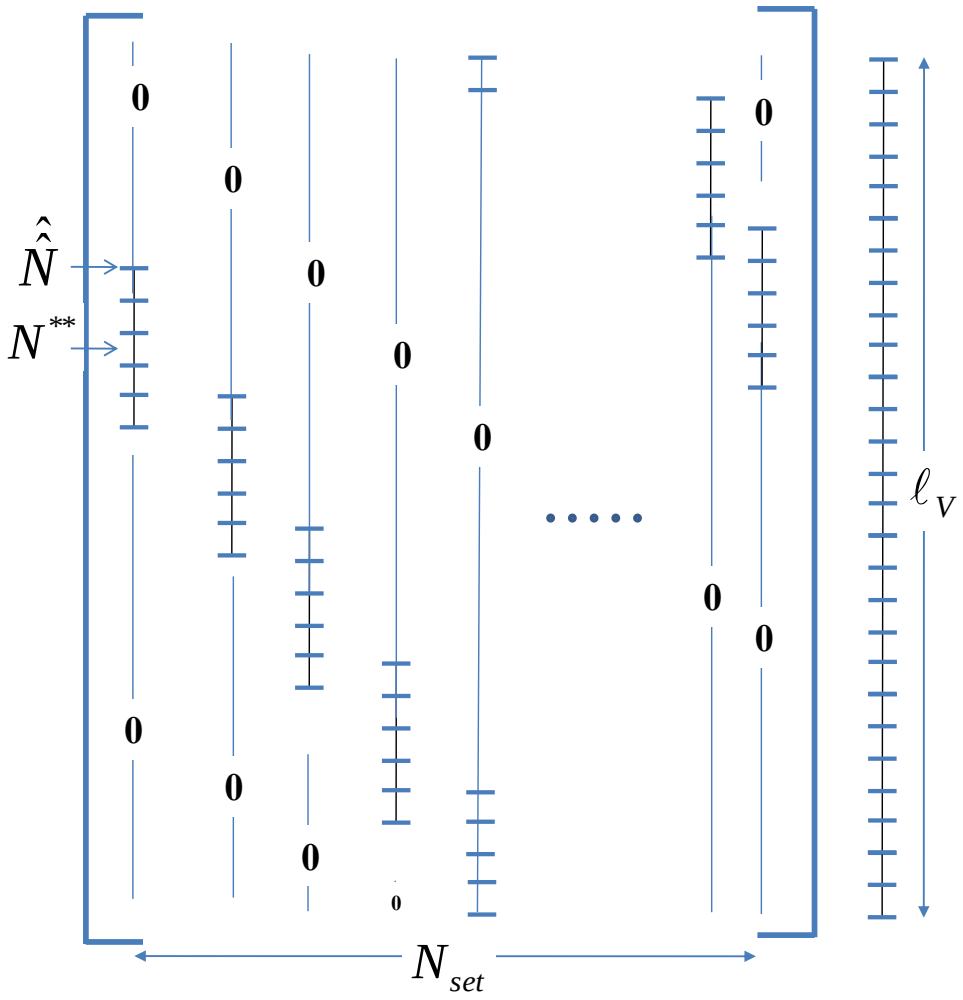

Figure 4.10: Assembly Holding Matrix ($Mv = 5$)

where

$$\hat{\hat{N}}_{ij} = N_{ij}^{**} - \text{floor}(\frac{\ell_E}{2}) \tag{4.18}$$

Each column of the Assembly Holding Matrix consists of zeros, except for the locations where data is inserted. The **Vibration Separation Vector** is created by summing across the columns.

4.5.3 Windowing

In order to ensure a smooth assembly, it is recommended that there is data overlap and that windowing is implemented. [41] Consistent with Samuels, a Tukey window is chosen which has the characteristic of being flat in the region of interest and tapers to zero at the sides as shown in Figure 4.11. [41] This symmetric windowing

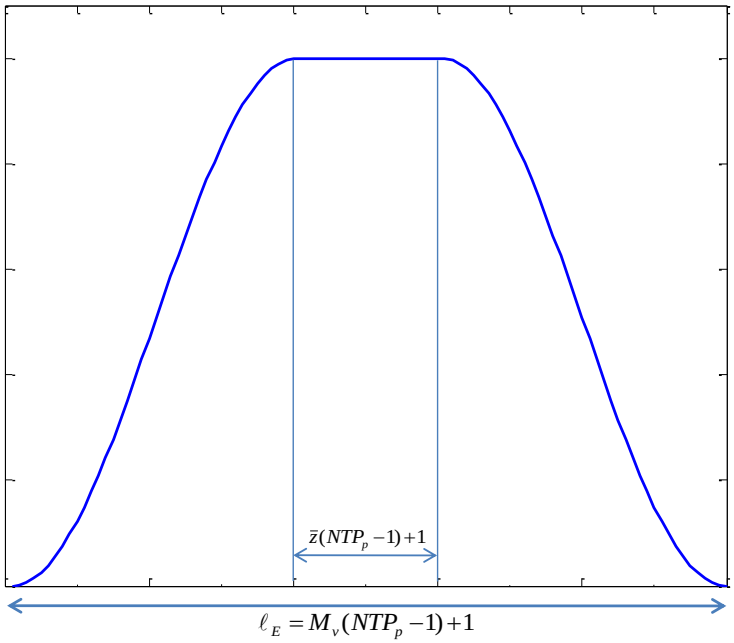

Figure 4.11: Tukey Window

function has length ℓ_E and is a function of 2 parameters: M_v, and $\bar{z}$ where M_v is the width of the Tukey window in units of **TMPs** and $\bar{z}$ is the number of **TMPs** for which the window is flat. A fundamental property that must be satisfied when combining windowed data is that the sum of the shifted window functions produce a constant. This means that if all the windows are positioned and summed in the **Assembly Holding Matrix**, the tapered regions will add to become the same amplitude as the flat region. The actual value of the constant region depends on the amount of

overlap.

4.5.4 Special Cases: Extraction

When extracting data near the ends of the carrier cycle, special precautions are necessary.

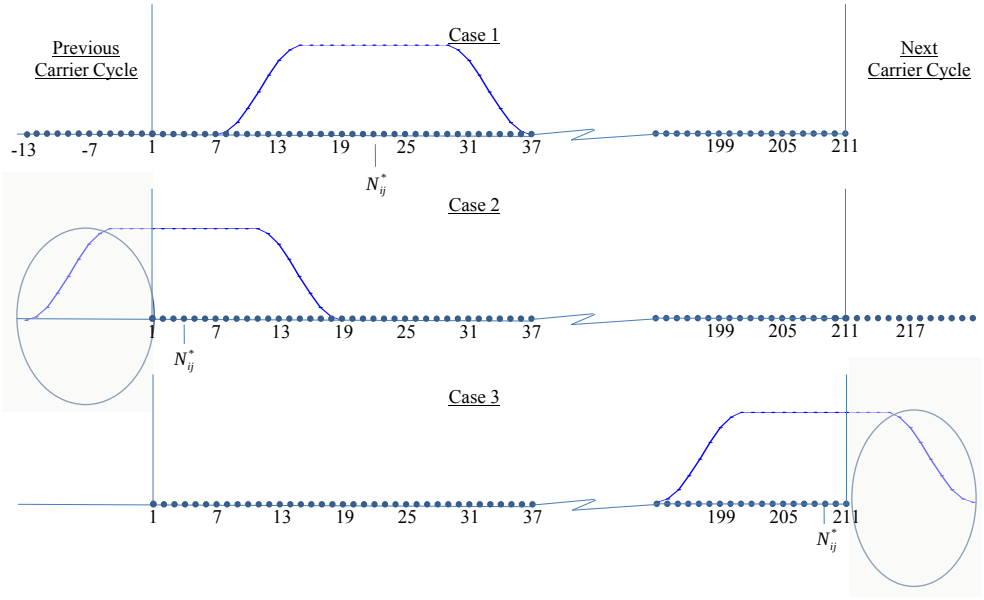

Figure 4.12: Vibration Separation Wrapping Schematic $NTP = 7$, $Mv = 5$

Figure 4.12 represent the three cases encountered when extracting data. Each row represents a set of data containing 211 points corresponding to 35 teeth and $NTP = 7$. A typical NTP is 89 points, but it is kept low for illustrative purposes.

Case 1 represents the ideal case in which the complete data set can be extracted from the current carrier cycle. If N_{ij}^* is close to the beginning of the carrier cycle, as in case 2, data from a previous cycle is used to obtain the necessary ℓ_E points. These points are extracted and prepended to the current set of data points and stored in the **Assembly Family**. Likewise, if the range of data extends beyond the carrier's

cycle as in case 3, data from the beginning of the next carrier cycle is extracted and appended to the end of the current set of data and stored. If the desired cycles are non-existent, as would be the case if the extracted cycles are from the first or last cycle, the missing data data is obtained from a waveform that is similar to the missing waveform. It is believed that errors due to these substitutions are minimal and that it is better make the substitutions than reject the entire carrier cycle.

4.5.5 Special Case: Mapping

As in the case for data extractions, special handling is required for placement when the range of data exceeds the **Assembly Holding Matrix** boundaries. If the data needs to be mapped to a region near sun tooth ID 1, it is possible that the edge will be exceeded. This condition requires a wrapping of values in which the points that extend beyond the beginning are mapped to the end of the **Assembly Holding Matrix** column. Likewise, if the data exceeds the end, the overflow portion is mapped to the beginning as in the beginning of the **Assembly Holding Matrix** column as in the fifth column of Figure 4.10. For all other cases, the **Assembly Family** column can fit within an **Assembly Holding Matrix** column without the need to wrap values about the boundaries.

An example output is given in Figure 4.13.

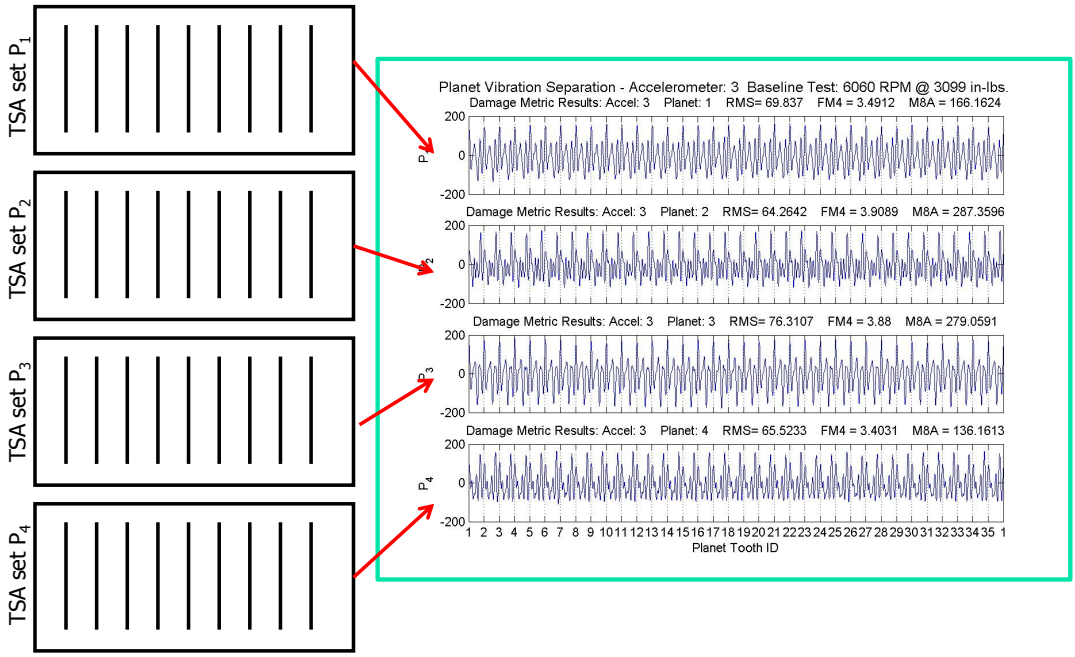

Figure 4.13: PGVS Example Output

4.6 Sun Gear Vibration Separation - General

Sun Gear Vibration Separation is challenging because it seeks to isolate dynamics associated with a given sun gear tooth through a simultaneously meshing planet gear. In addition, if the hunting tooth ratio between the sun gear and the ring gear is not equal to N_s, only a fraction of the teeth are aligned when data is extracted; thus, a direct tooth-to-tooth comparison is not possible for all teeth. Figure 4.14 show sun gears for the OH-58A and OH-58C, respectively.

The teeth are numbered clockwise. Each plot contain a set of asterisks at distinct angles. These are symbolic representations of the region of the sun gear that is aligned when a given planet is aligned with a given accelerometer. The simultaneously aligned planets are denoted by the three Planet IDs that accompany the markings and the sequence extends radially inward in the planet passing order.

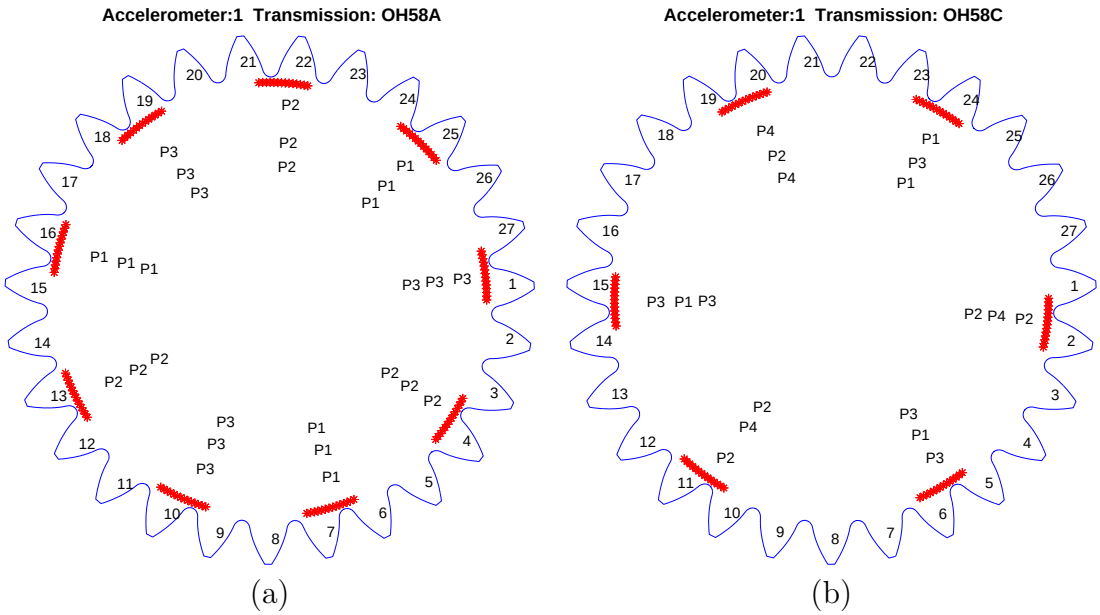

Figure 4.14: Sun Gear's Aligned Region $M_v = 1$ and A_1/P_2

As an example, Figure 4.14a shows the result after 27 planet passes on accelerometer A_1. There are only nine distinct regions of the sun gear that are aligned when any of the three planets are aligned with A_1. Recall that the hunting tooth ratio between the sun and ring gear is 3. Focusing on a single planet, say P_1, the regions near Sun Tooth ID 7,16, or 25 are the only ones "'seen"' through P_1. Similar results exist for all planets across all accelerometers. Since there are three planets, each with a set of three distinct locations, there are a total of nine sun teeth directly engaged when one of the three planets are aligned at a given accelerometer.

Figure 4.14b, representing 18 planet passes, shows some significant differences. For one, there are only six distinct regions aligned when one of the four planets is aligned. Looking at the Planet ID sequence reveals that diametrically opposing planets align with the same sun gear regions. The spacings of the regions are also unequal, due to the unequal spacing of the planets.

In the case for **PGVS**, since the hunting tooth ratio was N_p, extractions were possible when each planet tooth was in the same physical orientation. This allowed for each individual tooth mesh waveform to be directly compared to every other. However, for the current **SGVS** scenario, only three teeth can be directly compared if using only a single planet and only nine teeth for the OH-58A and six teeth for the OH-58C if using multiple planets. Another possibility is to compare the data corresponding to a span of teeth. This is accomplished by extracting data associated with multiple teeth, i.e., $M_v > 1$.

4.6.1 Sun "'seen"' through a Single Planet ($M_v > 1$)

The asterisks in Figure 4.14 represent a single **TMP** ($M_v = 1$). If data is extracted representing a longer duration, the span of teeth increases. Figure 4.15 shows the case for $M_v = 9$ through a single planet, P_2.

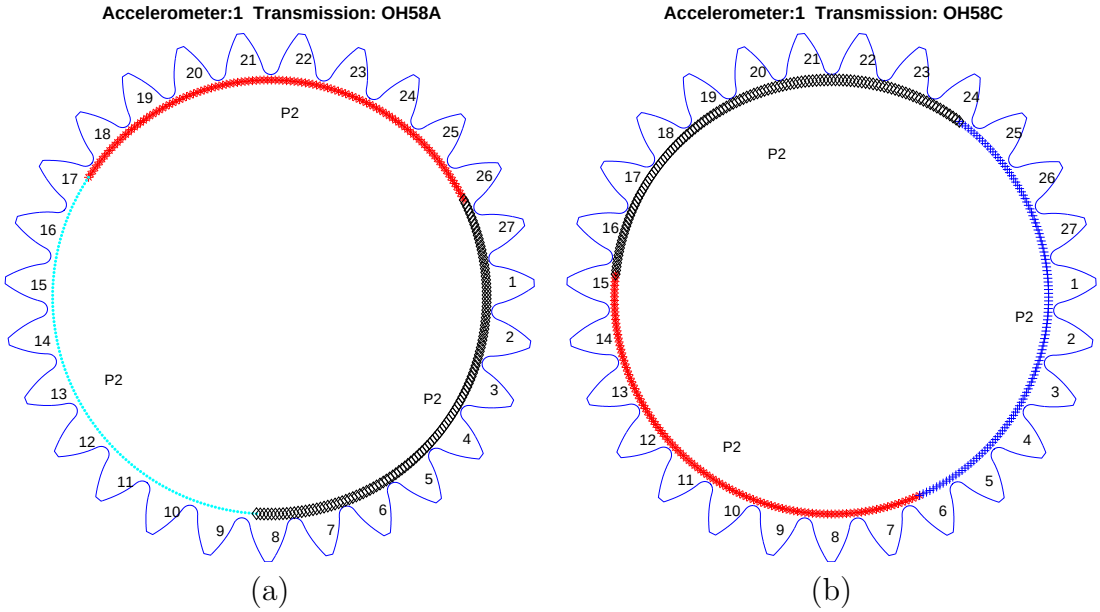

Figure 4.15: Sun Gear's Aligned Region $M_v = 9$ and A_1/P_2

Here, different symbols are used to represent the three different regions. These plots says that each time the planet P_2 passes by accelerometer A_1, extracted data corresponds to four **TMPs** prior to and 4 **TMPs** after planet/accelerometer alignment. The value of 9 is chosen to divide the sun's 27 teeth evenly. For both diagrams, there is no overlapping of symbols.

4.6.2 Multiple Planets ($M_v > 1$)

Another alternative is to extract data corresponding to multiple **TMPs** when each planet passes. The plots associated with this scenario are shown in Figure 4.16.

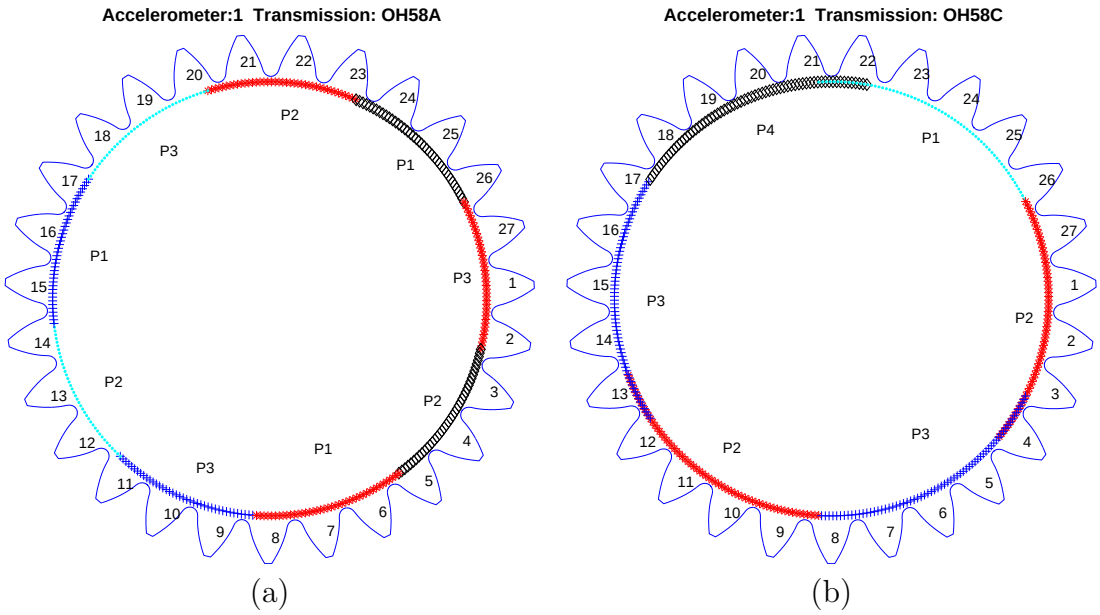

Figure 4.16: Sun Gear's Aligned Region A_1 and Multiple Planets

Due to the unequal spacing on the OH-58C in Figure 4.16b, there is some overlap of symbols at Sun Tooth ID: 4, 13, and 22. This is handled using special windowing techniques and is discussed in Section 4.8.1.

4.6.3 Multiple Accelerometers

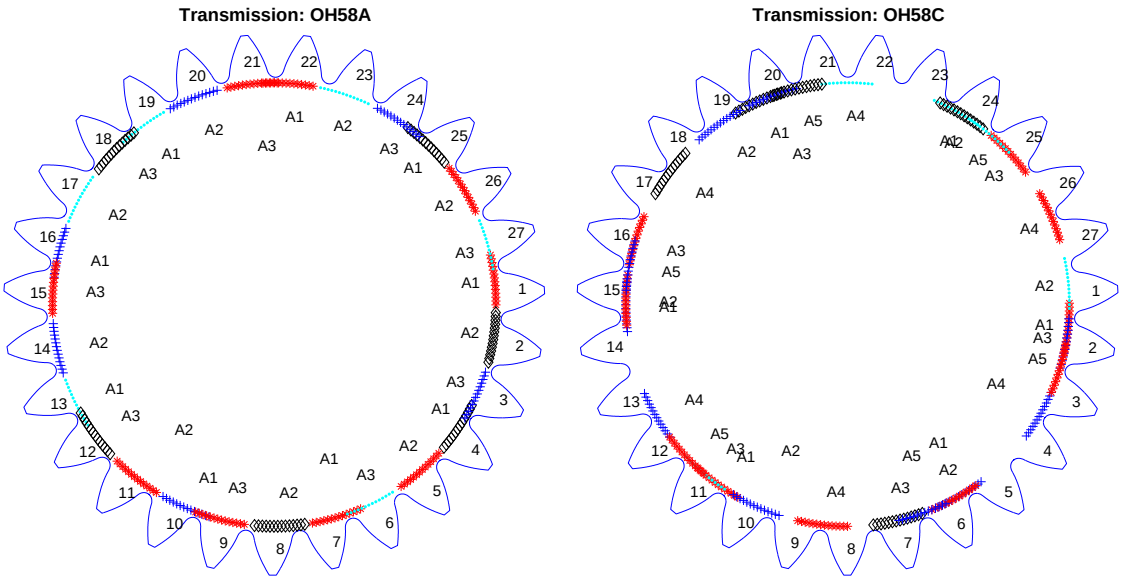

a b

Figure 4.17: Sun Gear's Aligned Region - Five Accelerometers - Current Layout

$M_v = 1$

Another alternative is using multiple accelerometers. Figure 4.17 combines all five accelerometers, giving a snapshot of direct tooth representation based on the current accelerometer layout for $M_v = 1$.

Notice that for the OH-58A, the current spacing is sufficient to obtain direct alignment from all sun teeth. However, for the OH-58C, most but not all teeth are directly engaged when either of the four planets are aligned. The ideal spacing for the OH-58A is one with three accelerometers spaced at the ring gear's tooth pitch. For the OH-58C, five accelerometers spaced at the ring gear's tooth pitch. Figure 4.18 shows the direct sun tooth representation obtained with ideally placed accelerometers for the OH-58A and OH-58C, respectively. Notice that A_5 produces redundant data

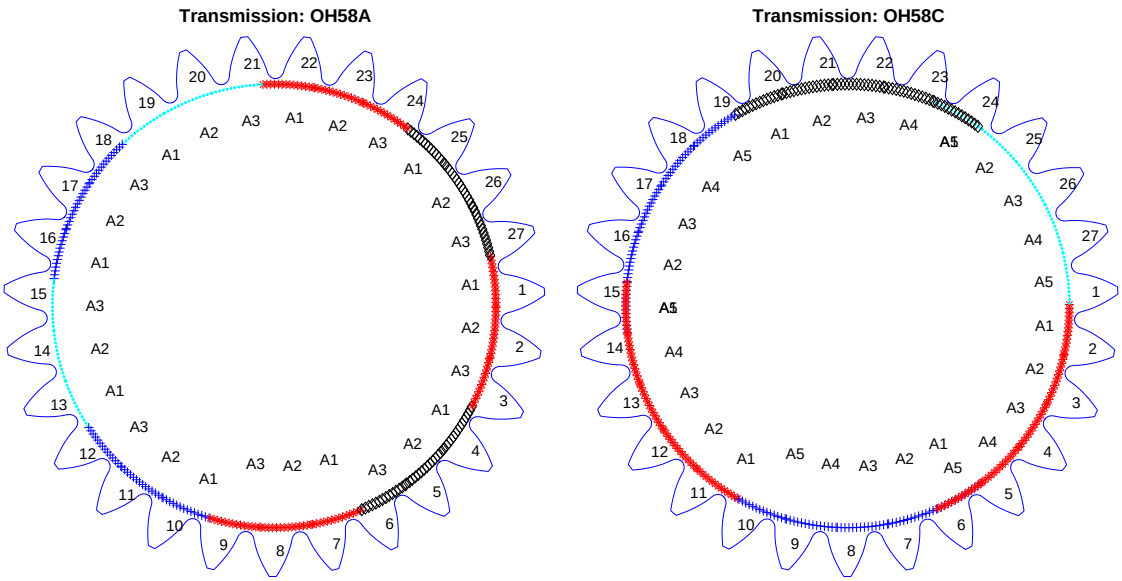

a b

Figure 4.18: Sun Gear's Aligned Region: a.) Three Accelerometers b.) Five Accelerometers - Ideal Layout $M_v = 1$

with A_1 at ID 4, 13, and ID 22 but is needed to cover the regions 8, 17,and 26.

Using multiple accelerometers requires data from different sensors to be combined. Ideally, the sensors should have a high degree of correlation but in practice, this is very difficult. Other researchers have experienced the same. [41,108] In this current work, data extracted from different accelerometers have low time-series correlation. This can be attributed to differences in sensor mounting and location. Some sensors are directly mounted to the casing, others are mounted to accelerometer adapters. In addition, the transmission housing lacks symmetry.

Due to these shortfalls, a damage detection scheme based on multiple accelerometers is not pursued. Current work in this area is being conducted using fiber optic strain gauge arrays. [109]

4.6.4 Sun Tooth Mesh Schedule

In order to match extracted dynamics with the correct sun tooth region, the sun tooth meshing shedule is needed. As the carrier rotates, the angle of sun Tooth ID 1, $\theta_s^1(i,j)$ is tracked. When P_i is aligned with A_j, the clockwise angle between $\theta_{s1}^{i,j}$ and A_j is used to determine the region of the sun tooth that is aligned. The angle $\theta_s^1(i,j)$ is given by:

$$\theta_s^1(i,j) = (1 + \frac{N_p}{N_r})(\theta_{sep}^{ij} + m(2\pi) + \Delta_{tooth} + \bar{\theta_s^1}) \tag{4.19}$$

where the identity:

$$\theta_s = (1 + \frac{N_r}{N_s})\theta_c \tag{4.20}$$

is used. The clockwise angle to A_j, corresponding to increasing Sun Tooth ID number, is given by

$$\theta_s^j = \overline{\mathbf{mod}}(\overline{\mathbf{mod}}(\theta_{s1}^{ij}, 2\pi) - \theta_A^j), 2\pi) \tag{4.21}$$

where $\bar{\theta_s^1}$ is the initial angle of Tooth ID 1. The Sun Tooth ID is found by counting the number of sun tooth pitches in θ_s^j. Since the sun tooth pattern repeats, it is possible to tabulate the sun tooth mesh schedule for both systems. Table 4.3 on page 117 and Table 4.4 on page 118 show the tooth meshing schedule in term of the approximate tooth ID, for the sun gear of the OH-58A ($M_v = 3$) and OH-58C ($M_v = 5$) respectively. Sun Tooth ID values are used instead of angular values to make the tables more intuitive. During implementation however, the actual angle is used.

Looking at Table 4.4, each column represents a carrier cycle and each row represents one of the five accelerometers. There are only three carrier cycles, since

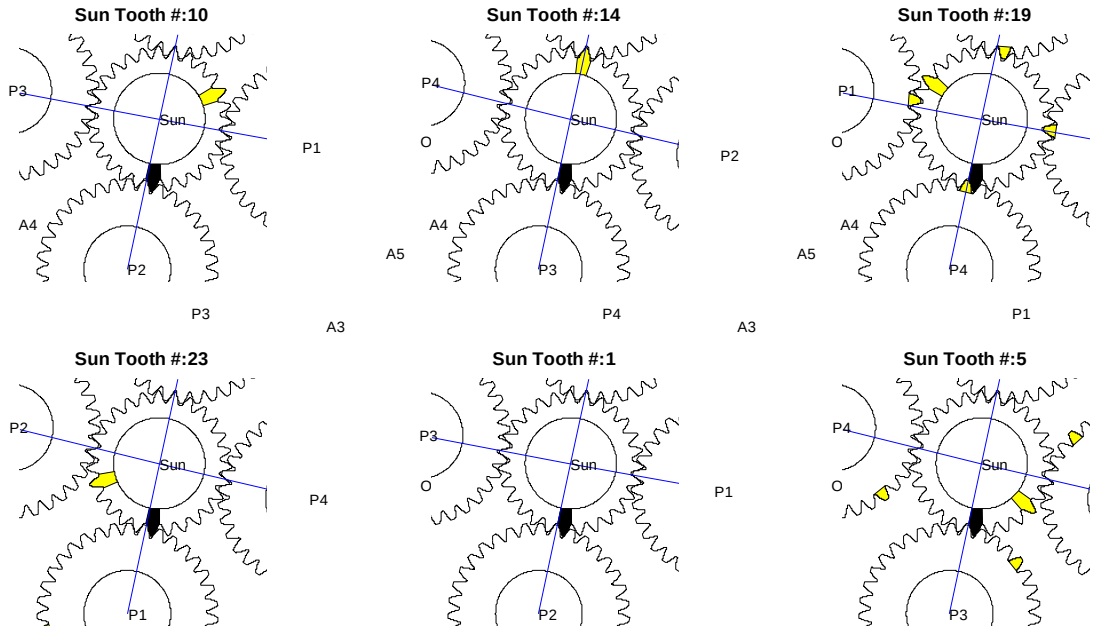

Figure 4.19: Sun Meshing Positions (Cycle 1, Accelerometer 1)

the pattern repeats, therefore Table 4.4 represents a complete set. The highlighted columns within each block represent the closest sun tooth associated with N_{ij}^{**}. Each row contains $M_v = 5$ tooth ID numbers represented per extraction. Figure 4.19 is a graphical representation of the first box of Table 4.4 for which the lightly shaded sun tooth represents Sun Tooth ID 1 and the darker tooth is the one represented in the table and indicated on top of each plot. When P_2 aligns with A_1, the sun gear is in mesh between teeth 10 and 11. The chart's value of 10 is rounded to the closest tooth for clarity. Data is extracted that corresponds to when sun teeth 7 through 13 are in contact with P_2 as P_2 passes A_1. This is then repeated when the next planet, P_3, arrives at A_1 and data associated with teeth 11 to 17 are extracted. As shown in Table 4.4, extractions associated with six consecutive planet passes are needed, (for $M_v = 5$), to get full tooth representation: four from the current cycle

and twp from the subsequent cycle. Also, this pattern is repeated every three cycles, so Table 4.4 represents a complete set. A similar discussion can be made for Table 4.3 corresponding to the OH-58A.

The aforementioned discussion provides the necessary background to the development of two sun gear vibration separation algorithms presented in the next two sections.

	Cycle 1			Cycle 2			Cycle 3		
	Accelerometer 1			Accelerometer 1			Accelerometer 1		
P2	21	22	23	12	13	14	3	4	5
P3	9	10	11	27	1	2	18	19	20
P1	24	25	26	15	16	17	6	7	8
P2*	12	13	14	3	4	5	21	22	23
P3*	27	1	2	18	19	20	9	10	11
P1*	15	16	17	6	7	8	24	25	26
P2**	3	4	5	21	22	23	12	13	14
P3**	18	19	20	9	10	11	27	1	2
P4**	6	7	8	24	25	26	15	16	17
	Accelerometer 2			Accelerometer 2			Accelerometer 2		
P2	25	26	27	16	17	18	7	8	9
P3	13	14	15	4	5	6	22	23	24
P1	1	2	3	19	20	21	10	11	12
P2*	16	17	18	7	8	9	25	26	27
P3*	4	5	6	22	23	24	13	14	15
P1*	19	20	21	10	11	12	1	2	3
P2**	7	8	9	25	26	27	16	17	18
P3**	22	23	24	13	14	15	4	5	6
P4**	10	11	12	1	2	3	19	20	21
	Accelerometer 3			Accelerometer 3			Accelerometer 3		
P2	8	9	10	26	27	1	17	18	19
P3	23	24	25	14	15	16	5	6	7
P1	11	12	13	2	3	4	20	21	22
P2*	26	27	1	17	18	19	8	9	10
P3*	14	15	16	5	6	7	23	24	25
P1*	2	3	4	20	21	22	11	12	13
P2**	17	18	19	8	9	10	26	27	1
P3**	5	6	7	23	24	25	14	15	16
P4**	20	21	22	11	12	13	2	3	4
	Accelerometer 4			Accelerometer 4			Accelerometer 4		
P3	24	25	26	15	16	17	6	7	8
P1	12	13	14	3	4	5	21	22	23
P2	27	1	2	18	19	20	9	10	11
P3*	15	16	17	6	7	8	24	25	26
P1*	3	4	5	21	22	23	12	13	14
P2*	18	19	20	9	10	11	27	1	2
P3**	6	7	8	24	25	26	15	16	17
P1**	21	22	23	12	13	14	3	4	5
P2**	9	10	11	27	1	2	18	19	20
	Accelerometer 5			Accelerometer 5			Accelerometer 5		
P3	27	1	2	18	19	20	9	10	11
P1	15	16	17	6	7	8	24	25	26
P2	3	4	5	21	22	23	12	13	14
P3*	18	19	20	9	10	11	27	1	2
P1*	6	7	8	24	25	26	15	16	17
P2*	21	22	23	12	13	14	3	4	5
P3**	9	10	11	27	1	2	18	19	20
P1**	24	25	26	15	16	17	6	7	8
P2**	12	13	14	3	4	5	21	22	23

Table 4.3: Sun Tooth Meshing Schedule OH-58A $M_v = 3$

	Cycle 1					Cycle 2					Cycle 3				
	Accelerometer 1					Accelerometer 1					Accelerometer 1				
P2	8	9	10	11	12	26	27	1	2	3	17	18	19	20	21
P3	12	13	14	15	16	3	4	5	6	7	21	22	23	24	25
P4	17	18	19	20	21	8	9	10	11	12	26	27	1	2	3
P1	21	22	23	24	25	12	13	14	15	16	3	4	5	6	7
P2*	26	27	1	2	3	17	18	19	20	21	8	9	10	11	12
P3*	3	4	5	6	7	21	22	23	24	25	12	13	14	15	16
	Accelerometer 2					Accelerometer 2					Accelerometer 2				
P2	13	14	15	16	17	4	5	6	7	8	22	23	24	25	26
P3	17	18	19	20	21	8	9	10	11	12	26	27	1	2	3
P4	22	23	24	25	26	13	14	15	16	17	4	5	6	7	8
P1	26	27	1	2	3	17	18	19	20	21	8	9	10	11	12
P2*	4	5	6	7	8	22	23	24	25	26	13	14	15	16	17
P3*	8	9	10	11	12	26	27	1	2	3	17	18	19	20	21
	Accelerometer 3					Accelerometer 3					Accelerometer 3				
P2	23	24	25	26	27	14	15	16	17	18	5	6	7	8	9
P3	27	1	2	3	4	18	19	20	21	22	9	10	11	12	13
P4	5	6	7	8	9	23	24	25	26	27	14	15	16	17	18
P1	9	10	11	12	13	27	1	2	3	4	18	19	20	21	22
P2*	14	15	16	17	18	5	6	7	8	9	23	24	25	26	27
P3*	18	19	20	21	22	9	10	11	12	13	27	1	2	3	4
	Accelerometer 4					Accelerometer 4					Accelerometer 4				
P4	6	7	8	9	10	24	25	26	27	1	15	16	17	18	19
P1	10	11	12	13	14	1	2	3	4	5	19	20	21	22	23
P2	15	16	17	18	19	6	7	8	9	10	24	25	26	27	1
P3	19	20	21	22	23	10	11	12	13	14	1	2	3	4	5
P4*	24	25	26	27	1	15	16	17	18	19	6	7	8	9	10
P1*	1	2	3	4	5	19	20	21	22	23	10	11	12	13	14
	Accelerometer 5					Accelerometer 5					Accelerometer 5				
P4	9	10	11	12	13	27	1	2	3	4	18	19	20	21	22
P1	13	14	15	16	17	4	5	6	7	8	22	23	24	25	26
P2	18	19	20	21	22	9	10	11	12	13	27	1	2	3	4
P3	22	23	24	25	26	13	14	15	16	17	4	5	6	7	8
P4*	27	1	2	3	4	18	19	20	21	22	9	10	11	12	13
P1*	4	5	6	7	8	22	23	24	25	26	13	14	15	16	17

Table 4.4: Sun Tooth Meshing Schedule OH-58C $M_v = 5$

4.7 Sun Gear Vibration Separation - **SASP** Method

This section presents a method that averages out the effect of a single planet and is able to isolate the dynamics associated with just the sun gear. The following development is tailored to the planetary systems in this research. In the previous section, it was shown that, when using a single planet gear, there are only three sun teeth simultaneously align. Given a layer of the **Assembly Family** corresponding to a given planet, every third cycle in the **Assembly Family** can be associated with one of the three teeth. Since there are 27 **TMPs** , the following development associates $M_v = 9$ **TMPs** to each tooth. The schematic in Figure 4.20 aids in this development.

In Figure 4.20, there is an **Assembly Family** for a single accelerometer. Planet P_1 for Accelerometer A_1 is isolated for the discussion, but the same type of analysis is applied to the others. A look at Table 4.4 on page 118 shows that the three teeth are 23, 14, and 5. These vectors are collected into pass groups where:

$$\text{Pass 1:} \quad 1 : 3 : N_{extract}$$

$$\text{Pass 2:} \quad 2 : 3 : N_{extract}$$

$$\text{Pass 3:} \quad 3 : 3 : N_{extract}$$

In Figure 4.20, the cycles associated with Pass 1 are plotted together on the first row. The same is true for Pass 2 and Pass 3. The fourth row is a comparison of the averages. The x-axis represents the sun tooth angle, but has been replaced by Sun

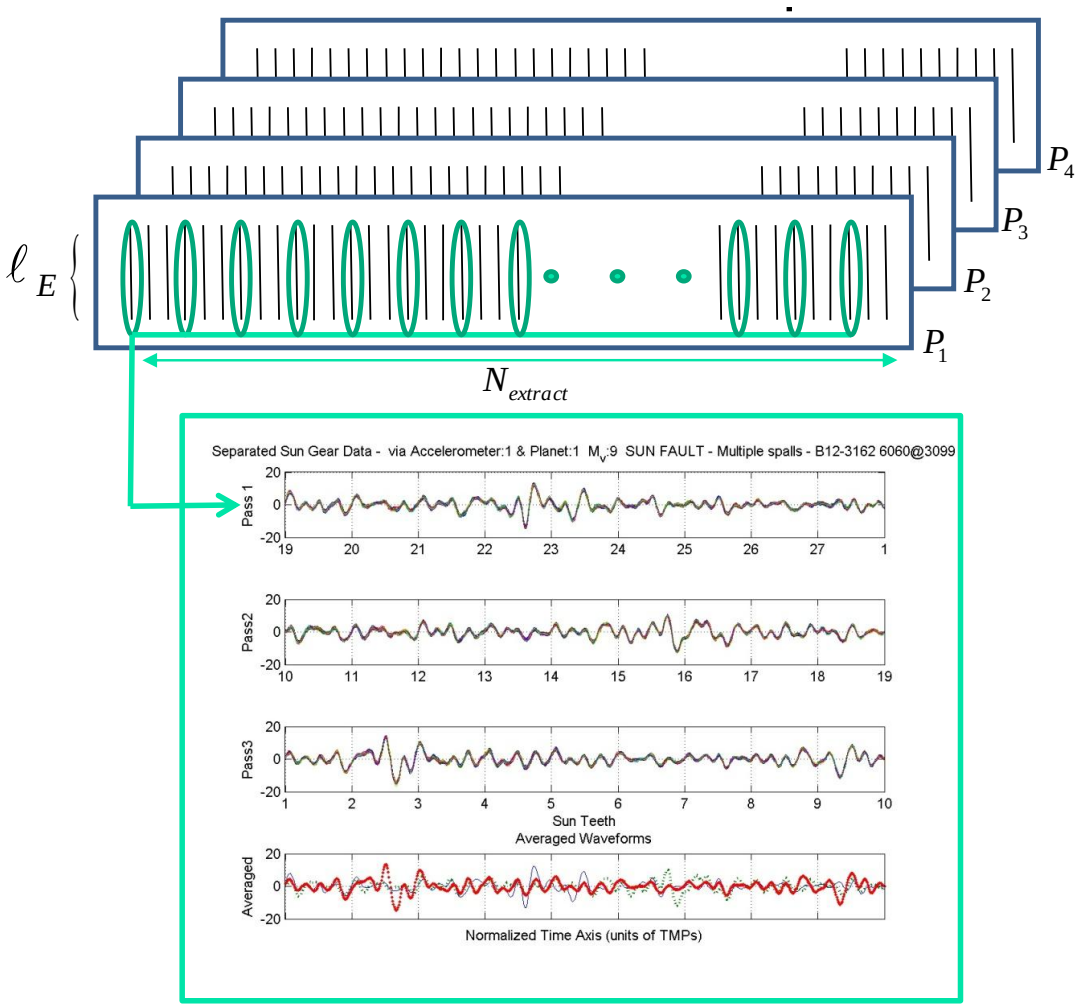

Figure 4.20: SGVS Schematic. P_1 **&** A_1

Tooth IDs to make the plot more intuitive. Notice that Sun Teeth ID 23, 14, and 5 are centered. Since each row represents the same sun tooth orientation and the points were initially interpolated to ensure angular consistency, averaging each row represents a **TSA** set.

In the example provided, a high degree of correlation is observed for each row but not along the columns. Had averaging been applied before separating into passes, these details would have been averaged out. In looking at the x-axis, it is noticed

that the **Vibration Separation Vector** can be generated by appending Pass 3 to Pass 1 and then appending Pass 2 to Pass 3. The diagnostics is then applied to this resultant signal.

4.8 Sun Gear Vibration Separation - **SAMP** Method

This method aims to extract data at a time when all planets are aligned with a given accelerometer. In the previous section, the sun was "'seen"' through only one planet and that extracted data was used to generate each **Vibration Separation Vector**. In this section, multiple planet passes are used. It is assumed that all planets are damage free and do not provide any type of biasing.

As was shown in Section 4.6, if multiple planet passes are used, then $M_v = 3$ for the OH-58A and $M_v = 5$ for the OH-58C can be used to get representation from all sun gear teeth. Due to the equal spacing of the OH-58A, there is no overlapping. However, overlapping occurs in three locations for the OH-58C. The overlapping is handled with windowing.

4.8.1 Windowing for **SGVS -SAMP**

In order to handle the case for which data for a particular tooth appears twice, a modified Tukey window is used. Using the first block of Table 4.4 as an example, tooth 12 is represented when both P_2 and P_3 passes A_1. There are zero duplications between $P3$ and $P4$. Tooth 21 is represented when both P_4 and P_1 passes A_1. However, when $P1$ and $P2$ pass, no sun teeth are duplicated. Finally, Sun Tooth ID 3 is shared when

P_2 and P_3 pass A_1. This $(M_v - 4) - -(M_v - 5) - -(M_v - 4)$ pattern continues for all six extractions, and similar patterns exist for other values of $M_v > 5$. For example, for $M_v = 7$, there is a 3–2–3 pattern of overlap. To handle these redundancies, two modified Tukey windows are used: $\overline{W}$ and $\overline{\overline{W}}$ for which the development is associated with $M_v = 7$. The first, $\overline{W}$, sets the points associated with the first mesh period to zero and inverts the points associated with the second mesh period. The second, $\overline{\overline{W}}$ sets the first two mesh periods to zero and inverts the points associated with the 3rd mesh period. Figure 4.21 illustrates the two modified Tukey windows:

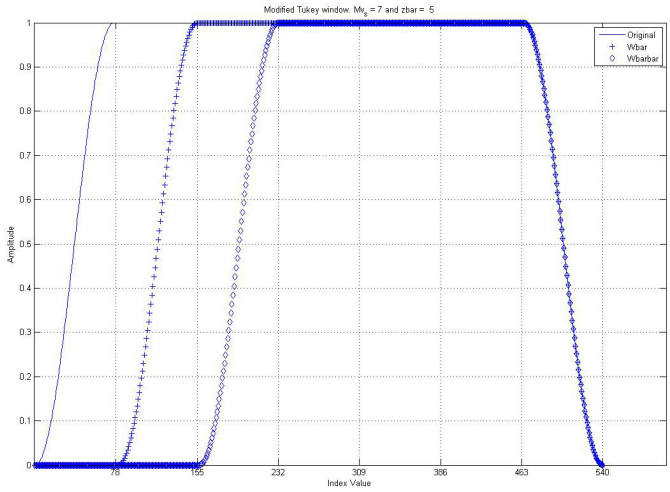

Figure 4.21: Modified Tukey

These two windows are applied in an alternating fashion. When the shifted versions are summed, they produce a constant.

4.8.2 Assembly

Figure 4.22 is a diagram containing the **Assembly Family** for a single accelerometer. In the SASP method, cycles are extracted across the layer corresponding

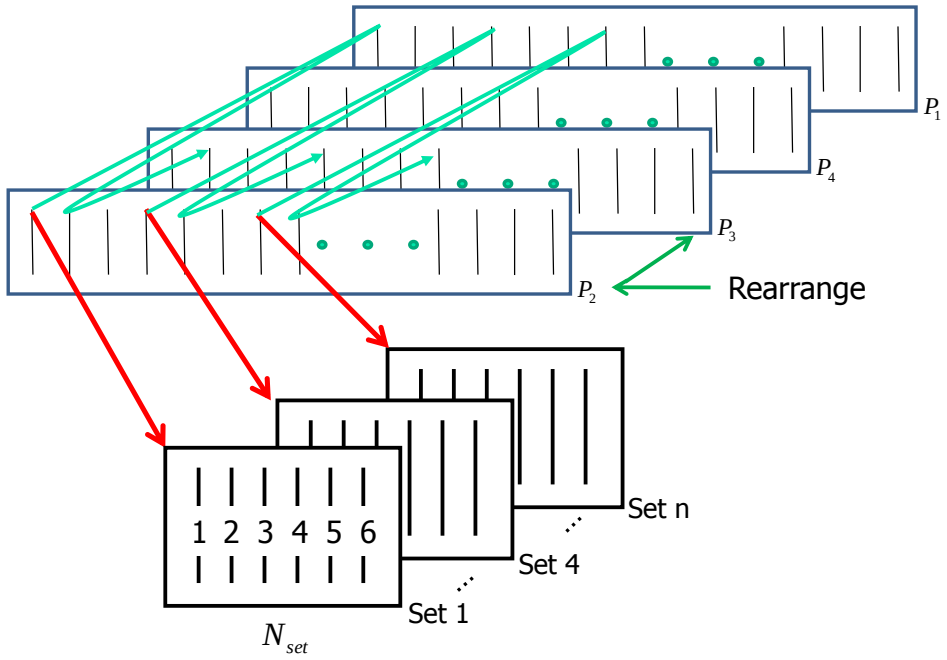

Figure 4.22: Assembly Stage SGVS-SAMP Method (OH-58C)

to a single planet. Recall from Section 4.6, 6 planet passes are needed for the OH-58C and 9 planet passes are needed for the OH-58A. This is achieved by extracting across multiple layers cycles as shown in Figure 4.22 for the OH-58C case. Here, extractions are used from the current cycle and two from the next cycle. It is important that the first planet to arrive at the accelerometer be noted because this governs subsequent ordering. For example, if the signal from A_2 is currently being analyzed, then it must be taken into consideration that the first planet to arrive at A_2 is P_2. Thus, the first

dataset to be pulled from the assembly family corresponds to the first cycle of the 2nd layer. Subsequent cycles include cycle 1 of layer 3, cycle 1 of layer 4, and cycle 1 of layer 1. Two additional datasets are needed from the 2nd column. It is important that the column is obtained from cycle 2 of layer 2 and finally cycle 2 of layer 3. This sequence corresponds to the sequence in Figure 4.19 and would not have been obtained by grabbing data from the first row and the first two from the second cycle.

For the OH-58A, which only has three layers, extractions are used from the current cycle and two subsequent cycles. The same treatment is needed to ensure proper ordering. The samples are collected into sets in a similar manner as that for **PGVS** . These sets have a length of ℓ_E and width N_{set}. Since subsequent cycles are needed, the number of sets is less than $N_{extract}$. For the OH-58A, there are $N_{extract}-2$ and for the OH-58C, $N_{extract}-1$.

Recall from the SASP Method development that every third cycle was collected. The same insight is used in this method to produce three **TSA sets** where every third set is combined. This is illustrated in Figure 4.23.

Figure 4.24 is an enlarged view of the **TSA set** for the OH-58C and differs in many respects when compared with Figure 4.9 for **PGVS** . Whereas each row in Figure 4.9 is a single cycle, each row in Figure 4.24 represent the **TSA sets**. For each row, the first column of the **TSA set** is designated by the Roman Numeral I and the order increases to VI. Each row corresponds to a different tooth mesh ordering, which determines how each extraction is finally placed in the **Vibration Separation Vector**. Since there are only three such orderings possible, they are shown explicitly in Figure 4.9. This pattern is maintained for all assemblies and is the reason only

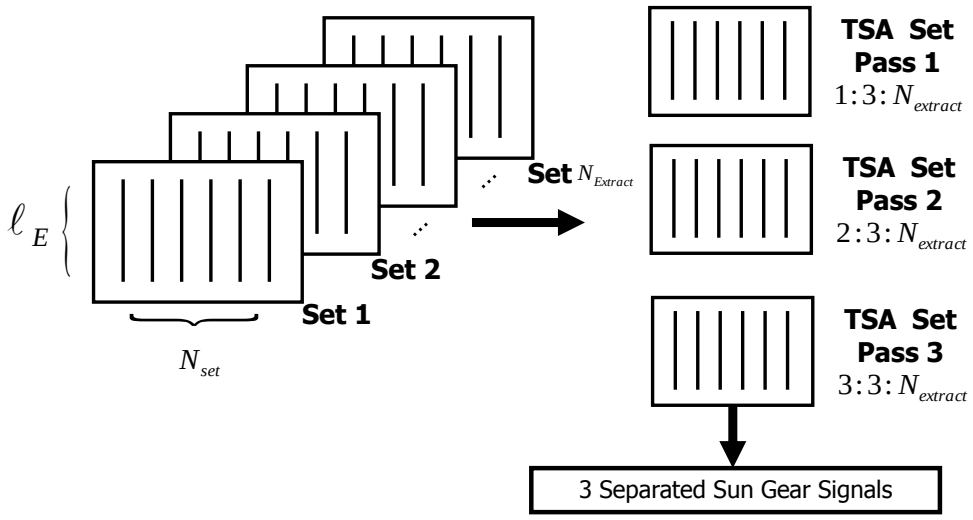

Figure 4.23: TSA stage - SAMP

three sets are shown. Each set is used to create its own **Vibration Separation Vector**. The end result are three **Vibration Separation Vector** to analyze using condition indicators.

A typical result is shown in Figure 4.25

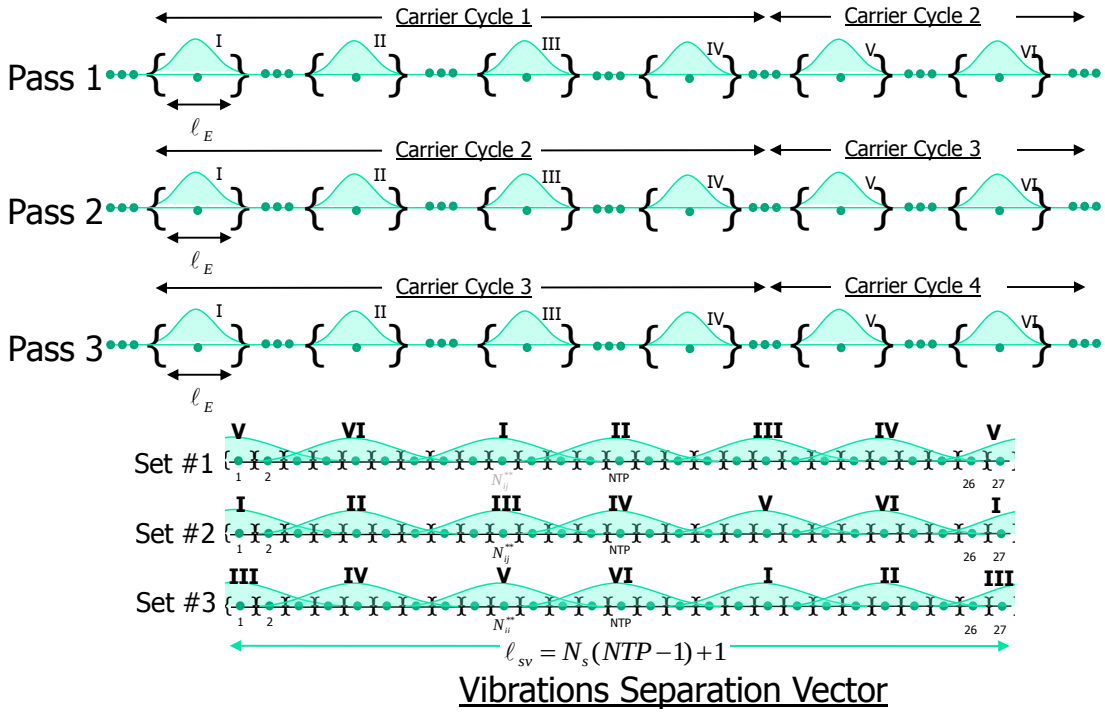

Figure 4.24: Sun Gear Vibration Separation Schematic

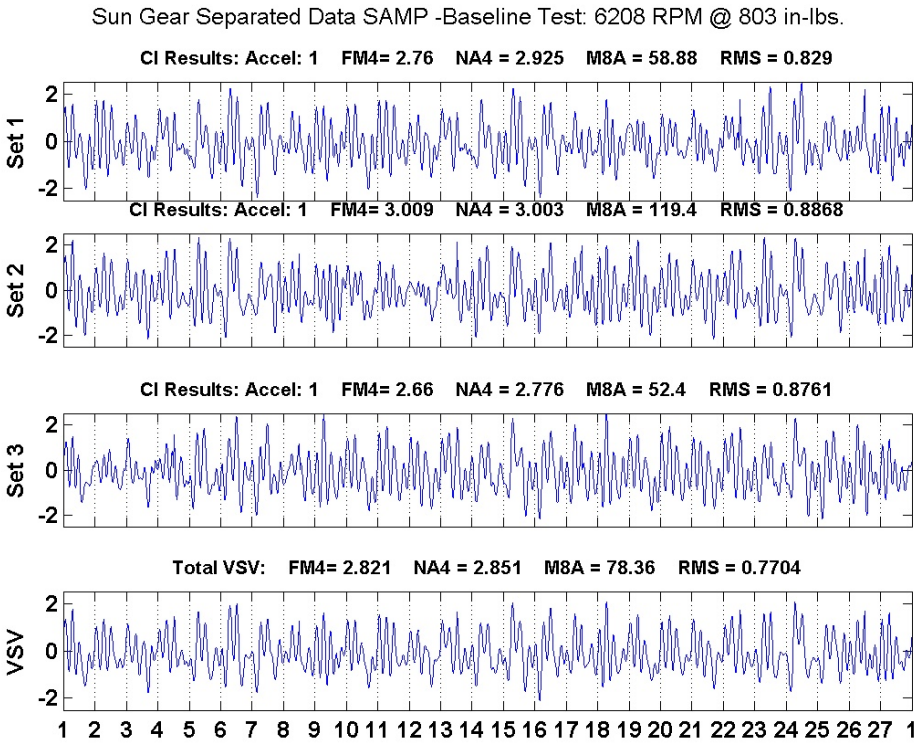

Figure 4.25: SAMP Result Baseline

4.9 Geometrically Synchronized Measurement Method to Planetary Diagnostics

If a gear tooth is damaged, the assumption is that, when engaged, it produces a waveform that is distinctive from the average. However, the transmission's vibrations spectrum is complicated by the many simultaneously meshing gears, and often these details are obscured, even after time-synchronous averaging. As was shown in the previous sections, special processing tools are needed to isolate the dynamics in order to be able to apply condition indicators to the individual components.

Typically, measurements are taken and the condition indicators are applied to the **TSA** signal. This technique has been ineffective for planetary transmission prompting the need to conduct vibration separation. In implementing vibration separation, a higher level of discipline is required in order to maintain proper indexing of the transmission's system with measurements. Some special precautions, which are discussed in more detail in Chapter 5, include implementing a special tool to maintain gear stage orientation during overhaul, a method to identify the correct spline to use when swapping different sun teeth, and the use of a planetary reset pulse that ensured that measurements begin when the transmission is in the pre-determined orientation. Because of these extra efforts to implement vibration separation, an alternative method to transmission diagnostics was made possible. One that exploits the geometric synchronization between the sensors and planetary geometry that allows simple TSA data to be re-evaluated.

The technique relates subsets of the **TSA** signal to the individual sun teeth

in mesh. Figure 4.26 shows an enlarged view of the sun gear region for the OH-58C configuration. At any given time, the sun gear is in mesh with four planets.

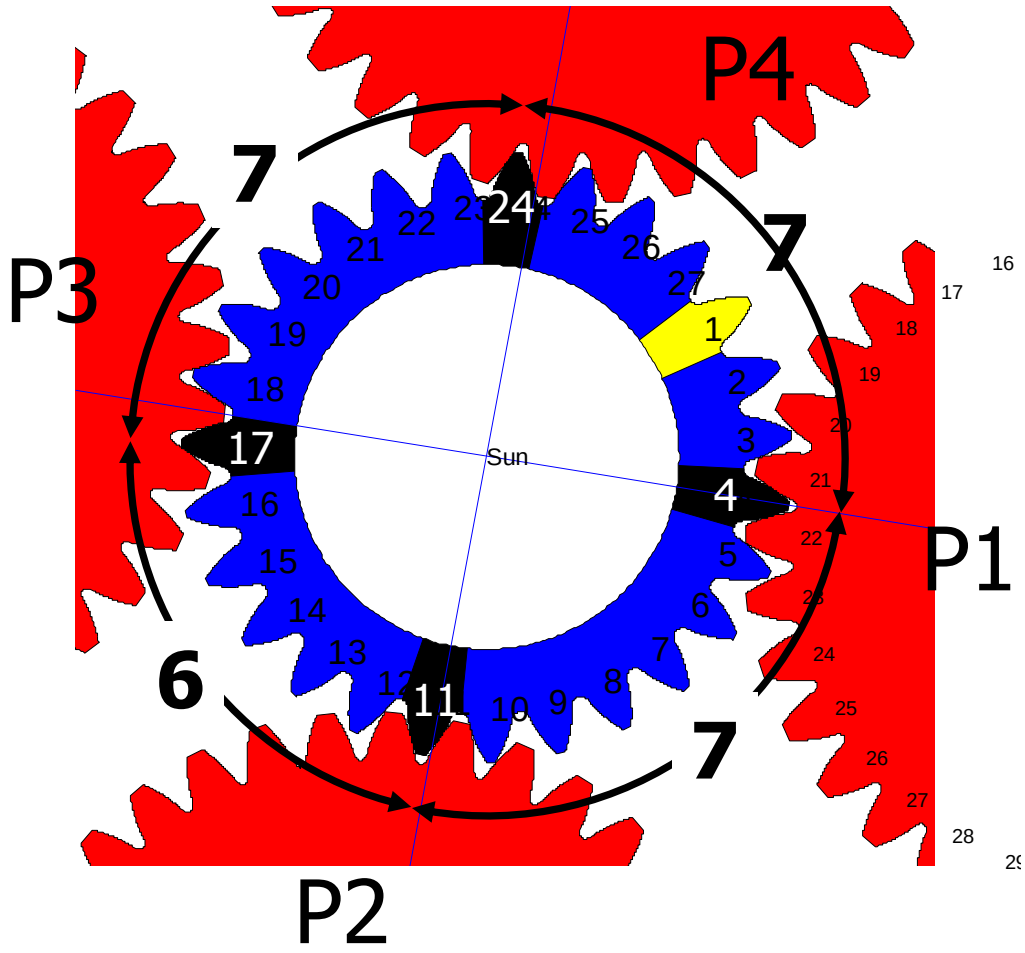

Figure 4.26: Mesh Groups (OH-58C)

Unfortunately, due to the non-sequential nature of the OH-58C, the engaged planets are in different meshing positions making it difficult to determine which teeth are "'most in mesh."' To eliminate ambiguity, the lines of centers between the sun and planets are used as references. The centers of each planet are tracked during meshing and then mapped to a region on the sun tooth. This collection of sun gear angles in mesh at any given time make up a mesh group.

The **GSMM** works by stepping through the **TSA** data in increments corresponding to a single **TMP**. A computation is done on the subset of data and the value is then assigned to all teeth in the current mesh group. Over time, if a given mesh group is responsible for the damage, a distinctive 4-bar pattern appears in the bar graph. If there is no biasing in the data, as would be the case for an undamaged system, then the bar heights are be fairly uniform.

The results are presented in two ways:

Individual Mesh Bins This method of presentation has the results from the calculation accumulating in single bins centered on angles separated by angles corresponding to the sun gear's pitch. If damage exists, a distinctive four bar pattern results.

Mesh Group Bins. In this presentation, each bin is a mesh group. Mesh angles are identified in the same manner; however, instead of a computed value being assigned to the closest angle, it is instead assigned to the mesh group that contains the closest angle. If damage exists, a single bar dominates the bar graph indicating the set of teeth in which damage exists.

Table 4.5 shows the mesh bins and the mesh groups for which they belong for the systems under study.

4.9.1 Damage Detection

The goal, similar to vibration separation, is to match measurements with the geometry of the planetary system, with the premise that the engaged teeth at the

MESH GROUP CENTERS (Degrees)							
	OH-58A			OH-58C			
Group 1	13.3	133.3	253.3	13.3	106.7	200.0	293.3
Group 2	26.7	146.7	266.7	26.7	120.0	213.3	306.7
Group 3	40.0	160.0	280.0	40.0	133.3	226.7	320.0
Group 4	53.3	173.3	293.3	53.3	146.7	240.0	333.3
Group 5	66.7	186.7	306.7	66.7	160.0	253.3	346.7
Group 6	80.0	200.0	320.0	80.0	173.3	266.7	360.0
Group 7	93.3	213.3	333.3	93.3	186.7	280.0	
Group 8	106.7	226.7	346.7				
Group 9	120.0	240.0	360.0				

Table 4.5: Sun Gear Mesh Groups

time of measurement are the source of the currently measured excitement. The first step is to prepare the **TSA** data set. Using insight from the previous chapters, the data is separated into three pass groups and each group is **TSA'd**. These cycles are then combined to produce a **TSA** signal that is three cycles long.

The next step is to sequentially step through the data, and at each step, to calculate a condition indicator. For that step, the sun angles in mesh are identified and matched with the closest mesh bin. The computed **CI** is then attributed to all of the identified mesh bins. A vector that contains elements for each mesh bin or each mesh group is used to tally the obtained values. After three cycles, corresponding to

$3N_r$ **TMPs**, a bar graph is produced highlighting the contribution of each mesh bin or mesh group. A simulation program was written which animated the process and a typical display is given in Figure 4.27.

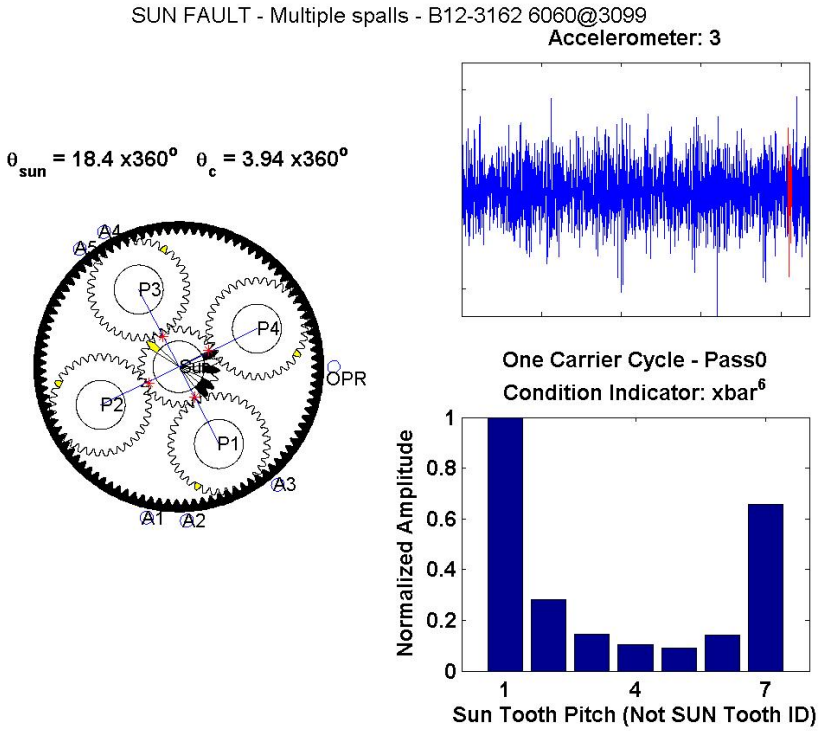

Figure 4.27: Simulation Output - GSM

4.9.2 Choosing a Condition Indicator

At each step, the data representing a single tooth mesh period is analyzed using a condition indicator. The **CIs** that were discussed in Chapter 2, namely FM4,and NA4, were attempted, but showed little effectiveness. The RMS **CI** showed promise but the final bar graph did not provide enough discrimination. The **CI** providing the most useful outcome is a modification of the RMS signal. Instead of squaring

each component before summing, each component is raised to the sixth power. This produces a **CI** that is more sensitive to spikes, which is ideal since spalls are known to produce pulses.

Chapter 5

Experimental Setup

5.1 Setup Introduction

Tests were conducted on the OH-58 500HP transmission test rig located at NASA Glenn Research Center (GRC) in Cleveland, Ohio. A drawing of the stand is shown in Figure 5.1 along with the location of various sensors. [10]

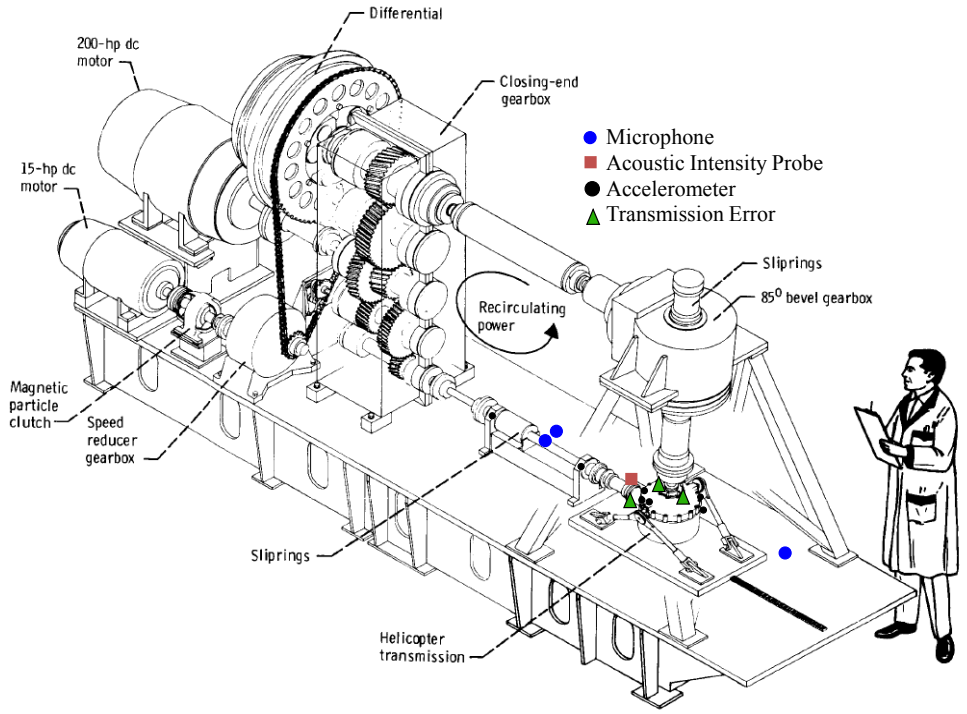

Figure 5.1: NASA GLEN 500 hp Helicopter Transmission Test Stand

Vibration, acoustic, and oil debris information was measured using nine accelerometers, five microphones, and an oil debris monitor. Four of the nine accelerometers were used on the input and output torsional acceleration adapters to be used to measure aggregate transmission error. The remaining five accelerometers were mounted to the transmission housing at several locations. Information on the accelerometers used is given in Table 5.1 and a schematic showing the accelerometer positions is given in Figure 5.2:

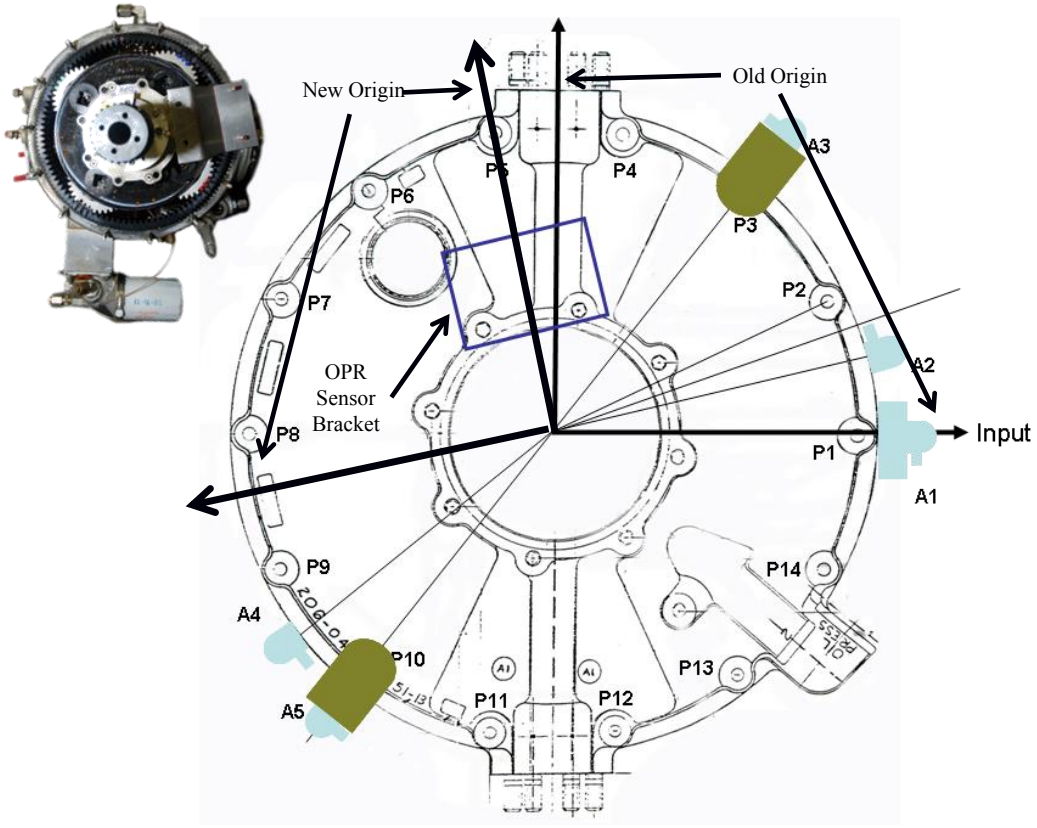

Figure 5.2: Sensor Placement on the OH58 Test Transmission

Sensor	Position (angle)	Model Num.	Sensitivity (mV/g)	S/N
A1	Axial Bevel (258°)	7259A-10	10.02 mV/g	DD12
A2	Case Stud next to Pinion (273°)	7259A-10	12.77 mV/g	BC52
A3	Bracket-Closest to Pinion (310°)	7259A-10	11.05 mV/g	AD341
A4	Case Stud Back (119°)	7259A-10	9.82 mV/g	DD10
A5	Bracket - back (113°)	7259A-10	11.26 mV/g	DG-57

Table 5.1: Case Mounted Accelerometers

Figure 5.2 is shown with the once-per-rev sensor taken as the origin, putting the input shaft at an angle of 258^o. Although not intuitive schematically, this does simplify the signal processing. Three seeded fault cases were tested. All measurement were conducted at full mast loading. The damage cases and test matrix appear in Table 5.2 and the test components are given in Table 5.3.

Damage Cases						
OH-58C					**OH-58A**	
Baseline	**Sun Gear Single Spall**	**Sun Gear Multiple Faults**			**Baseline**	**Bearing Fault** Planet 3

Test Matrix						
Input Speed (RPM)	Output Speed (RPM)	Input Torque (in-lbs.)	Output Torque ($x10^3$)	Rated Speed (%)	Rated Torque (%)	Power (HP)
6060	348	3099	5.41	100	100	298
6255	359	2476	4.32	103	80	246
6294	361	1717	2.99	103	55	171
6208	356	803	1.4	102	26	79.1

Table 5.2: Test Matrix (x 3 faults)

	Damaged Component	Serial Number
II-1	Sun gear (Severe Spall single tooth)	B12-3993
II-3	Sun gear (spall and scoring on many teeth)	B12-3162
II-4	Planet gear/bearing (Fatigue spall on inner race) 1908 previous, undocumented, flight hours	B12-25780

Table 5.3: Test Components

5.2 The OH-58 Helicopter Transmission

The OH-58 is a single-engine, land-based light observation helicopter. Table 5.4 provides a comparison between the transmissions of two models: OH-58A and OH-58C. The two transmission are similar. They both are 2 two-stage reduction

Model	**N**	N_4	N_s	N_p	**Rated Power**	**Operating Speed**	**Carrier Type**	**Reduction Ratio**	**Planet Bearing Type**
OH-58A	3	99	27	35	210 HP	6180 RPM/	Spider	17.44	spherical roller
OH-58C	4	99	27	35	317 HP	6180 RPM/ 354 out	Carrier	17.44	double-row cylindrical roller

Table 5.4: Comparison: OH-58A and OH-58C

gearboxes consisting of a bevel stage and a planetary stage with an overall reduction of 17.44:1. The bevel stage consists of a 19-tooth spiral bevel pinion meshing with a 71-tooth gear. The bevel gear is splined to the 27-tooth sun gear which is the input to the second stage. The sun gear drives the planet against a 99-tooth ring gear, which is splined to the transmission housing. The carrier is splined to the mast output shaft which powers the helicopter's rotors. The main difference between the two models is the planetary stage shown in Figure 5.3. The OH-58C increases load handling capability from 210 HP to 317 HP. In addition, the planets are straddle-mounted on cylindrical roller bearings which are attached to the planet carrier rather than overhung on spherical bearings.

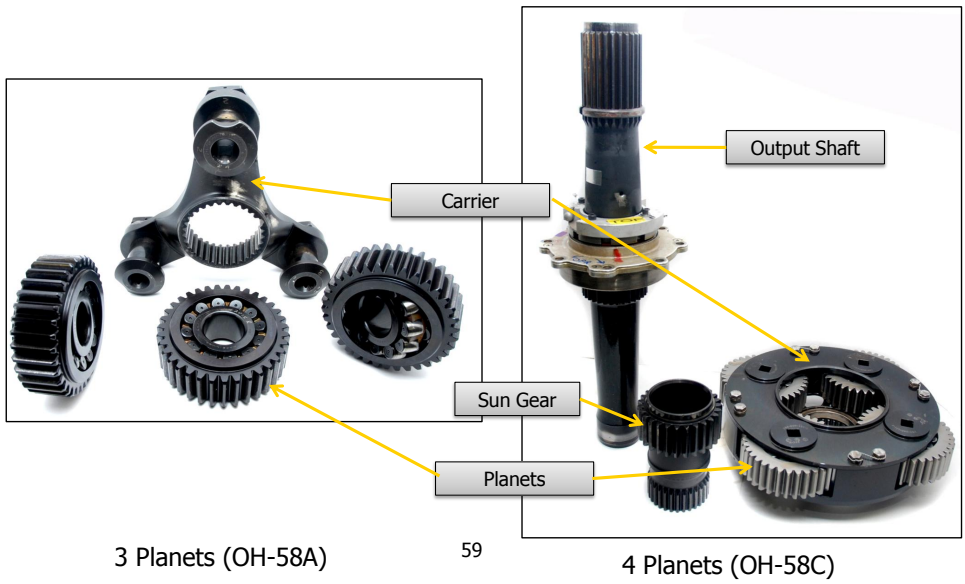

Figure 5.3: Planet Carriers of the OH-58

5.3 Transmission Test Rig

The transmission rig is a four-square configuration which recirculates the power via a return loop that adds the power back to the input via differential. The output of the transmission is attached to a 85 degree bevel gearbox which matches the mast angle of the actual helicopter. The output of the bevel gearbox passes through a hollow shaft in the closing-end gearbox and is connected to the differential gearbox. The output of the differential is attached to the hollow shaft in the closing-end gearbox which in turn, is connected to the transmission input. Power is supplied using a 200 hp DC motor. Since the power is recirculated, only the friction losses need to be replenished, making for an efficient setup. Torque is applied using a 15hp DC motor to drive a magnetic particle clutch.

The transmission is lubricated with turbine oil 555 (DOD-L-85734), using an

internal oil pump. The differential, bevel, and closing end gearbox are lubricated using a facility oil-pumping and cooling system. These systems are also equipped with accelerometers and thermocouples that are used by the facilities control system to monitor the system's condition and can trigger an automatic shutdown if thresholds are exceeded. On the helicopter, the oil is cooled by flight hardware. In the test stand, the cooling is provided using heat exchangers.

Mast loadings are simulated using load cylinders powered by a 2,000 psig nitrogen gas system. Two vertical cylinders and one horizontal cylinder are connected to a loading yoke and are capable of supplying both a vertical force to simulate lift and a side force to simulate mast bending.

Tachometers were used on both the input and output shafts. The output tachometer signal is 1.) used to partition the measured data into individual carrier cycles and 2.) used by the Daytronic system to count the number of output shaft cycles and produce a reset pulse to indicate when the planetary geometry has returned to its initial orientation. The planetary system has a repeat cycle of 105 output shaft cycles. This is determined by finding the integer number of carrier cycles that solves the equation:

$$\text{mod}\ (\theta_{planet}, 2\pi) + \quad \text{mod}\ (\theta_{sun}, 2\pi) + \quad \text{mod}\ (\theta_{carrier}, 2\pi) = 0 \tag{5.1}$$

where

$$\theta_{planet} = (1 - \frac{N_r}{N_p})\theta_{carrier} \tag{5.2}$$

and

$$\theta_{sun} = (1 + \frac{N_r}{N_s})\theta_{carrier} \tag{5.3}$$

5.4 Closing End Gearbox

As noted earlier, a typical vibration spectrum contains information at multiples of the mesh frequency of the planetary system as well as the input bevel gear stage. The regenerative feedback system feeds back power through a closing end gearbox which has its own dynamic components which can also find its way into the measurement signal. A schematic of the closing end gearbox is given in Figure 5.4 where gears are numbered and bearings are lettered. [1] The fundamental mesh frequencies are relative to the planet mesh frequency.

[1] Drawing provided by Dr. Lewicki NASA/ARL

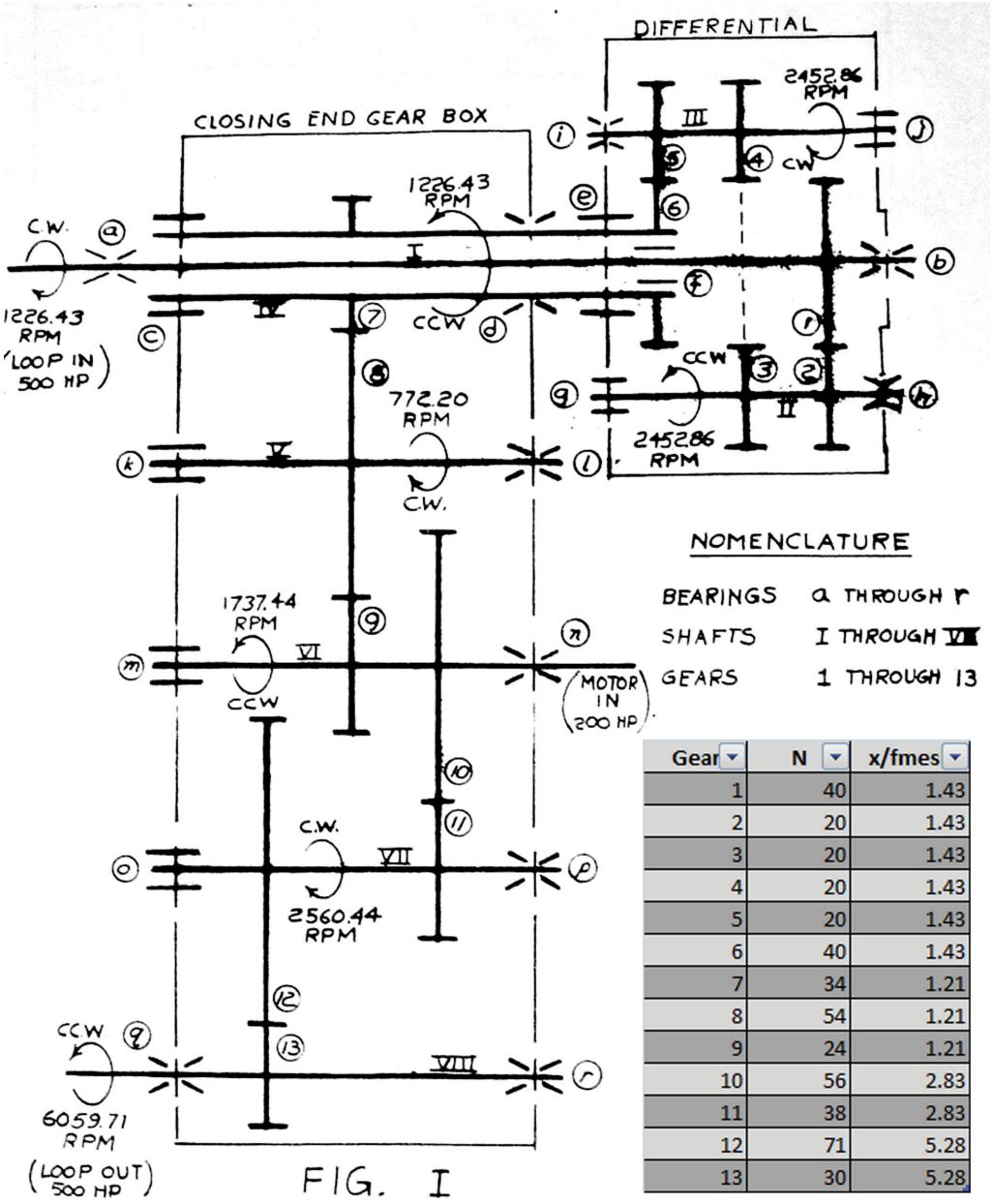

Gear	N	x/fmes
1	40	1.43
2	20	1.43
3	20	1.43
4	20	1.43
5	20	1.43
6	40	1.43
7	34	1.21
8	54	1.21
9	24	1.21
10	56	2.83
11	38	2.83
12	71	5.28
13	30	5.28

Figure 5.4: Closing End Gearbox Schematic

5.5 Accelerometer Placement

The accelerometers are Endevco 7259A-10 with a bandwidth of 50khz. Accelerometer A_1 was mounted to the input end of the transmission just above the pinion. The input spiral bevel pinion has a thrust load against its tri-plex ball bearing and single roller bearing. This is the direction of Accelerometer 1's sensitivity axis and is aligned to the rotational axis of the input shaft. [110] Accelerometer A_2 is positioned 15 degrees counter-clockwise from A_1 and mounted on the side of the transmission housing. Accelerometers A_3 and A_5 are mounted to a special bracket. This is the same bracket, and bracket location, used in flight tests [42] These two accelerometers are located 180 degrees apart. Accelerometer A_4, like A_2, is mounted to the side of the transmission housing. All accelerometers have their sensitivity axis in the transmission's radial direction. It was found from previous tri-axial accelerometer tests that this direction provided the best results. [111] All five accelerometers were conditioned using an Isotron 2972B conditioner. From previous tests A_1, had the spiral bevel as the dominant components [108]. In this work, Accelerometer A_3, produced the highest levels of vibration where the dominant features were attributed to the spiral bevel pinion and planetary mesh. Accelerometers A_4 and A_5 also had significant spiral bevel mesh components.

5.6 Microphone Placement

Microphones were placed at various locations around the gearbox as shown in Figure 5.1. Typically, in a test cell, there are three acoustic regions that are all a

function of the sound's frequency: near field, free field, and reverberant field. The near field is characterized by the pressure and particle velocity being out of phase. The reverberant field is a region located near a reflecting plane such that the reflections may be just as strong as the incident wave leading to errors in the measurements. The free field is the best place to measure the direct sound. Test were conducted inside the test cell to determine a positions that could be considered the acoustic free field which is characterized by a 6dB reduction for a doubling of distance. Measurements were taken 12.5", 25" and 37.5" and it was found that the microphone location cannot be treated as a free field and thus analysis based on free field assumptions cannot be made. Nonetheless, it is felt that since the signal processing code works on a statistical basis, and in a real helicopter environment, space is also limited, therefore, the signals measured are still useful when correlated with measured vibration and transmission error signals. There were two types of microphones: An omni-directional condenser microphone and a directional microphone with a beam width of 120° at 1kHz. Both microphones were placed halfway between the pinion input and the closing end gearbox just above the shaft.

In addition to the two microphones, another omni-directional microphone was located just outward from accelerometer A_4. The purpose of this microphone was to provide an additional signal to provide data for determining whether there is a strong correlation between it and accelerometers A_4 and A_5.

5.7 Oil Debris Sensor

An oil debris monitoring system was used to calculate the amount of metal passing through in the oil supply. This is a strong indicator that damage may be present. This system counts both ferromagnetic and non-ferromagnetic particles, can also determine the particle's size and weight and can partition the counts into particle size categories. A reading is taken prior to testing as well as after each run.

5.8 Test Components

This research looks at the three damaged components given in Figures 5.5 through 5.7. The first two cases were tested on the OH-58C and the second was tested on the OH-58A.

The first damage case tested was a sun gear with a single spall on Sun Tooth ID 9 shown in Figure 5.5. This spall covers around 75% of the toothface. No other appreciable damage was noticed via visual inspection on any of the other teeth.

The second component tested was the sun gear shown in Figure 5.6. This gear had four teeth with severe damage. On ID 10 a spall about one-third the facewidth exists. On tooth ID 12, there a chip at the tip which extends about one-sixth the facewidth. Tooth ID 14 has spall covering about 80% of the facewidth and, on tooth ID 15, almost the full facewidth is spalled.

Figure 5.7 shows a planet bearing used with P_3 on the OH-58A. It has spall at various locations along its inner race. No other damage was observed on any other component of the bearing through visual inspection.

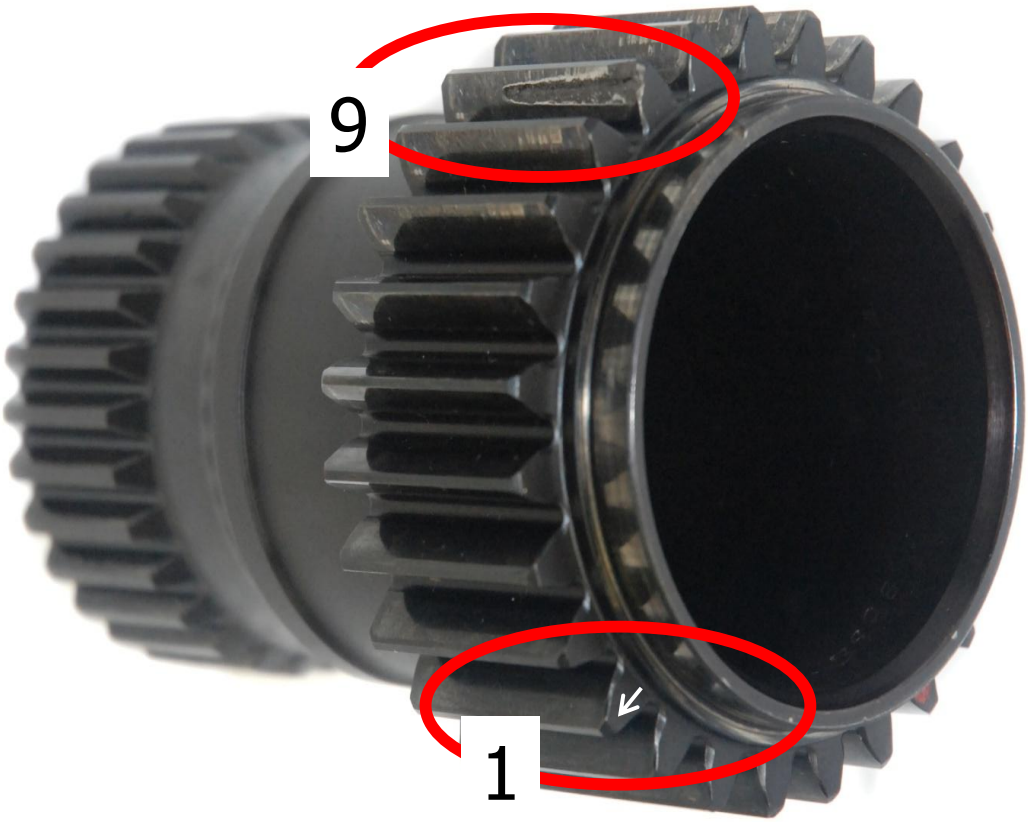

Figure 5.5: Sun Gear: Spalled Sun Gear Case - B12-3993

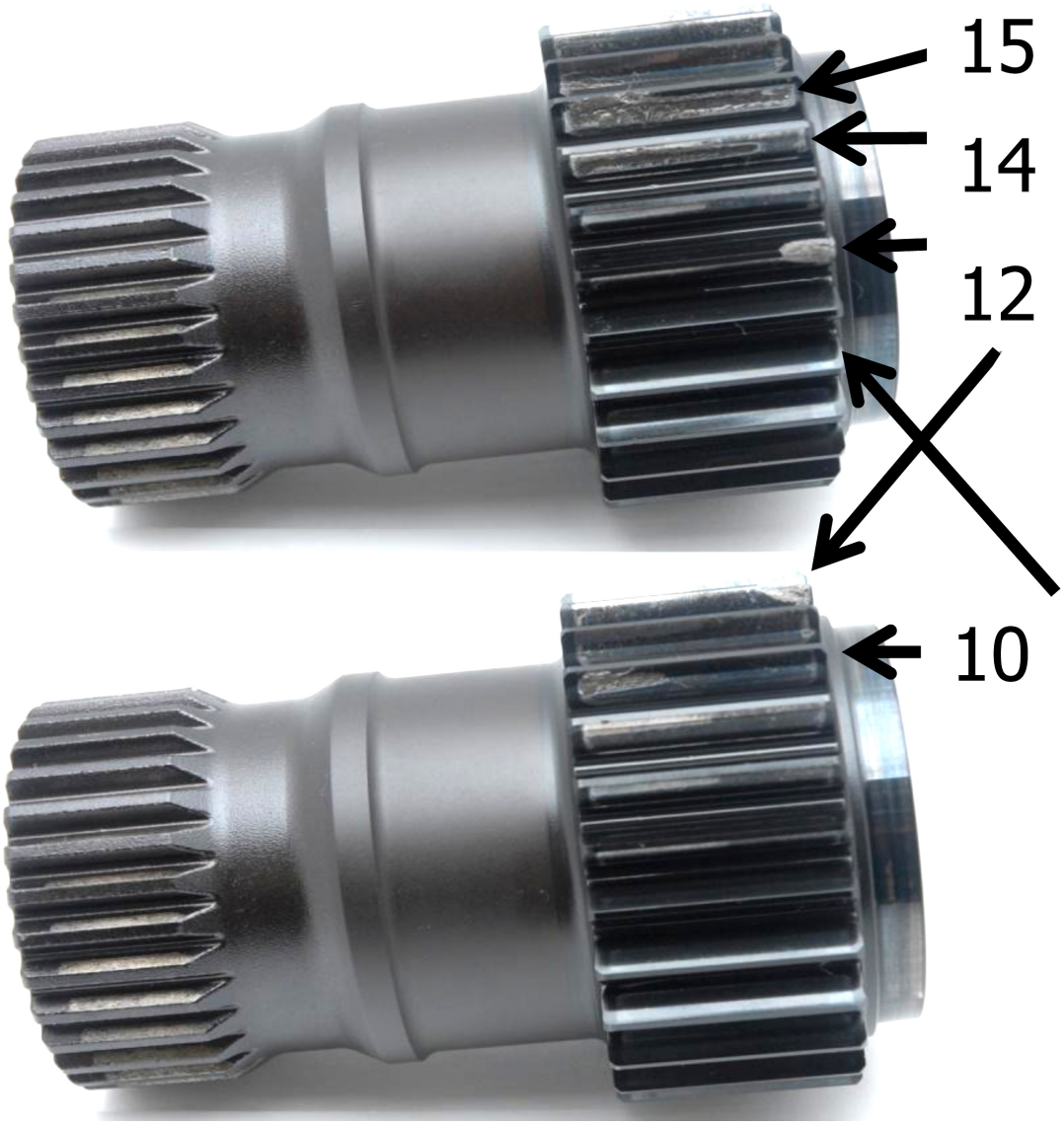

Figure 5.6: Sun Gear: Multiple Tooth Spall Case - B12-3160

Figure 5.7: Bearing: Spall Case

5.9 Assembly and Disassembly

In order to keep track of the tooth locations, it is necessary to ensure that, as parts are swapped, they maintain the same orientation as the reference orientation. The reference orientation is such that the output shaft tachometer is aligned with the right edge of the marker tape and also that the count on the Daytronic counter is zero. All data is referenced to this trigger. The original zero point was chosen arbitrarily, but maintained throughout testing. As mentioned earlier, the planetary system repeats its orientation every 105 revolutions of the output shaft amounting to 18.13s for a 6,060 RPM input speed. Information on some of the alignment procedures is found in Appendix C.

5.10 The DAQ Program

The data acquisition system was designed using Matlab™. It communicates with three National Instruments PCI-MIO-16E DAQ boards using 24 channels. The output is a structured variable containing the measured data as well as data acquisition parameters. This system also communicates with the MetalScan Oil Debris Monitoring System (ODM) via the PC's serial port using the MODBUS protocol. The planetary cycle is 105 revolutions of the output shaft. For the RPM cases tested, this amounts to around 18 seconds of data corresponding to one planetary cycle. A Daytronic system, which services both the input and output tachometer signals, is also set up to count the cycles of the output shaft and produce a pulse after counting 105 (it needs to be set at 104, however, to get the correct counts). This pulse

is captured by Hardware channel 2 on each DAQ board and the start of the DAQ system is triggered by this signal. This allows the ability to produce "pseudo long time captures" by combining the individual time captures (which may be off by one or more cycles, to simulate a continuous time capture). This is done to bypass computer memory issues associated with long durations at high sampling rates.

It was noticed that significant phase between like signals occurred when the number of channels being used on each board differed. Therefore, it was decided that all 24 channels would be used, even if there is no usable signal. Each device has three channels dedicated to input tachometer (HWchan0), output tachometer (HWchan1), and the Daytronic counter pulse (HWchan2). This DAQ scheme is set up to make multiple data captures for durations of a little over 18 seconds. For each capture, four data files are produced. Three are associated with the DAQ boards: DEVICE1-0x.daq, DEVICE2-0x.daq, DEVICE3-0x.daq with each file containing the data from the eight channels of each device. Matlab™automatically indexes the filename for each run and the test cases are stored in separate directories. The fourth file contains the cumulative ODM counts as well as the raw ODM data at the end of each run. Each file is time-stamped to correspond to the beginning of the run. In addition to the saved data files, two plots are produced providing snapshots of the data. The 24 time traces are placed in the DAQ folder. A typical screen-shot is give in Figure 5.8.

All signals, including the tachometer signals, are first sent through an 8- pole elliptical filter with cutoff set to 20kHz.

The channel layout is given in Table 5.5

	Hardware Channel							
	0	1	2	3	4	5	6	7
DEV1	In. Tach	Out Tach	Daytronic	TE1	TE2	TE3	TE4	TORQUE
DEV2	In. Tach	Out Tach	Daytronic	A_1	A_2	A_3	A_4	A_5
DEV3	In. Tach	Out Tach	Daytronic	Mic1	Mic2	Mic3	HB1	HBII (rear)

Table 5.5: Hardware Channel Layout

Hardware channels 6 and 7 of Device 3 were connected to the facility accelerometers located on the two hanger bearings that supported the shaft coupling the transmission and the closing end gearbox.

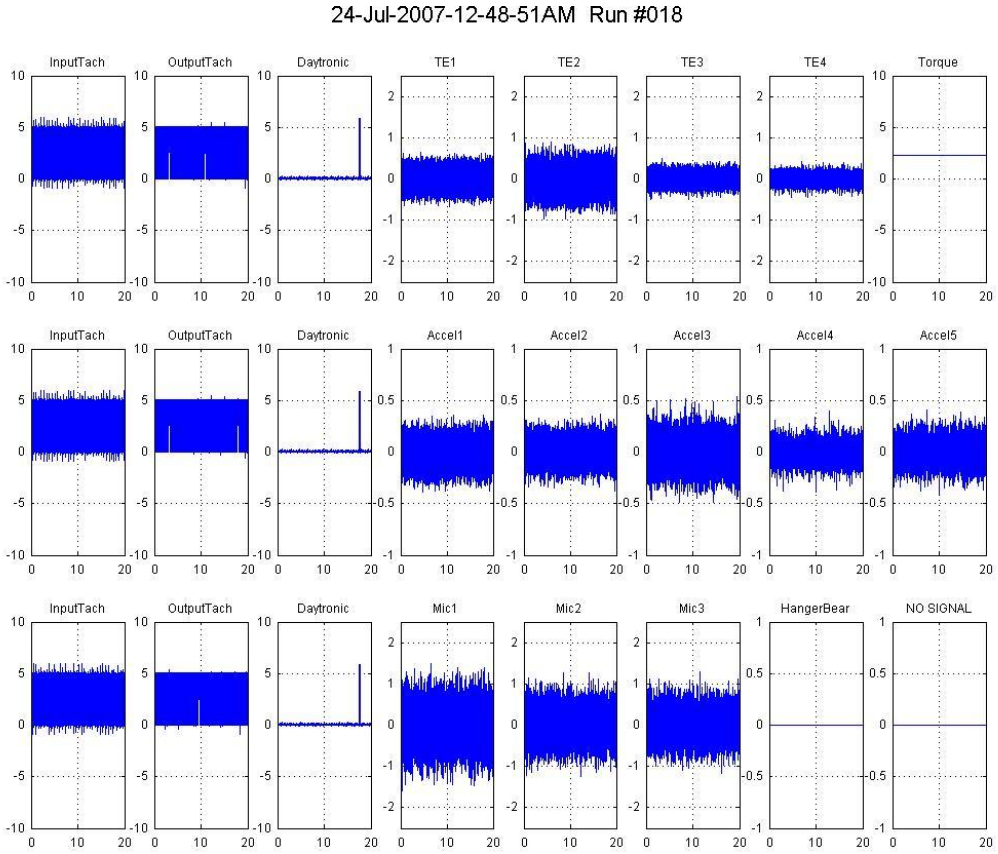

Figure 5.8: Typical DAQ Screen Output

Chapter 6

Results

6.1 Introduction

During testing, the transmission ran continuously. The DAQ system waited for a trigger indicating that the planetary orientation was in the pre-determined position and proceeded to take data for either 20 or 40 seconds. The DAQ would then wait again for the planetary reset trigger and acquire another data set. This continued until multiple runs were stored in individual files. The durations and number of runs captured are given in Table 6.1. On average, each test case took about 50 minutes to complete.

	Baseline				Mid-Damage				High-Damage			
	B1	B2	B3	B4	M1	M2	M3	M4	H1	H2	H3	H4
OH-58C	← 54min. →				← 47min. →				← 45min. →			
Duration per run (s)	20	20	20	40	40	40	40	10	7	10	10	10
Number of Runs	11	12	13	9	10	10	10	10	10	10	10	10
Total Duration (s)	220	240	260	180	400	400	400	400	280	400	400	400
OH-58A	← 51min. →								← 44min. →			
Duration per run (s)	40	40	40	40					40	40	40	40
Number of Runs	10	10	10	9					10	10	9	10
Total Duration (s)	400	400	400	360					400	400	360	400

Table 6.1: Test Matrix

The columns are organized into three groups: B group (B1-B4), M group (M1-

M4), and H group (H1-H4) (B for baseline, M for mid-damage, and H for high-damage). The mid-damage case refers to the sun gear with a single spall. The high-damage cases refers to either the multi-tooth fault of the sun gear or the planet bearing spall. The ordering is of increasing torque. The tables of **CI** values in the Appendix follow the same format.

For each test case, each run was loaded, partitioned into carrier cycles, interpolated, notch-filtered to remove the pinion dynamics and low-pass filtered to remove dynamics above the sixth planet mesh frequency. The results were temporarily stored until all of the runs were processed in the same manner. The **Assembly Family** was produced representing the average of all the runs. Averaging across the runs was performed after interpolation to allow for like points to be averaged. Information for all five accelerometers were stored in a single structured variable, as described in Section 4.3 of Chapter 4.

6.2 Organization of Results

The results are given for all 5 accelerometer signals. The oil debris counts did not see any significant change. This is possibly due to the short-duration runs. For this reason, no oil debris results are given.

The organization of the results is given in Table 6.2. The analysis of the OH-58C and OH-58A transmissions are analyzed separately. Under each transmission type, each sensor's signal is processed in the following six ways:

Frequency Response: The FFT is plotted against an x-axis normalized to the

Vibration			
OH-58C		OH-58A	
FR	**CIs** on **TSA**	FR	**CIs** on **TSA**
PGVS	**SGVS -SASP**	**PGVS**	**SGVS -SASP**
GSMM	**SGVS -SAMP**	**GSMM**	**SGVS -SAMP**

Table 6.2: Presentation Order of Results

planet mesh frequency. These plots represent a single carrier cycle of data without any filtering or averaging.

CIs on TSA: The **CIs** for each **TSA** signal is computed and tabulated. This is the average of all interpolated carrier cycles within an **Assembly Family**. This would represent a system in general monitoring mode, trying to detect damage across many systems. The purpose of this test is to determine what information can be obtained from just a blind processing of the **TSA** data.

PGVS: The purpose for doing **PGVS** is two-fold: 1.) to test the algorithm to ensure expected results are obtained; 2.) to ensure the planets are damage free.

SGVS-SASP: For each damage case and each accelerometer / planet combination, a **Vibration Separation Vector** is produced with condition indicator values computed for each. Plots showing representative results are given and the **CI** values are tabulated in the Appendix.

SGVS-SAMP: For each damage case and each accelerometer, three **Vibration**

Separation Vectors are given. The table produced reflect **CI** values based on the average of the three **Vibration Separation Vectors** for all accelerometers.

GSMM These plots show a simulation snapshot of the final frame displaying the bar chart of mesh group values.

6.3 Producing the Tables

For each section, except Frequency Response and **GSMM** , 11 condition indicators are calculated and tabulated. The plots remain local; however, the tables are organized in their respective sections of the Appendix. The damage cases are measured against the baseline cases. Therefore, the tables have the following format: for the baseline cases, the values of the **CIs** are given; for the damage cases, the ratio of damage **CI** value to baseline **CI** value is given.

For each of the three vibration separation methods, n **Vibration Separation Vectors** were created for each A_i/P_j combination. For **PGVS** and **SGVS -SASP** , $n = 1$, for **SGVS -SAMP** , $n = 3$. For each **Vibration Separation Vector**, 11 condition indicators were computed. All of the results are combined into a 5D structure, $D(k, n, c, i, j)$, where k represents the test number, n represents the **Vibration Separation Vectors** , and c represents the condition indicator for each A_i/P_j combination. In order to present a 2D table of values, three variables must be locked. The tables are presented such that the rows represents the damage indicator, (c), and the columns represent the damage case, (k = 1 to 20). Each value represents a A_{in}/P_{jn} combination where in, jn are used to represent the n^{th} **Vibration**

Separation Vector for the A_i/P_j combination. Multiple tables are needed to vary either i,j, or n. To keep the number of tables reasonable, and to allow for consistency in presentation, tables for different A_i are given. This means that each table corresponds to a single planet, P_j and single **Vibration Separation Vector**. The choice of **Vibration Separation Vector** only corresponds to the **SGVS -SAMP** method. For this case, there are four options: the three from each **TSA set** or the average of the three. The tables produced uses the average.

With the assumption of undamaged planets, an additional reduction is used for the **SGVS -SASP** method. Since it was observed that there is a high degree of correlation between the A_i/P_1 and A_i/P_3 pair as well as the A_i/P_2 and A_i/P_4 pair, they were averaged. Thus, for **SGVS -SASP**, two sets of tables are produced. Since $n = 1$ for this method, the component for one set of tables could be written as $A_i/P_{1,3}$ and $A_i/P_{2,4}$ for the other. For all other tables, P_3 is locked.

6.4 Accelerometer Results OH-58A

The following are the vibration results for the OH-58C.

6.5 Frequency Response: Vibration (OH-58C)

The frequency responses for the five accelerometer signals are given in Figures 6.1 - 6.2 for all three test cases. These figures clearly show the periodic structure of the the system. For all three test cases, the spiral bevel pinion's first mesh frequency, $(3.35f_g)$, is noticeably dominant for the three accelerometers located in close proximity

to the pinion, A_1, A_2, and A_3. One exception is A_3 in Figure 6.2, in which its amplitude is almost halved. The accelerometers A_4 and A_5 were not as sensitive to the pinion. For all three damage cases, A_2 had the largest response. This is consistent with previous researchers. [108]

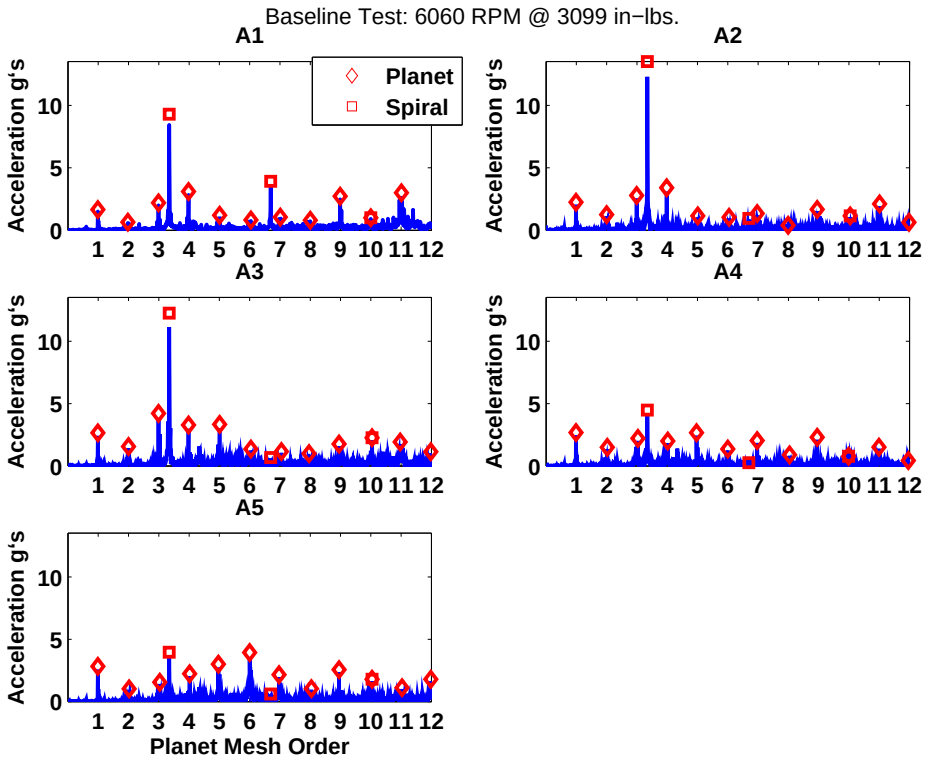

(a)

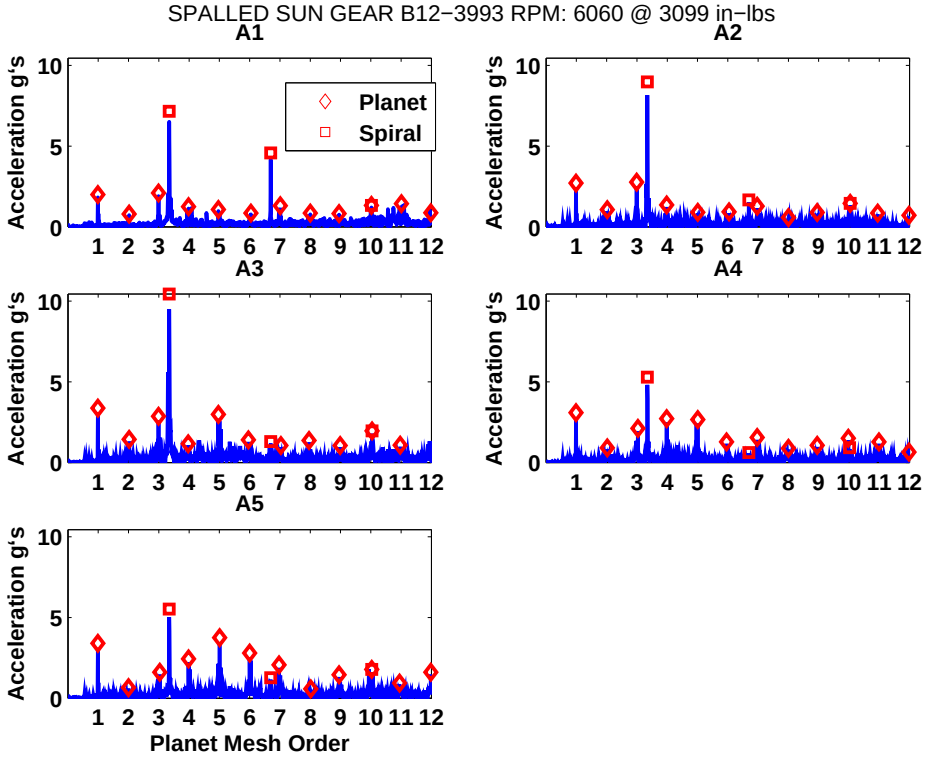

(b)

Figure 6.1: Frequency Response: Accelerometers Vibration (OH-58C) - a.) Baseline b.) Single Fault

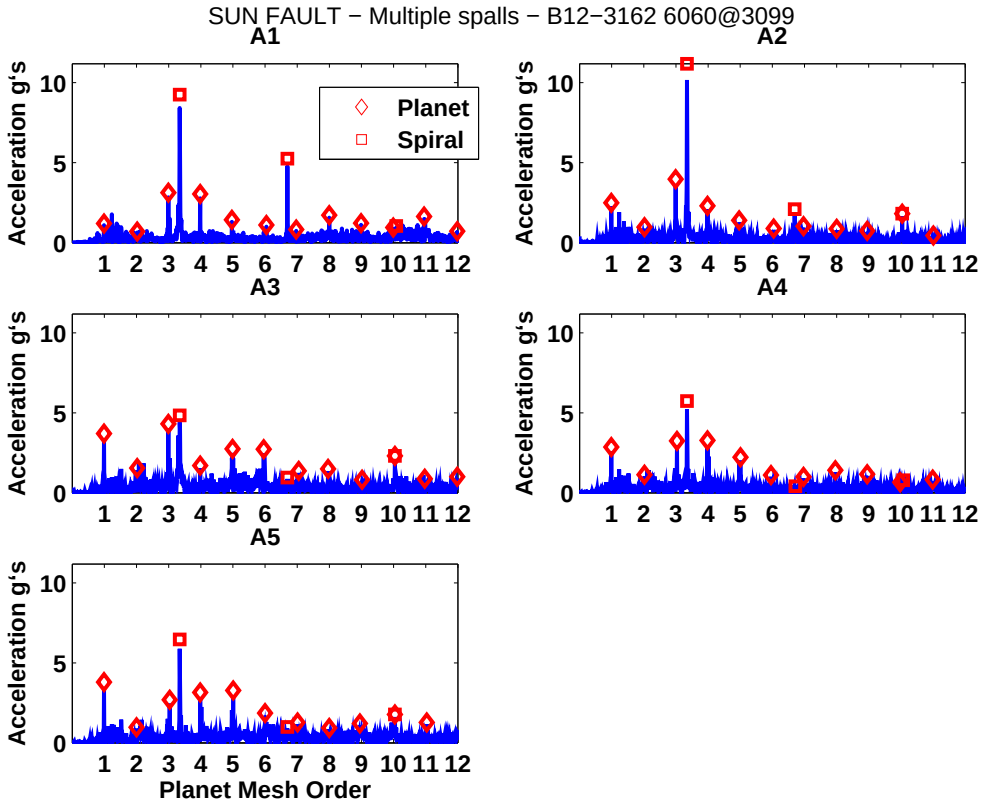

Figure 6.2: Frequency Response: Accelerometers Vibration (OH-58C) - Multiple Faults

6.6 Condition Indicators applied to **TSA** data: Vibration (OH-58C)

Table D.1 shows the values for 11 indicators, across 12 tests on the OH-58C, for each of the five accelerometers. As mentioned earlier, the **CI** values are given for the baseline cases and the ratio is given for the damage cases. Figures 6.3 and 6.4 compare different accelerometers and **CI** values for the three different damage cases. The **CIs** highlighted are FM4, NA4, M8A and RMS. The three waveforms are representative **TSA** carrier cycles corresponding to the baseline case (BL), single tooth spall (MD), and multiple faults (HD) as measured by A_3. Inside the bar of the damage cases are percent changes relative to the baseline.

In all three plots, the four-lobe modulation due to the passing planets is noticeable. With the exception of the RMS chart, a line is drawn in the bar graph to mark the value of 3 which indicates a normal distribution of the difference or residual signals. In Figure 6.3a, all of the FM4 values for the baseline are very close to this value. For the single spall case, the largest change in value was 18% for A_3. Similar results were obtained from the NA4 **CI** . Recall that for these short duration tests, NA4 only differs from FM4 in that it preserves its first-order sidebands.

The M8A indicator, based on higher powers of the difference signal, tends to exaggerate the outliers of the FM4 results. This is demonstrated in Figure 6.4a, where, for the single tooth spall case, the maximum change is 137% for A_3. This suggests a strong sensitivity to the known damage. In Figure 6.4b, the RMS indicator increased on three accelerometers and decreased on two. This **CI** gives a more physical representation than the others, since the RMS can be thought of as a measure of energy.

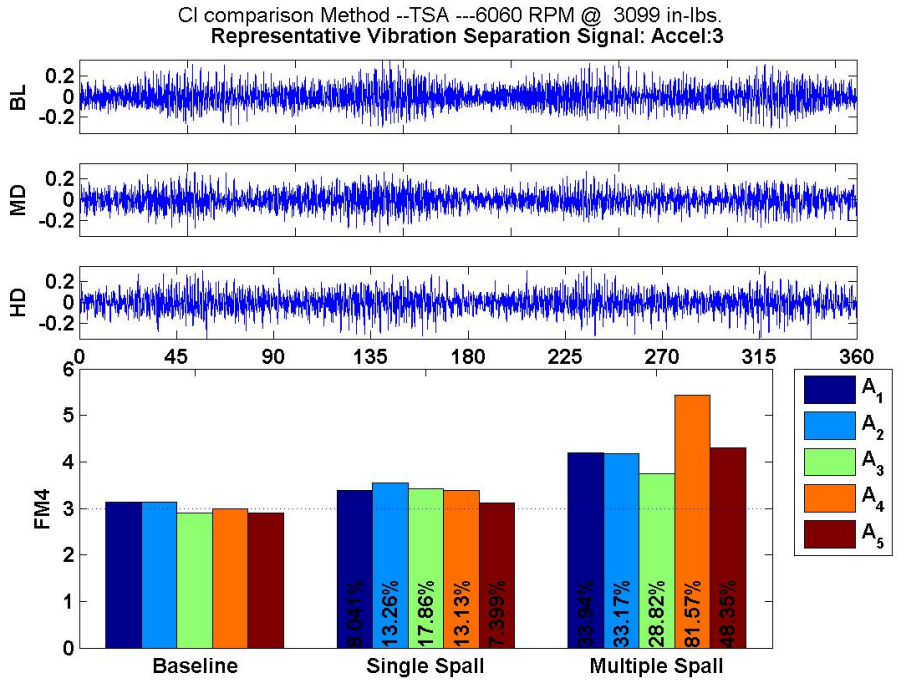

(a)

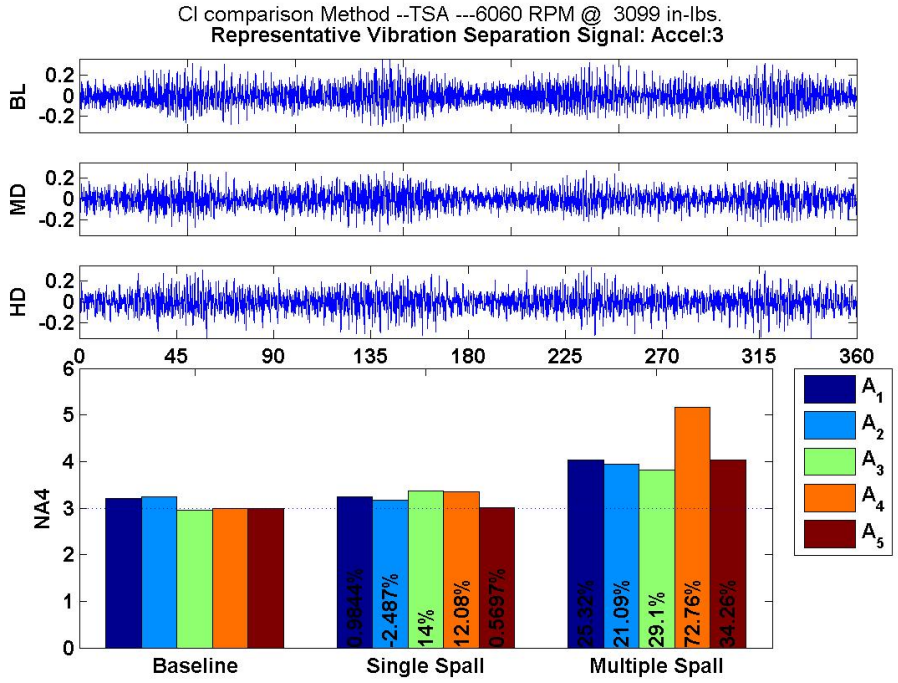

(b)

Figure 6.3: CI on TSA Data: Vibration (OH-58C) a.) FM4 b.) NA4 Sensor: A_3

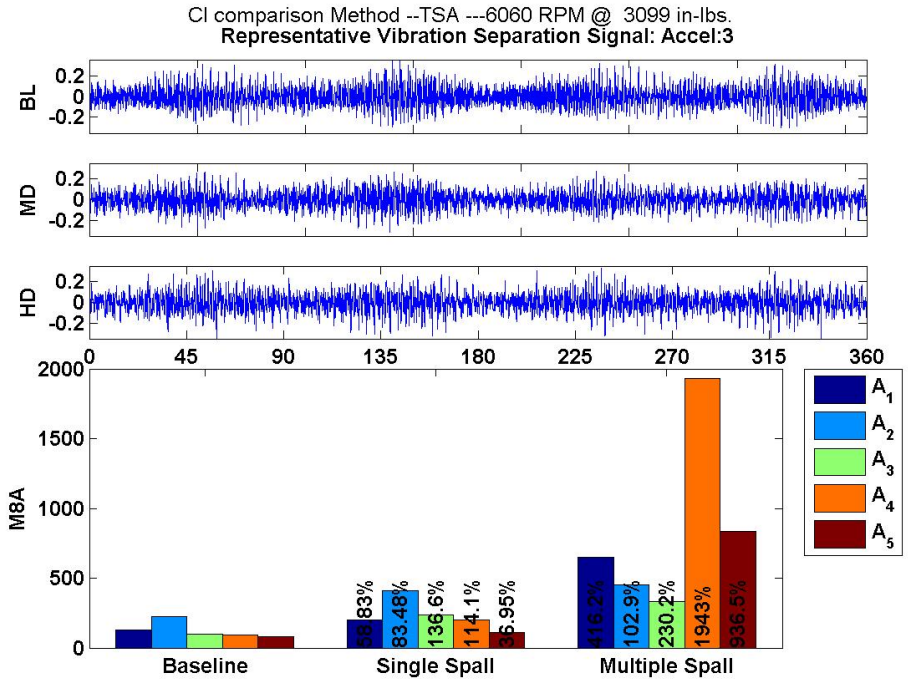

(a)

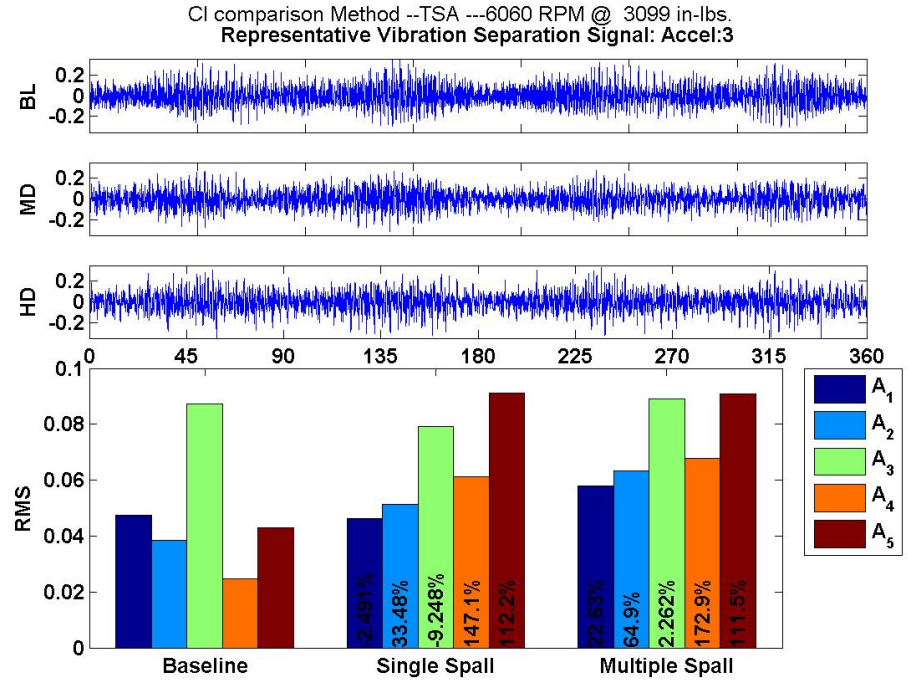

(b)

Figure 6.4: CI on TSA Data: Vibration (OH-58C) a.) M8A b.) RMS Sensor: A_3

On A_4, located opposite the pinion, an increase in RMS of 112% was experienced. A_1 and A_3 saw decreases.

FM4 and NA4 had similar results for the multiple fault case. All accelerometers increased in value on average 45.2% with the largest increase of 82% experienced by A_4, located on the opposite side of the input pinion. For M8A, the bar graphs for the multiple fault case dominate the plot. The value of A_4 increased by a factor of 20!. The RMS **CI** shows an upward trend on all sensors supporting intuition that vibration levels increase with damage. The two rear accelerometers experienced the largest increases with 172% on A_4 and 114% on A_5.

Thresholds on **CIs** are usually set statistically using metrics taken over many trials. This is usually done so it can be applied over many independent systems. For this work, since the same transmission is used as well as the same sensors, setting the thresholds using the baseline case is valid. Thus, for the remainder of the text, plots showing relative changes are used.

Figure 6.5 shows the previous information for A_2 for two power levels. For the 80 HP case, the FM4 and NA4 values for the single tooth spall case dropped slightly and the RMS value increased slightly. For the multiple spall case, the FM4 and NA4 values experienced an increase of around 55% and the RMS around 24% For the 298 HP case, the FM4 had a slight increase of 6% and the NA4 value decreased slightly, 3% for the single tooth spall case. For the multiple fault case, these values averaged an increase of around 25%. In all plots shown, the M8A value dwarfed all other **CI** values, indicating its ability to exaggerate the FM4 metric.

The above charts show that using only the **TSA** data and comparing results

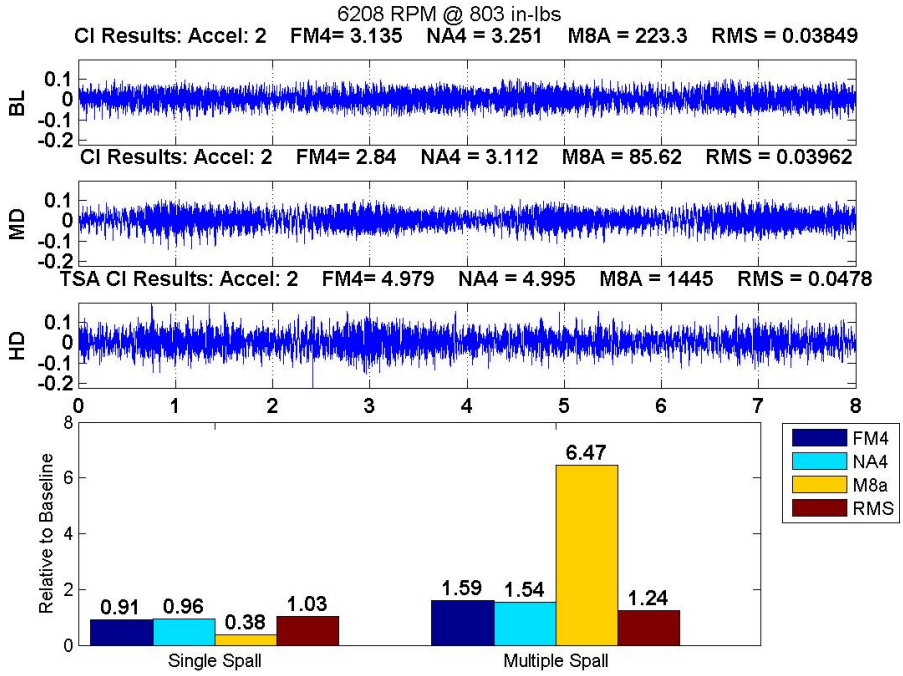

(a)

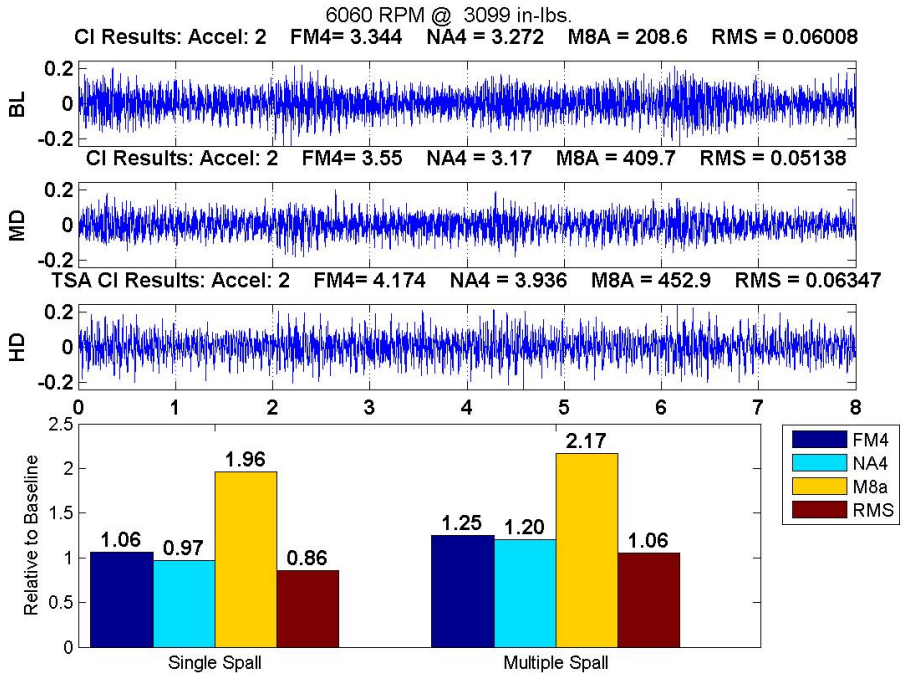

(b)

Figure 6.5: Condition Indicator Comparison: TSA a) 80 HP b.) 298 HP A_2

to the baseline case suggests that the transmission may be damaged. In order to increase the confidence of the assessment, a higher level of interrogation is needed. This is the role of vibration separation-based analysis, to serve as a secondary tool to aid in detecting and locating the damage. This increases the confidence in the find and aids in reducing the number of false alarms.

6.7 **PGVS** Vibration (OH-58C)

Figures 6.6 and 6.7 display the resulting **Vibration Separation Vectors** from **PGVS** for the three damage cases tested. The signal from Accelerometer A_3 is used in these plots. Each plot highlights the same four **CI** values discussed in the previous section. The remaining **CI** values are tabulated in Table E.1.

Figure 6.6a is an example of a baseline transmission that is considered damage free. There are two ways to interpret these plots. One is through inspection by looking for tooth-to-tooth consistency in the waveform. Another is by comparing the **CI** values compared to the baseline results. The role of the **CI** is to eliminate the need for a visual inspection. However, it is first important to establish a correlation between what is observed and the **CI** value.

For all three damage cases, the tooth-to-tooth waveform correlation is high for all assemblies. This is the desired result for undamaged planet gears and demonstrates that the vibration separation algorithm is working properly. It is interesting to note the variation in waveform shapes for the same accelerometer. This is due to the fact that the OH-58C is non-sequential. A look at the results for the sequential OH-58A,

(later in this chapter), reveals waveforms with high correlation between the different assemblies.

Plots comparing **Vibration Separation Vectors** for A_3/P_1 and their associated **CI** values are given in Figure6.8. For the 80 HP case, the FM4 value increased about 65% and the RMS **CI** increased by a factor of 3.6. Thus, the effects of the damage are reflected in the condition indicator values. The tooth-to-tooth consistancy of the waveforms suggests that the effect of damage is averaged across all individual tooth mesh waveforms. For the 298 HP case, FM4 values changed only slightly for the single tooth spall case and 26% for the multiple fault case. This shows the dependence of the FM4 metric on operating conditions. It appears to be more sensitive at lower torque levels.

Another way of looking at the results is to see how the signal from each accelerometer was used to build the vibration separated signal. Figures 6.9 - 6.10 show the assemblies for planet P_4 for each accelerometer. The desired result is one in which all of the accelerometers create the same signal but these plots illustrate the variability among accelerometers. A large part of this variation is due to the accelerometer's location and mounting, as discussed in Chapter 4. However, it also has to do with phasing of the transmission. These plots illustrate the challenge of using a multi-accelerometer approach to vibration separation. Although there is a trend of increasing value of the indicators as sun gear damage increase, inspection of the individual waveforms reveals that they are undamaged. It is encouraging that even for the severe spall case there is no strong indication of tooth damage using **PGVS**. The increase in **CI** value is due to the sun's damage affecting all teeth. This is important

because subsequent sun gear fault detection tests assume fault- free planets.

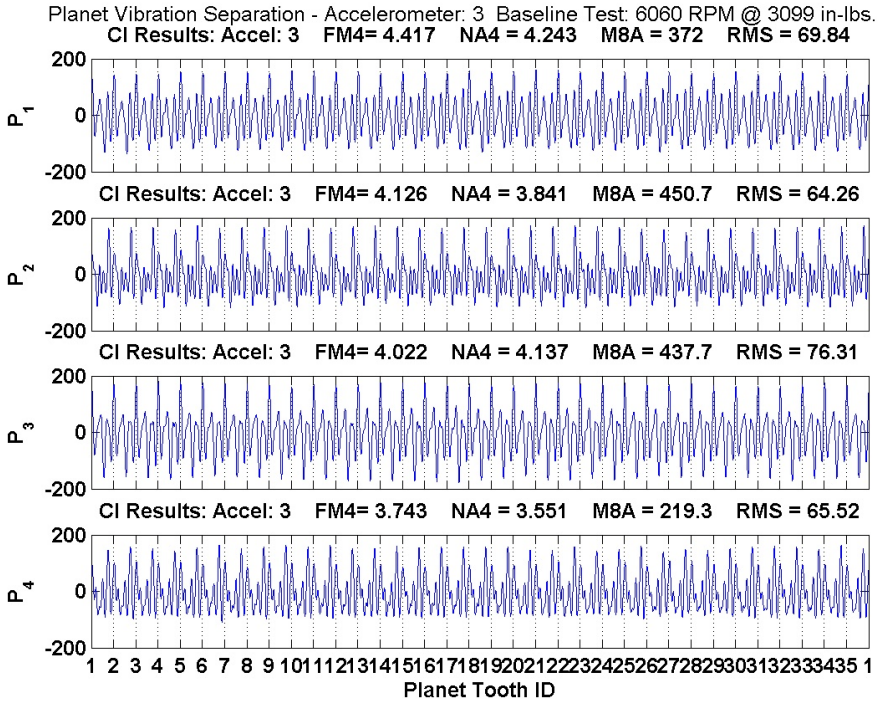

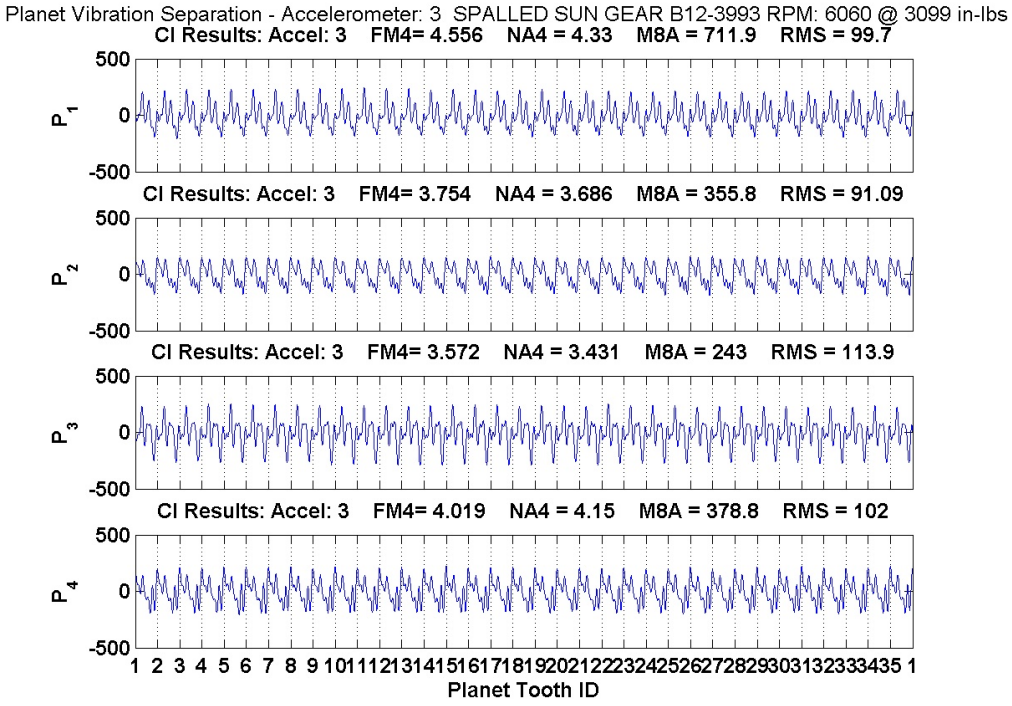

Figure 6.6: PGVS Comparison: Vibration (OH-58C) a.) Baseline b.) Single Spall Sensor: A_3

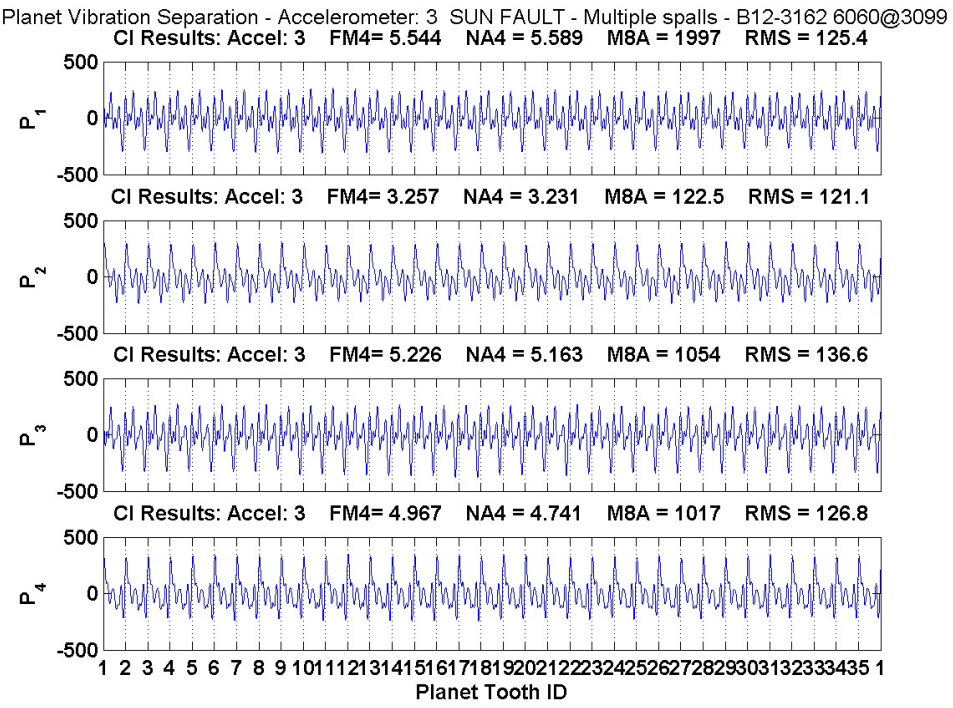

Figure 6.7: PGVS Comparison: Vibration (OH-58C) Multiple Spall Sensor: A_3

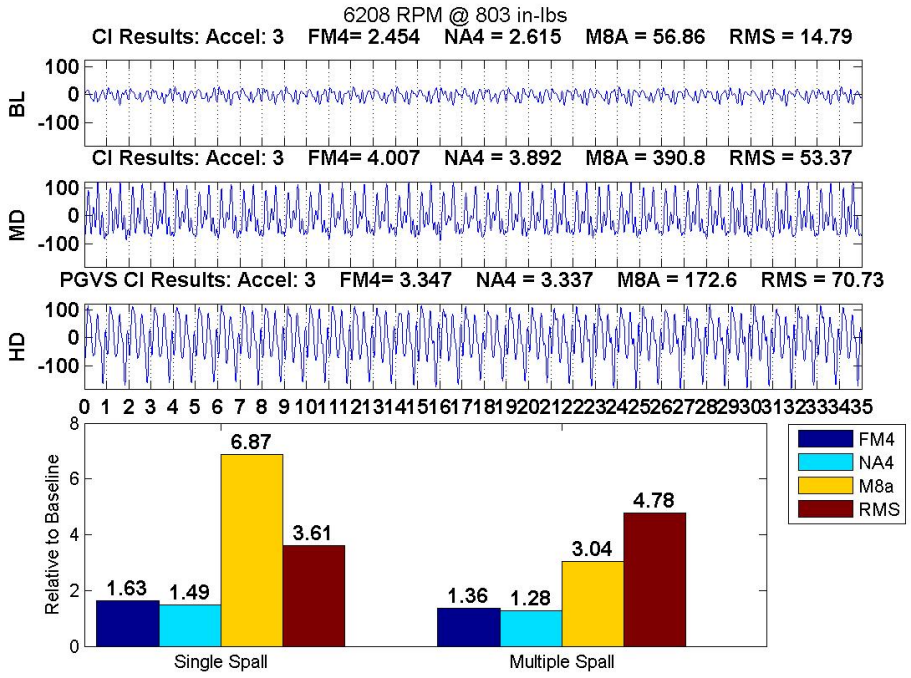

(a)

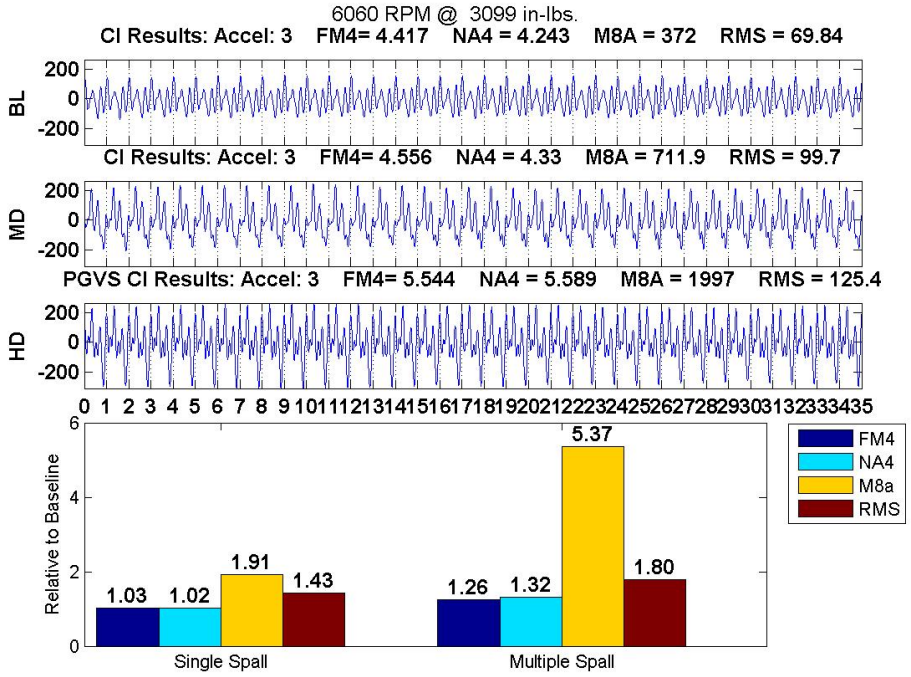

(b)

Figure 6.8: CIs on PGVS Data: Vibration (OH-58C) a.) 80 HP b.) 298 HP A_3/P_1

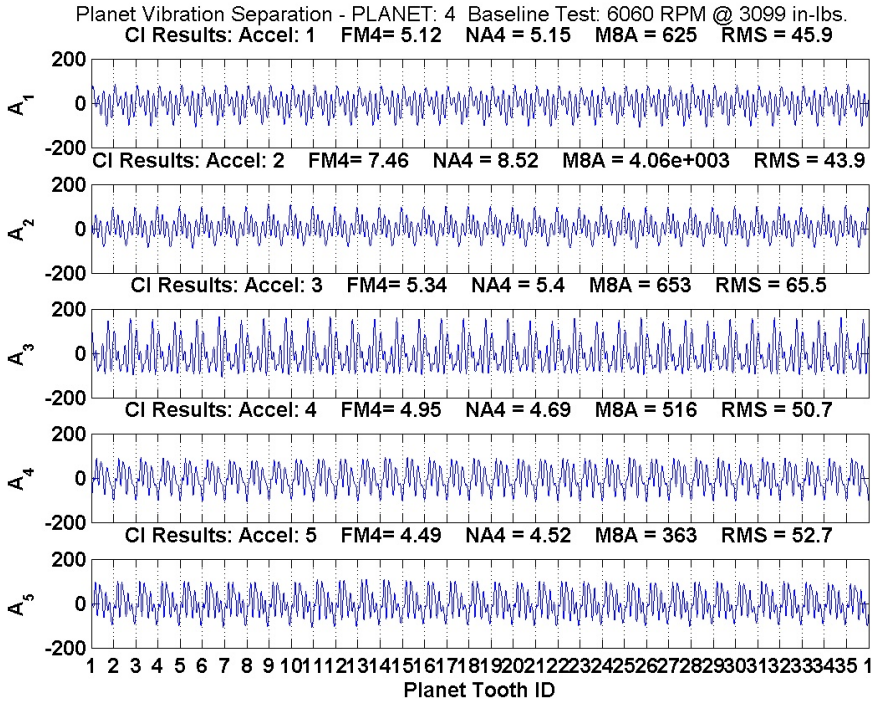

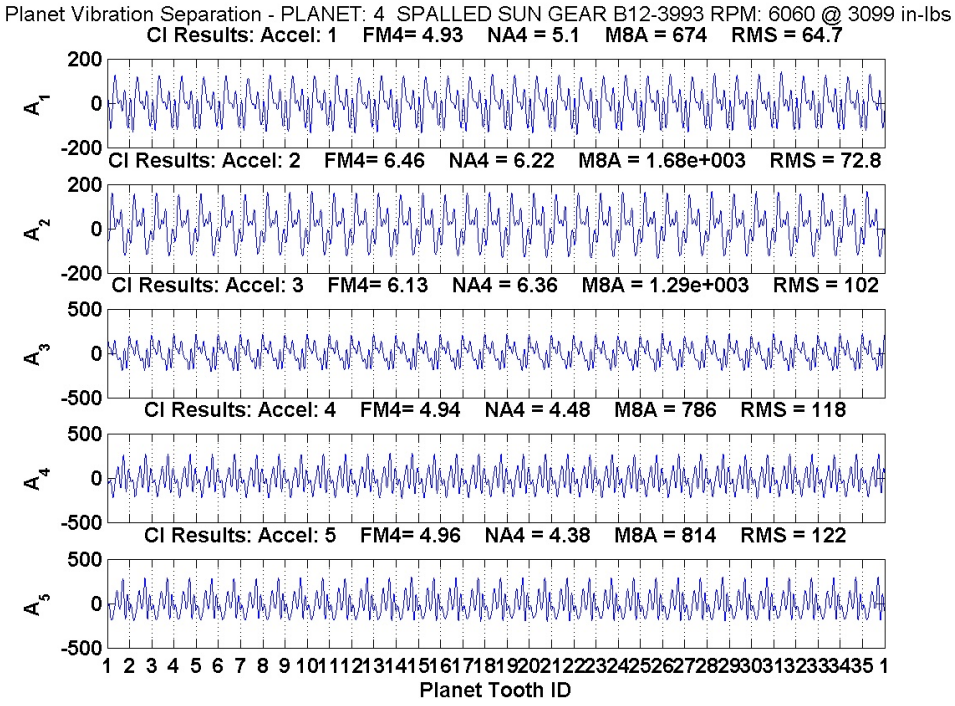

Figure 6.9: Assembly of P_4 by Different Accelerometers: Vibration (OH-58C)

a.) Baseline b.) Single Tooth Spall

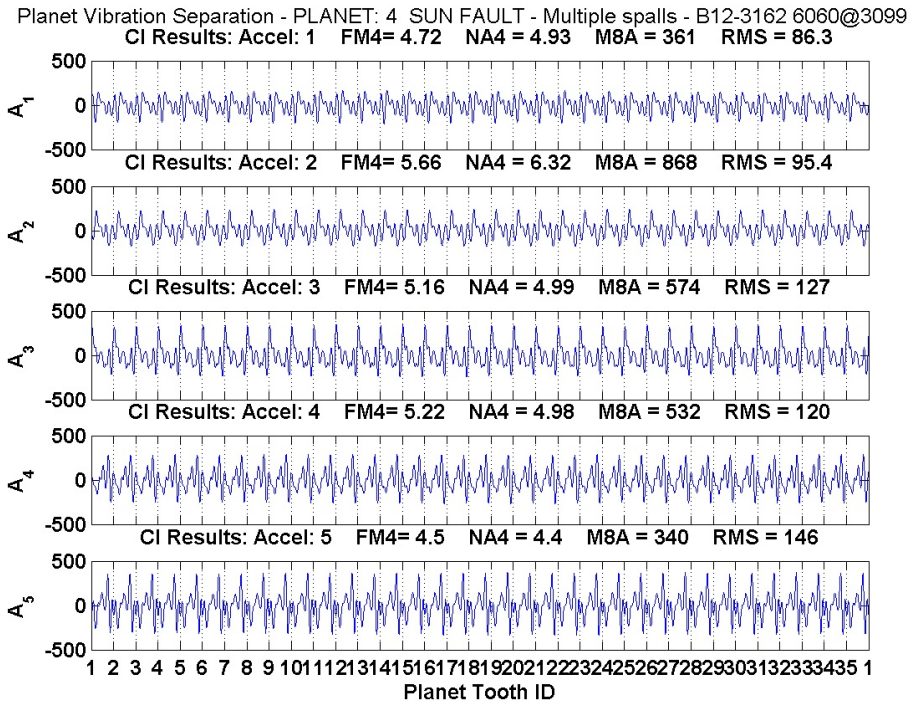

Figure 6.10: Assembly of P_4 by Different Accelerometers: Vibration (OH-58C) Multiple Tooth Faults

6.8 **SGVS -SASP** Method Vibration (OH-58C)

This section shows **SGVS** results using the **SASP** method for all three damage cases. Recall that this method takes the measured signal, arrange it into three pass groups, averages within the pass groups, and then assembles the **Vibration Separation Vector** by connecting the three waveforms. The signal from accelerometer A_3 as "'seen"' through planet P_3 is used for the plots. Figure 6.11a shows the individual pass groups for a baseline case.

Each pass group represents the collection of 34 waveforms illustrating the high correlation between waveforms in the same pass groups but not necessarily between different pass groups. One of the key benefits of this technique is that averaging in pass groups preserves of fine individual tooth mesh waveform details. This would not be the case if all the waveforms were simply averaged together. Figure 6.11b shows the **Vibration Separation Vector** as "'seen"' through each planet. The pass groups from above were used to create the assembly of the second row. Opposing planets are plotted adjacent to one another to highlight their similarity. Because of this similarity, the damage **CIs** computed on the assemblies for P_1 were averaged with those for P_3. The same was done for P_2 and P_4. The FM4 and NA4 indicators vary only slightly between planets which is to be expected for damage free planets. Figure 6.12 is the result for a single tooth spall. Four locations are highlighted that show significant deviation from corresponding **TMPs** from adjacent pass groups. Looking at the Sun Tooth ID number reveals that this set forms a mesh group as discussed in Chapter 4. These same locations are circled in the **Vibration Separation Vector** in Figure

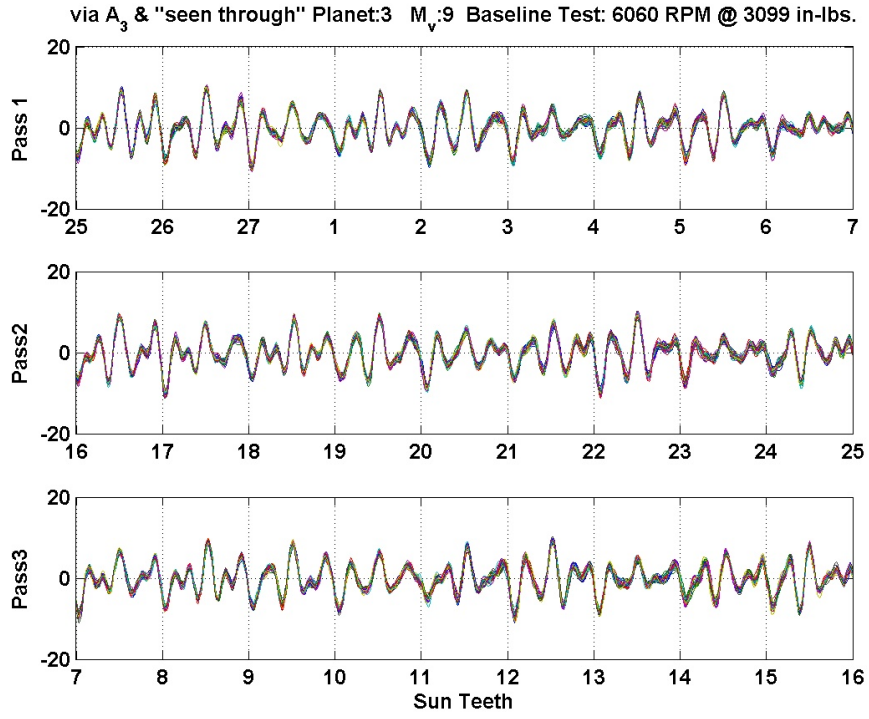

(a)

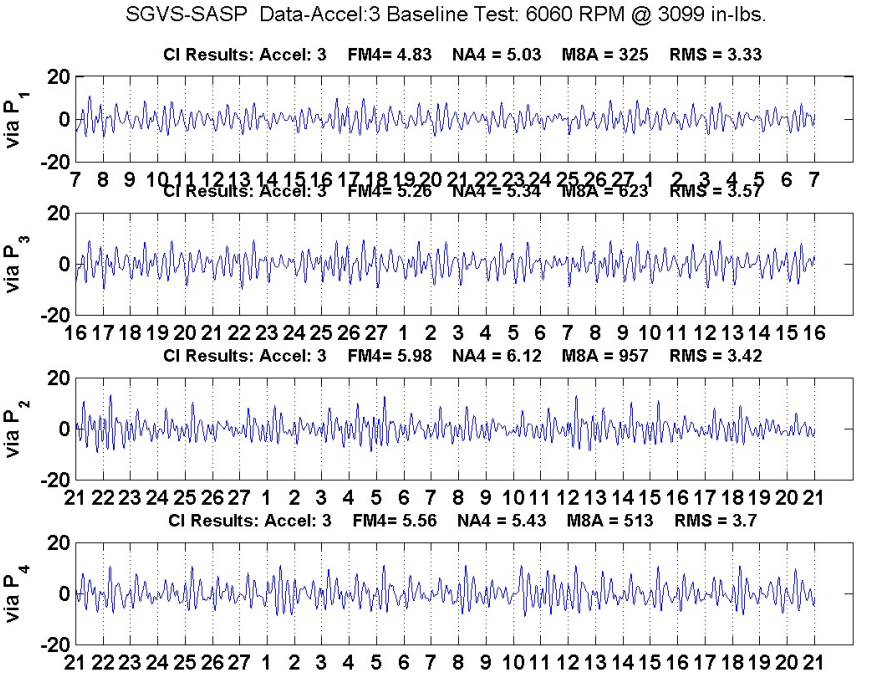

(b)

Figure 6.11: Baseline: SGVS -SASP Pass Group Comparison: Vibration (OH-58C) Sensor: A_3

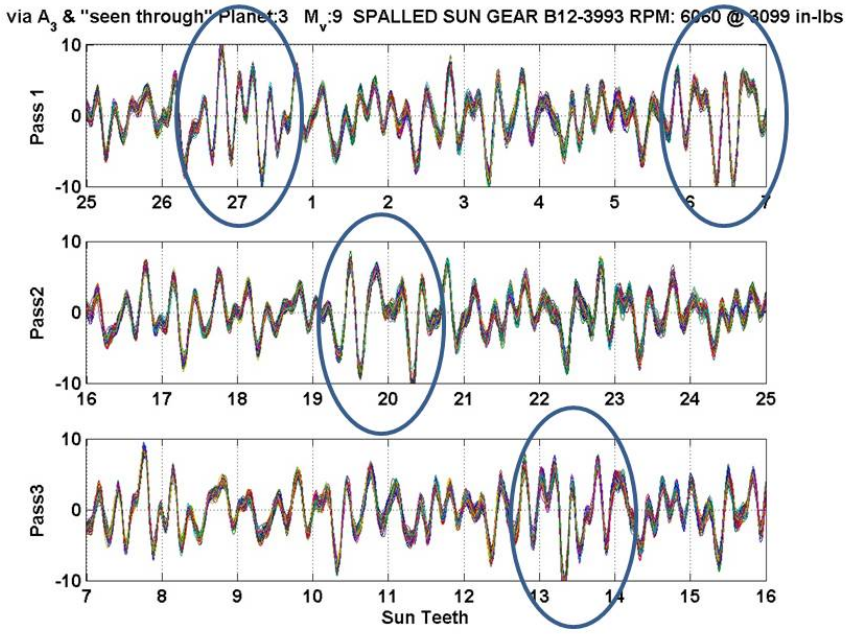

(a)

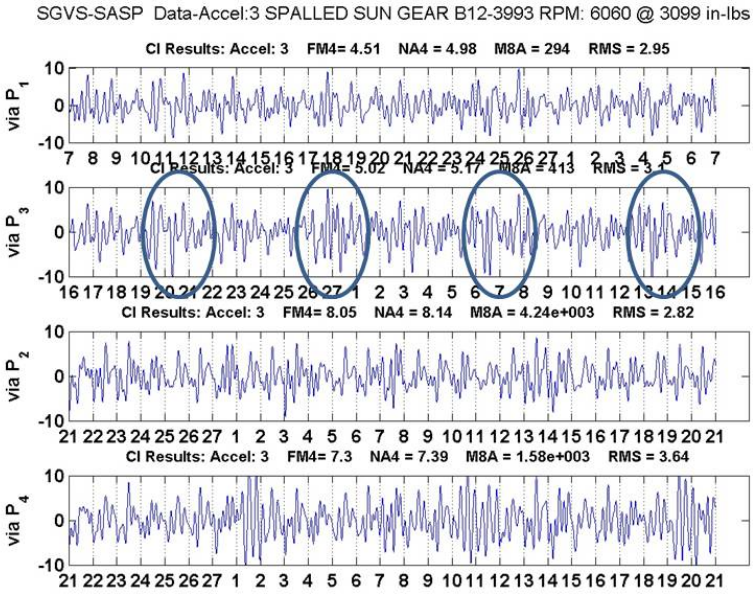

(b)

Figure 6.12: Single Spall: SGVS -SASP Pass Groups Comparison: Vibration (OH-58C) A_3

6.11b. This is important because it demonstrates that when a damaged tooth meshes, no matter where, a deviation in the measured baseline waveform results. Recall from Section 2.3.2 of Chapter 2 that when a periodic waveform has multiple abberations, its FM4 value increases, albeit, not as much for a single abberation. This is akin to the sun's damage being sensed by all sensors each time it meshes. Thus, it turns out that waveform deviations in sun gear mesh groups are strong indicators of sun tooth damage. Figure 6.13 shows the result for the multiple fault case. This plot clearly shows the damage results of the sun gear. The circle region represents a sun gear mesh group. When combined into a **Vibration Separation Vector**, the damage is even more apparent.

Figure 6.14 compares **CI** values for the $A3/P_1$ combination. For both power levels, the **CI** values for the single tooth fault case barely changed. However, the FM4 value for the 80 HP case increases by a factor of 3. For the higher power case, the factor is 1.8. The damage is very distinctive in the low power case and with the damage occurring in mesh groups, confirms that sun tooth damage is the culprit.

The results for all of the 11 **CIs** are tabulated in Tables F.1 and F.2. The values for most of the **CIs** show an increasing trend with damage.

Plots similar to Figure 6.13, where the damage is clearly visible, are also obtained using different accelerometer / planet combinations. Figure 6.15 shows the results using A_3/P_1. Results for the A_5/P_2 combination are shown in Figure 6.16 and results for the A_3/P_2 combination are shown in Figure 6.17. The combination A_3/P_2 and A_5/P_2 are chosen because the two accelerometers oppose one another. The results for the single tooth spall case shows no clear distinction from

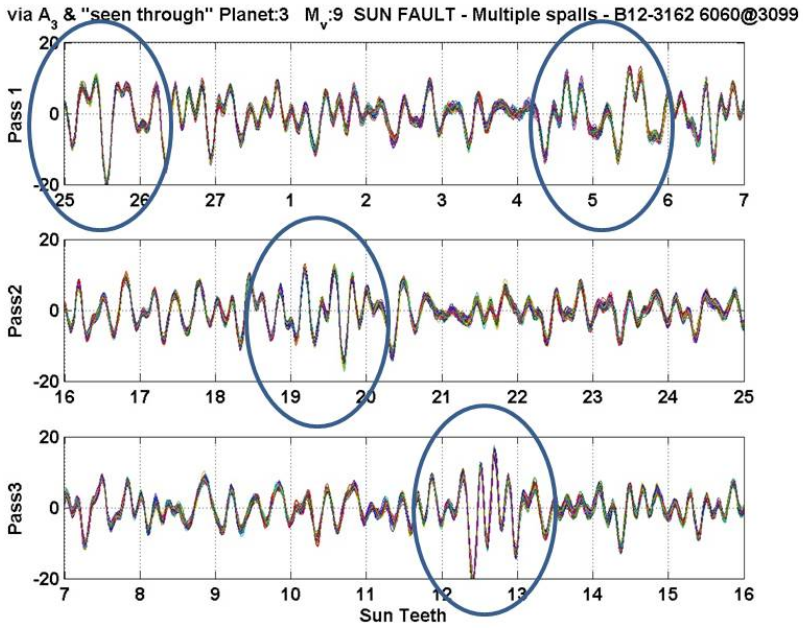

(a)

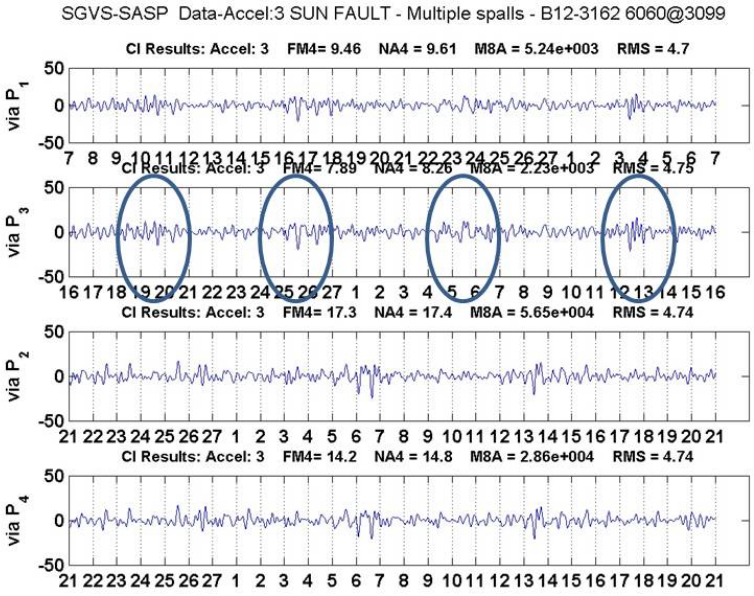

(b)

Figure 6.13: Multiple Spall: SGVS -SASP Pass Groups Comparison: Vibration (OH-58C) A_3

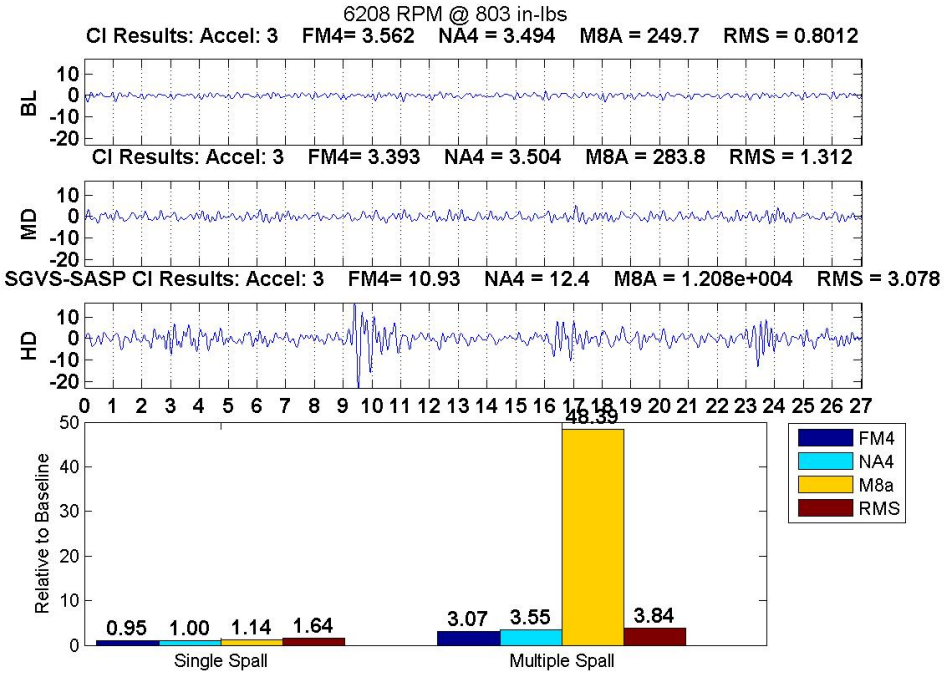

(a)

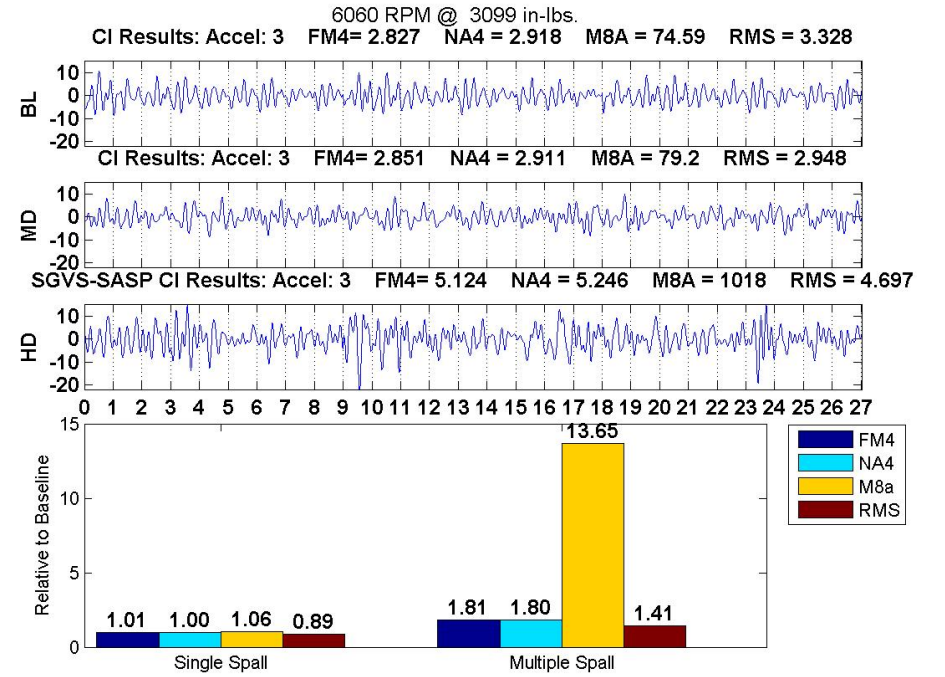

(b)

Figure 6.14: CI Comparison: SGVS -SASP a.) 80 HP b.) 298 HP A_3/P_1

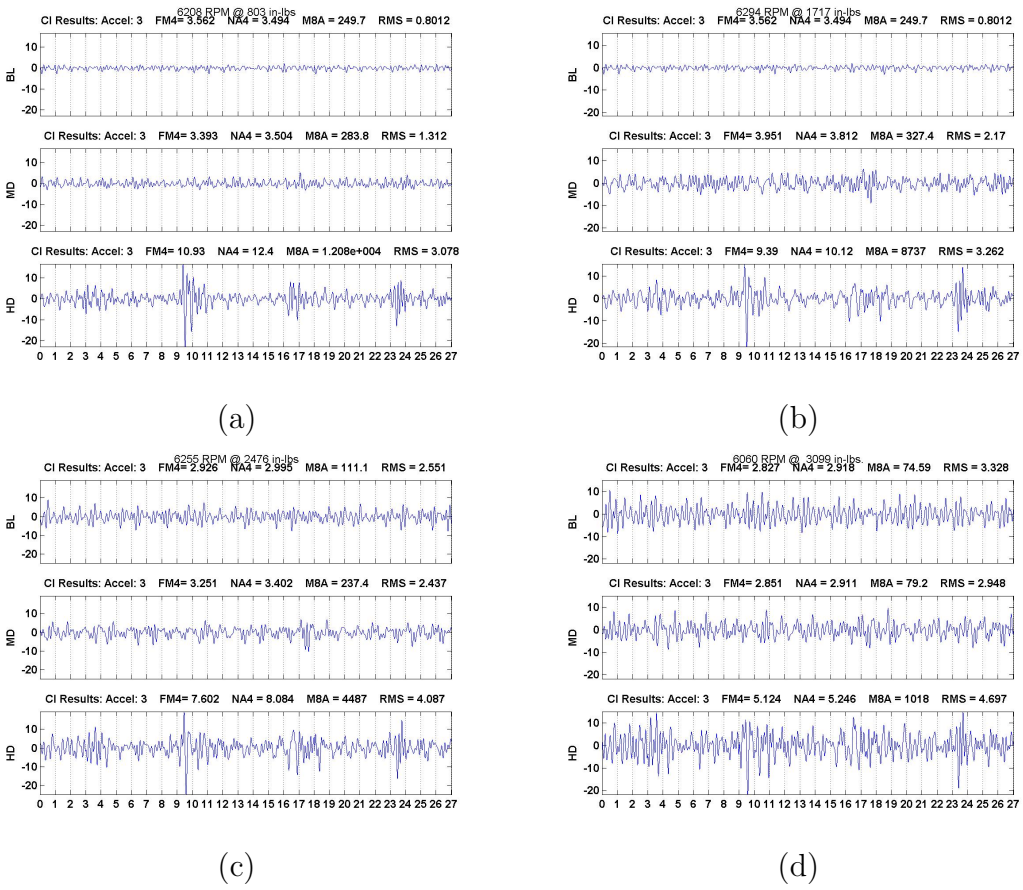

Figure 6.15: SGVS -SASP Vibration Separation Vector Comparison: Vibration (OH-58C) Accelerometer: A_3/P_1

the baseline. In the A_3/P_1 results, there is a single abberation for the single spall case but does not appear in all plots, so one could not be confident its due to the single spall.

The results for the multiple faults test were positive. In all three plots, the damage was distinctive and repeated for different accelerometer/planet pairings. In addition, the damage appears in a mesh group pattern, making it a strong indicator of sun gear damage for the multiple fault case. The damage was most apparent in the low power tests, which also had the highest FM4 values.

The next section presents the results from another method that uses multiple

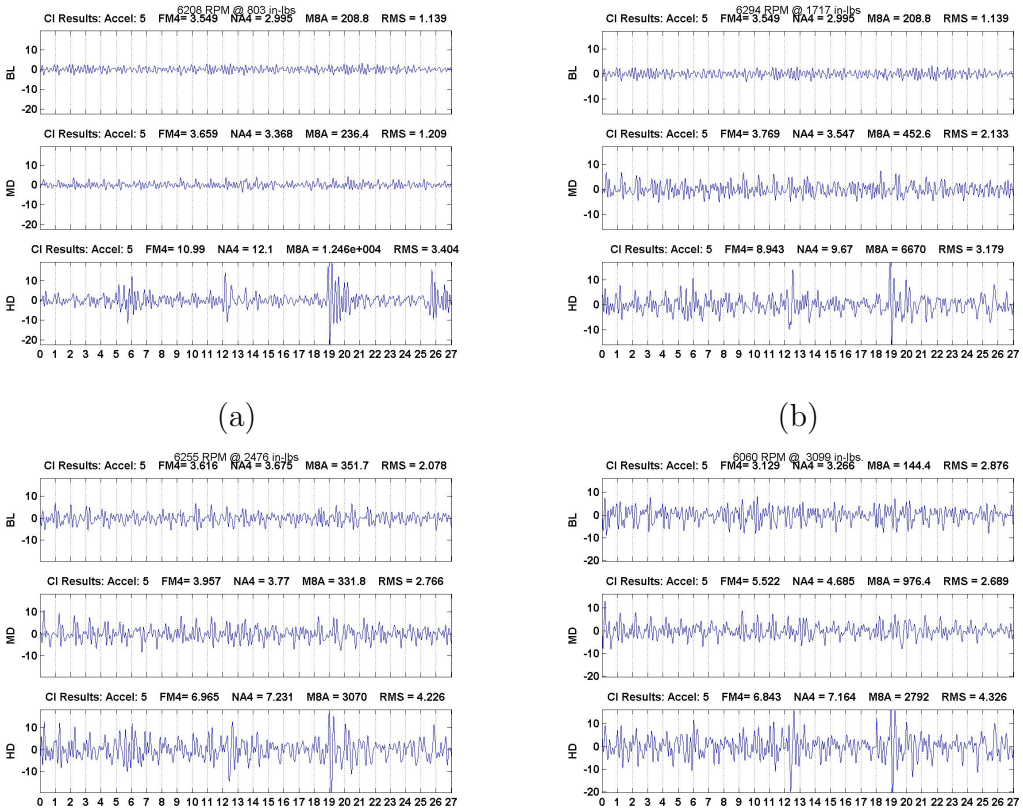

(a) (b)

(c) (d)

Figure 6.16: SGVS -SASP Vibration Separation Vector Comparison: Vibration (OH-58C) Accelerometer: A_5/P_2

planet passes to synthesize the **Vibration Separation Vector.**

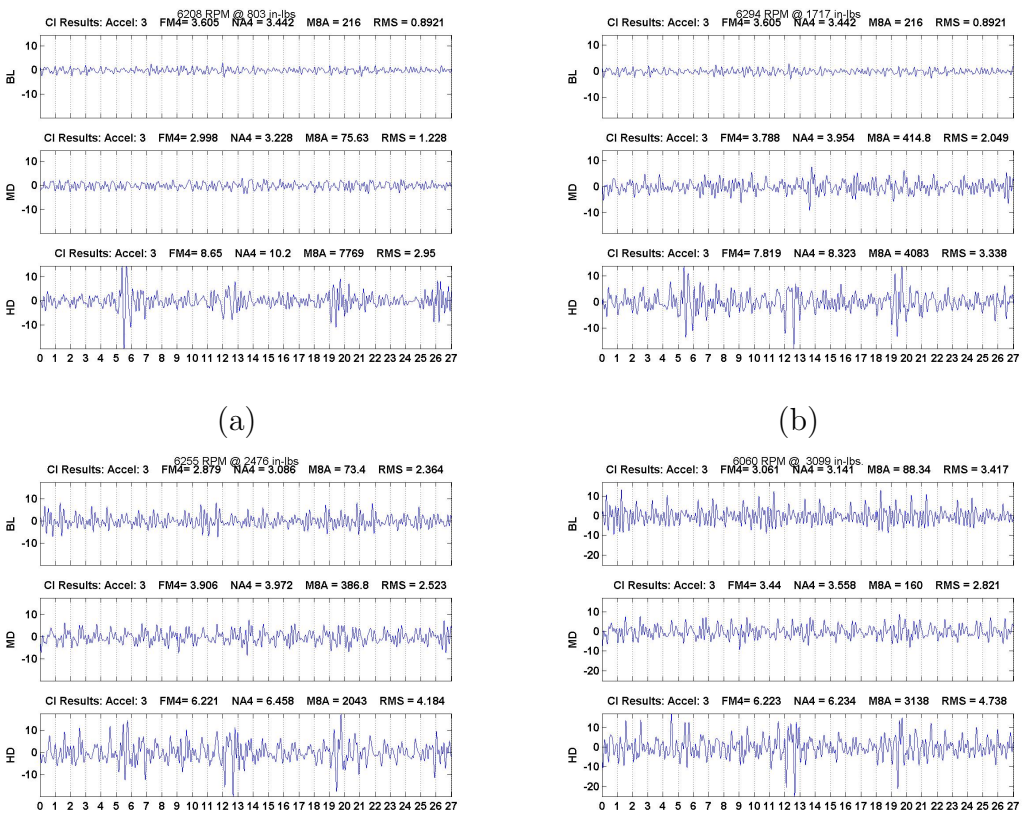

Figure 6.17: SGVS -SASP Vibration Separation Vector Comparison: Vibration (OH-58C) Accelerometer: A_3/P_2

6.9 **SGVS -SAMP** method Vibration (OH-58C)

In the previous section, the results demonstrated that, even with a low hunting tooth ratio, "seeing" the sun gear through one planet was suffice to determine if the sun gear was damaged for the multiple fault case. This section investigates using multiple planets.

Figures 6.18 - 6.19 show the individual **Vibration Separation Vectors** for the operating condition using the **SGVS -SAMP** method for $M_v = 5$. Each test produces three **Vibration Separation Vectors** for each accelerometer. In order to keep the number of tables reasonable, only a table of the average **Vibration**

Separation Vector is provided. These **CI** results are tabulated in Table G.1.

Recall that this method extracts data as multiple planets pass a given accelerometer. This allows each tooth to be represented in 1.5 cycles for $M_v = 5$ compared to the three cycles used for the **SASP** method ($M_v = 9$). In addition, a lower value for M_v allows analysis of the meshing sun gears when they are closer to accelerometers. Figure 6.18a shows the results for the baseline case. There appears to be a modest degree of correlation across sets.

Figure 6.18b shows the results for a single spalled tooth. A single large deviation is noticed around Sun Tooth ID 20 in all three sets. This is consistent with the P_3/P_1 finding from the **SASP** results. However, this deviation cannot immediately be attributed to the damaged tooth, since, as seen previously, many teeth seem to be affected. Despite this, the **CI** values changed slightly, with the exception of M8A. For set 2, the FM4 went from 5.46 to 9.93 and NA4 rose from 5.59 to 10.5. Figure 6.19 shows the results for the multiple fault case. The damage is clearly seen in the resultant waveforms. Five locations are circled. It is interesting to note that the deviation pattern does not span across all sets. Nonetheless, the locations represent a mesh group clearly indicating that this is sun tooth damage.

Figure 6.20 compares the **CIs** . As with the case for **SGVS -SASP** , the **CI** values for the single tooth spall barely changed. For the multiple fault case, larger increases in value were experienced, especially for the low-power case, in which the FM4 **CI** increased by a factor of 1.65.

Results for the A_2 combination are shown in Figure 6.21 Results for the A_3 combination are shown in Figure 6.22

Results for the A_5 combination are shown in Figure 6.23

As with the case for **SGVS -SAMP**, the multiple faults were most apparent in the low-power case. Also, this method was unable to determine conclusively the single fault on the sun gear.

The following section presents the results from an alternative method that does not use any vibration separation and works directly with the **TSA** data for the carrier cycle.

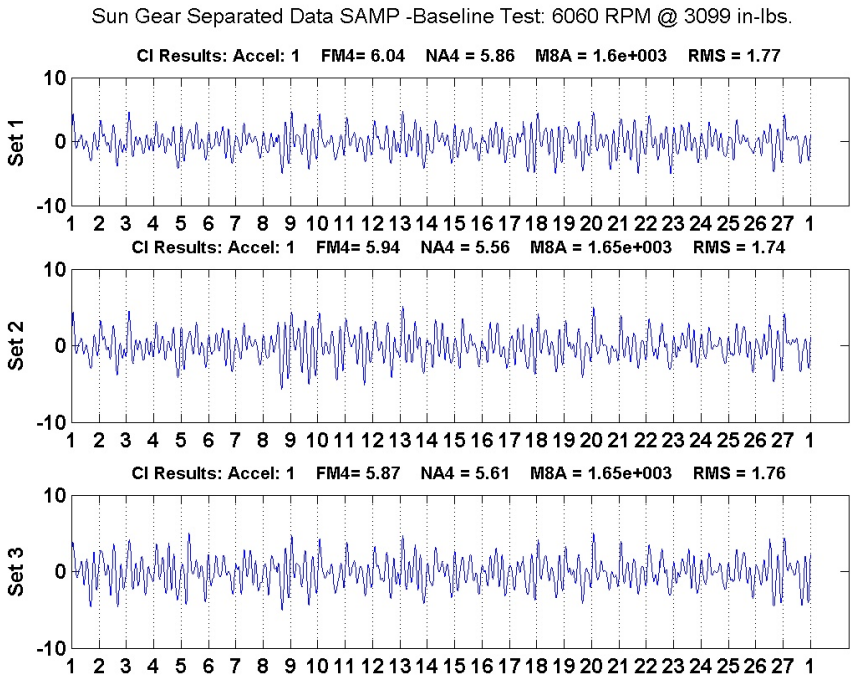

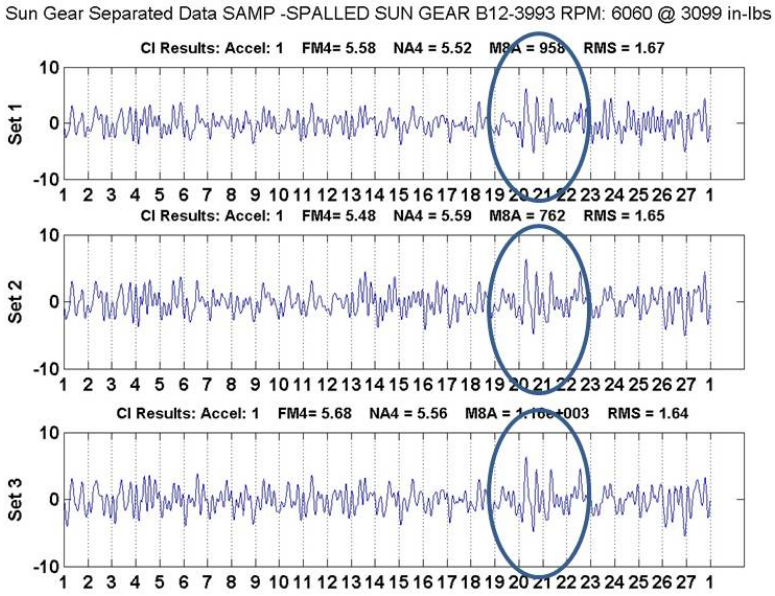

Figure 6.18: Baseline and Single Spall: SGVS -SAMP Pass Groups Comparison: Vibration (OH-58C) A_3,$M_v = 5$

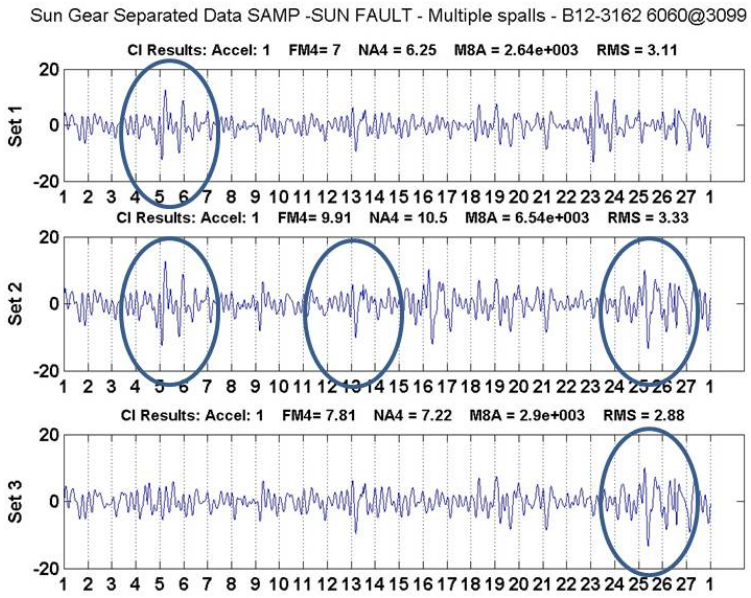

Figure 6.19: Multiple Spall: SGVS -SAMP Pass Groups Comparison: Vibration (OH-58C) A_3**,**$M_v = 5$

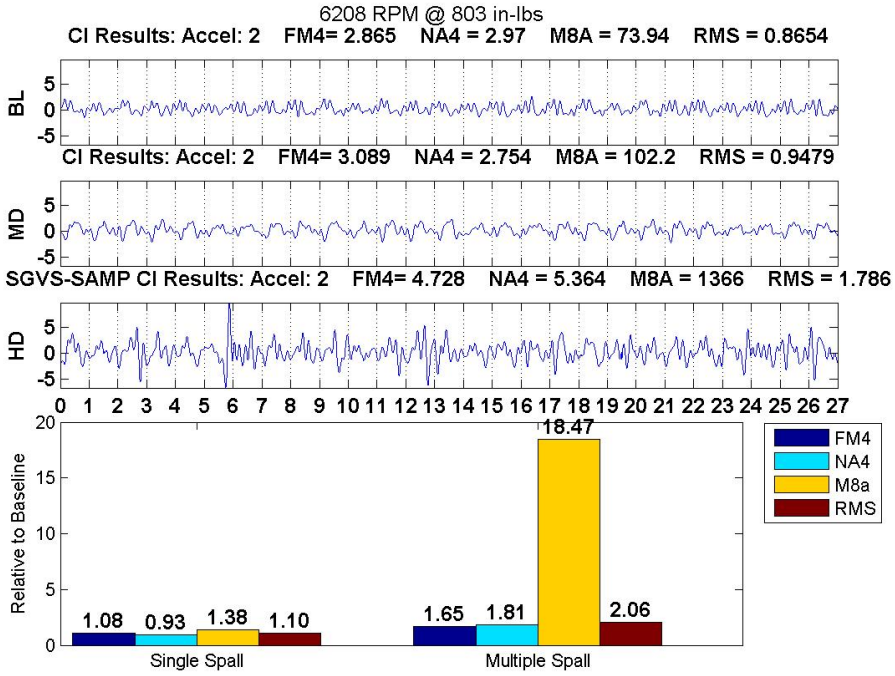

(a)

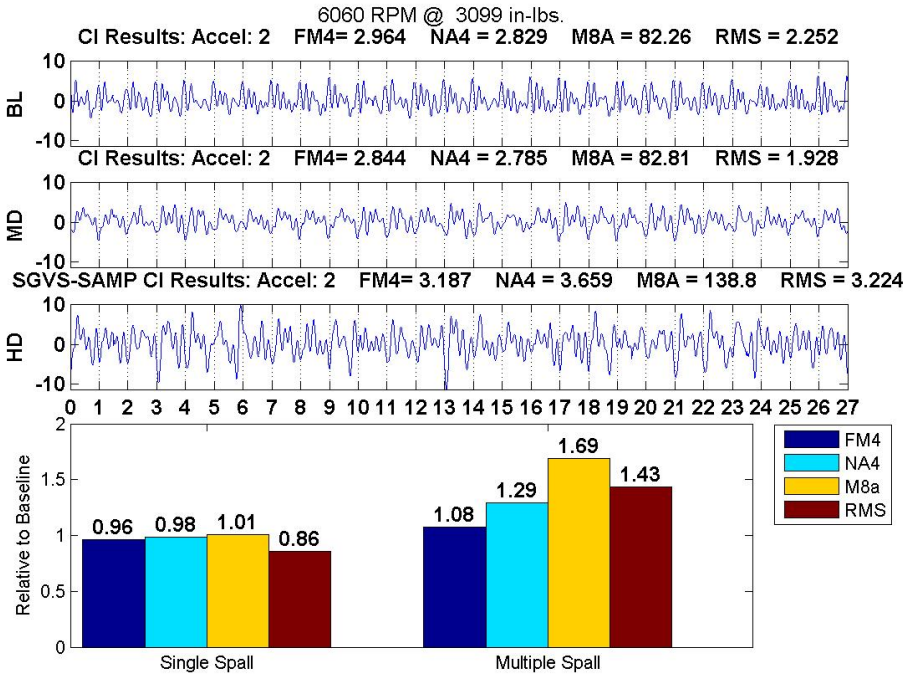

(b)

Figure 6.20: CI Comparison SGVS -SAMP : A_1/P_1

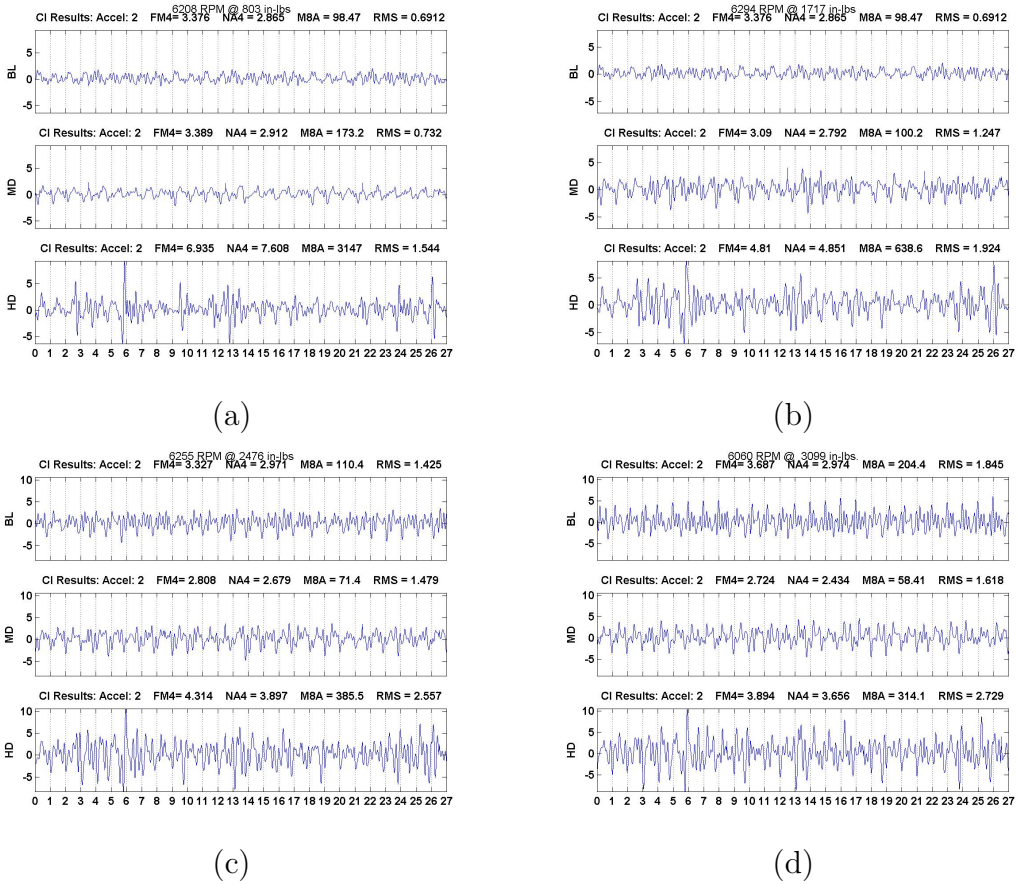

Figure 6.21: SGVS -SAMP Vibration Separation Vector Comparison: Vibration (OH-58C) Accelerometer: A_2

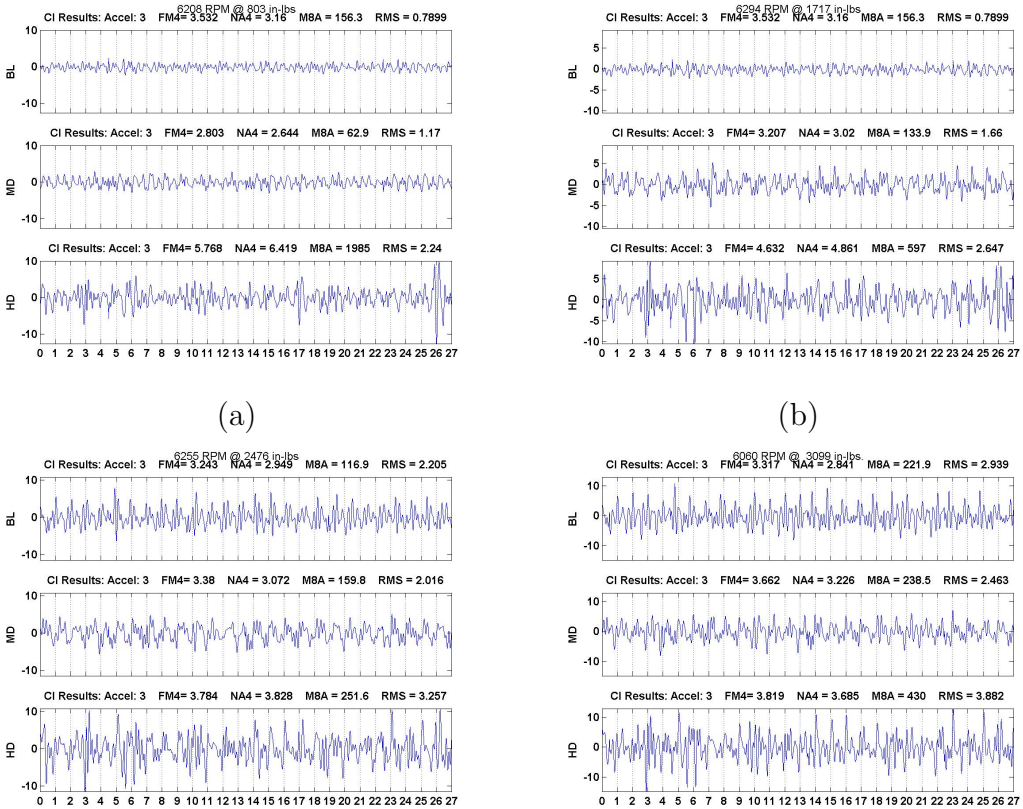

(a) (b)

(c) (d)

Figure 6.22: SGVS -SAMP Vibration Separation Vector Comparison: Vibration (OH-58C) Accelerometer: A_3

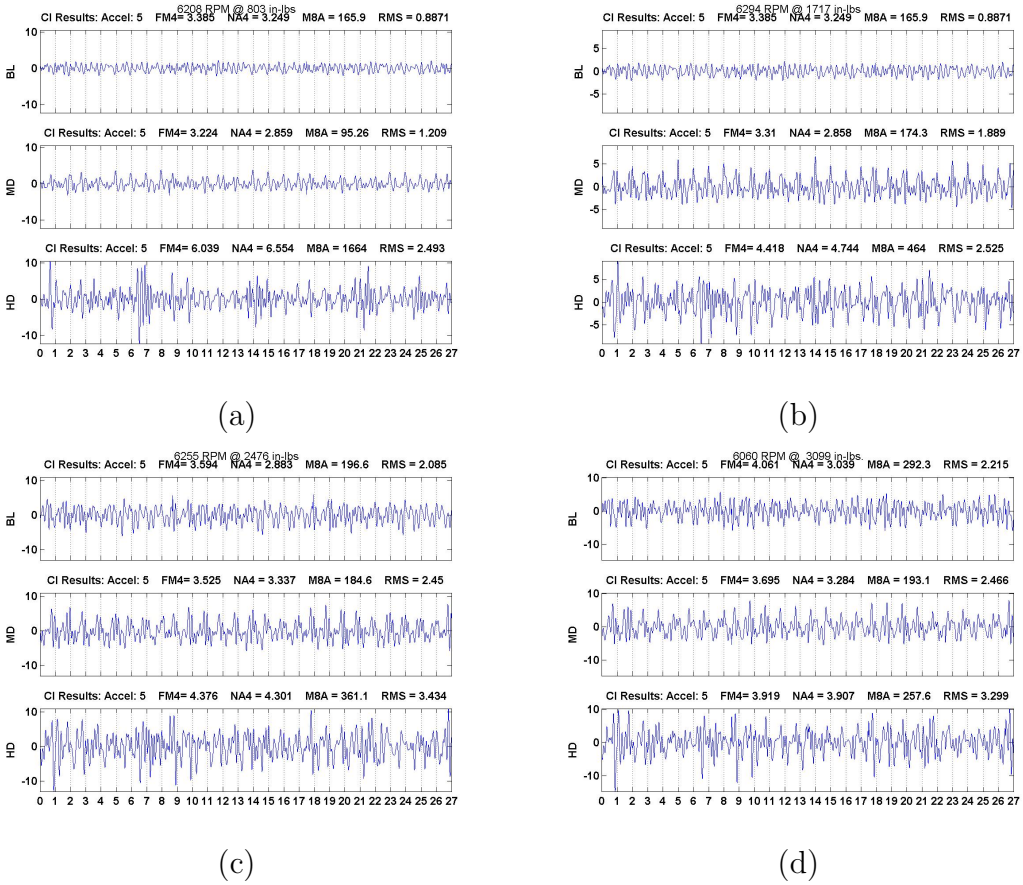

Figure 6.23: SGVS -SAMP Vibration Separation Vector Comparison: Vibration (OH-58C) Accelerometer: A_5

6.10 Geometrically Synchronized Measurements Method (**GSMM**) Vibration (OH-58C)

The following plots are results for the GSMM. As shown in the previous two sections, the damage is best detected at the low power cases so the results shown are for the 80 HP case. For these plots, the **CI** value was assigned to the mesh bins that contained the closest sun gear mesh angle. The plots show a schematic of the transmission on the left. The four positions along the sun gear intersecting the line of centers make up the mesh groups. The top right figure is the **TSA** data. It represents one of three carrier cycles of data being processed. The accelerometer is A_4. As the simulation runs, data is analyzed using a metric that is sensitive to peaks. As discussed in Chapter 4, after trial and error, $\bar{x}^6$ was used. This method operates on the premise that damage produces spikes in the data and that the positioning of the major spikes corresponds to the moment when a damaged tooth meshes. The expected result is a uniform bar height for the non-damaged case. For the damaged case, a mesh group pattern consisting of 4 bins, separated in the 6/7/7/7 pattern, is expected to dominate. Figure 6.24a gives the case for the baseline. The y-axis is normalized to unity and most of the bars are about the same height suggesting that no bias exists due to damage. Figure 6.24b shows the case for a single tooth spall. Compared to the baseline case, a pattern emerges that looks to approach the 4 bin, 6/7/7/7 pattern, correctly indicating sun tooth damage on the mesh group [3 9 16 23]. However, there are other, non-adjacent bins with significant heights, namely, [7 14 20]. Because of this, the plot does not provide enough distinction to allow a

decision based on the bar graph alone. Figure 6.25 gives the results for the multiple fault case. The mesh group pattern is distinctive enough to leave little doubt that the the transmission is damaged and the sun gear is the culprit.

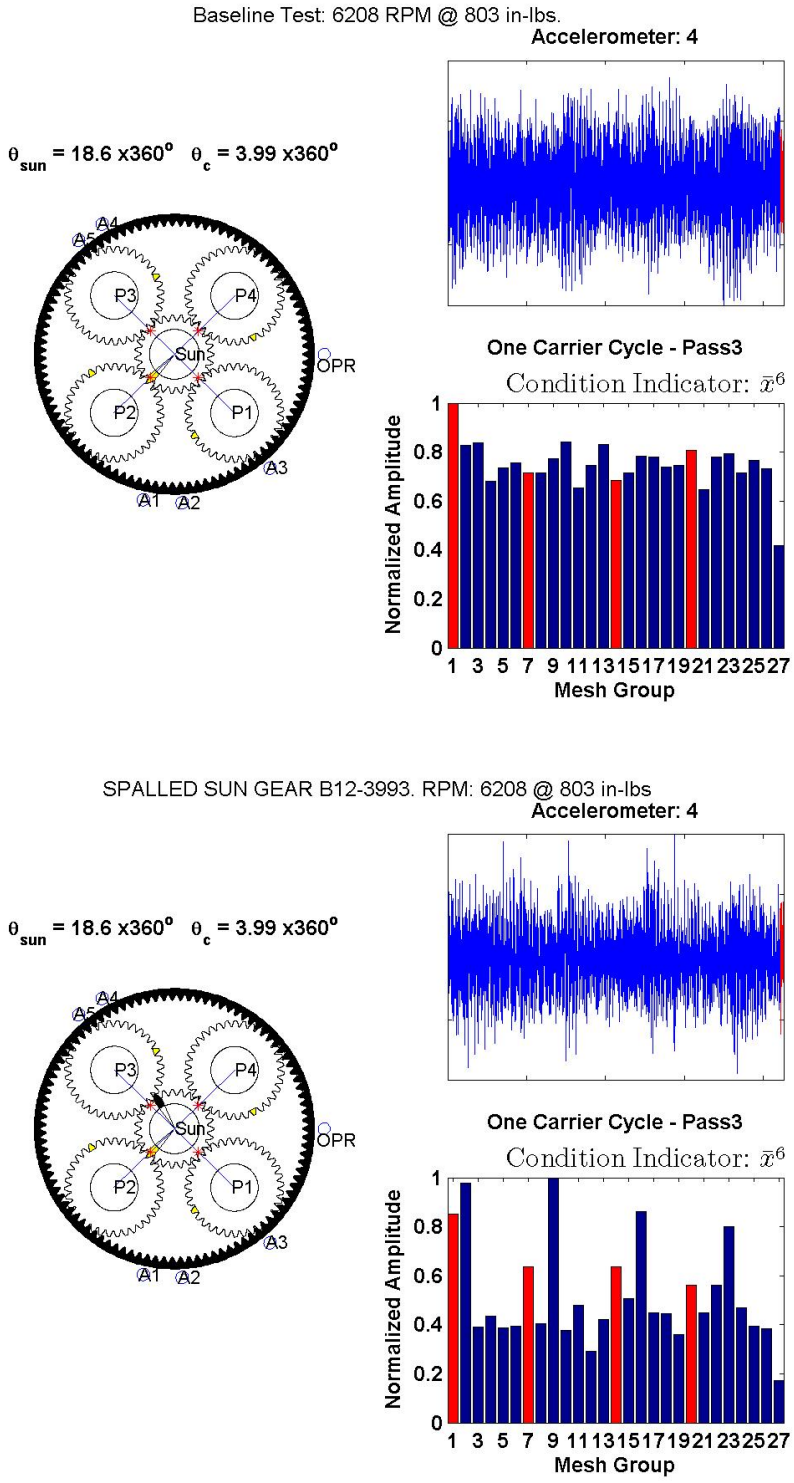

Figure 6.24: Baseline and Single Tooth Spall: Vibration (OH-58C) GSMM

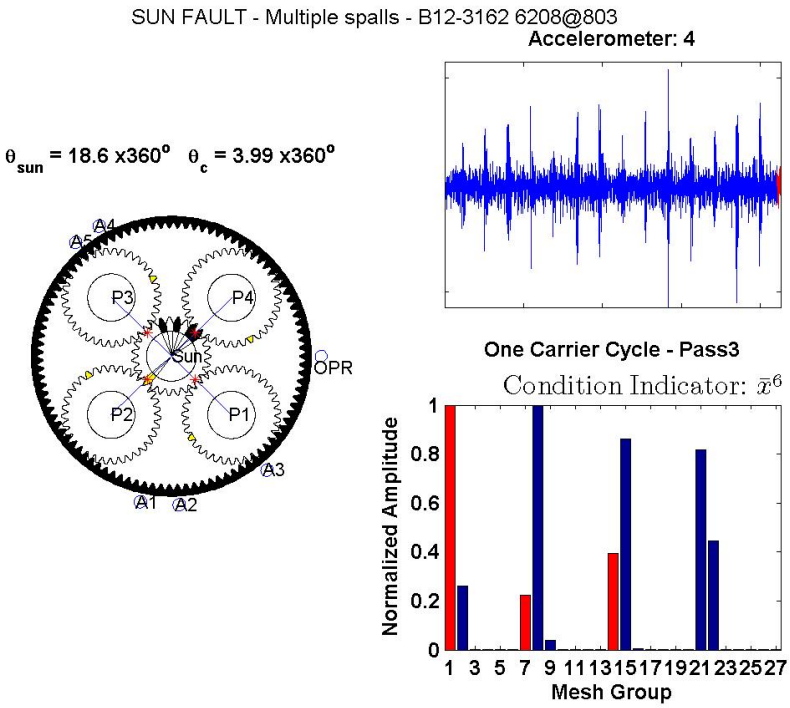

Figure 6.25: Multiple Tooth Faults: Vibration (OH-58C) GSMM

6.11 Results for the OH-58A

The next section discusses the results obtained for the OH-58A.

6.12 Frequency Response Vibration (OH-58A)

The frequency responses for the accelerometer signals are given in Figure 6.26. As in the case for the OH-58C, the spectrum for the accelerometers closest to the input spiral bevel are dominated by its first mesh frequency. Its interesting to note that the higher harmonics of the planet mesh frequency are larger than the lower harmonics. For example, in the baseline case, the 8th, 9th, and 10th planet mesh components of A_1 are larger. For A_3, its the 4th, 5th, and 6th and it's the 8th and 9th for A_4. For A_5, its the 6th, 8th, and 9th. There were no noticeable changes in the spectrum for the spalled planet bearing.

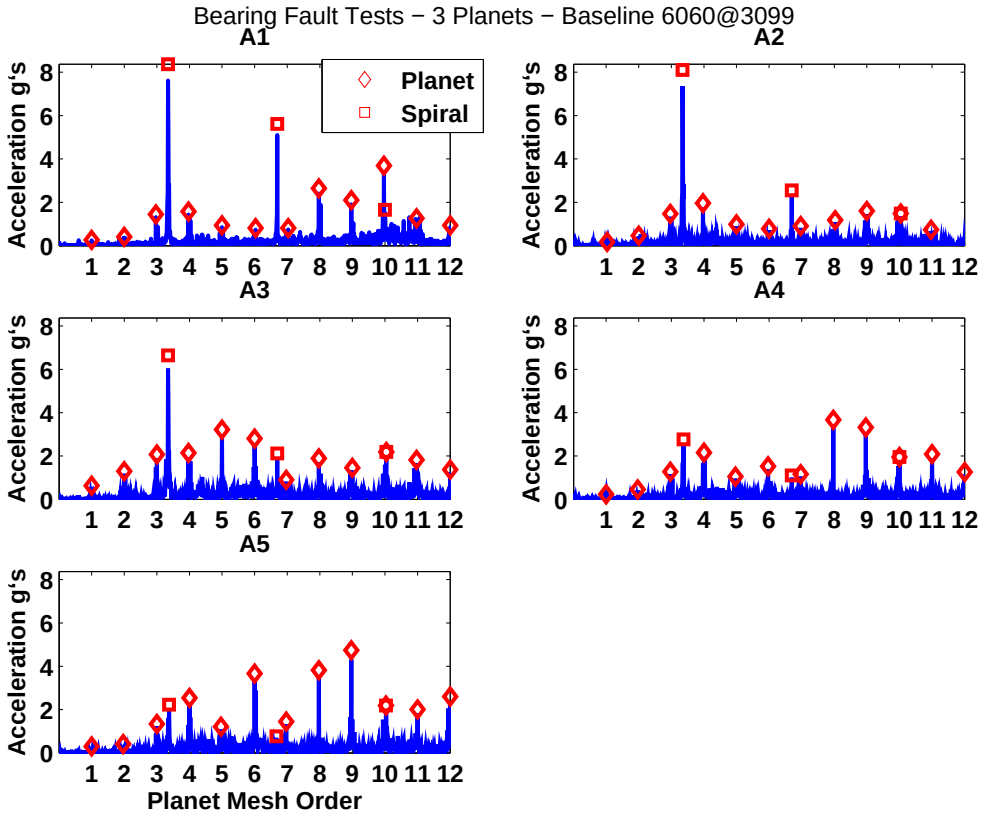

(a)

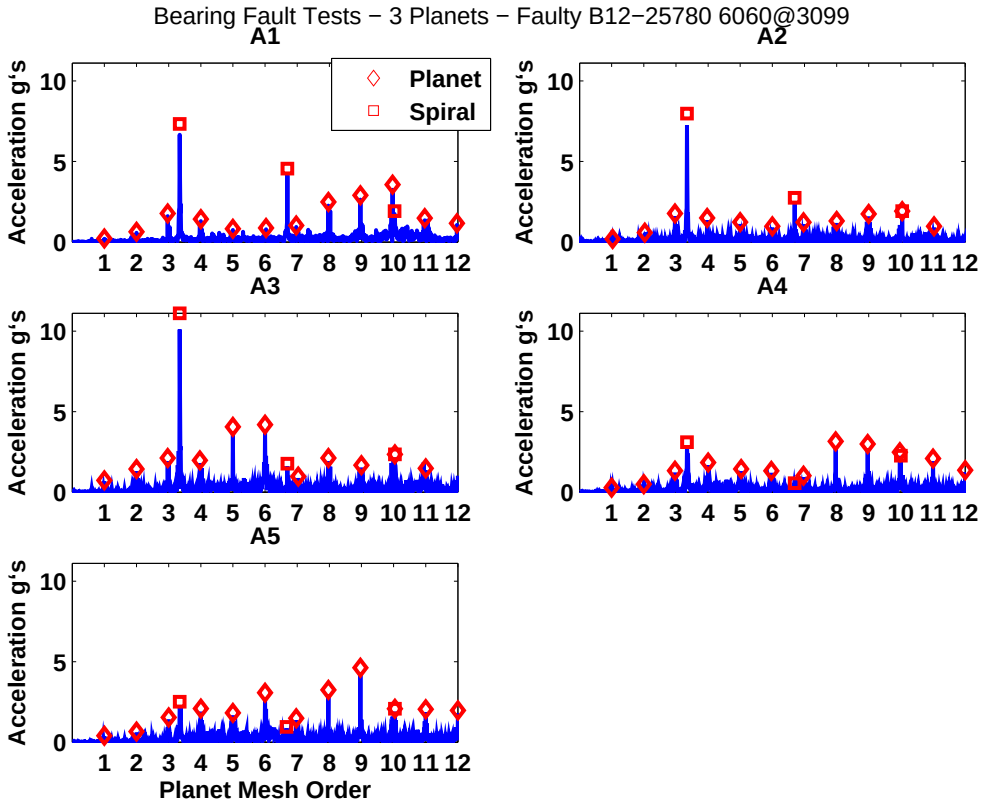

(b)

Figure 6.26: Frequency Response: Vibration (OH-58A) - a.) Baseline b.) Bearing Fault

6.13 Condition Indicators Applied to **TSA** Data Vibration (OH-58A)

Table D.2 shows the values for 11 indicators for the 8 tests on the OH-58A. Figures 6.27 and 6.28 give comparison plots for the **CIs** FM4, NA4, RMS, and M8A. Looking at the two time series plots in Figure 6.27 as well as the frequency plots reveals that the two signals are not very different. This is also evident in the FM4 and NA4 **CIs** which are almost identical. There is a slight increase in A_3 and A_4 for the FM4 and a slight increase in A_4 and decrease in A_5 for the NA4 metric.

Figure 6.28a shows the **CI** for M8A. There is a noticeable difference between A_3 and A_4. This is an example of the M8A metric exaggerating the FM4 metric. In Figure 6.28b, the RMS value did not change much as well. Similar results are found with the other indicators in Table D.2

Figure 6.29 gives the relative change for the damage case.

A 35% increase in RMS is shown for the 80 HP case. There is barely any change in value for the 298 HP case.

These values show that the planet gear damage would not be detected using **TSA** data.

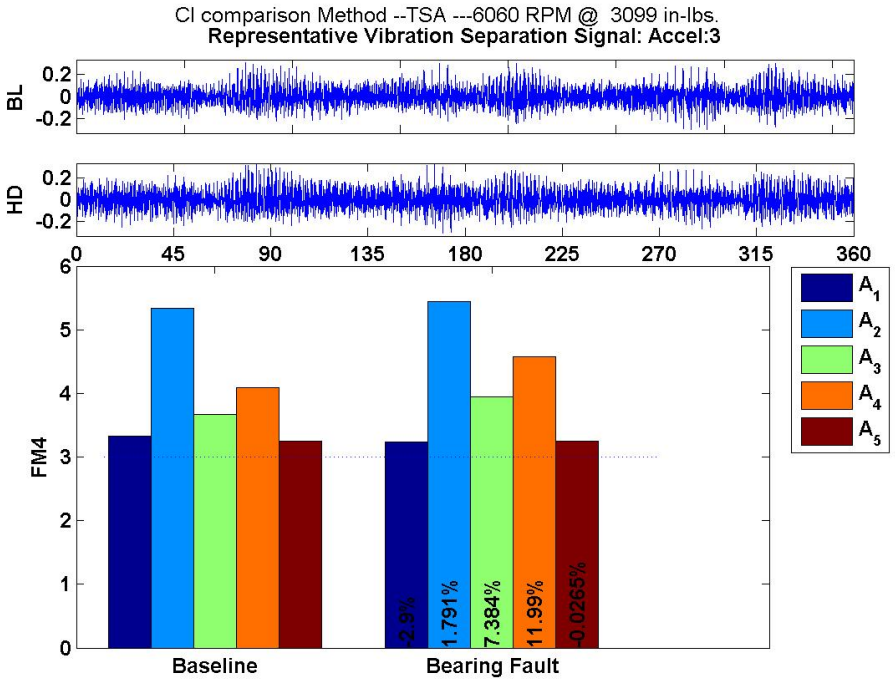

(a)

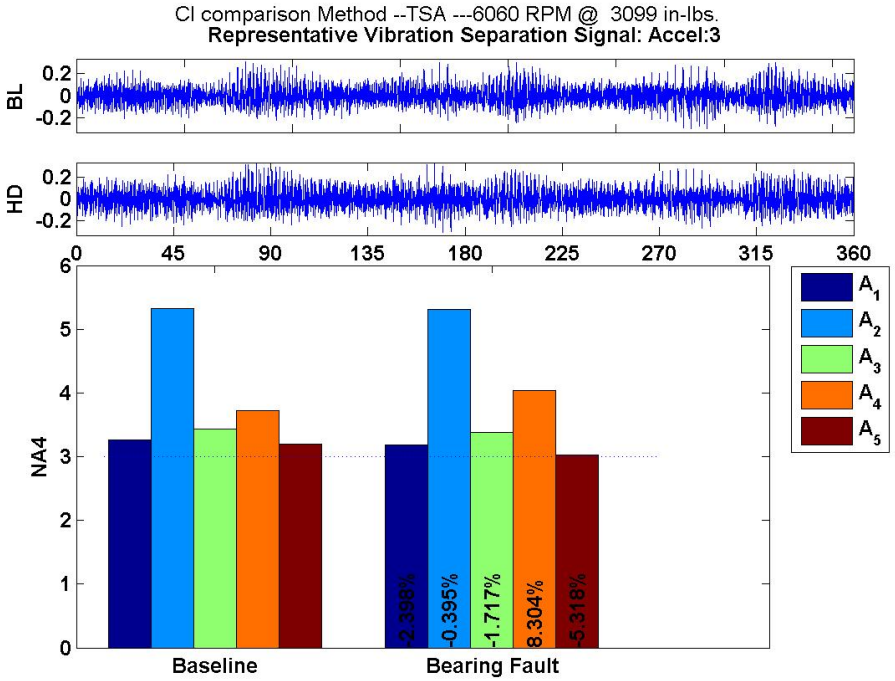

(b)

Figure 6.27: CIs on TSA data: Vibration (OH-58A) a.) FM4 b.) NA4 Sensor: A_3

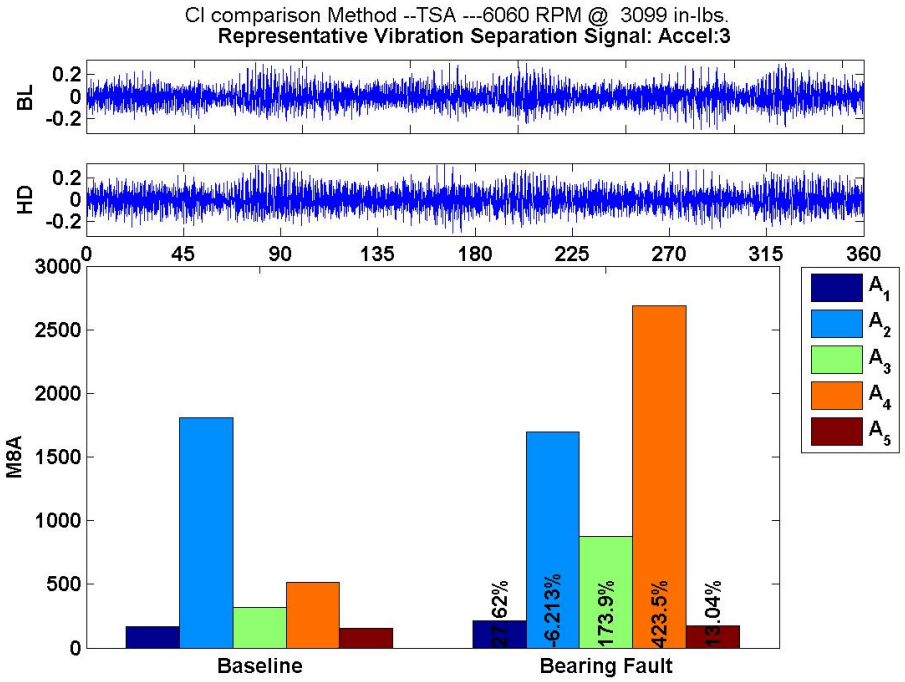

(a)

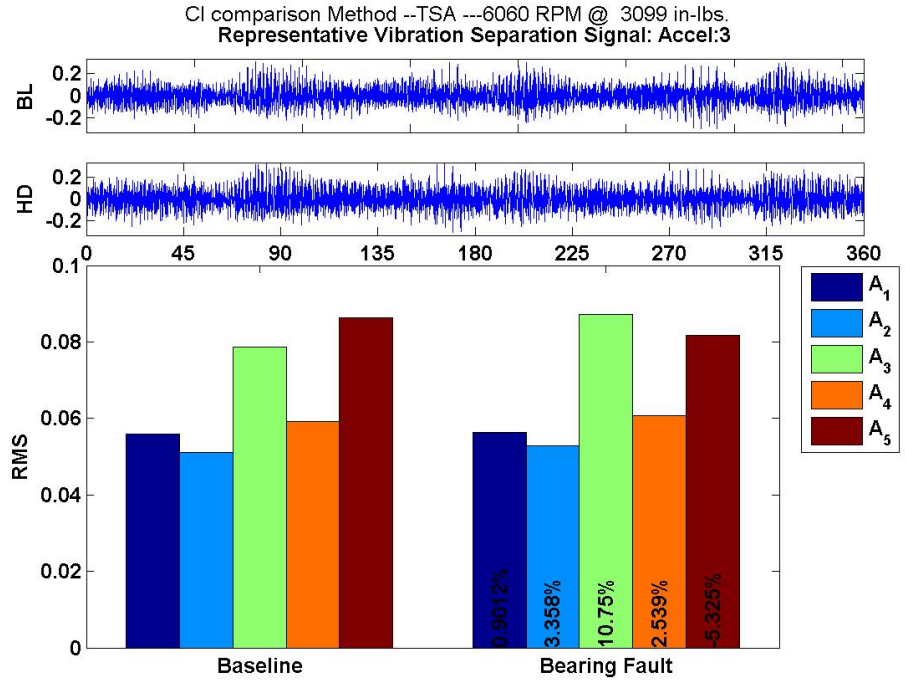

(b)

Figure 6.28: CIs on TSA data: Vibration (OH-58A) a.) M8A .b) RMS Sensor: A_3

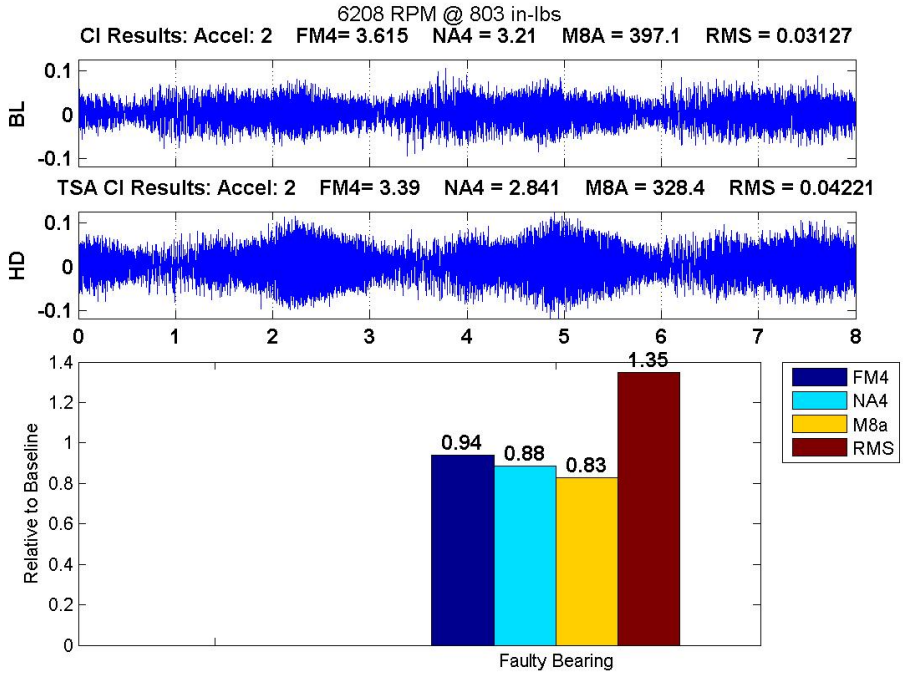

(a)

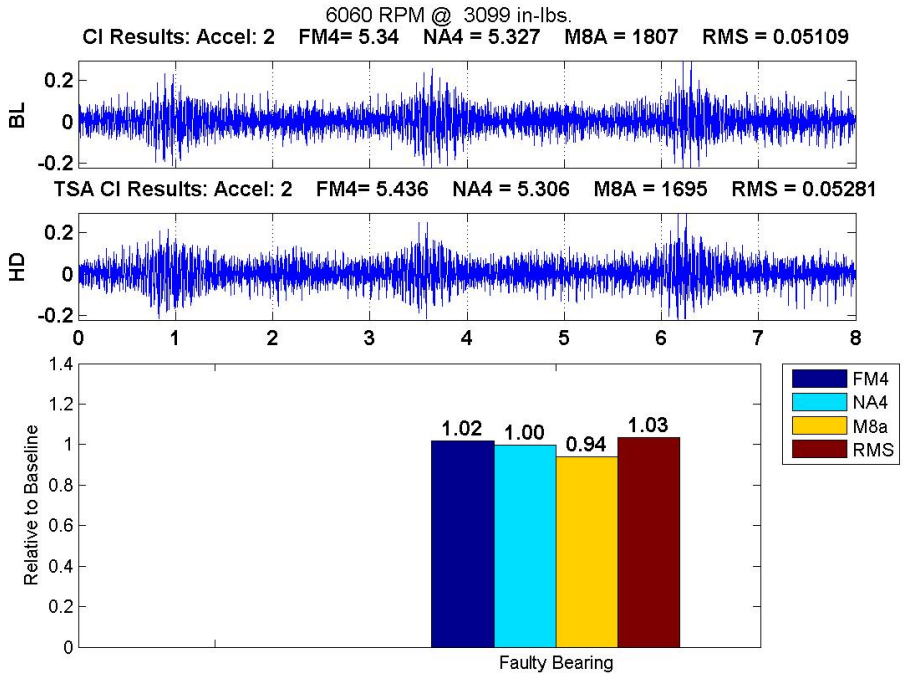

(b)

Figure 6.29: CI Comparison TSA a.) 80 HP b.) 298 HP Vibration (OH-58A)

6.14 **PGVS** Vibration (OH-58A)

Figure 6.30 displays the resulting **Vibration Separation Vectors** from PGVS using accelerometer A_3 for the 2 damage cases tested. Spanning the waveforms along each row and along each column reveals a high degree of correlation between the undamaged individual tooth mesh waveforms. This is different than the case for the OH-58C and is related to planet spacing. The values for the FM4 and NA4 metrics are close for all three planets, but the M8A metric varies from 502 to 2190. The RMS values varied from 103 to 131 revealing that when the different planets mesh at A_3, although similar in shape, the amplitude varied, possibly indicating a slight imbalance.

The relative changes in **CI** values is given in Figure 6.31. For the low power conditions, the FM4 value saw an increase of 29% and 28% for the high power case.

For this case, **PGVS** provides an indication of possible bearing damage which serve as an alert that further analysis should be conducted. The following sections searches for sun gear damage using the methods developed. The **SGVS** method used should not reveal any damage since the sun gear is healthy.

The values for the 11 **CIs** are found in Table E.2.

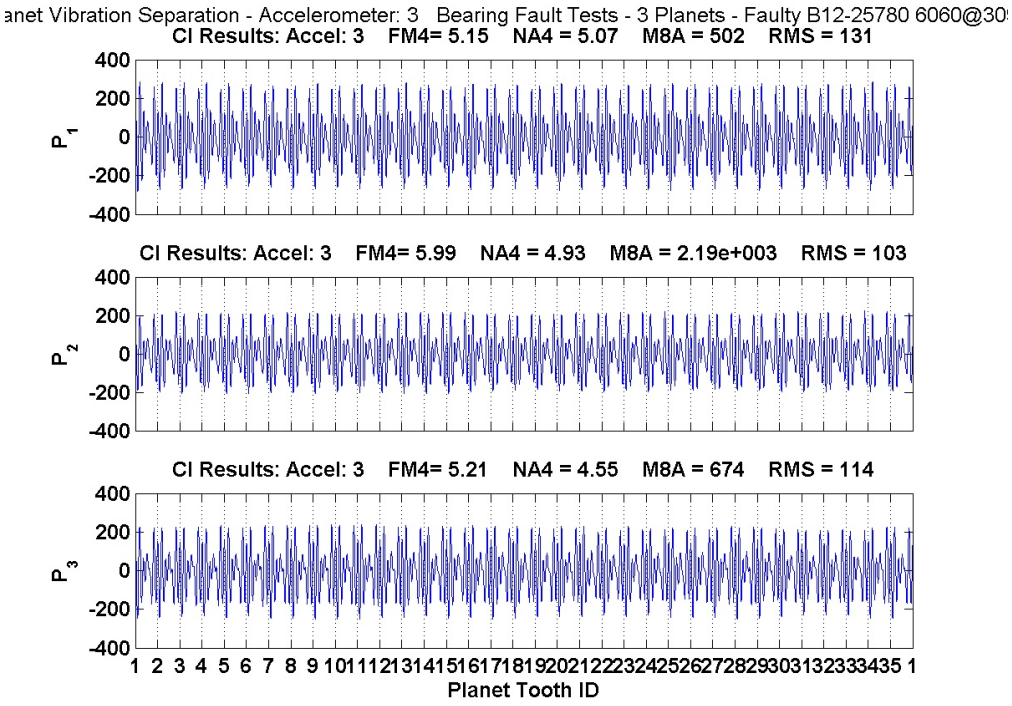

(a)

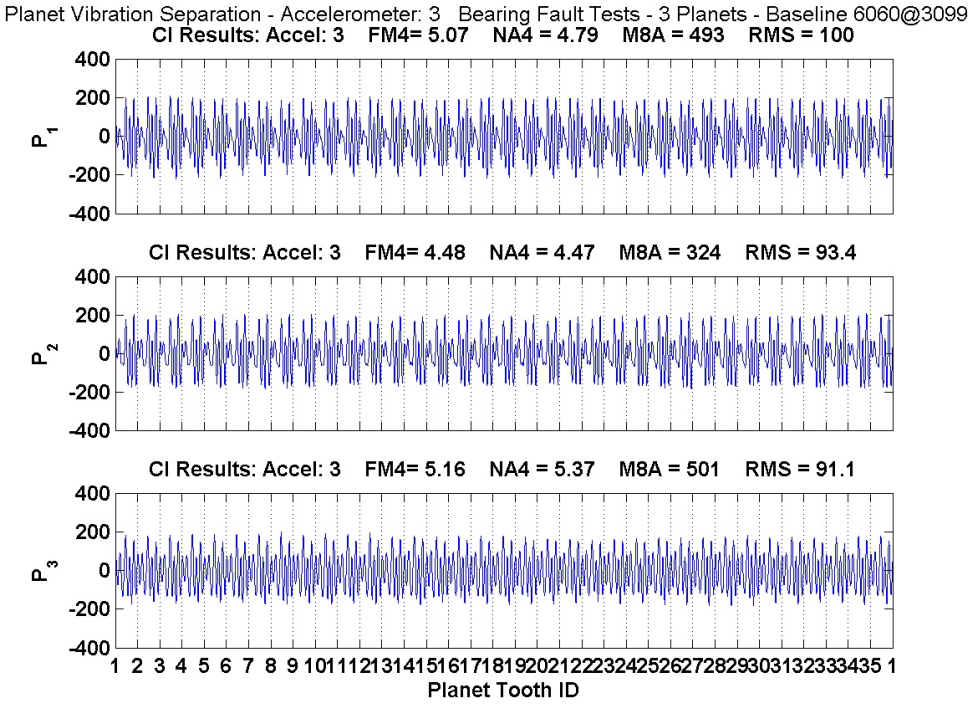

(b)

Figure 6.30: PGVS Comparison: Vibration (OH-58A) a.) Baseline b.) Bearing Fault A_3

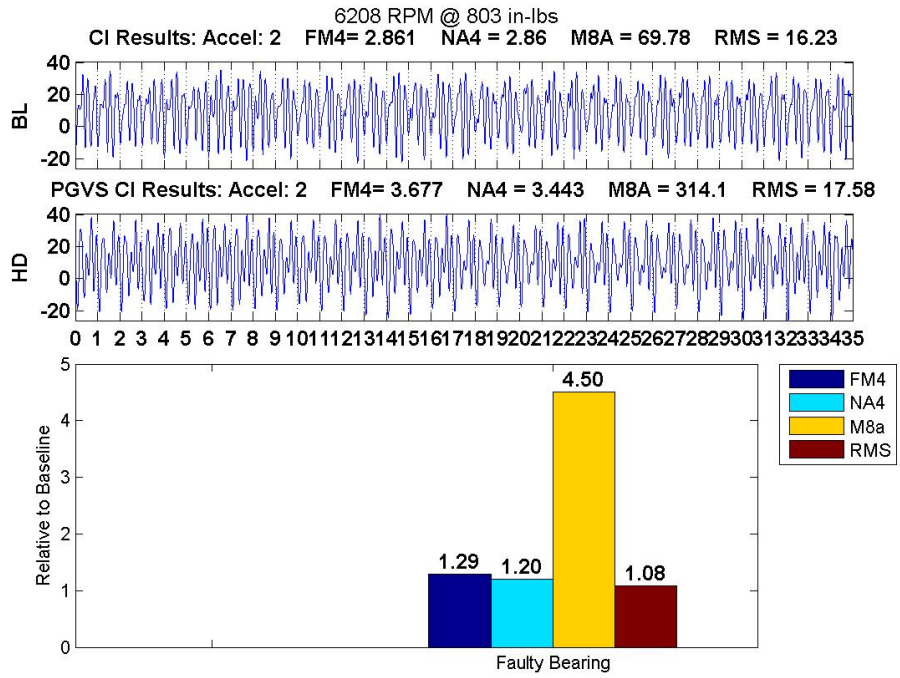

(a)

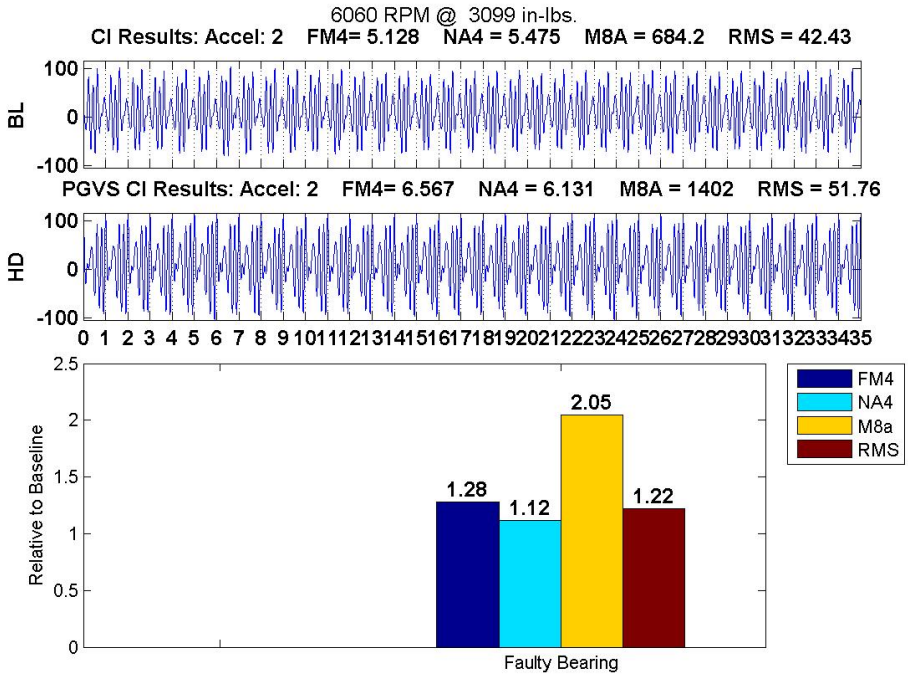

(b)

Figure 6.31: CI Comparison PGVS a.) 80 HP b.) 298 HP Vibration (OH-58A)

6.15 **SGVS -SASP** Vibration (OH-58A)

Figures 6.32 and 6.33 show the **SGVS -SASP** results for the baseline and bearing fault cases respectively. Figure 6.32a show the pass groups. As is the case for the OH-58C, there is a high degree of correlation in each pass group. Also, compared to the OH-58C signal, this signal appears a little noisier. Figure 6.32b shows the **Vibration Separation Vectors** as "'seen"' through each planet. The **CI** values for FM4 do not vary much, from 4.98 to 5.38. Also, the NA4 metric varied from 5.01 to 5.81.

Figure 6.33 shows the result for the bearing fault spall case. Unlike the case for the OH-58C, no noticeable deviations are observed when compared to the baseline case. This is a desirable result, since it shows that **SGVS - SAMP** is capable of isolating damage to the sun gear. Figure 6.34 gives the relative change for the damage case.

The results for other **CIs** are tabulated in Tables F.3 and F.4

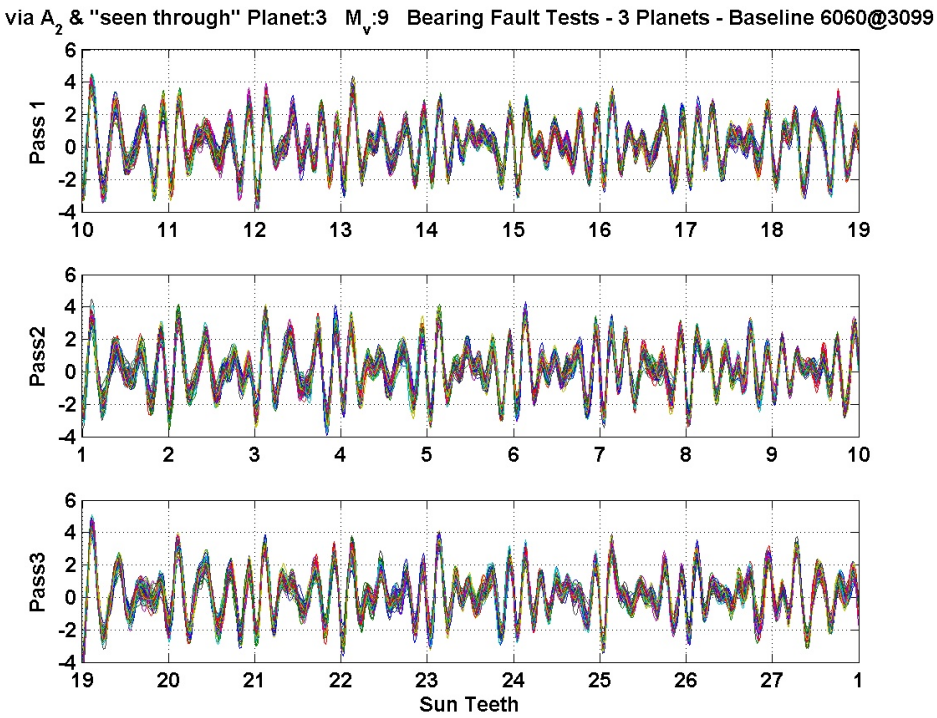

(a)

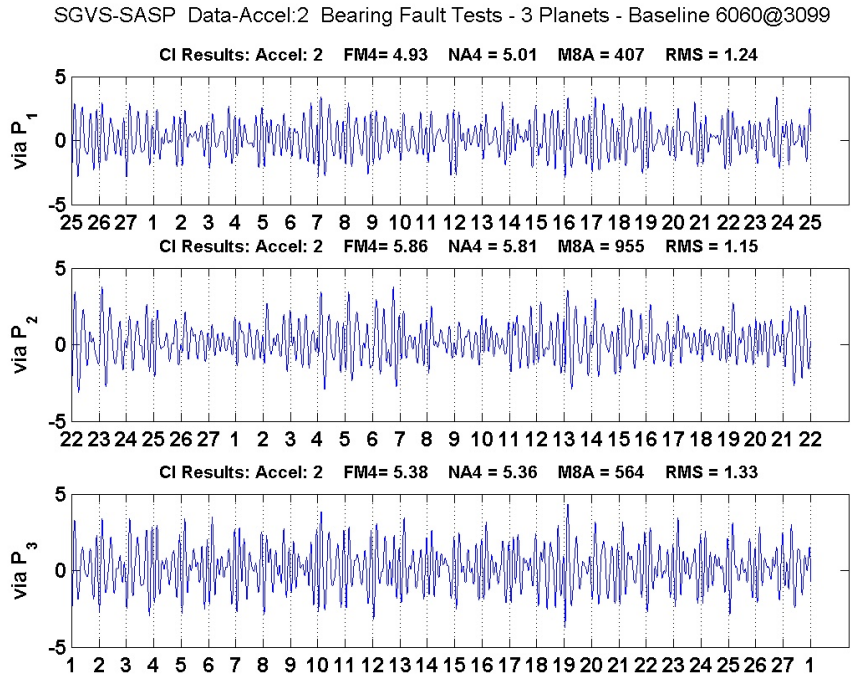

(b)

Figure 6.32: Baseline: SGVS -SASP Pass Groups Comparison A_3

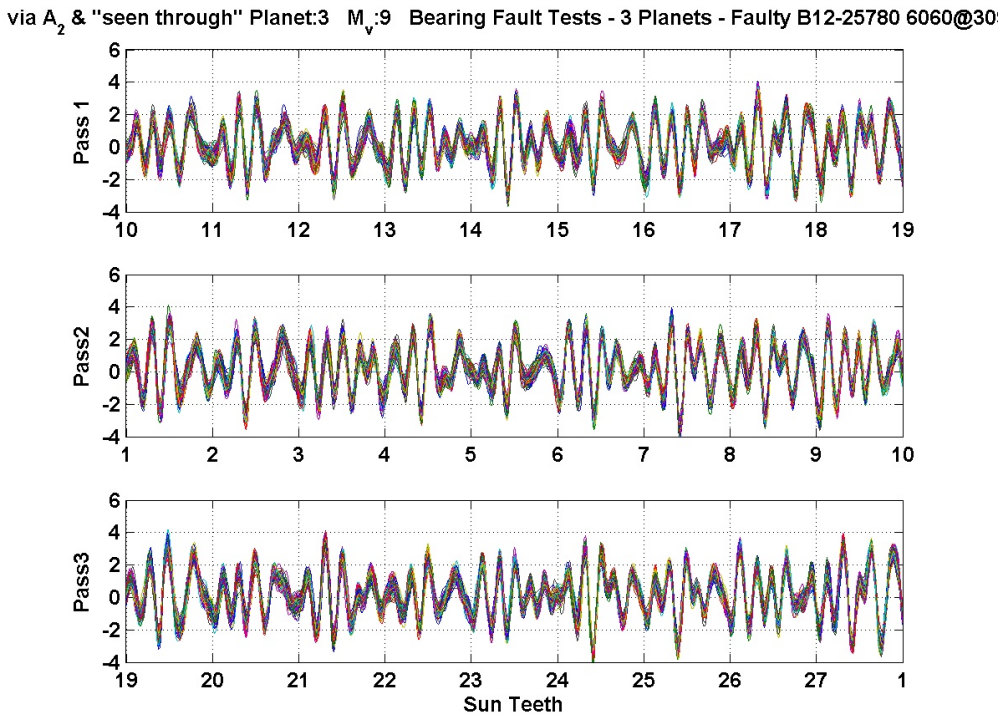

(a)

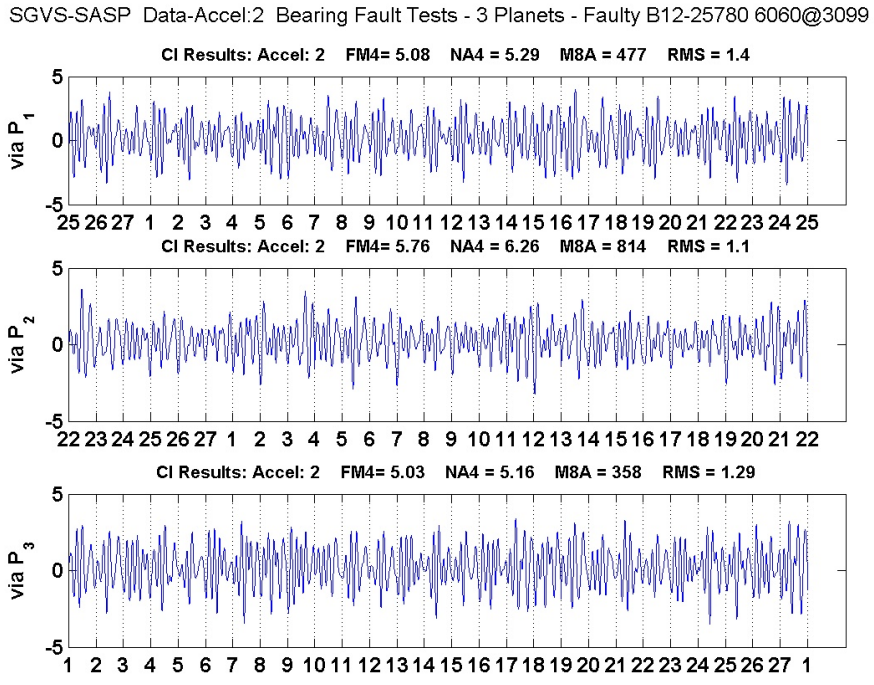

(b)

Figure 6.33: Bearing Fault: SGVS -SASP Pass Groups Comparison A_3

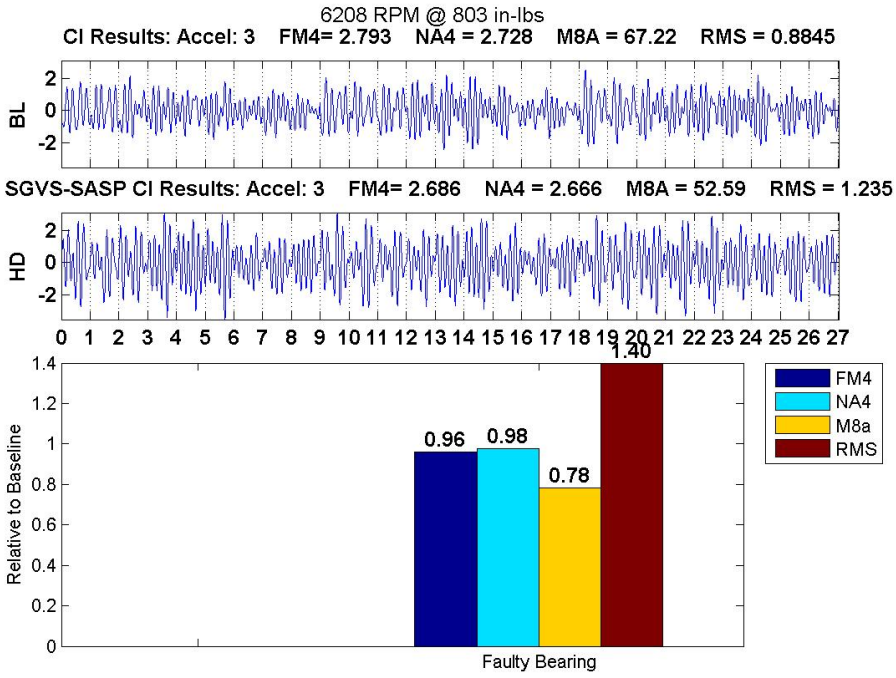

(a)

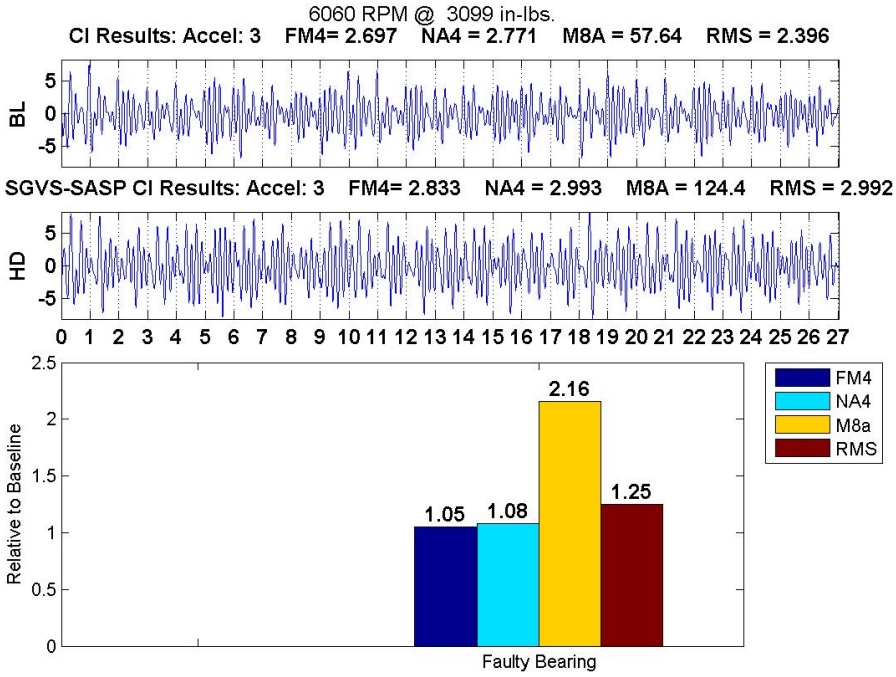

(b)

Figure 6.34: CI Comparison PGVS a.) Low Power b.) High Power Vibration (OH-58A)

6.16 **SGVS - SAMP** Method Vibration (OH-58A) $M_v = 9$

Figures 6.35 shows the separated vectors for the operating condition using the **SAMP** method.

Figure 6.36 gives the relative change for the damage case.

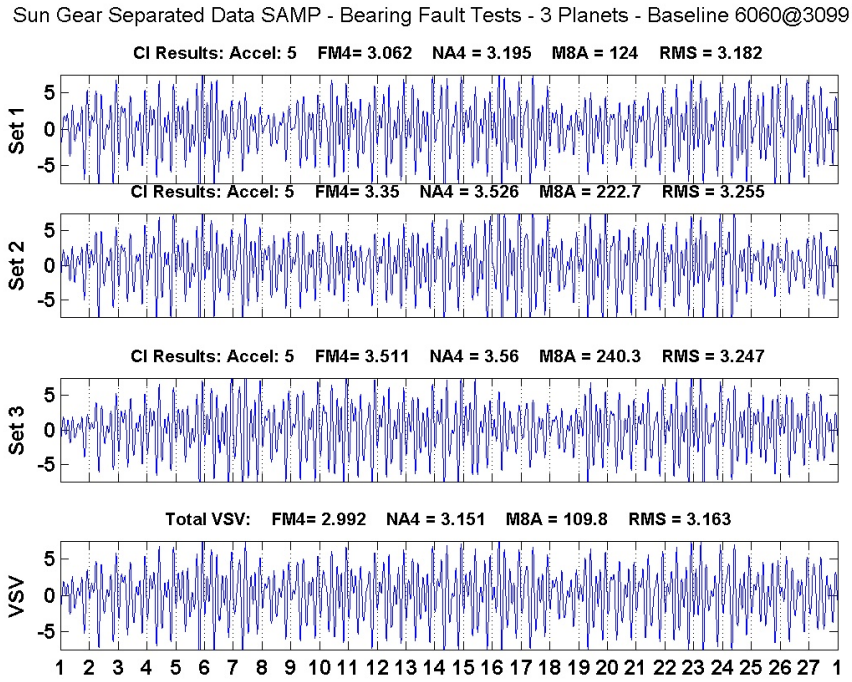

(a)

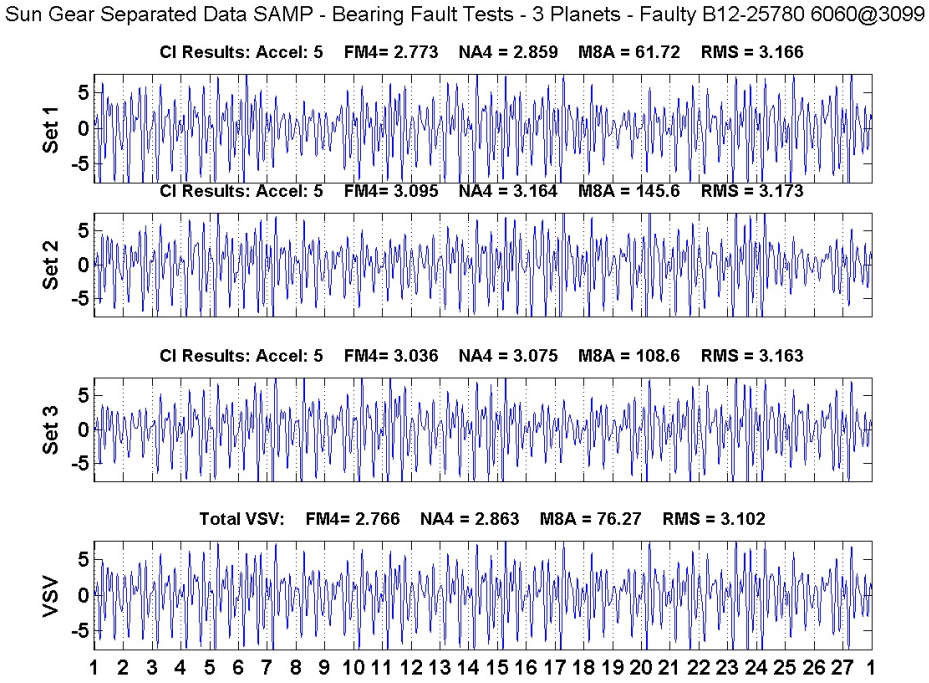

(b)

Figure 6.35: Baseline and Bearing Fault: SGVS -SAMP Pass Groups Comparison A_5

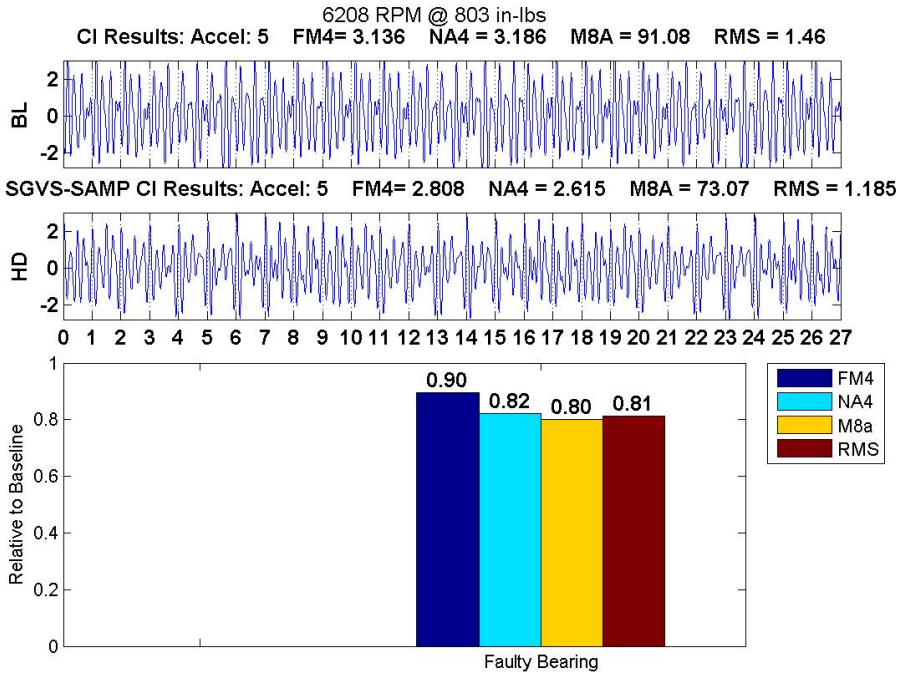

(a)

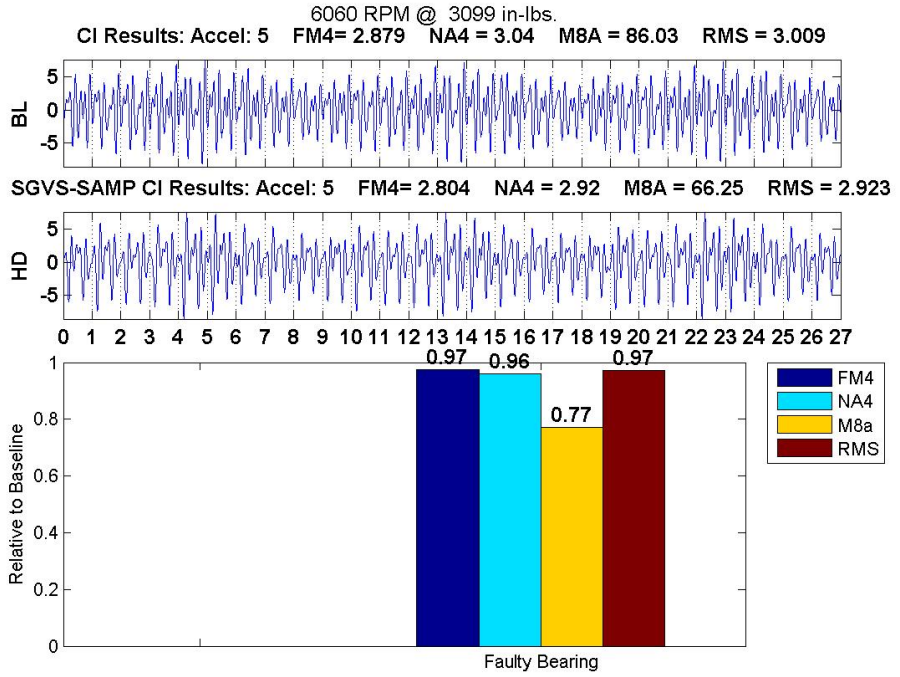

(b)

Figure 6.36: CI Comparison PGVS a.) Low Power b:) High Power Vibration (OH-58A)

6.17 Geometrically Synchronized Measurements Method (**GSMM**) Vibration (OH-58A)

Figure 6.37 show the results for the GSMM. Instead of the **CI** values being attributed to individual mesh bins, as was done for the OH-58C, they are grouped into the nine sun mesh groups. The results indicate that there is a nearly uniform representation for all mesh groups. It would also support, based on the results for the OH-58C, that the sun gear is not damaged.

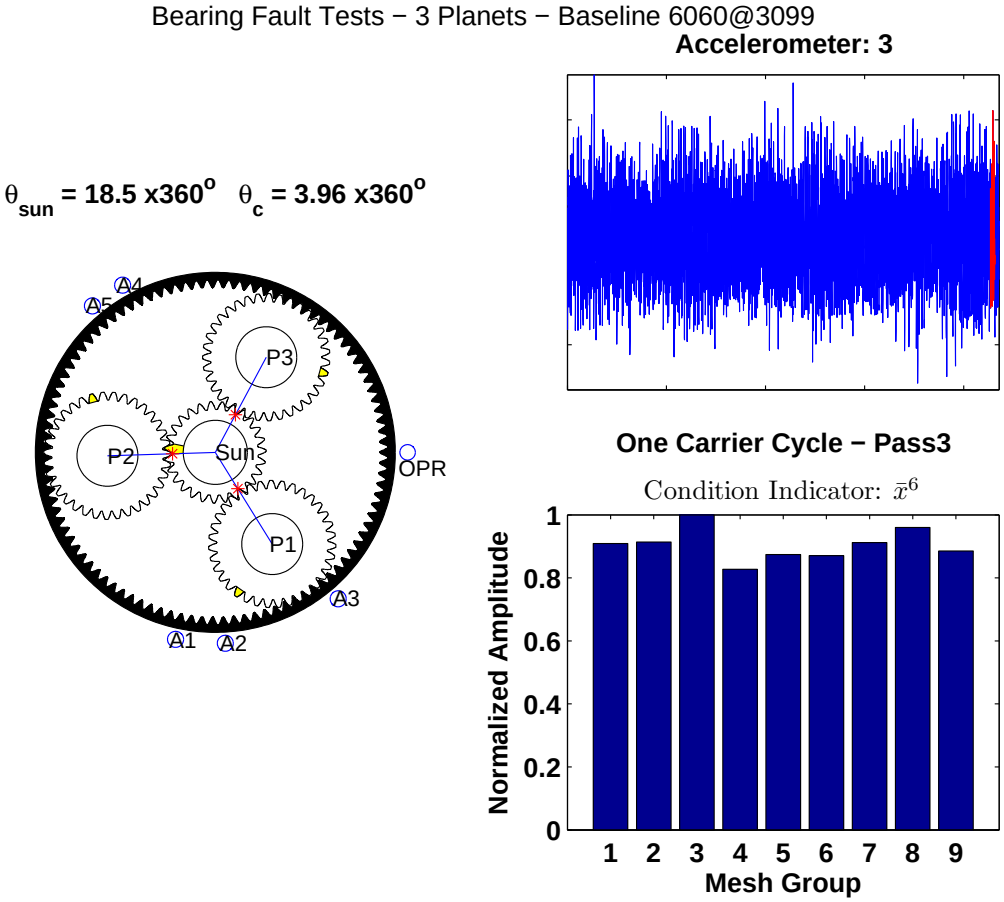
Bearing Fault Tests − 3 Planets − Baseline 6060@3099
Accelerometer: 3
θsun = 18.5 x360o θc = 3.96 x360o
A4
A5
P3
P2
Sun
OPR
P1
A3
A1
A2
One Carrier Cycle − Pass3
Condition Indicator: x̄6
Normalized Amplitude
0
0.2
0.4
0.6
0.8
1
1 2 3 4 5 6 7 8 9
Mesh Group

(a)

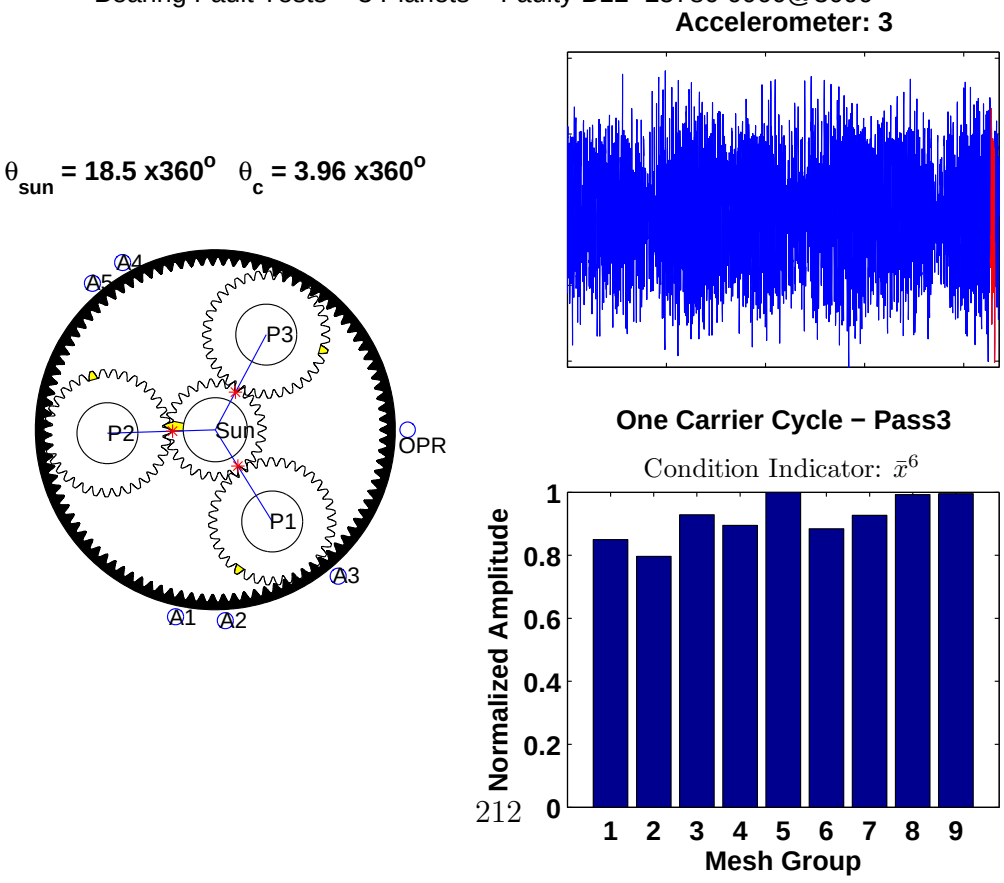
Bearing Fault Tests − 3 Planets − Faulty B12−25780 6060@3099
Accelerometer: 3
θsun = 18.5 x360o θc = 3.96 x360o
A4
A5
P3
P2
Sun
OPR
P1
A3
A1
A2
One Carrier Cycle − Pass3
Condition Indicator: x̄6
Normalized Amplitude
0
0.2
0.4
0.6
0.8
1
1 2 3 4 5 6 7 8 9
Mesh Group

(b)

Chapter 7

Summary, Conclusions, and Recommendations

Three methods for detecting sun gear faults have been developed and demonstrated on a full-scale OH-58 transmission. In just under a year, three damage cases and two baseline cases were tested. For each test, the planet gears, ring gear, sun gear, bevel gear pair, and their associated bearing were all inspected for damage. The test components were chosen from a set of parts damaged from a previous endurance test. These included two faulty sun gears and a faulty planet bearing.

The main goals of this research was to determine if it was possible to isolate the dynamics of the sun gear and detect any damage, independent of the other components. This higher level of interrogation improves on any indication of damage from the **TSA** data by actually determining the source, thus providing an effective means to reduce the number of false alarms. In addition, it was important to determine the effect the different types of damage had on the measured dynamic signal to aid in improving condition indicators and develop prognosis.

Planetary gear diagnostics have been demonstrated to be an effective tool to detect planet gear damage, but detecting faults on the sun gear remains a challenge. One reason for this is because the sun gear's dynamics is determined indirectly, through a meshing planet gear. The dynamics of the planet gear and sun gear are commensurate; thus, time-synchronous averaging could not be used as a separation tool as it

may be for the sun and bevel gear components. In addition, the low hunting tooth ratio between the sun gear and the ring gear allows only a small subset of sun gear teeth to be compared directly. This is different than the case for **PGVS** where an extraction of dynamics associated with each tooth, at the same roll angle, can be made. This allowed for the creation of a **Vibration Separation Vector** that is highly periodic and lends itself to analysis tools that look at deviations from this periodicity, such as the FM4 condition indicator. Another obstacle arises from the non-synchronous meshing and unequal spacing of the system's planets. This adds a further level of complexity when working with the waveforms, requiring the need to separate data into different **TSA** groups and also the use of a modified Tukey window.

All three methods performed well in detecting damage for the multiple fault case. The **SGVS -SASP** method produced dominant tooth mesh waveforms in its **Vibration Separation Vector** with spacings in accord with a sun gear mesh group. In addition, the details of the individual waveforms are preserved, possibly allowing additional analysis to determine the level of damage for prognosis. Although a couple of **Vibration Separation Vectors** for the single tooth spall case indicated some singular tooth mesh activity, the findings from inspecting the waveform as well as the FM4 parameters was inconclusive.

The **SGVS -SAMP** method is very similar to **PGVS** in the manner the extractions are organized, windowed, and placed into a **Vibration Separation Vector.** For the OH-58C, a modified Tukey window is used to account for the unequal spacing of the planets. Due to the low hunting tooth ratio, data extractions incorporating

multiple teeth are needed, with the number chosen based on the minimum required to get full tooth representation. This method allowed damage to be detected for the multiple spall case. Distinctive individual tooth mesh waveform patterns were observed in the low-power cases. As with the **SGVS -SASP** method, this approach was unable to determine single tooth spall damage conclusively.

The third method exploited the use of the kinematic simulation program and the carefully monitored geometry of the planetary system during testing. The geometrically synchronized measurement method matches the signal's response with the sun gear teeth in mesh and tallies a condition indicator parameter. For this study, the sum of the sixth power of the amplitude was used. Other **CIs** , such at FM4, M8A, and RMS, have been tried, but the one chosen ultimately produced the best results. Consistent with the other two methods, the best responses are obtained for the low-power cases. This is due to the increased vibration often associated with lower powers. The high exponent on the amplitude heavily weights the outliers, which are believed to be caused by damage. The pattern that represents sun tooth damage is one that appears in mesh groups. The assumption is that even if a single tooth is damaged, the effect would be experienced by all sensors, making the true source difficult to isolate. However, this method assumes the source can be isolated down to the mesh group. Plots showed that for the baseline case, there was no biasing of the values of each bin. For the sun gear with a single tooth spall, there was an emergence of mesh groups indicating increased damage, but the result, based on the condition indicator used, was inconclusive. The results for the multiple spall case clearly show that the damage is on the sun gear.

Bearing fault tests were conducted on the OH-58A. These tests were used to determine the robustness of the methods developed for **SGVS** for other faulty components. The goal was to see if the bearing damage would manifest as sun gear damage or planet tooth damage. The results for **SGVS** indicate that the effects of damage bearing did not show up in the results. In addition, using **PGVS**, the separated waveform of the planet hosting the damaged gear appeared noisy across all teeth. This uniformly distributed disturbance is a characteristic of bearing damage.

The parameters followed in this work were FM4, NA4, M8A, and RMS. The NA4 **CI** , which is designed for longer duration tests, was almost indistinguishable from FM4 for these short-run tests. The M8A condition indicator fluctuated wildly, from sub 100 to vales on the order of 10,000!. This indicator served to exaggerate the findings of the FM4 and in that regard, did not provide information that could not also be obtained from the FM4. The RMS value gave an intuitive measurement of the system increased as damage increased.

7.1 Future Work

- This work focused on vibration measurements. However, during testing, acoustic and transmission error measurements were taken. It is recommended that similar analysis be conducted using these signals. An example output using **SGVS -SASP** on Microphone 2 located near A_4 is given in Figure H.1.

- In this work, only FM4, NA4, M8A, and RMS were analyzed. A combination of **CIs** as a means to produce a new **CI** should be explored.

- The metric used for **GSMM** was from trial and error. A study to find the optimum **CI** or combination of **CIs** to be used for this type of analysis is recommended.

Appendices

Appendix A

Helicopter and Fixed-Wing Accident Rates

	Total Accidents		Total Flight Hours (100,000 flight hours)		Accident Rate (per 100,000 flight hours)		Ratio (x100)
	Fixed Wing	Rotorcraft	Fixed Wing	Rotorcraft	Fixed Wing	Rotorcraft	Helicopter/Airplane
1975	3644	264.0	283.9	9.7	12.8	27.1	211.2
1976	3695	248.0	292.0	11.0	12.6	22.5	177.8
1977	3745	246.0	301.7	11.7	12.4	21.0	169.5
1978	3850	283.0	331.6	14.0	11.6	20.3	174.7
1979	3477	265.0	367.6	15.2	9.5	17.4	184.0
1980	3233	261.0	341.5	18.9	9.5	13.8	145.7
1981	3161	257.0	341.1	23.0	9.3	11.2	120.4
1982	2886	255.0	277.8	15.0	10.4	16.9	163.1
1983	2736	234.0	267.1	15.8	10.2	14.9	145.1
1984	2703	224.0	273.0	14.7	9.9	15.2	153.7
1985	2466	205.0	263.6	15.8	9.3	13.0	139.3
1986	2301	190.0	251.5	15.6	9.2	12.2	133.1
1987	2250	179.0	253.1	12.8	8.9	14.0	157.1
1988	2131	180.0	250.7	18.1	8.5	10.0	117.1
1989	1999	187.0	258.6	16.9	7.7	11.1	143.3
1990	1955	194.0	266.1	15.7	7.3	12.3	168.0
1991	1945	170.0	246.8	20.9	7.9	8.1	103.3
1992	1833	178.0	218.1	15.7	8.4	11.3	134.6
1993	1827	162.0	199.4	15.3	9.2	10.6	115.9
1994	1738	190.0	191.9	15.5	9.1	12.2	135.1
1995	1844	152.0	203.1	19.2	9.1	7.9	87.3
1996	1683	168.0	218.4	17.3	7.7	9.7	125.7
1997	1629	158.0	225.1	15.9	7.2	9.9	137.1
1998	1627	189.0	226.7	15.5	7.2	12.2	169.7
1999	1664	192.0	259.0	22.9	6.4	8.4	130.8
2000	1549	206.0	243.6	19.1	6.4	10.8	169.9
2001	1478	177.0	222.9	17.7	6.6	10.0	150.5
2002	1443	201.0	222.3	17.3	6.5	11.6	178.9
2003	1517	197.0	226.4	18.5	6.7	10.7	159.1
2004	1422	165.0	216.0	17.7	6.6	9.3	141.9
2005	1446	190.0	197.0	19.3	7.3	9.8	134.0

Table A.1: Accident Rate Comparison - NTSB 1995-2005

Appendix B

Table of Condition Indicators

Below is a table of **CIs** and Figure B.1 is a flowchart showing how various **CIs** are related.

CI	Description
RMS	The Root Mean Square value is given by $s_{rms} = \sqrt{\frac{1}{N}\sum_{i=1}^{N} s_i^2}$ where s_i is the i^{th} member of dataset s, and N is the number of points in dataset s. The RMS value does not increase with the isolated peaks in the signal. Its value increases as tooth failure progresses. Generally, the RMS value of the vibration signal is a very good descriptor of the overall condition of the tested gearboxes. This parameter is sensitive to gearbox load and speed changes. The main usage of this parameter is to monitor the overall vibration level. Then the test can be stopped when the vibration energy reaches the critical value and the gearbox destruction can be treated. Typically, the time history of the RMS value for the overall vibration signal is recorded and monitored. As the gearbox consequently wears out and/or pitting damage occurs, the vibration level increases. As pitting damage progresses, the overall vibration level increases rapidly.
Δ RMS	This parameter is the difference between two consequent RMS values and is sensitive to load change. The premise behind this parameter is that damage produces a rapid increase in RMS when compared to no damage cases.
Crest factor	This parameter is sensitive to very tiny surface damages. It is defined as the peak value of the signal divided by the RMS value of the signal: $CF = \frac{s_{pk-pk}}{s_{rms}}$ When only one tooth is damaged, there is minimal change in the RMS value of the vibration signal during one rotation however, the peak value increases thus increasing the crest factor. As the damage progresses the root mean square value of the vibration signal increases its value and the crest factor decreases.
Kurtosis	The Kurtosis describes the peakiness or flatness of the signal's amplitude distribution and is given by $Kurt(s) = \frac{N\sum_{i=1}^{N}(\Delta s_i - \bar{s})^4}{(\sum_{i=1}^{N}(\Delta s_i - \bar{s})^2)^2}$ where $Kurt$ is the kurtosis, N is the number of points in the time history of the signal s, and s_i is the i-th point in the time history of signal s. Its value is compared to 3 which represents a normal distribution.
Energy Operator	The energy operator is computed as the normalized kurtosis from the signal where each point is computed as the difference of two squared neighborhood points of the original signal. It is given by: $EO = \frac{N^2\sum_{i=1}^{N}(\Delta x_i - \Delta\bar{x})^4}{(\sum_{i=1}^{N}(\Delta x_i - \Delta\bar{x})^2)^2}$ Where EO is the energy operator, $\Delta\bar{x}$ is the mean value of signal $\Delta\bar{x}$, $\Delta x_i = s_{i+1}^2 - s_i^2$, and N is the number of points in dataset x
Energy Ratio	This parameter is a good indicator for heavy wear, where more than one tooth is damaged. The energy ratio is defined as the ratio between the energy of the difference signal and the energy of the regular meshing components and is given by: $ER = \frac{\sigma(d)}{\sigma(r)}$ where $\sigma(d)$ is the standard deviation of the difference signal and $\sigma(r)$ is the standard deviation of the regular signal. The idea of this indicator is that the energy is transferred from the regular meshing component to the rest of the signal as wear progresses.

Table B.1: Fault Detection Algorithms

CI	Description
Sideband Index	The sideband index is defined as the average amplitude of the sidebands of the fundamental gear mesh frequency.
Sideband Level Factor	The sideband level factor is defined as the sum of the first order sideband about the fundamental gear mesh frequency divided by the standard deviation of the time signal average. A low value is obtained for a gearbox in good condition.
FM0	This parameter is defined as the quotient of the peak-to-peak value of the signal divided into the energy of the mesh frequency and its harmonics. It is given by: $FM0 = \frac{S_{pk-pk}}{\sum_{i=1}^{N} A(i)}$ where S_{pk-pk} is the peak to peak value of the vibration signal in the time domain, $A(i)$ is the amplitude of the i-th mesh frequency harmonics.
FM4 parameter	This parameter is a measure of the amplitude distribution of the difference signal compared to a normal distribution. The parameter assumes that a gearbox in good condition has a difference signal with a Gaussian amplitude distribution, whereas a gearbox with defective teeth produces a difference signal with structure. It is given as the kurtosis of the difference signal: $FM4 = \frac{N\sum_{i=1}^{N}(\Delta d_i - \bar{d})^4}{(\sum_{i=1}^{N}(\Delta d_i - \bar{d})^2)^2}$ where d_i is the i-th point in the difference signal in the time record and N is the total number of points in the data record.
NA4 Parameter	The NA4 parameter was developed to improve the behavior of the FM4 parameter when more than one tooth is damaged. The NA4 uses a residual signal to compute kurtosis which is the original signal with its gear mesh and harmonic components removed. In addition, this parameter is normalized by an average value of the variance instead of the variance of the current signal. Therefore, if the gear damage spreads from one tooth to another tooth the value of the average variance increases slowly allowing the NA4 parameter to grow. The NA4 parameter is defined by: $NA4 = \frac{N\sum_{i=1}^{N}(\Delta r_i - \bar{r})^4}{(\frac{1}{M}\sum_{j=1}^{M}\sum_{i=1}^{N}(\Delta r_{ij} - \bar{r}_j)^2)^2}$ where r_i is the i-th point in the time record of the residual signal, r_{ij} is the i-th point in the j-th time record of the residual signal, j is the current time record, i is the data point number per reading, M is the current time record in the run ensemble, and N is the number of points in the time record. When gear damage progresses the averaged variance value increases rapidly, which results in a decrease of the NA4 parameter. To overcome this problem the NA4* parameter was introduced.
NA4*	The fourth centralized moment of the residual signal is normalized with the average variance for a gearbox in good condition. This allows the NA4* parameter to grow as the damage progresses. $NA4* = \frac{N\sum_{i=1}^{N}(\Delta r_i - \bar{r})^4}{(var(r_{OK}))^2}$ The value $var(r_{OK})$ is the variance for a gearbox in good condition. The value of the signal for a gearbox in good condition is usually assumed from the variance for a well-functioning gearbox.

Table B.2: Fault Detection Algorithms (continued)

CI	Description
NB4 Parameter	The NB4 [22] parameter is designed from the NA4 parameter. NA4 is computed from the residual signal whilstNB4 is computed from the envelope signal. The computation procedure follows. A raw vibration signal is bandpass filtered about the gear meshing frequency. Each recommendation for the bandwidth is different. Some authors suggest using a band pass filter with the bandwidth giving the maximum amount of the sidebands, whilst others use a filter with the bandwidth limited by the first harmonic different from the gear mesh frequency. After the unwanted part of signal has been filtered out, the Hilbert transform (Eq.12) is used to create an analytic signal $H[a(t)] = \tilde{t} = \frac{1}{\pi}\int_{-\infty}^{\infty} a(\tau)\cdot\frac{1}{t-\tau}\,d\tau$ Where $a(t)$ is the Hilbert transform, $a(\tau)$ is the input real analog signal. From the analytic signal the envelope is simply calculated according to Eq. 13. The result is the input for the NA4 parameter. $\lvert\tilde{a}(t)\rvert = \sqrt{a^2(t)+\tilde{a}^2(t)}$ where $\lvert\tilde{a}(t)\rvert$ is the envelope of the analytic signal, $a(t)$ is the input analog signal, and $\tilde{a}$ is the Hilbert transform of the input signal.
M6A and M8A	M6A and M8A were proposed by Martin [6] to detect surface damage on machinery components. Both of these features are applied to the difference signal. The theory behind M6A and M8A is the same as that for FM4, except that M6A and M8A are expected to be more sensitive to peaks in the difference signal. The equations for M6A and M8A are as follows: $M6A = \frac{N^2\sum_{i=1}^{N}(\Delta d_i-\bar{d})^6}{(\sum_{i=1}^{N}(\Delta d_i-\bar{d})^2)^3}$ and $M6A = \frac{N^3\sum_{i=1}^{N}(\Delta d_i-\bar{d})^8}{(\sum_{i=1}^{N}(\Delta d_i-\bar{d})^2)^4}$
NP4	The NP4 is the normalized kurtosis of the instantaneous signal power given as $NP4(n) = \frac{1}{N}\sum_{i=1}^{N}(\frac{P_n(t_i)-\overline{P_n}}{\sigma})^4 - 3$ where $P_n(t)$ is the signal power and n represents the number of gear mesh harmonics removed in the residual measured signal. If the two parameters, $NP4(0)$ and $NP4(1)$ are greater that some positive threshold number, it would indicate damage.
CAL4	The Constrained Adaptive Lifting metric, developed by Samuel and Pines, uses the prediction error between a model developed from healthy gears and the data taken from current gears as a metric to determine damage [41]. The adaptive lifting scheme was modified by constraining certain basis characteristics because this technique alone was too flexible to be reliable. In particular a subset of bases within the dictionary were used with the goal of dividing the individual tooth mesh waveform into monotonic waveforms and approximated by low order spline functions. Thus, if damage is present, it will manifest itself as higher order features, thus producing large prediction errors. The model for the healthy system is created off-line using the lowest order spline approximation that produces a sufficiently small prediction error and the adaptation ceases after model development. For subsequent measurements, each waveform will produce a vector of prediction error values associated with each monotonic region. The metric is quantified using the normalized kurtosis of the prediction error vector for the whole gear $\mathbf{R}$: CAL4 $= \frac{N\Sigma_{i=1}^{N}(\mathbf{R}_i-\overline{\mathbf{R}})^4}{\left[\Sigma_{i=1}^{N}(\mathbf{R}_i-\overline{\mathbf{R}})^2\right]^2}$.

Table B.3: Fault Detection Algorithms (continued)

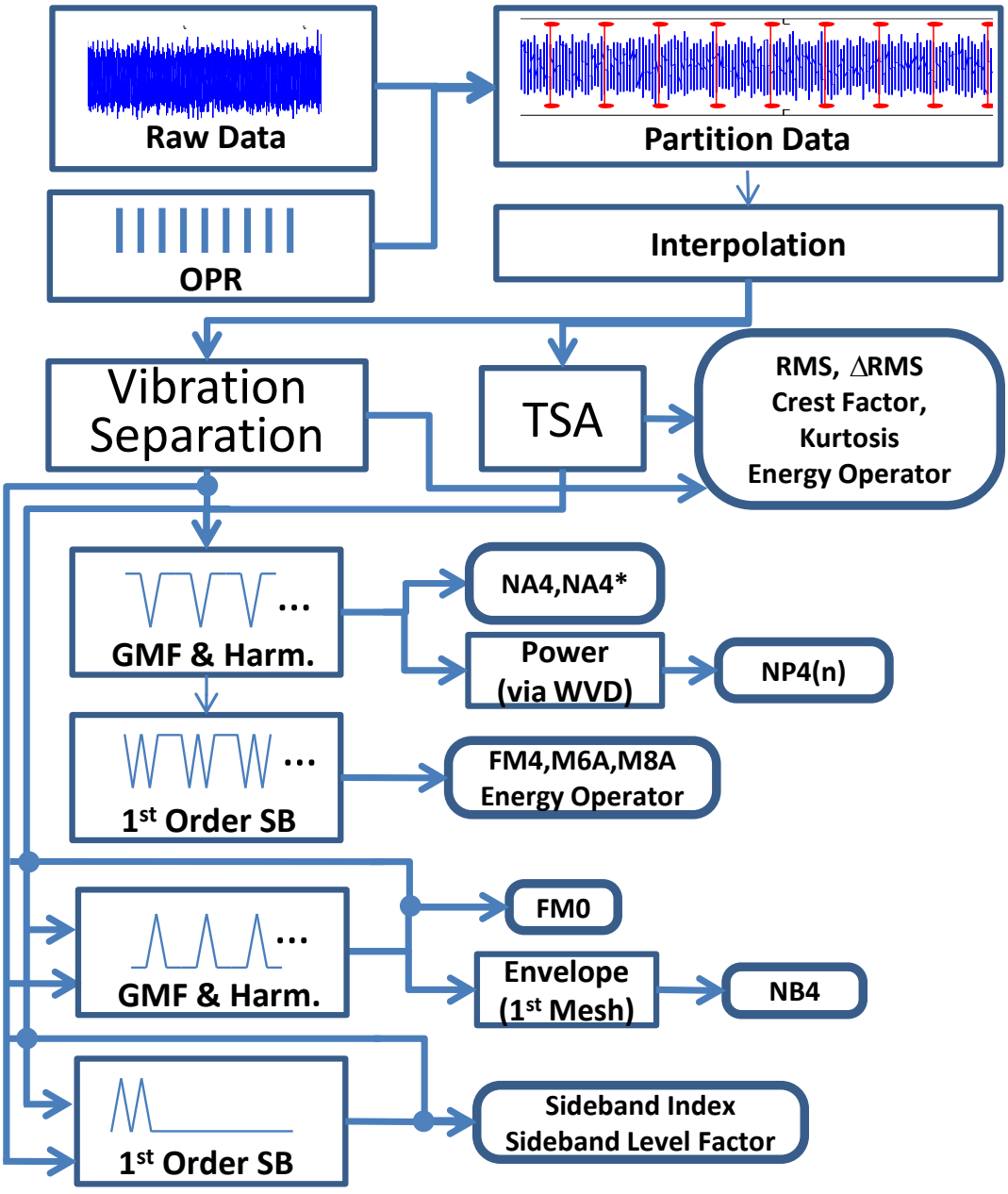

Figure B.1: CI Flowchart

Appendix C

Transmission Assembly and Disassembly

There are several things to consider to ensure that the transmission maintains its orientation between overhauls.

1. After running a test, the system was slowed down so that it could be turned off when the Daytronic counter reached zero and the planetary assembly returned to its initial orientation. This is illustrated in Figure C.1. The tachometer moves slightly beyond the edge of the marker tape and is repositioned by reversing the rotation slightly by hand until the tachometer aligns with the edge. Vertical markers on the rotating shaft and a fixed retainer were also used to lock this orientation.

2. After the tachometer is correctly positioned, the input shaft can be locked in place, as shown in Figure C.2. This step is very important to ensure that the bevel pinion, bevel gear, and the splined sun gear do not rotate upon disassembly. Since the ring gear is also locked by the transmission cover, locking the input locks the whole transmission, ensuring that there will be no movement as the transmission is transported from its testing location to its disassembly location.

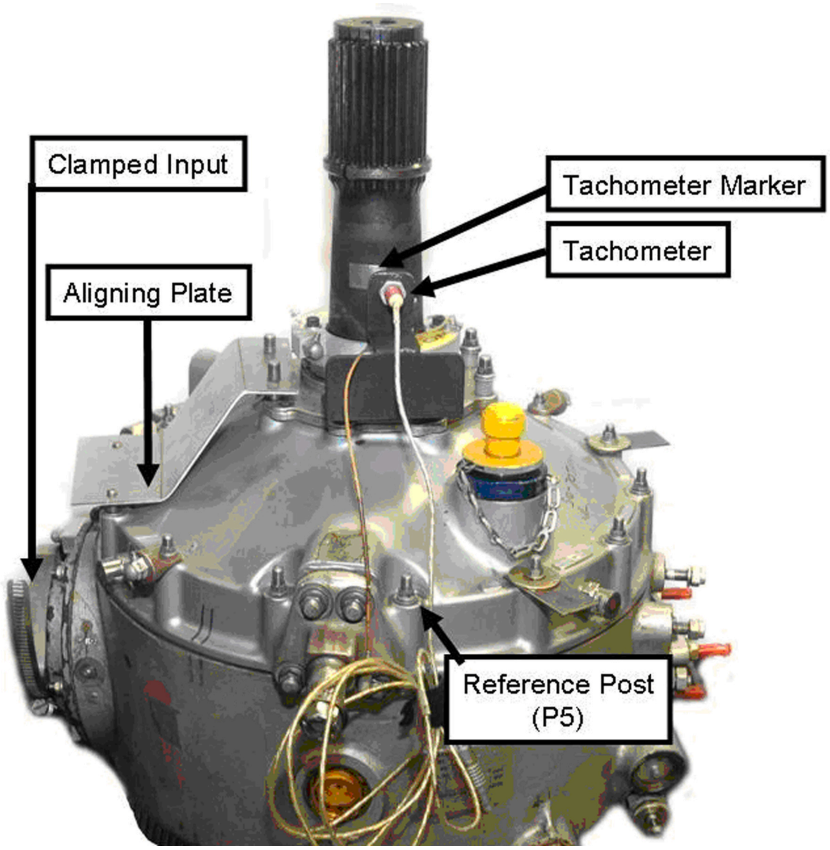

Figure C.1: Alignment

3. Before the cover can be removed, the shaft has to be removed from its spline position with the carrier. In order to ensure that the shaft is re-positioned into the correct carrier spline once the cover is removed, it was necessary to create a tool that allowed for the correct spline position to be verified. This tool, made of sheet metal, was bent and holes placed in it such that the fixed transmission posts 1 and 2 aligned with a set of retainer bolts. This is shown in Figure C.1. Since the shaft can rotate with respect to the retainer, once the retainer is aligned with the transmission using this tool, the correct spline was such that shaft marker and retainer markers aligned. Now that the gears were exposed,

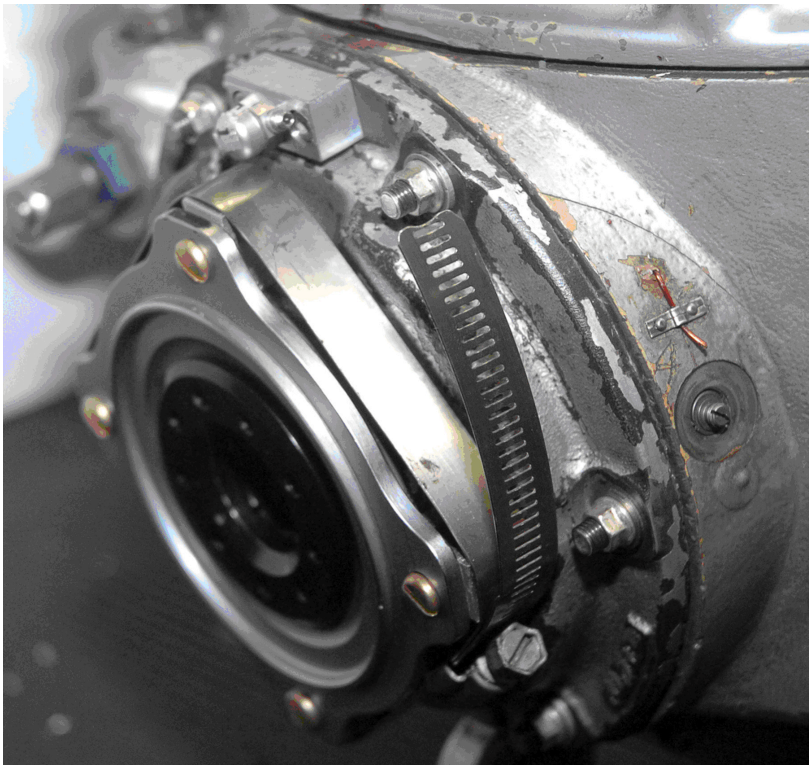

Figure C.2: Shaft Locking Mechanism

positioning markers were etched into the parts. For each of the four planets, three teeth were identified as being in mesh with the ring gear. As shown in Figure C.3, three markers were etched into the side of the planet teeth as well as in the ring.

Note: Once the cover is removed, the ring gear is unrestrained, and it, as well as the each planet, it free to rotate. Care was taken when the original markers were made that the ring gear and planets did not rotate much (at most one ring pitch). Once the shaft was correctly aligned, the ring gear and planets moved back to their original positions. This was verified by purposely

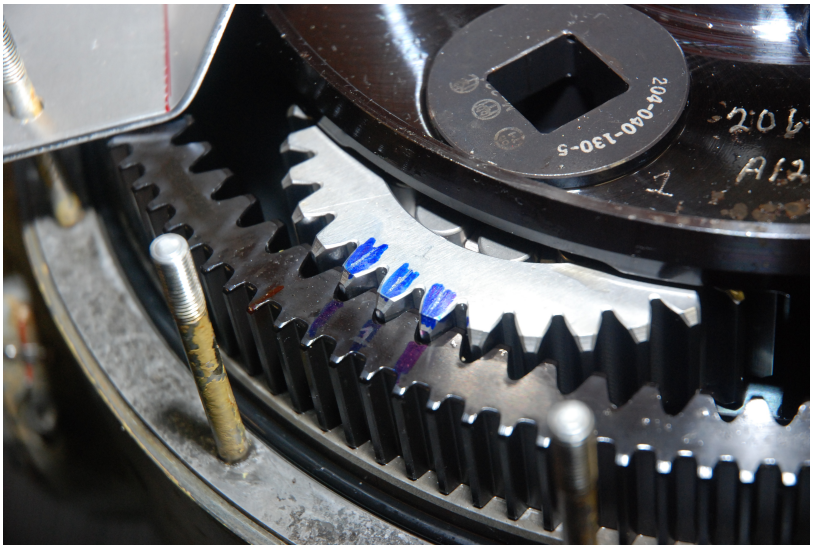

Figure C.3: Tooth Identification

placing the output shaft into adjacent carrier spline locations and then aligning the shaft/retainer/transmission. The final ring gear position was such that it rotated about four ring teeth, either clockwise or counter-clockwise. It is believed that this level of inadvertent shifting of the ring was not achieved during disassembly giving confidence that the marked position of the ring gear is correct.

4. Figure C.4 shows the alignment of the output shaft's tachometer. The fifth transmission stud (P5), counting counter-clockwise from the stud above the input bevel, was used as the fixed transmission reference point for the tachometer. This is because the bracket for mounting the tachometer uses two retainer plate studs and the tachometer's location is in the center of the bracket. Since the center of the two studs aligns with P5, the tachometer also aligns with P5. Therefore, P5 provides a convenient reference point. The ring gear is also

marked with respect to this post.

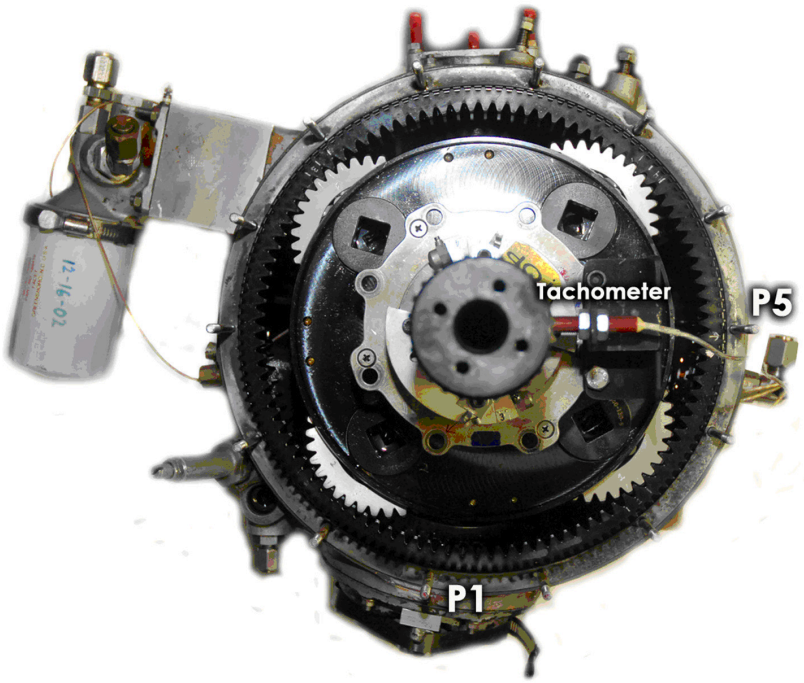

Figure C.4: Overhead Photo of Open Transmission

5. Another requirement is that the sun gear is splined with the bevel gear in the same orientation. Since the number of spline and the number of teeth differ, their pitches differ, which means that if the sun is placed inside the bevel gear randomly, there is a good chance that the sun tooth orientation will not match that of the original sun gear. This has the effect of modifying the orientation of the sun gears in order to properly mesh and slide the carrier over the sun gear. This, in turn, modifies the meshing position between the planet and ring gear. The misalignment is not great and depends on the bevel gear spline chosen.

However, the goal is to match the original alignment as closely as possible. The sun gear has 27 teeth and 30 splines, giving a ratio of 9 teeth for every 10 splines. Therefore, the spline/tooth pattern repeats every 120 degrees. What is needed is a way to identify a reference tooth. A method was developed to be able to match sun gears by locating a reference tooth. A squaring tool with a 1/16" thick rule was used. The rule was placed in the root of each tooth and its alignment with the land of the spline was assessed, as shown in Figure C.5.

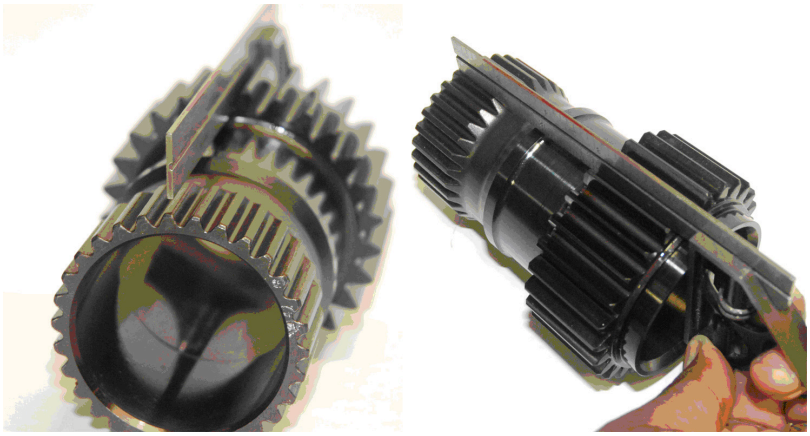

Figure C.5: Aligning the Sun Gear

As shown in Figure C.6, markers were placed at locations for which the rule aligned with the land. This method verified the 120-degree pattern of the splines. Before the original sun gear was removed, the tooth that best aligned with the tachometer (based on post 5) was etched with an arrow. This reference tooth was three teeth counter-clockwise to the splines identified by the aforementioned method. Therefore, all subsequent sun teeth will use this same

reference gear tooth. **Note:** due to symmetry, there are 3 valid choices. The one chosen is the one that will keep the damaged portion of the sun gear farthest from the tack pulse so that in the signal, there is adequate data points before and after the signal. It would not be ideal to have the damaged portion of the signal being in either the beginning of the cycle or at the end of the cycle.

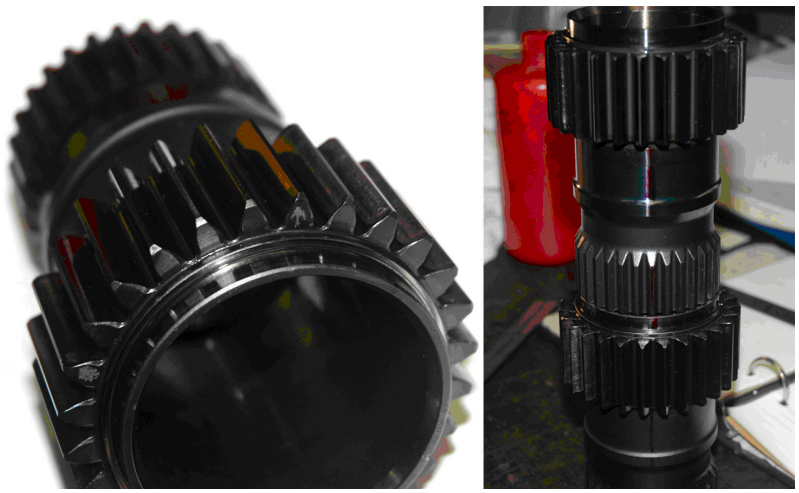

Figure C.6: CarrierHousing

6. When re-inserting the carrier and ring into the transmission housing, it is easiest to first align the planet teeth with the ring on a workbench as shown in Figure C.7.

This makes it much easier to drop the assembly into the transmission preserving the correct orientation. The correct placement of the assembly is when the

Figure C.7: Carrier Housing

etched arrow on the ring gear is aligned with P5 of the transmission as shown in the Figure C.8.

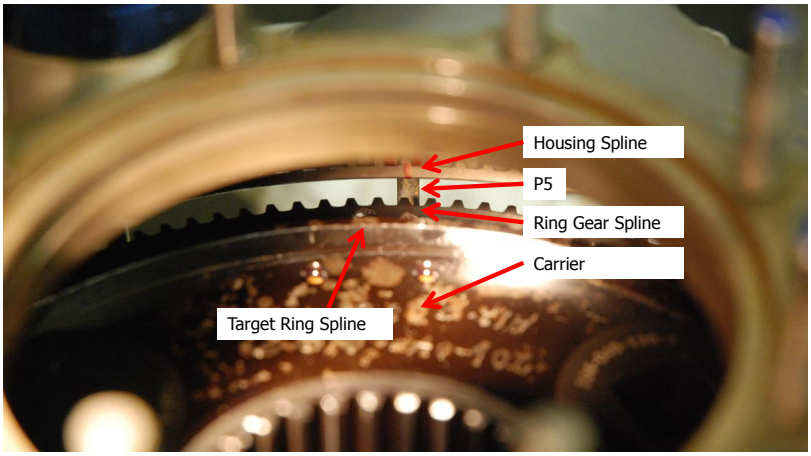

Figure C.8: Aligning Closeup

Appendix D

Condition Indicator Results: **TSA** Data

Condition Indicators using Vibration TSA data (OH-58C)												
	CI Values				Ratio to Baseline							
Accel:1	**B1**	**B2**	**B3**	**B4**	**M1**	**M2**	**M3**	**M4**	**H1**	**H2**	**H3**	**H4**
RMS	0.05	0.04	0.07	0.06	0.98	0.93	0.87	0.76	1.10	0.84	0.99	0.96
CF	2.76	3.61	2.78	3.38	0.97	1.00	1.08	1.28	1.21	1.11	1.21	1.01
ER	0.36	0.40	0.36	0.44	0.93	1.09	1.06	1.39	2.00	2.70	2.00	1.92
FM0	1.55	1.35	1.42	1.27	1.07	1.07	1.15	1.13	1.58	1.96	1.54	1.73
Kurt.	2.23	2.65	2.70	2.95	0.99	1.02	0.89	1.01	1.28	1.23	1.08	1.21
EO	3.95	7.41	6.30	7.83	1.03	0.91	0.72	1.12	2.30	1.82	1.05	2.01
FM4	3.14	2.91	2.99	3.11	0.95	1.13	1.07	1.09	1.27	1.40	1.28	1.35
M6A	16.68	13.61	15.91	17.01	0.87	1.56	1.19	1.26	1.82	2.49	2.08	2.39
M8A	125.83	85.08	131.85	135.87	0.77	2.62	1.26	1.47	2.64	5.00	3.72	4.78
NB4	2.03	1.85	1.81	1.88	1.06	1.06	1.02	1.00	0.94	1.00	1.16	1.12
NA4	3.22	2.88	2.98	2.87	0.98	1.08	1.08	1.13	1.22	1.39	1.29	1.40
Accel:2	**B1**	**B2**	**B3**	**B4**	**M1**	**M2**	**M3**	**M4**	**H1**	**H2**	**H3**	**H4**
RMS	0.04	0.03	0.05	0.06	1.03	1.07	0.94	0.86	1.24	1.02	1.07	1.06
CF	2.71	3.76	4.25	3.63	1.00	1.12	0.79	1.08	1.52	0.93	0.76	1.07
ER	0.33	0.43	0.40	0.45	1.02	1.16	1.23	1.10	2.11	2.48	2.06	1.73
FM0	1.44	1.44	1.55	1.54	1.18	1.22	1.04	0.97	2.04	1.65	1.36	1.39
Kurt.	2.31	3.21	2.82	3.11	1.10	1.13	0.99	0.92	1.24	1.02	1.11	1.07
EO	4.22	11.40	11.34	7.95	1.28	1.74	0.83	1.65	3.47	1.85	1.03	1.86
FM4	3.13	3.48	3.06	3.34	0.91	1.09	1.14	1.06	1.59	1.19	1.58	1.25
M6A	19.55	26.10	15.54	21.12	0.68	1.21	1.62	1.31	3.16	1.33	3.53	1.67
M8A	223.27	352.47	106.61	208.57	0.38	1.24	2.79	1.96	6.47	1.19	9.11	2.17
NB4	1.87	1.84	1.95	2.09	1.12	1.06	1.02	0.96	0.99	1.08	1.10	1.04
NA4	3.25	3.28	3.04	3.27	0.96	1.11	1.11	0.97	1.54	1.20	1.48	1.20
Accel:3	**B1**	**B2**	**B3**	**B4**	**M1**	**M2**	**M3**	**M4**	**H1**	**H2**	**H3**	**H4**
RMS	0.09	0.06	0.09	0.09	1.00	1.11	1.02	0.90	0.97	1.01	1.09	1.02
CF	2.52	4.13	3.93	3.95	1.21	0.68	0.74	0.89	1.30	0.93	0.88	0.95
ER	0.24	0.42	0.33	0.42	0.88	0.93	1.09	1.16	2.37	1.65	1.62	1.73
FM0	1.75	1.58	1.87	1.43	1.23	0.91	0.86	1.06	1.43	1.38	1.18	1.36
Kurt.	2.25	3.17	3.02	3.36	0.95	0.87	0.85	1.00	1.18	0.96	0.94	1.05
EO	2.46	14.10	11.27	17.75	1.94	0.40	0.44	0.84	2.31	1.05	0.73	0.78
FM4	2.91	3.07	3.00	2.95	1.10	1.02	1.12	1.16	1.51	1.30	1.33	1.27
M6A	14.34	15.95	15.05	14.02	1.21	1.24	1.45	1.64	2.99	1.90	2.21	2.03
M8A	101.15	115.78	107.98	89.47	1.24	1.95	2.04	2.67	6.33	2.74	3.89	3.73
NB4	2.05	1.99	2.05	2.09	1.03	0.99	0.96	0.96	0.95	0.99	0.97	0.99
NA4	2.96	2.93	2.91	3.10	1.11	1.05	1.12	1.09	1.46	1.30	1.27	1.23
Accel:4	**B1**	**B2**	**B3**	**B4**	**M1**	**M2**	**M3**	**M4**	**H1**	**H2**	**H3**	**H4**
RMS	0.02	0.03	0.05	0.06	1.05	1.13	1.07	0.96	1.60	1.10	1.23	1.06
CF	3.02	3.92	3.74	4.46	1.32	1.02	1.10	0.92	1.64	1.11	1.10	0.87
ER	0.47	0.44	0.50	0.56	0.96	0.95	0.93	0.83	2.61	2.06	1.60	1.32
FM0	1.34	1.45	1.59	1.73	1.15	1.06	1.04	0.90	2.19	1.86	1.45	1.22
Kurt.	2.99	3.32	3.46	3.57	1.15	1.08	1.01	0.89	1.77	1.08	1.06	0.98
EO	8.90	16.21	27.83	35.61	1.26	1.05	1.04	0.61	5.18	4.69	1.19	0.61
FM4	3.00	3.07	3.34	3.80	1.02	1.13	1.01	0.89	2.14	1.82	2.09	1.43
M6A	14.57	15.64	19.65	30.45	1.07	1.54	1.14	0.70	6.01	4.67	6.84	2.67
M8A	94.54	106.95	161.49	387.11	1.16	2.47	1.50	0.52	17.30	13.34	24.11	4.99
NB4	1.95	1.87	1.93	2.04	1.15	1.05	0.98	0.94	1.00	1.03	1.02	1.00
NA4	2.99	3.18	3.51	3.75	1.01	1.06	1.02	0.89	2.07	1.70	1.97	1.37
Accel:5	**B1**	**B2**	**B3**	**B4**	**M1**	**M2**	**M3**	**M4**	**H1**	**H2**	**H3**	**H4**
RMS	0.04	0.05	0.07	0.09	1.31	1.16	1.16	0.98	1.47	1.01	1.25	0.98
CF	3.47	3.10	3.96	3.20	0.97	1.22	1.01	1.11	1.46	1.44	1.09	1.13
ER	0.58	0.47	0.48	0.46	0.76	0.91	0.88	0.99	1.95	1.86	1.42	1.51
FM0	1.43	1.24	1.30	1.47	1.05	1.11	1.13	0.94	2.03	1.79	1.68	1.30
Kurt.	2.89	2.87	3.23	3.35	0.83	1.02	0.97	0.90	1.52	1.15	0.96	1.00
EO	8.97	8.17	9.55	15.26	0.48	0.84	0.71	0.84	3.10	3.05	1.46	0.70
FM4	2.90	2.94	2.78	3.02	0.95	1.09	1.07	1.03	1.75	1.49	1.72	1.43
M6A	13.33	14.53	11.95	15.90	0.92	1.25	1.20	1.01	4.37	2.70	4.64	2.93
M8A	80.35	100.68	66.83	123.28	0.93	1.48	1.40	0.89	12.36	5.11	14.72	6.76
NB4	1.96	1.94	2.01	2.16	1.10	1.02	0.98	0.93	1.00	1.03	1.01	0.99
NA4	3.00	2.97	2.92	3.01	0.96	1.05	0.99	1.00	1.72	1.42	1.59	1.34

Table D.1: Condition Indicators using Vibration TSA data (OH-58C)

Condition Indicators using Vibration TSA data (OH-58A)								
	CI Values				Ratio to Baseline			
Accel:1	**B1**	**B2**	**B3**	**B4**	**H1**	**H2**	**H3**	**H4**
RMS	0.04	0.04	0.07	0.06	1.27	1.19	1.09	1.01
CF	2.53	3.30	3.39	3.42	1.02	0.90	0.93	1.09
ER	0.33	0.37	0.30	0.44	0.81	0.83	0.91	0.98
FM0	1.98	1.53	1.66	1.33	1.09	0.94	0.98	1.05
Kurt.	2.28	2.72	2.63	3.51	0.84	0.87	0.93	0.95
EO	5.17	11.32	10.51	8.43	0.79	0.53	0.64	1.05
FM4	3.02	3.85	3.32	3.33	0.99	0.87	0.98	0.97
M6A	16.42	34.62	20.91	19.71	0.91	0.57	0.95	1.01
M8A	138.28	605.24	210.84	165.01	0.75	0.27	0.94	1.28
NB4	2.34	1.98	2.03	2.45	0.99	1.19	1.15	0.93
NA4	2.78	3.51	3.18	3.26	1.01	0.84	1.00	0.98
Accel:2	**B1**	**B2**	**B3**	**B4**	**H1**	**H2**	**H3**	**H4**
RMS	0.03	0.03	0.05	0.05	1.35	1.13	1.14	1.03
CF	3.38	4.34	5.38	5.88	0.89	1.25	1.22	0.95
ER	0.34	0.59	0.47	0.56	0.90	0.86	0.88	0.97
FM0	2.21	1.97	2.05	2.07	1.08	1.01	1.20	0.88
Kurt.	2.28	5.26	4.55	4.53	0.98	0.82	0.90	0.92
EO	5.73	40.91	39.47	48.71	0.74	0.81	2.45	0.92
FM4	3.62	5.21	5.84	5.34	0.94	0.89	1.05	1.02
M6A	28.54	71.60	87.09	75.64	0.87	0.76	1.35	1.01
M8A	397.09	1581.70	2004.08	1807.29	0.83	0.68	2.02	0.94
NB4	2.77	2.69	2.78	2.39	0.94	0.92	0.80	0.97
NA4	3.21	4.99	6.11	5.33	0.88	0.86	0.98	1.00
Accel:3	**B1**	**B2**	**B3**	**B4**	**H1**	**H2**	**H3**	**H4**
RMS	0.06	0.04	0.09	0.08	0.89	1.06	0.96	1.11
CF	2.70	4.26	4.40	3.91	1.16	1.16	1.07	0.97
ER	0.26	0.56	0.40	0.48	0.98	0.85	0.94	0.93
FM0	1.92	1.66	1.73	1.43	1.05	1.16	0.96	0.99
Kurt.	2.01	3.43	2.91	3.47	1.13	1.05	1.10	0.90
EO	3.24	22.17	16.38	11.89	1.16	1.30	1.21	0.90
FM4	3.74	4.23	3.56	3.67	0.95	1.11	1.04	1.07
M6A	31.73	75.43	23.35	27.25	0.78	0.89	1.16	1.48
M8A	528.40	3926.36	231.59	319.57	0.52	0.49	1.36	2.74
NB4	2.54	2.52	2.42	2.45	0.96	0.90	1.09	1.08
NA4	3.20	3.79	3.39	3.44	1.01	1.13	1.06	0.98
Accel:4	**B1**	**B2**	**B3**	**B4**	**H1**	**H2**	**H3**	**H4**
RMS	0.02	0.03	0.05	0.06	1.02	1.00	1.04	1.03
CF	3.90	4.17	5.78	5.41	0.91	0.86	0.98	0.95
ER	0.46	0.55	0.50	0.45	1.07	0.98	0.88	1.00
FM0	2.04	1.75	1.93	1.92	0.88	0.96	0.91	0.93
Kurt.	3.48	4.13	5.04	5.36	0.94	0.95	0.77	0.97
EO	42.05	39.05	41.44	24.46	0.33	1.08	0.93	1.47
FM4	4.19	5.49	5.13	4.08	1.01	0.86	0.86	1.12
M6A	44.54	89.73	66.45	36.10	1.33	0.64	0.63	1.96
M8A	843.46	2396.15	1373.37	513.47	2.25	0.49	0.44	5.23
NB4	3.43	3.25	2.89	2.96	1.07	0.90	1.07	1.05
NA4	3.90	5.41	4.89	3.72	0.96	0.92	0.90	1.08
Accel:5	**B1**	**B2**	**B3**	**B4**	**H1**	**H2**	**H3**	**H4**
RMS	0.06	0.05	0.09	0.09	0.87	1.08	0.98	0.95
CF	2.68	4.41	3.42	3.13	1.08	0.75	1.00	1.12
ER	0.31	0.47	0.36	0.42	1.06	0.84	0.96	0.98
FM0	1.89	1.73	1.52	1.40	0.98	0.82	0.92	0.96
Kurt.	2.27	3.81	2.85	2.97	1.04	0.77	0.98	1.04
EO	3.85	15.62	8.02	8.74	1.12	0.45	0.83	1.07
FM4	3.37	3.58	3.41	3.25	0.92	1.00	0.94	1.00
M6A	21.93	26.28	21.44	18.49	0.80	0.94	0.89	1.03
M8A	214.90	328.36	198.36	155.62	0.74	0.80	0.87	1.13
NB4	3.32	3.07	2.76	2.77	1.05	0.89	1.11	1.03
NA4	3.50	3.39	3.34	3.20	0.89	0.98	0.98	0.95

Table D.2: Condition Indicators using Vibration TSA data (OH-58A)

Appendix E

Condition Indicator Results: **PGVS**

Condition Indicators (OH-58C): PGVS P_3												
	CI Values				Ratio to Baseline							
Accel:1	**B1**	**B2**	**B3**	**B4**	**M1**	**M2**	**M3**	**M4**	**H1**	**H2**	**H3**	**H4**
RMS	18.17	29.03	29.77	32.07	2.41	1.81	2.20	1.85	2.27	1.31	2.05	2.64
CF	2.51	2.19	2.22	1.82	0.80	1.05	1.00	1.18	1.05	1.27	1.19	0.95
ER	0.22	0.11	0.10	0.07	0.33	0.74	1.09	1.06	0.39	2.05	0.72	0.64
FM0	2.49	2.33	2.75	2.39	1.01	0.97	0.83	1.10	1.07	1.11	0.84	0.98
Kurt.	2.58	2.30	2.45	2.71	1.12	1.07	0.96	0.92	1.29	1.61	1.29	0.83
EO	3.33	1.69	2.43	2.58	0.69	1.47	1.08	1.04	1.02	2.53	1.11	0.89
FM4	1.90	2.46	2.77	3.74	1.48	1.28	0.82	0.76	1.75	0.77	1.08	1.14
M6A	4.74	9.13	15.23	27.71	2.59	1.83	0.53	0.47	4.12	0.53	0.97	1.31
M8A	14.08	43.39	133.26	317.89	4.97	2.70	0.30	0.27	11.22	0.36	0.71	1.38
NB4	1.94	1.95	1.94	1.94	1.00	1.00	1.00	1.00	1.00	0.99	1.00	1.00
NA4	1.99	2.50	2.87	3.93	1.37	1.33	0.80	0.75	1.66	0.77	1.07	1.11
Accel:2	**B1**	**B2**	**B3**	**B4**	**M1**	**M2**	**M3**	**M4**	**H1**	**H2**	**H3**	**H4**
RMS	15.32	24.23	28.46	39.52	2.36	2.06	2.14	1.82	2.41	1.82	2.24	2.25
CF	2.69	2.61	2.14	2.05	0.80	0.81	0.91	0.90	0.97	1.01	0.95	0.88
ER	0.13	0.07	0.07	0.06	0.58	0.82	0.79	0.86	0.50	1.07	0.78	0.69
FM0	2.48	2.35	2.43	2.38	1.09	1.04	1.10	1.11	0.96	1.10	1.04	1.13
Kurt.	2.39	2.50	3.38	3.23	1.46	0.89	0.89	1.07	1.09	1.21	0.98	1.03
EO	6.07	3.84	2.70	2.68	0.56	0.94	1.89	1.76	0.45	0.93	1.51	1.63
FM4	2.50	3.76	3.50	3.72	1.65	0.80	1.13	1.17	1.52	0.95	1.61	1.79
M6A	9.39	24.20	23.00	25.10	3.70	0.58	1.58	1.69	3.26	1.18	3.76	5.41
M8A	45.87	203.40	233.27	238.58	9.14	0.41	2.42	2.51	8.62	1.79	8.85	17.12
NB4	1.94	1.95	1.93	1.94	1.00	1.00	1.00	1.00	1.00	0.99	1.00	1.00
NA4	2.72	3.85	3.85	4.00	1.38	0.82	1.00	1.06	1.27	0.95	1.36	1.49
Accel:3	**B1**	**B2**	**B3**	**B4**	**M1**	**M2**	**M3**	**M4**	**H1**	**H2**	**H3**	**H4**
RMS	17.76	42.22	51.81	76.31	2.80	1.78	1.61	1.49	4.15	2.02	1.87	1.79
CF	2.47	2.55	2.55	2.39	0.91	0.60	0.71	0.94	0.60	0.76	0.54	0.84
ER	0.23	0.10	0.07	0.06	0.48	0.86	1.07	0.97	0.34	1.14	0.97	0.91
FM0	2.34	2.45	2.35	2.75	1.07	0.85	1.10	1.00	0.87	1.07	1.03	1.00
Kurt.	2.27	2.60	2.84	2.80	1.00	0.64	0.75	1.15	0.95	1.14	1.54	1.15
EO	4.11	2.19	2.49	2.25	1.38	1.14	1.07	1.02	0.59	1.84	2.18	1.05
FM4	2.39	2.72	3.87	4.02	1.31	1.06	0.72	0.89	1.33	0.98	0.85	1.30
M6A	8.46	10.75	31.87	33.54	2.17	1.29	0.39	0.73	2.30	1.05	0.56	1.83
M8A	37.56	51.81	405.13	437.71	4.62	1.76	0.18	0.56	4.87	1.24	0.30	2.41
NB4	1.93	1.94	1.94	1.94	1.01	1.00	1.00	1.00	1.00	0.99	1.00	1.00
NA4	2.44	2.98	3.99	4.14	1.34	1.00	0.72	0.83	1.31	0.90	0.81	1.25
Accel:4	**B1**	**B2**	**B3**	**B4**	**M1**	**M2**	**M3**	**M4**	**H1**	**H2**	**H3**	**H4**
RMS	18.81	41.05	50.89	50.63	2.84	2.23	2.08	2.05	3.81	2.20	2.31	1.93
CF	2.53	1.97	2.17	2.13	1.10	1.28	0.95	0.94	0.80	0.96	1.16	1.08
ER	0.11	0.06	0.06	0.06	0.61	0.86	0.86	0.75	0.49	0.81	0.65	0.81
FM0	2.37	2.66	2.61	2.20	1.00	0.83	0.94	1.21	1.02	0.89	0.93	1.06
Kurt.	2.51	2.27	2.41	2.48	1.43	1.20	0.94	0.92	1.00	0.97	1.17	0.95
EO	3.38	1.92	2.72	1.98	1.39	2.36	0.62	1.41	0.77	1.63	0.90	0.99
FM4	3.06	4.63	5.93	5.92	1.35	1.40	0.81	0.96	1.38	0.86	1.17	1.03
M6A	15.81	42.10	66.34	76.53	1.98	2.27	0.70	0.94	2.20	0.93	1.63	0.98
M8A	110.09	511.48	931.95	1328.26	2.86	3.75	0.64	0.97	3.56	1.16	2.34	0.89
NB4	1.93	1.93	1.94	1.94	1.00	1.00	1.00	1.00	1.00	1.00	1.00	1.00
NA4	3.11	4.63	5.65	5.54	1.36	1.24	0.93	0.94	1.27	0.90	1.15	1.10
Accel:5	**B1**	**B2**	**B3**	**B4**	**M1**	**M2**	**M3**	**M4**	**H1**	**H2**	**H3**	**H4**
RMS	20.08	38.82	48.99	60.98	2.87	2.21	2.07	1.63	3.99	2.21	2.29	1.63
CF	2.65	1.94	2.28	2.35	0.95	1.27	0.87	0.98	0.94	0.96	1.02	0.83
ER	0.14	0.07	0.07	0.06	0.57	0.83	0.75	0.84	0.48	0.94	0.67	0.90
FM0	2.17	2.44	2.59	2.15	0.97	0.94	0.89	1.24	1.17	0.99	0.93	0.99
Kurt.	2.50	2.29	2.37	2.35	1.06	1.09	0.91	1.20	1.31	1.06	1.00	0.89
EO	3.18	1.82	2.28	2.20	1.06	2.84	0.94	1.60	1.14	1.35	1.02	1.07
FM4	2.99	3.98	5.18	5.72	1.53	1.10	0.96	1.35	1.68	0.78	0.91	1.12
M6A	16.22	32.03	57.25	67.73	3.16	1.40	0.94	2.46	3.54	0.55	0.77	1.52
M8A	132.90	380.60	840.77	1048.36	6.65	1.88	1.00	4.66	7.23	0.37	0.64	2.22
NB4	1.93	1.94	1.94	1.94	1.00	1.00	1.00	1.00	1.00	0.99	1.00	0.99
NA4	3.08	3.80	4.53	5.19	1.53	1.09	1.04	1.32	1.61	0.82	0.96	1.25

Table E.1: Condition Indicators (OH-58C): PGVS P_3

Condition Indicators (OH-58A): PGVS P_3								
	CI Values				Ratio to Baseline			
Accel:1	**B1**	**B2**	**B3**	**B4**	**H1**	**H2**	**H3**	**H4**
RMS	17.60	18.42	22.54	54.60	0.91	1.52	1.11	0.83
CF	1.87	2.17	2.98	2.13	1.14	0.77	0.60	1.13
ER	0.23	0.25	0.60	0.07	0.89	0.62	0.28	1.20
FM0	2.44	2.49	2.81	2.40	0.99	1.00	0.87	1.02
Kurt.	1.95	2.48	2.65	2.44	1.13	1.26	1.31	1.15
EO	4.43	4.76	3.13	1.70	0.81	0.92	2.45	1.21
FM4	2.49	2.47	1.70	6.10	1.12	1.20	1.69	0.93
M6A	8.78	8.98	3.52	107.12	1.45	1.62	3.70	0.73
M8A	38.21	41.56	8.30	2934.72	2.15	2.30	9.17	0.52
NB4	2.05	1.99	1.96	1.94	1.02	1.00	0.99	1.00
NA4	2.51	2.54	1.73	5.62	1.13	1.20	1.67	1.05
Accel:2	**B1**	**B2**	**B3**	**B4**	**H1**	**H2**	**H3**	**H4**
RMS	18.49	21.56	27.11	49.31	0.96	1.30	0.89	0.98
CF	2.37	2.99	2.72	2.68	1.15	0.92	1.12	0.86
ER	0.17	0.17	0.30	0.07	0.94	0.73	0.49	1.17
FM0	2.04	2.59	2.31	2.66	1.13	0.86	1.00	0.95
Kurt.	1.84	3.11	2.21	3.10	1.14	0.83	1.14	0.89
EO	3.45	5.88	3.34	2.41	1.31	0.79	2.25	0.98
FM4	2.78	2.75	2.06	5.75	1.07	1.28	1.86	0.92
M6A	12.00	11.41	6.19	87.24	1.22	1.99	5.06	0.63
M8A	68.15	59.94	25.02	1909.07	1.50	3.39	16.38	0.37
NB4	2.14	2.21	1.96	1.94	0.94	0.94	0.99	1.01
NA4	2.83	2.88	2.11	5.90	1.02	1.27	1.77	0.93
Accel:3	**B1**	**B2**	**B3**	**B4**	**H1**	**H2**	**H3**	**H4**
RMS	30.94	42.27	58.56	91.11	1.29	1.25	1.32	1.25
CF	2.34	1.97	1.85	2.17	0.92	1.14	1.26	0.96
ER	0.15	0.13	0.18	0.06	0.71	0.84	0.43	1.05
FM0	2.49	2.34	2.21	2.28	0.97	0.99	1.14	1.09
Kurt.	2.51	2.59	2.00	2.01	0.75	0.89	1.25	1.18
EO	2.09	2.34	2.58	6.04	1.29	1.98	1.23	0.28
FM4	2.98	2.77	2.07	4.62	1.15	1.06	2.28	1.37
M6A	16.65	12.49	5.90	43.34	1.24	1.17	9.24	2.11
M8A	139.79	77.94	20.70	556.36	1.20	1.39	48.06	3.10
NB4	2.17	2.04	1.96	1.95	0.99	0.95	0.99	1.02
NA4	2.95	2.81	2.25	4.45	1.17	1.07	1.98	1.38
Accel:4	**B1**	**B2**	**B3**	**B4**	**H1**	**H2**	**H3**	**H4**
RMS	32.87	38.87	54.31	53.18	0.86	1.10	1.19	0.86
CF	2.48	1.96	2.45	2.16	0.98	1.12	0.89	0.97
ER	0.10	0.11	0.17	0.07	0.99	0.91	0.42	1.24
FM0	2.88	2.05	2.38	2.51	0.94	0.99	1.00	1.08
Kurt.	2.20	2.22	2.67	2.53	0.83	0.92	1.03	1.46
EO	3.62	2.02	2.72	2.48	1.24	1.18	0.66	2.23
FM4	3.07	3.57	1.98	3.23	0.96	0.93	1.86	1.18
M6A	15.98	23.81	5.37	18.25	0.92	0.82	5.31	1.72
M8A	114.10	221.98	18.50	137.98	0.92	0.71	19.11	2.76
NB4	2.18	2.00	1.93	1.96	0.96	0.97	1.01	1.02
NA4	3.06	3.57	2.09	3.11	0.97	0.94	1.72	1.18
Accel:5	**B1**	**B2**	**B3**	**B4**	**H1**	**H2**	**H3**	**H4**
RMS	31.75	43.68	78.08	66.95	0.87	1.21	1.21	0.96
CF	2.08	2.38	2.17	2.18	1.25	0.95	1.17	1.02
ER	0.13	0.12	0.10	0.08	1.08	0.81	0.69	1.07
FM0	2.52	2.37	2.41	2.82	1.07	0.92	1.02	1.03
Kurt.	1.96	2.47	2.20	2.76	1.08	0.74	1.15	1.36
EO	1.94	3.46	3.22	2.54	1.70	0.77	0.88	1.50
FM4	3.21	3.48	3.18	3.33	0.88	1.01	1.68	1.16
M6A	18.64	20.82	17.20	22.23	0.74	1.01	4.52	1.54
M8A	159.77	166.49	125.91	228.11	0.62	1.01	14.40	2.23
NB4	2.28	1.95	1.95	1.99	0.88	1.00	1.00	1.00
NA4	3.20	3.55	3.52	2.98	0.94	0.97	1.36	1.36

Table E.2: Condition Indicators (OH-58A): PGVS P_3

Appendix F

Condition Indicator Results: **SGVS -SASP**

Condition Indicators (OH-58C):(SGVS-SASP): P_1/P_3												
	CI Values				Ratio to Baseline							
Accel:1	**B1**	**B2**	**B3**	**B4**	**M1**	**M2**	**M3**	**M4**	**H1**	**H2**	**H3**	**H4**
RMS	0.87	1.50	1.60	1.72	1.21	0.97	1.07	0.97	2.23	1.53	1.95	1.91
CF	2.79	2.84	3.12	3.01	0.98	1.10	0.91	1.02	1.69	1.62	1.43	1.31
ER	0.50	0.41	0.54	0.57	1.06	1.51	1.18	1.09	2.71	4.30	2.87	2.03
FM0	3.02	3.30	3.50	3.19	1.16	0.95	0.90	1.02	1.71	1.88	1.53	1.41
Kurt.	2.88	2.89	2.98	2.86	1.12	0.99	0.91	1.06	2.31	2.28	1.84	1.74
EO	144.88	4.16	11.39	7.77	0.07	16.40	21.04	20.45	0.22	13.88	2.50	3.65
FM4	2.75	3.27	3.08	3.12	1.10	1.00	1.03	1.11	2.17	1.91	1.76	1.64
M6A	12.25	18.04	17.29	16.56	1.27	1.04	1.03	1.32	5.76	4.83	3.80	3.19
M8A	75.68	133.44	141.97	123.17	1.47	1.16	0.97	1.61	14.61	12.56	7.93	5.86
NB4	1.94	1.94	1.94	1.94	1.00	1.00	1.00	1.00	1.12	1.12	1.06	1.07
NA4	2.80	3.21	3.20	3.15	1.17	1.03	1.01	1.12	2.41	2.11	1.77	1.64
Accel:2	**B1**	**B2**	**B3**	**B4**	**M1**	**M2**	**M3**	**M4**	**H1**	**H2**	**H3**	**H4**
RMS	0.78	1.12	1.46	1.95	1.23	1.30	1.17	0.97	2.54	2.09	1.99	1.62
CF	3.47	3.60	2.91	2.56	0.84	0.86	0.94	1.10	1.65	1.51	1.56	1.65
ER	0.53	0.52	0.57	0.47	0.85	1.06	1.14	1.29	2.73	2.92	2.32	2.33
FM0	3.18	3.33	2.88	2.56	1.11	1.04	1.05	1.16	2.45	2.19	1.99	1.87
Kurt.	2.83	3.09	2.82	2.63	1.26	0.88	1.04	1.10	5.24	3.14	2.39	1.87
EO	116.98	15.62	12.20	35.98	0.50	13.93	3.70	0.16	0.60	5.42	3.94	8.93
FM4	3.15	3.32	2.66	2.94	1.10	0.94	1.07	0.98	3.87	2.65	2.62	2.10
M6A	17.24	20.65	11.32	13.58	1.29	0.86	1.34	1.00	22.66	10.62	11.60	6.81
M8A	129.52	188.16	65.70	81.30	1.56	0.80	1.94	1.06	129.51	39.59	53.26	24.18
NB4	1.94	1.93	1.93	1.93	1.00	1.00	1.00	1.00	1.13	1.10	1.10	1.09
NA4	3.01	3.34	2.77	2.89	1.11	0.95	1.09	1.05	4.81	3.05	2.94	2.39
Accel:3	**B1**	**B2**	**B3**	**B4**	**M1**	**M2**	**M3**	**M4**	**H1**	**H2**	**H3**	**H4**
RMS	0.86	1.80	2.48	3.45	1.46	1.14	0.97	0.88	3.59	1.83	1.66	1.37
CF	2.45	3.36	3.43	2.93	1.46	0.83	0.81	1.09	2.30	1.43	1.38	1.11
ER	0.62	0.45	0.46	0.49	0.97	1.43	1.83	1.68	2.15	2.66	2.64	2.01
FM0	2.80	3.00	3.27	3.18	1.14	1.13	1.18	1.15	2.55	1.94	1.64	1.25
Kurt.	2.83	2.87	3.21	2.97	1.01	0.95	0.99	1.08	4.52	2.70	1.96	1.36
EO	9.08	42.62	9.41	176.25	0.98	0.47	2.28	0.04	5.60	0.79	3.66	0.10
FM4	3.55	3.07	2.84	2.62	0.92	1.37	1.09	1.10	3.25	2.94	2.60	1.81
M6A	24.15	16.64	13.47	10.53	0.84	2.17	1.39	1.29	15.53	13.76	10.84	4.62
M8A	235.69	127.27	88.50	55.65	0.85	3.34	2.02	1.52	67.77	60.32	43.78	13.02
NB4	1.94	1.93	1.93	1.93	1.01	1.00	1.00	1.00	1.06	1.05	1.06	1.05
NA4	3.50	3.14	2.96	2.72	0.95	1.32	1.10	1.09	3.81	3.14	2.66	1.81
Accel:4	**B1**	**B2**	**B3**	**B4**	**M1**	**M2**	**M3**	**M4**	**H1**	**H2**	**H3**	**H4**
RMS	0.91	1.88	2.42	2.46	1.56	1.16	1.02	1.03	2.87	1.44	1.44	1.36
CF	2.94	2.60	2.57	2.54	1.48	1.33	1.09	1.01	1.67	1.27	1.23	1.47
ER	0.45	0.35	0.32	0.45	0.87	1.10	1.16	0.90	2.24	2.47	2.54	2.06
FM0	2.77	2.93	2.82	2.86	1.26	1.01	1.00	0.93	1.89	1.21	1.33	1.44
Kurt.	2.67	2.45	2.47	2.79	1.38	1.27	1.01	0.93	2.53	1.35	1.53	1.66
EO	106.45	307.52	87.40	39.50	0.43	1.20	0.68	6.68	0.29	0.05	0.89	0.57
FM4	3.19	2.49	2.67	3.24	1.96	1.67	1.49	1.28	2.49	2.06	2.05	1.64
M6A	17.31	9.39	11.35	18.63	6.44	4.43	3.00	1.90	8.30	5.78	5.77	3.35
M8A	127.54	46.39	66.03	156.39	21.56	13.33	6.45	2.74	26.73	16.24	16.31	6.33
NB4	1.93	1.93	1.93	1.93	1.00	1.00	1.00	1.00	1.02	1.04	1.02	1.05
NA4	3.31	2.62	2.76	3.07	1.73	1.53	1.36	1.30	2.71	1.94	2.00	1.74
Accel:5	**B1**	**B2**	**B3**	**B4**	**M1**	**M2**	**M3**	**M4**	**H1**	**H2**	**H3**	**H4**
RMS	1.05	1.93	2.46	2.73	1.42	1.17	1.07	0.97	3.06	1.59	1.55	1.33
CF	3.45	2.73	2.49	3.05	0.95	1.16	1.12	0.94	1.24	1.14	1.38	0.99
ER	0.60	0.40	0.40	0.46	0.75	1.07	1.08	1.14	2.08	2.54	2.39	2.46
FM0	3.10	2.91	2.71	2.79	0.84	1.00	0.98	1.09	1.58	1.20	1.30	1.30
Kurt.	2.90	2.57	2.60	2.69	1.05	1.17	1.02	1.10	2.73	1.57	1.47	1.76
EO	185.77	74.39	116.66	36.94	0.79	0.11	0.21	1.06	0.09	0.20	0.10	0.45
FM4	3.97	3.21	3.13	3.43	0.94	1.93	1.88	1.26	1.77	1.37	1.39	1.23
M6A	31.71	17.90	17.32	20.56	0.89	6.62	6.42	2.17	3.56	1.90	2.23	1.86
M8A	369.82	139.47	135.09	171.29	0.85	24.75	25.16	4.34	7.03	2.38	3.76	2.94
NB4	1.93	1.93	1.93	1.93	1.01	1.00	1.00	1.00	1.01	1.01	1.01	1.03
NA4	3.76	3.16	2.95	3.29	0.91	1.73	1.91	1.34	2.08	1.48	1.50	1.30

Table F.1: Condition Indicators (OH-58C):(SGVS-SASP): P_1/P_3

Condition Indicators (OH-58C):(SGVS-SASP): P_2/P_4												
	CI Values				Ratio to Baseline							
Accel:1	**B1**	**B2**	**B3**	**B4**	**M1**	**M2**	**M3**	**M4**	**H1**	**H2**	**H3**	**H4**
RMS	0.78	1.58	1.95	2.09	1.14	0.83	0.82	0.81	2.47	1.41	1.53	1.54
CF	3.26	2.88	2.67	3.02	0.85	1.08	1.18	1.23	1.87	2.13	2.04	1.51
ER	0.59	0.36	0.37	0.52	0.93	1.72	1.73	1.35	2.50	4.53	3.54	2.19
FM0	3.60	3.70	3.62	3.46	0.80	0.87	0.95	1.01	1.69	1.86	1.70	1.58
Kurt.	3.03	2.44	2.79	2.96	0.89	1.25	1.07	1.10	2.68	3.15	2.35	1.95
EO	13.01	10.45	10.73	7.77	35.81	1.58	2.71	2.51	3.06	6.56	7.79	7.52
FM4	3.01	4.01	4.60	3.51	1.11	0.97	0.79	1.08	2.61	2.54	2.42	2.71
M6A	14.79	34.96	48.77	22.68	1.23	0.87	0.54	1.37	11.16	7.86	7.55	12.20
M8A	97.78	465.84	754.81	201.16	1.34	0.73	0.37	1.85	49.93	20.36	21.16	56.08
NB4	1.94	1.94	1.93	1.93	1.00	1.01	1.00	1.00	1.02	1.03	1.03	1.04
NA4	3.18	3.42	4.04	3.19	1.05	1.14	0.91	1.23	2.69	3.03	2.88	2.89
Accel:2	**B1**	**B2**	**B3**	**B4**	**M1**	**M2**	**M3**	**M4**	**H1**	**H2**	**H3**	**H4**
RMS	0.75	1.28	1.71	2.09	1.08	1.09	1.00	0.92	2.65	1.94	1.87	1.58
CF	2.92	3.21	2.81	3.05	0.98	1.03	1.12	1.62	2.32	1.38	1.56	1.43
ER	0.46	0.44	0.47	0.43	1.36	1.43	1.46	1.49	2.98	2.54	2.09	2.27
FM0	2.91	3.33	3.16	2.93	1.07	1.12	1.15	1.45	1.97	1.29	1.32	1.52
Kurt.	2.61	2.67	2.88	2.85	1.15	1.23	1.04	1.35	3.55	1.86	1.38	1.47
EO	23.40	59.14	124.60	223.84	10.94	0.39	0.06	0.13	3.19	0.56	1.49	1.06
FM4	3.30	2.86	3.28	3.63	1.05	1.18	0.95	1.18	2.82	2.37	1.94	1.48
M6A	21.10	14.52	21.93	30.47	1.00	1.40	0.87	1.91	9.93	6.92	4.43	2.19
M8A	210.06	106.22	225.59	425.89	0.85	1.56	0.83	3.02	29.63	18.75	9.25	2.76
NB4	1.94	1.93	1.93	1.93	1.00	1.00	1.00	1.00	1.05	1.06	1.04	1.04
NA4	3.41	2.99	3.57	3.90	1.02	1.11	0.88	1.21	3.06	2.48	1.88	1.50
Accel:3	**B1**	**B2**	**B3**	**B4**	**M1**	**M2**	**M3**	**M4**	**H1**	**H2**	**H3**	**H4**
RMS	1.04	1.80	2.63	3.56	1.36	1.21	1.03	0.91	2.86	1.90	1.62	1.33
CF	2.85	3.10	3.16	3.45	0.87	1.13	0.93	0.92	1.67	1.40	1.36	1.03
ER	0.52	0.64	0.64	0.74	1.00	1.29	1.52	1.40	2.46	1.75	1.79	1.53
FM0	2.90	3.14	3.21	3.38	0.98	1.25	1.15	1.02	1.97	1.46	1.41	1.27
Kurt.	2.78	3.05	3.19	3.51	0.90	1.18	0.89	0.89	3.24	1.85	1.53	1.42
EO	33.87	31.59	35.37	7.64	11.29	0.41	0.38	45.65	1.24	0.85	0.49	7.33
FM4	4.15	3.11	3.07	3.24	0.78	1.14	1.17	1.13	2.06	2.37	1.84	1.79
M6A	35.42	15.73	15.19	16.63	0.47	1.56	1.63	1.33	5.86	8.65	4.82	5.47
M8A	437.85	103.59	98.57	108.64	0.25	2.61	2.60	1.60	16.49	33.15	14.22	20.71
NB4	1.93	1.93	1.93	1.93	1.01	1.01	1.00	1.00	1.08	1.04	1.01	1.03
NA4	4.05	3.17	3.13	3.25	0.85	1.16	1.15	1.12	2.41	2.46	1.87	1.80
Accel:4	**B1**	**B2**	**B3**	**B4**	**M1**	**M2**	**M3**	**M4**	**H1**	**H2**	**H3**	**H4**
RMS	0.87	1.14	1.84	2.59	1.22	1.53	1.23	1.01	3.33	2.65	2.13	1.59
CF	2.79	3.02	2.61	2.60	1.17	0.94	1.05	1.20	2.06	1.70	1.68	1.55
ER	0.49	0.71	0.46	0.46	1.28	0.85	1.12	0.97	2.51	1.42	2.02	1.92
FM0	2.78	3.40	2.83	2.74	1.23	0.86	1.01	1.05	2.26	1.36	1.41	1.37
Kurt.	2.54	2.93	2.61	2.58	1.08	0.94	1.10	1.05	4.16	2.01	1.77	1.71
EO	224.36	17.98	117.23	7.67	0.05	0.21	0.03	13.71	0.23	3.59	0.34	3.27
FM4	4.17	2.89	3.32	4.17	1.23	1.32	1.06	0.98	2.86	2.97	1.93	1.40
M6A	32.02	13.56	21.24	37.32	1.70	2.40	1.15	0.82	13.08	13.96	4.66	1.88
M8A	328.81	87.24	206.45	529.95	2.33	5.06	1.21	0.58	61.69	66.63	10.59	2.14
NB4	1.94	1.93	1.93	1.93	1.00	1.01	1.00	1.00	1.07	1.02	1.01	1.01
NA4	3.71	3.07	3.44	4.31	1.38	1.17	1.04	0.96	3.70	3.15	2.04	1.52
Accel:5	**B1**	**B2**	**B3**	**B4**	**M1**	**M2**	**M3**	**M4**	**H1**	**H2**	**H3**	**H4**
RMS	1.14	1.47	2.26	2.82	1.04	1.43	1.25	1.02	2.99	2.20	1.95	1.56
CF	2.91	2.46	3.19	3.10	1.16	1.30	1.08	1.35	2.02	2.22	1.35	1.22
ER	0.54	0.69	0.58	0.62	1.40	0.93	0.91	0.81	2.53	1.56	1.52	1.45
FM0	2.79	3.06	2.84	3.03	1.21	0.93	1.07	1.10	2.29	1.60	1.38	1.20
Kurt.	2.51	2.81	2.90	2.88	1.28	1.07	1.16	1.28	4.26	2.06	1.47	1.61
EO	7.78	28.73	151.91	11.38	3.53	0.23	0.07	1.14	3.37	1.48	0.26	34.48
FM4	4.05	3.42	3.81	3.54	0.93	1.06	0.96	1.32	2.57	2.40	1.65	1.76
M6A	31.37	20.04	28.22	23.32	0.81	1.34	0.86	1.87	8.77	9.03	3.62	3.97
M8A	344.13	159.92	309.50	216.81	0.68	1.99	0.74	2.73	29.37	33.86	7.76	9.01
NB4	1.94	1.93	1.93	1.93	1.01	1.02	1.00	1.00	1.09	1.03	1.02	1.02
NA4	3.50	3.34	3.88	3.56	0.98	1.04	0.94	1.20	3.31	2.68	1.70	1.79

Table F.2: Condition Indicators (OH-58C):(SGVS-SASP): P_2/P_4

Condition Indicators (OH-58A):(SGVS-SASP): P_1/P_3								
	CI Values				Ratio to Baseline			
Accel:1	**B1**	**B2**	**B3**	**B4**	**H1**	**H2**	**H3**	**H4**
RMS	0.54	0.65	0.89	1.26	0.99	1.13	1.04	0.96
CF	3.13	2.81	2.83	2.59	0.95	1.07	1.04	1.01
ER	0.99	1.26	1.21	0.68	1.28	1.13	1.11	1.17
FM0	4.09	3.38	3.32	2.90	0.92	1.11	1.14	1.09
Kurt.	3.17	2.88	2.79	2.72	0.97	1.00	1.08	1.06
EO	9.36	11.71	116.51	8.68	12.66	1.00	0.10	1.38
FM4	3.19	2.81	3.02	2.95	1.05	0.96	0.89	1.01
M6A	16.76	12.43	14.18	14.22	1.27	0.90	0.78	1.06
M8A	118.34	72.00	85.99	91.19	1.74	0.86	0.69	1.18
NB4	2.13	1.98	1.94	1.94	0.99	0.99	1.00	1.00
NA4	3.12	2.88	2.95	2.94	1.05	0.98	0.94	1.04
Accel:2	**B1**	**B2**	**B3**	**B4**	**H1**	**H2**	**H3**	**H4**
RMS	0.52	0.69	0.95	1.24	1.00	1.05	0.99	1.02
CF	3.42	3.24	3.17	3.10	0.88	1.10	1.08	0.94
ER	0.87	0.97	0.96	0.76	1.00	1.15	1.13	1.04
FM0	3.48	3.53	3.45	3.00	0.90	1.09	1.01	1.04
Kurt.	2.93	2.90	2.80	2.78	0.93	1.04	1.15	0.96
EO	18.88	43.59	29.00	257.17	0.84	0.74	12.68	0.20
FM4	3.37	3.05	3.26	3.51	0.93	0.98	0.95	0.86
M6A	20.25	14.68	18.31	22.40	0.81	1.10	0.92	0.67
M8A	172.33	91.50	140.21	202.18	0.68	1.54	0.89	0.49
NB4	2.00	2.32	2.21	2.00	1.01	0.92	0.92	1.00
NA4	3.06	3.05	3.29	3.38	0.96	1.04	0.99	0.93
Accel:3	**B1**	**B2**	**B3**	**B4**	**H1**	**H2**	**H3**	**H4**
RMS	0.82	1.08	1.75	2.41	1.30	1.20	1.17	1.19
CF	2.68	2.70	2.61	2.94	0.94	0.94	1.06	1.01
ER	0.59	0.64	0.56	0.60	0.77	0.76	0.83	0.89
FM0	3.03	2.87	2.84	3.37	0.99	1.01	1.10	0.98
Kurt.	2.72	2.61	2.37	2.70	0.89	0.98	1.01	1.00
EO	6.12	71.19	205.85	70.96	0.75	0.38	0.15	0.10
FM4	3.50	2.70	2.90	3.10	0.98	1.09	1.09	1.13
M6A	23.74	11.27	13.09	16.75	1.15	1.20	1.33	1.45
M8A	242.62	61.61	75.91	127.94	1.81	1.32	1.82	1.98
NB4	2.00	1.95	1.96	1.99	1.02	1.00	1.00	0.98
NA4	3.46	2.69	2.77	3.18	0.93	1.08	1.10	1.13
Accel:4	**B1**	**B2**	**B3**	**B4**	**H1**	**H2**	**H3**	**H4**
RMS	0.82	0.84	1.26	1.24	0.88	0.99	1.03	0.95
CF	2.97	3.26	2.99	3.65	1.05	0.97	0.88	0.74
ER	0.52	0.57	0.42	0.65	1.24	0.99	1.05	1.08
FM0	3.79	3.40	2.84	3.18	1.00	0.89	0.92	0.93
Kurt.	2.88	2.96	2.70	2.72	1.06	0.97	0.99	1.05
EO	17.10	327.84	6.46	885.03	2.68	0.02	0.60	0.10
FM4	4.15	3.23	3.27	4.28	1.04	0.98	1.03	1.17
M6A	34.98	21.69	19.34	47.72	1.06	0.80	1.03	1.07
M8A	438.23	257.13	166.29	893.79	1.06	0.50	0.99	0.76
NB4	1.97	1.94	1.94	1.95	1.00	1.00	1.02	1.00
NA4	3.27	3.44	3.16	4.36	1.06	0.89	1.07	1.06
Accel:5	**B1**	**B2**	**B3**	**B4**	**H1**	**H2**	**H3**	**H4**
RMS	0.89	1.08	1.88	1.78	0.89	1.05	1.10	1.01
CF	3.24	3.45	3.04	2.99	0.96	0.99	0.95	1.13
ER	0.57	0.55	0.37	0.62	1.30	0.94	0.96	1.14
FM0	3.95	3.68	2.95	3.17	0.88	0.85	0.98	1.12
Kurt.	3.21	3.20	2.56	2.74	0.88	0.87	0.98	1.18
EO	6.39	10.77	155.70	112.55	4.42	1.33	0.03	0.07
FM4	4.01	3.33	3.28	2.93	0.93	1.05	0.96	1.01
M6A	27.23	21.20	19.29	13.86	0.94	1.02	0.97	1.04
M8A	237.57	209.57	161.47	88.41	1.03	0.90	1.03	1.09
NB4	1.98	1.95	1.94	1.95	0.99	1.00	1.01	1.00
NA4	3.56	3.35	3.18	2.98	1.05	1.02	0.99	1.06

Table F.3: Condition Indicators (OH-58A):(SGVS-SASP): P_1/P_3

Condition Indicators (OH-58A):(SGVS-SASP): P_2/P_4								
	CI Values				Ratio to Baseline			
Accel:1	**B1**	**B2**	**B3**	**B4**	**H1**	**H2**	**H3**	**H4**
RMS	0.54	0.65	0.89	1.26	0.99	1.13	1.04	0.96
CF	3.13	2.81	2.83	2.59	0.95	1.07	1.04	1.01
ER	0.99	1.26	1.21	0.68	1.28	1.13	1.11	1.17
FM0	4.09	3.38	3.32	2.90	0.92	1.11	1.14	1.09
Kurt.	3.17	2.88	2.79	2.72	0.97	1.00	1.08	1.06
EO	9.36	11.71	116.51	8.68	12.66	1.00	0.10	1.38
FM4	3.19	2.81	3.02	2.95	1.05	0.96	0.89	1.01
M6A	16.76	12.43	14.18	14.22	1.27	0.90	0.78	1.06
M8A	118.34	72.00	85.99	91.19	1.74	0.86	0.69	1.18
NB4	2.13	1.98	1.94	1.94	0.99	0.99	1.00	1.00
NA4	3.12	2.88	2.95	2.94	1.05	0.98	0.94	1.04
Accel:2	**B1**	**B2**	**B3**	**B4**	**H1**	**H2**	**H3**	**H4**
RMS	0.52	0.69	0.95	1.24	1.00	1.05	0.99	1.02
CF	3.42	3.24	3.17	3.10	0.88	1.10	1.08	0.94
ER	0.87	0.97	0.96	0.76	1.00	1.15	1.13	1.04
FM0	3.48	3.53	3.45	3.00	0.90	1.09	1.01	1.04
Kurt.	2.93	2.90	2.80	2.78	0.93	1.04	1.15	0.96
EO	18.88	43.59	29.00	257.17	0.84	0.74	12.68	0.20
FM4	3.37	3.05	3.26	3.51	0.93	0.98	0.95	0.86
M6A	20.25	14.68	18.31	22.40	0.81	1.10	0.92	0.67
M8A	172.33	91.50	140.21	202.18	0.68	1.54	0.89	0.49
NB4	2.00	2.32	2.21	2.00	1.01	0.92	0.92	1.00
NA4	3.06	3.05	3.29	3.38	0.96	1.04	0.99	0.93
Accel:3	**B1**	**B2**	**B3**	**B4**	**H1**	**H2**	**H3**	**H4**
RMS	0.82	1.08	1.75	2.41	1.30	1.20	1.17	1.19
CF	2.68	2.70	2.61	2.94	0.94	0.94	1.06	1.01
ER	0.59	0.64	0.56	0.60	0.77	0.76	0.83	0.89
FM0	3.03	2.87	2.84	3.37	0.99	1.01	1.10	0.98
Kurt.	2.72	2.61	2.37	2.70	0.89	0.98	1.01	1.00
EO	6.12	71.19	205.85	70.96	0.75	0.38	0.15	0.10
FM4	3.50	2.70	2.90	3.10	0.98	1.09	1.09	1.13
M6A	23.74	11.27	13.09	16.75	1.15	1.20	1.33	1.45
M8A	242.62	61.61	75.91	127.94	1.81	1.32	1.82	1.98
NB4	2.00	1.95	1.96	1.99	1.02	1.00	1.00	0.98
NA4	3.46	2.69	2.77	3.18	0.93	1.08	1.10	1.13
Accel:4	**B1**	**B2**	**B3**	**B4**	**H1**	**H2**	**H3**	**H4**
RMS	0.82	0.84	1.26	1.24	0.88	0.99	1.03	0.95
CF	2.97	3.26	2.99	3.65	1.05	0.97	0.88	0.74
ER	0.52	0.57	0.42	0.65	1.24	0.99	1.05	1.08
FM0	3.79	3.40	2.84	3.18	1.00	0.89	0.92	0.93
Kurt.	2.88	2.96	2.70	2.72	1.06	0.97	0.99	1.05
EO	17.10	327.84	6.46	885.03	2.68	0.02	0.60	0.10
FM4	4.15	3.23	3.27	4.28	1.04	0.98	1.03	1.17
M6A	34.98	21.69	19.34	47.72	1.06	0.80	1.03	1.07
M8A	438.23	257.13	166.29	893.79	1.06	0.50	0.99	0.76
NB4	1.97	1.94	1.94	1.95	1.00	1.00	1.02	1.00
NA4	3.27	3.44	3.16	4.36	1.06	0.89	1.07	1.06
Accel:5	**B1**	**B2**	**B3**	**B4**	**H1**	**H2**	**H3**	**H4**
RMS	0.89	1.08	1.88	1.78	0.89	1.05	1.10	1.01
CF	3.24	3.45	3.04	2.99	0.96	0.99	0.95	1.13
ER	0.57	0.55	0.37	0.62	1.30	0.94	0.96	1.14
FM0	3.95	3.68	2.95	3.17	0.88	0.85	0.98	1.12
Kurt.	3.21	3.20	2.56	2.74	0.88	0.87	0.98	1.18
EO	6.39	10.77	155.70	112.55	4.42	1.33	0.03	0.07
FM4	4.01	3.33	3.28	2.93	0.93	1.05	0.96	1.01
M6A	27.23	21.20	19.29	13.86	0.94	1.02	0.97	1.04
M8A	237.57	209.57	161.47	88.41	1.03	0.90	1.03	1.09
NB4	1.98	1.95	1.94	1.95	0.99	1.00	1.01	1.00
NA4	3.56	3.35	3.18	2.98	1.05	1.02	0.99	1.06

Table F.4: Condition Indicators (OH-58A):(SGVS-SASP): P_2/P_4

Appendix G

Condition Indicator Results: **SGVS -SAMP**

Condition Indicators (OH-58C): (SGVS-SAMP) Avg. of sets												
	CI Values				Ratio to Baseline							
Accel:1	**B1**	**B2**	**B3**	**B4**	**M1**	**M2**	**M3**	**M4**	**H1**	**H2**	**H3**	**H4**
RMS	1.03	1.98	2.13	2.05	1.10	0.78	0.89	0.87	1.96	1.10	1.39	1.72
CF	2.79	2.23	2.22	2.37	0.89	1.73	1.32	1.43	1.51	1.64	1.67	1.47
ER	0.36	0.23	0.28	0.47	1.06	2.13	1.95	1.39	3.28	6.56	4.62	1.95
FM0	2.74	2.80	3.06	3.27	1.09	1.23	1.08	1.00	1.55	1.65	1.39	1.20
Kurt.	2.83	1.94	2.21	2.54	0.99	1.51	1.27	1.20	1.81	2.17	1.73	1.40
EO	7.95	3.61	2.90	4.36	0.44	5.14	1.47	1.35	2.05	6.29	9.98	5.64
FM4	2.67	2.71	2.56	2.43	1.17	1.27	1.33	1.64	1.98	1.54	1.66	1.92
M6A	10.99	10.67	10.75	8.35	1.51	2.02	1.94	4.31	5.35	3.17	3.78	6.09
M8A	58.80	51.27	64.99	35.08	2.11	3.82	2.67	13.91	14.87	7.35	8.91	24.04
NB4	1.93	1.94	1.94	1.93	1.00	1.00	1.00	1.00	1.09	1.09	1.08	1.08
NA4	2.68	2.90	2.59	2.52	1.16	1.23	1.31	1.59	2.14	1.52	1.74	1.89
Accel:2	**B1**	**B2**	**B3**	**B4**	**M1**	**M2**	**M3**	**M4**	**H1**	**H2**	**H3**	**H4**
RMS	0.88	1.48	1.79	2.30	1.11	1.09	1.07	0.88	2.35	1.70	1.82	1.51
CF	2.89	2.60	2.54	3.03	1.03	1.06	1.15	0.90	2.37	1.71	1.71	1.33
ER	0.40	0.39	0.46	0.40	1.19	1.42	1.40	1.47	2.91	2.51	2.04	2.31
FM0	2.55	3.24	3.05	2.67	1.22	0.97	1.16	1.08	2.29	1.36	1.45	1.53
Kurt.	2.37	2.36	2.47	2.54	1.09	1.09	1.13	1.05	3.49	1.87	1.58	1.40
EO	4.54	3.52	4.78	4.76	3.70	2.31	1.00	0.94	13.80	8.59	4.91	7.96
FM4	2.91	2.52	2.43	2.71	1.03	1.25	1.03	0.95	2.52	2.05	2.11	1.64
M6A	13.27	9.49	8.43	11.22	1.15	1.80	1.05	0.91	13.74	5.92	6.71	3.96
M8A	77.08	45.70	35.75	59.06	1.41	2.74	1.05	0.87	86.53	18.51	23.86	11.00
NB4	1.94	1.93	1.94	1.93	1.00	1.01	1.00	1.00	1.01	1.01	1.00	1.00
NA4	3.02	2.79	2.67	2.66	0.94	1.14	0.96	1.01	2.78	2.02	2.04	1.84
Accel:3	**B1**	**B2**	**B3**	**B4**	**M1**	**M2**	**M3**	**M4**	**H1**	**H2**	**H3**	**H4**
RMS	1.00	2.19	3.05	3.99	1.42	1.01	0.91	0.84	3.14	1.67	1.49	1.30
CF	2.96	3.00	3.18	3.14	0.85	1.16	0.87	0.95	1.66	1.35	1.20	0.97
ER	0.42	0.38	0.43	0.48	1.01	1.52	1.83	1.48	2.54	2.54	2.34	1.99
FM0	2.62	2.81	3.33	3.48	1.00	1.42	1.10	1.00	2.11	1.54	1.30	1.14
Kurt.	2.57	3.18	3.13	2.95	0.88	1.00	0.84	1.05	3.49	1.41	1.29	1.50
EO	7.53	3.57	7.55	7.03	0.84	6.81	1.07	0.85	10.17	8.32	2.76	3.45
FM4	2.94	2.66	2.84	3.38	1.00	1.34	1.21	0.99	2.93	2.70	2.12	1.96
M6A	14.02	10.22	12.55	19.70	1.02	2.74	1.74	0.98	15.84	12.98	7.95	7.47
M8A	90.17	48.68	71.87	151.26	1.03	7.30	2.95	1.05	89.34	67.61	34.56	32.56
NB4	1.93	1.93	1.93	1.93	1.01	1.01	1.00	1.00	1.01	1.01	1.01	1.03
NA4	3.00	2.68	2.84	3.56	1.13	1.38	1.20	0.90	3.33	2.74	2.07	1.74
Accel:4	**B1**	**B2**	**B3**	**B4**	**M1**	**M2**	**M3**	**M4**	**H1**	**H2**	**H3**	**H4**
RMS	1.02	1.83	2.72	3.03	1.32	1.36	1.16	1.12	2.82	1.76	1.56	1.39
CF	3.00	2.97	2.79	2.28	1.44	1.09	0.99	1.17	1.37	1.13	1.03	1.26
ER	0.35	0.33	0.25	0.28	1.09	0.96	1.13	0.99	2.75	2.44	2.84	2.76
FM0	2.84	3.16	2.97	2.63	1.29	0.97	0.96	1.00	1.52	1.08	1.11	1.32
Kurt.	2.69	2.75	2.61	2.63	1.71	1.11	1.00	1.01	1.59	1.13	1.11	1.16
EO	4.68	9.47	6.99	6.25	3.96	0.47	0.46	0.58	5.23	2.34	1.60	1.19
FM4	3.06	2.73	2.86	3.68	1.45	1.03	0.91	0.79	1.80	1.67	1.37	0.99
M6A	15.98	11.66	12.81	24.90	2.75	1.14	0.81	0.54	4.46	3.32	2.02	0.92
M8A	115.16	65.68	74.47	229.26	5.67	1.32	0.72	0.35	11.19	6.66	2.87	0.84
NB4	1.94	1.94	1.93	1.94	1.00	1.00	1.00	0.99	1.00	1.00	1.00	1.00
NA4	3.18	2.66	2.60	3.16	1.56	1.01	0.99	1.00	1.69	1.66	1.45	1.12
Accel:5	**B1**	**B2**	**B3**	**B4**	**M1**	**M2**	**M3**	**M4**	**H1**	**H2**	**H3**	**H4**
RMS	1.21	2.00	2.88	2.78	1.23	1.35	1.20	1.21	2.88	1.73	1.61	1.58
CF	2.34	2.71	3.21	2.71	1.35	1.14	0.93	1.22	1.71	0.97	0.86	1.12
ER	0.42	0.37	0.34	0.38	1.04	0.97	0.99	0.96	2.45	2.09	1.98	2.21
FM0	2.85	2.95	3.38	2.86	0.98	0.98	0.80	1.03	1.48	1.03	0.90	1.01
Kurt.	2.21	2.85	2.65	2.63	1.40	1.06	1.06	1.19	2.21	1.09	1.12	1.14
EO	5.01	9.88	9.88	5.95	1.67	0.64	0.51	1.06	2.96	1.82	0.86	2.15
FM4	3.32	3.60	3.92	2.93	0.97	0.80	0.81	1.21	1.59	1.07	0.91	1.13
M6A	18.23	23.21	32.31	12.91	0.98	0.56	0.51	1.67	3.80	1.11	0.71	1.42
M8A	128.94	201.57	385.14	71.08	1.05	0.37	0.30	2.47	11.30	1.06	0.54	1.90
NB4	1.93	1.93	1.94	1.93	1.00	1.00	1.00	1.00	1.01	1.01	1.00	1.01
NA4	3.20	3.52	3.73	2.90	0.91	0.86	0.89	1.27	1.83	1.11	0.98	1.22

Table G.1: Condition Indicators (OH-58C): (SGVS-SAMP) Avg. of sets

Condition Indicators (OH-58A): (SGVS-SAMP) Avg. of sets								
	CI Values				Ratio to Baseline			
Accel:1	**B1**	**B2**	**B3**	**B4**	**H1**	**H2**	**H3**	**H4**
RMS	0.81	0.99	1.21	2.24	0.94	1.09	1.06	0.89
CF	2.48	2.30	2.88	2.69	1.12	1.33	1.05	1.04
ER	0.77	0.90	0.92	0.41	1.11	1.14	1.26	1.23
FM0	3.38	3.11	3.29	2.86	1.16	1.23	1.18	1.09
Kurt.	2.70	2.76	2.95	2.60	1.11	1.12	0.96	1.14
EO	5.36	5.59	5.64	3.54	1.86	1.50	0.90	1.39
FM4	3.38	2.93	3.24	2.73	0.86	1.00	0.84	1.00
M6A	21.13	13.69	18.16	11.61	0.66	1.02	0.62	0.97
M8A	188.48	82.75	138.79	64.65	0.49	1.09	0.43	0.95
NB4	2.09	1.93	1.94	1.93	1.06	1.00	1.00	1.00
NA4	3.52	2.91	3.12	2.77	0.81	0.99	0.87	1.03
Accel:2	**B1**	**B2**	**B3**	**B4**	**H1**	**H2**	**H3**	**H4**
RMS	0.87	1.09	1.46	2.05	0.99	1.02	1.01	1.06
CF	2.84	3.30	3.03	3.19	1.03	0.97	0.95	0.82
ER	0.56	0.70	0.60	0.43	1.12	1.11	1.19	1.01
FM0	2.87	3.00	2.90	3.21	1.03	1.05	1.00	0.88
Kurt.	2.25	3.02	2.59	3.04	1.13	0.92	1.10	0.83
EO	5.02	7.72	3.70	4.61	0.96	0.74	1.66	0.92
FM4	3.03	3.33	2.96	2.97	1.00	1.05	1.03	0.82
M6A	16.06	20.43	14.29	13.95	0.97	1.06	1.08	0.63
M8A	124.54	182.37	92.71	84.84	0.92	1.07	1.12	0.48
NB4	1.95	1.99	1.96	1.97	1.01	1.03	1.00	0.99
NA4	3.00	3.45	2.78	2.82	0.99	1.04	1.11	0.87
Accel:3	**B1**	**B2**	**B3**	**B4**	**H1**	**H2**	**H3**	**H4**
RMS	1.51	2.01	3.45	4.55	1.40	1.26	1.16	1.24
CF	2.42	2.73	2.34	2.73	1.08	0.94	0.97	0.96
ER	0.38	0.40	0.32	0.36	0.85	0.80	0.84	0.87
FM0	2.76	2.99	2.81	3.22	1.14	0.96	0.93	0.92
Kurt.	2.43	2.45	2.15	2.55	0.94	0.94	0.99	1.01
EO	3.74	4.47	5.93	5.58	0.86	1.14	0.85	0.47
FM4	3.04	2.66	2.76	3.01	1.13	1.09	1.12	1.41
M6A	15.50	10.33	11.71	15.65	1.43	1.28	1.42	2.47
M8A	109.99	49.64	63.44	112.48	1.87	1.57	2.03	4.50
NB4	2.01	1.94	1.94	1.96	0.97	1.00	1.00	0.99
NA4	3.30	2.66	3.02	3.20	1.05	1.16	0.99	1.33
Accel:4	**B1**	**B2**	**B3**	**B4**	**H1**	**H2**	**H3**	**H4**
RMS	1.48	1.43	2.34	2.14	0.78	1.04	1.06	0.92
CF	2.72	2.42	2.05	2.67	0.94	1.07	1.33	0.85
ER	0.27	0.37	0.27	0.35	1.30	0.85	0.98	0.91
FM0	3.25	2.48	2.32	2.86	1.08	0.97	1.10	0.96
Kurt.	2.00	2.30	2.44	2.47	1.10	0.97	1.08	1.26
EO	7.64	4.11	2.92	2.97	0.58	0.75	1.06	2.32
FM4	2.81	3.09	2.87	3.07	1.06	0.91	1.04	0.85
M6A	12.06	16.74	12.71	16.06	1.29	0.76	1.12	0.61
M8A	65.11	128.90	73.33	115.52	1.91	0.59	1.20	0.40
NB4	1.95	1.94	1.93	1.93	1.00	1.00	1.00	1.00
NA4	3.03	3.37	2.77	3.16	1.01	0.81	1.10	0.88
Accel:5	**B1**	**B2**	**B3**	**B4**	**H1**	**H2**	**H3**	**H4**
RMS	1.49	1.90	3.74	3.16	0.83	1.06	1.13	0.98
CF	2.55	2.35	2.29	2.55	1.05	1.07	1.16	1.01
ER	0.30	0.34	0.19	0.35	1.36	0.86	1.02	1.08
FM0	3.19	2.43	2.49	3.03	0.91	0.94	1.02	1.02
Kurt.	2.39	2.46	2.07	2.72	1.06	0.79	1.22	1.09
EO	3.37	2.64	4.01	3.85	1.10	1.48	0.69	0.96
FM4	3.22	2.58	3.08	2.99	0.95	1.07	0.88	0.92
M6A	19.10	10.00	15.92	15.19	0.80	1.15	0.70	0.82
M8A	166.08	49.99	111.01	109.80	0.60	1.19	0.52	0.69
NB4	1.95	1.93	1.94	1.94	1.00	1.00	1.00	1.00
NA4	3.11	2.74	3.22	3.15	0.90	1.07	0.86	0.91

Table G.2: Condition Indicators (OH-58A): (SGVS-SAMP) Avg. of sets

Appendix H

Example **SGVS -SASP** using Acoustic Signal

The following plot was created by replacing the signal for A_4 with that of microphone 2 in the **SGVS -SASP** code.

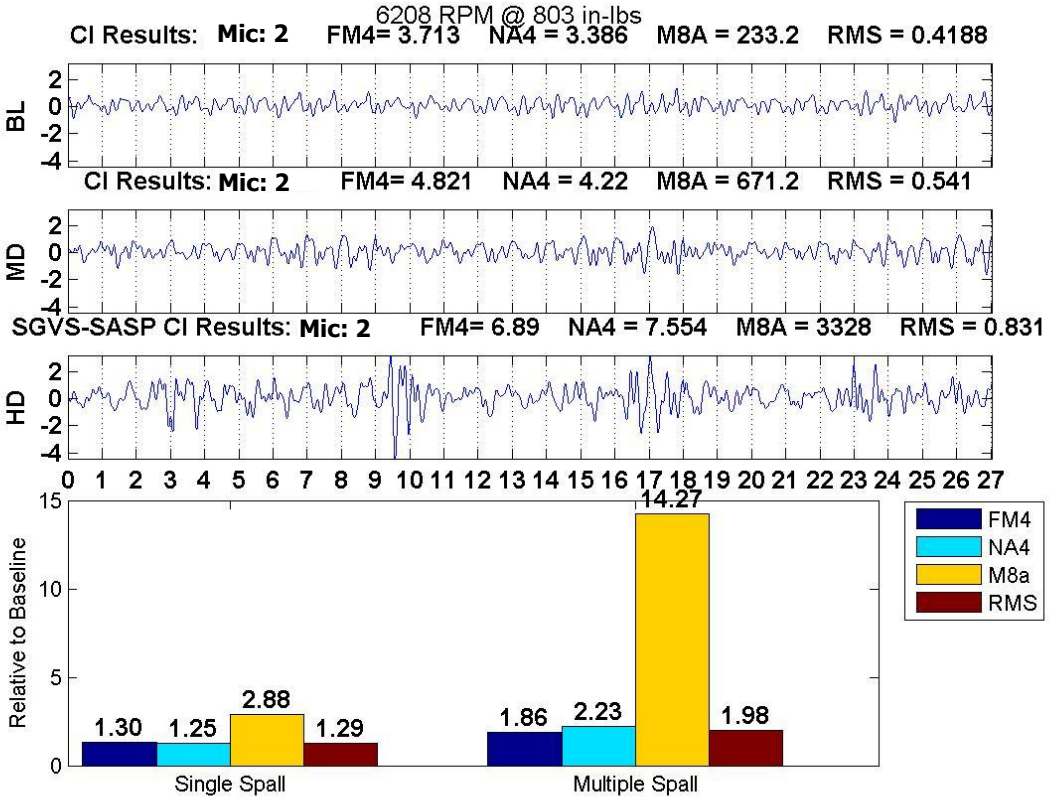

Figure H.1: Example SGVS -SASP Result Using Acoustic Signal (Mic 2)

Bibliography

[1] P.D. Samuel and D. J. Pines. A review of vibration-based techniques for helicopter transmission diagnostics. *Journal of Sound and Vibration*, 282:475–508, 2005.

[2] J. Land and C. Weitzman. How HUMS systems have the potential of significantly reducing the direct operating cost for modern helicopters through monitoring. *Proceedings of the American Helicopter Society 51st Annual Forum, Fort Worth, TX*, pages 744–757, 1995.

[3] P.M. Pawar and R. Ganguli. Helicopter rotor health monitoring - a review. *Proc. ImechE*, 221(G):631–647, 2007.

[4] B.D. Larder. Helicopter hum/fdr: Benefits and developments. *Proceedings of the AHS 55th Forum, Montreal, Quebec, Canada*, May 25-27, 1999.

[5] J.J. Zakrajsek. A review of transmission diagnostics research at NASA lewis research center. *NASA TM-106746*, ARL-TR-599, 1994.

[6] Dennis P. Townsend, editor. *Dudley's Gear Handbook*. McGraw-Hill, 1991.

[7] R.M. Stewart. Some useful analysis techniques for gearbox diagnostics. *Report MHM/R/10/77 - Machine Health Monitoring Group-Institute of Sound and Vibration Research, University of Southampton*, July 1997.

[8] J.J. Zakrajsek, D.P. Townsend, and H.J. Decker. An analysis of gear fault detection methods as applied to pitting fatigue failure data. *NASA TM-105950*, AVSCOM TR-92-C-035, 1993.

[9] H.J. Decker, R.F. Handschuh, and J.J. Zakrajsek. An enhancement to the na4 gear vibration diagnostic parameter. *NASA TM-106553*, ARL-TR-389, 1994.

[10] D. G. Lewicki, H. J. Decker, and J. T. Shimski. Development of a full-scale transmission testing procedure to evaluate advanced lubricants. Technical Report NASA TP-3265, AVSCOM TR-91-C-026, NASA and the U.S. Army Aviation Systems Command, August 1992.

[11] D.G. Lewicki, L. Spievak, P. Wawrynek, A. Ingraffea, and R.F. Handschuh. Consideration of moving tooth load in gear crack propagation predictions. *NASA TM-2000-210227*, July 2000.

[12] F.K. Choy, S. Huang, J.J. Zakrajsek, R.F. Handschuh, and D. Townsend. Vibration signature analysis of a faulted gear transmission system. *NASA TM-106623*, 1994.

[13] H. Chin, K. Danai, and D. Lewicki. Efficient fault diagnosis of helicopter gearbox transmission,. *NASA TM-106253*, TR-92-C-034, 1992.

[14] H. Chin, K. Danai, and D. Lewicki. Fault detection of helicopter gear boxes using the multi-valued influence matrix method,. *NASA TM-106100*, AVSCOM TR-92-C-015, 1992.

[15] V.B. Jammu, K. Danai, and D.G. Lewicki. Unsupervised connectionist network for fault diagnosis of helicopter gearboxes. *Proceedings of the AHS 53rd Forum, Virginia Beach, VA*, pages 1297–1307, April 29-May 1, 1997.

[16] P.D. McFadden. Detecting fatigue cracks in gears by amplitude and phase demodulation of the meshing vibration. *Journal of Vibration, Acoustics, Stress, and Reliability in Design*, 108:165–170, April 1986.

[17] M.J. Brennan, M.H. Chen, and A.G. Reynolds. Use of vibration measurements to detect local tooth defects in gears. *Sound and Vibration*, 31(11):12–17, November 1997.

[18] B.D. Larder. An analysis of HUMS vibration diagnostic capabilities. *Proceedings of the AHS 53rd Forum, Virginia Beach, VA*, pages 1308–1315, April 29-May 1, 1997.

[19] B.D. Forrester. Analysis of gear vibration in the time-frequency domain. *44th Meeting of the Mechanical Failure Prevention Group*, February 1990.

[20] P.D. McFadden and W.J. Wang. Time-frequency domain analysis of vibration signal for machinery diagnostics (ii) the weighted wigner-ville distribution. *Report OUEL 1891,University of Oxford*, 1991.

[21] Paul D. Samuel, Darryll J. Pines, and David G. Lewicki. A comparison of stationary and non-stationary metrics for detecting faults in helicopter gearboxes. *Journal of the American Helicopter Society*, 1998.

[22] Paul D. Samuel and Darryll J. Pines. Classifying helicopter gearbox faults using a normalized energy metric. *Smart Materials and Structures*, 9, 2000.

[23] J. Zakrajsek, P. Dempsey, E. Huff, M. Augustin an R. Safa-Bakhsh, A. Duke, P Ephraim, P. Grabil, and H. Decker. Rotorcraft health management issues and challenges. *TM 2006-214022*, TM 2006-214022:1–20, 2006.

[24] E. Lim, I. Mareels, and A. Wong. Fault detection in geared transmission systems using an acoustic array. *Proceedings-Information, Decision and Control, 1999. IDC 99*, IDC99:207–211, 1999.

[25] Naim Baydar and Andrew Ball. A comparative study of acoustic and vibration signals in detection of gear failures using wigner-ville distribution. *Mechanical Systems and Signal Processing*, 15(6):1091–1107, 2001.

[26] J. Zakrajsek, P.Dempsey, E. Huff, M. Augustin, R. Safa-Bakhs, A. Duke, P. Ephraim, P. Grabil, and H. Decker. Rotorcraft health management issues and challenge. *NASA TM-2006-214022*, 2006.

[27] D. Houser and M. Drosjack. Vibration signal analysis techniques - final report. 1 jul 72-15 jun 73. *DTIC AD0776397*, Dec 1973.

[28] A.K. Wong. Vibration-based helicopter gearbox health monitoring-an overview of the research program in dsto. *DSTO-HUM2001*, 1:1–12, 2001.

[29] M. Lebold, K. Reichard, and D. Boylan. Utilizing dcom in an open system architecture framework for machinery monitoring and diagnostics. *Aerospace Conference Proceedings*, May:3–1227–3–1236, 2003.

[30] Department of Defense. Condition based maintenance plus (cbm+) for material maintenance. *DOD Mandate*, 4151.22, Dec 2007.

[31] R. Ganguli, I. Chopra, and D. Haas. Formulation of a helicopter rotor system damage detection methodology. *Journal of the American Helicopter Society*, 41(4):302–313, 1996.

[32] R. Reddy and R. Ganguli. Structural damage detection in a helicopter rotor blade using radial basis function neural networks. *Smart Materials and Structures*, 12:232–241, 2003.

[33] K. A. Lakshmanan and Darryll J. Pines. Modeling damage in rotorcraft flexbeams using wave mechanics. *SPIE: Smart Materials and Structures*, 6:383–392, 1997.

[34] R. M . Stewart. Some useful analysis techniques for gearbox diagnostics. Technical Report MHM/R/10/77, Machine Health Monitoring Group, Institute of Sound and Vibration Research, University of Southampton, July 1977.

[35] Martin S. Roden. *Analog and Digital Communication Systems 3rd Edition*. Prentice Hall, NJ, USA, 1991.

[36] P.D. McFadden. Detection of gear faults by decomposition of matched differences of vibration signals. *Journal of Mechanical Systems and Signal Processing*, 14(5), 2000.

[37] P.D. McFadden. Proposal for modifications to the wessex helicopter main rotor gearbox vibration monitoring program. In *DSTO Technical Report*, 1985. ARL-AERO-PROP-TM-422.

[38] H. R. Martin. Statistical moment analysis as a means of surface damage detection. In *Proceedings of the 7th International Modal Analysis Conference, Society for Experimental Mechanics*, pages 1016–1021, Schenectady, NY, January 1989.

[39] V.V. Polyshchuk. *Detection and Quantification of the Gear Tooth Damage From The Vibration and Acoustic Signatures*. PhD thesis, University of Akron, Akron, OH, MAY 1999.

[40] V. V. Polyshchuk, F. K. Choy, and M. J. Braun. Gear fault detection with time-frequency based parameter NP4. In *Proceedings of the 8th International Symposium on Transport Phenomena and Dynamics of Rotating Machinery (ISROMAC-8)*, Honolulu, HI, March 2000.

[41] Paul D. Samuel. *Helicopter Transmission Diagnostics using Constrained Adaptive Lifting. PH.D Dissertation*. PhD thesis, University of Maryland, College Park, MD 20742 USA, 2003.

[42] M. Mosher and E. Huff. Analysis of in-flight measurements from helicopter transmissions. *American Heliopter Society 60th Annual Forum, Baltimore, MD 2004*, 2004.

[43] M. Mosher, A. H. Pryor, and E. M. Huff. Evaluation of standard gear metrics in helicopter flight operations. *56th Mechanical Failure Prevention Technology Conference, Virginia Beach*, April 15-19, 2002. Submitted.

[44] E. Huff, I. Tumer, and M. Mosher. An experimental comparison of transmission vibration responses for oh-58 and ah-1 helicopters. *American Helicopter Society 57th Annual Forum, Washington, DC May 9-11, 2001*, 2001.

[45] P. J. Dempsey, M. Mosher, and E. M. Huff. Threshold assessment of gear diagnostic tools on flight and test rig data. In *Proceedings of the American Helicopter Society 59th Annual Forum / NASA TM 2003-212220*, pages 1244–1262, Phoenix, AZ, May 2003.

[46] P. Nachtsheim. Detecting tooth damage in geared drive trains. *NASA TM 112207*, Aug. 1997.

[47] F. B. Oswald, J. J. Zakrajsed, D. P. Townsend, W. Atherton, and H. H. Lin. Effect of operating conditions on gearbox noise. *International Power Transmission and Gearing Conference*, 2:669–674, 1992.

[48] K. Choy F, W. Qian, J. J. Zakrajsed, and F.B. Oswald. Vibration and noise analysis of a gear transmission system. *NASA TM-106162*, 1993.

[49] D.Houser, F.B. Oswald, M.J. Valco, R.Drago, and J. Lenski Jr. Comparison of transmission error predictions with noise measurements for several spur and helical gears. *NASA TM-106647 / ARL-TR 493*, 1994.

[50] F.B. Oswald, A.F. Seybert, T.W. Wu, and Atherton. Comparison of analysis and experiment for gearbox noise. *International Power Transmission and Gearing Conference (Vol 2)*, 1992.

[51] D.G. Lewicki. Evaluation of low-noise, improved-bearing-contact spiral bevel gears. *NASA TM 2003-212353*, June 2003.

[52] P.M. Flanagan and W. J. Atherton. Investigation on experimental techniques to detect, locate, and quantify gear noise in helicopter transmissions. *NASA CR-3847*, January 1985.

[53] J.D. Smith. *Gear Noise and Vibration*. Marcel Dekker, Inc., New York, 1999.

[54] J. Herrmann. On the effect of the gearcase on the sound radiation from gear sets, and design measures for reducing sound radiation. *PhD Dissertation: RWTH Aachen*, 1963.

[55] K. Shibata, A. Takahashi, and T. Shirai. Fault diagnostics of rotating machinery through visualization of sound signals. *Mechanical Systems and Signal Processing*, 14(2):229–241, 2000.

[56] M.N.Badi and D. Guastamacchia. Alternative methods of detecting gear faults. *Engineering Systems Design and Analysis*, 8(A):235–240, 1994.

[57] C. James Li, Hyungdae Lee, and Suk Hwan Choi. Estimating size and gear tooth root crack using embedded modelling. *Mechanical Systems and Signal Processing*, 16(5):841–852, 2002.

[58] P. J. Dempsey, R. F. Handschuh, and Abdollah A. Afjeh. Spiral bevel gear damage detection using decision fusion analysis. Technical Report NASA TM-2002-211814, ARL-TR-2744, NASA and the U.S. Army Research Laboratory, 2002.

[59] K. G. Church, R. R. Kolesar, M. E. Phillips, and R. C. Garrido. Air vehicle diagnostic system CH-46 aft main transmission fault diagnostic final report. Technical Report NRaD Technical Document 2966, Office of Naval Research, June 1997.

[60] J.J. Zakrajsek, D.P. Townsend, D.G. Lewicki, H.J. Decker, and R.F. Handschuh. Transmission diagnostic research at NASA lewis research center. *NASA TM-106901/ARL-TR 748*, July 1995.

[61] M. Mosher. Results from a new separation algorithm for planetary gear system vibration measurements. *ASME 2005 Int. Des. Engineering Technical Conferences and Computer and Information in Engineering Conference*, Sept 25005, 2005.

[62] M. Mosher, A. Pryor, and D. Lewicki. Detailed vibration analysis of pinion gear with time frequency methods. *NASA TM-2003-212269*, NASA TM-2003-212269, 2003.

[63] A.A. Ross. High speed gears. *American Gear Manufacturers Association Paper*, 1927.

[64] E. Buckingham. Dynamic loads on gear teeth. *American Society of Mechanical Engineers Special Research Publication, New York*, 1931.

[65] H. Kohler. Gear dynamics, noise and vibration-a selective bibliography with abstracts. *British Gear Association-Design Sub Committee*, 1988.

[66] A. Parey and N. Tandon. Spur gear dynamic models including defects: A review. *The Shock and Vibration Digest*, 35(6), November 2003.

[67] W. A. Tuplin. Gear tooth stresses at high speed. *Proceedings of the Institution of Mechanical Engineering*, 16:162–167, 1950.

[68] W. A. Tuplin. Dynamic loads on gear teeth. *Machine Design*, 25:203–211, 1953.

[69] H. Strauch. Zahnradschwin-gungen (gear vibration). *Zeitschrift des Vereines Deutscher Ingiere*, 95:159–163, 1953.

[70] J.B. Reswick. Dynamic loads on spur and helical gear teeth. *Transactions of the American Society of Mechanical Engineers*, 77:635–644, 1955.

[71] T. Nakada and M. Utagawa. The dynamic loads on gears caused by the varying elasticity of the mating teeth of spur gears. *Proceedings of the 6th Japanese National Congress on Applied Mechanics*, pages 493–497, 1956.

[72] J. Zeman. Dynamische zusatzkrafter. *Zahnbradgetrieben, Zeitschrift des Vereines Deutscher Ingiere*, 9(244), 1957.

[73] S.L. Harris. Dynamic loads on the teeth of spur gears. *Proceedings of the Institution of Mechanical Engineers*, 172:87–112, 1958.

[74] H. Kohler. The mechanism and measurement of dynamic loading in spur gears. *PhD Dissertation: Univeristy of Sheffield*, 1959.

[75] B. Wood. Sources of vibration excitation in spur gears. *PhD Dissertation: University of Leeds*, 1960.

[76] M. Utagawa and T. Harada. Dynamic loads on spur gear teeth at high speed (influence of the pressure angle errors and comparison between the reduction gear and the speed up gears). *Bulletin of the Japanese Society of Mechanical Engineers*, 4:706–713, 1961.

[77] M. Utagawa and T. Harada. Dynamic loads on spur gears teeth having pitch errors at high speed. *Bulletin of the Japanese Society of Mechanical Engineers*, 5:374–381, 1962.

[78] A.Y. Attia. Dynamic loading of spur gear teeth. *Journal of Engineering for Industry*, pages 1–9, 1959.

[79] R.G. Munro. The dynamic behavior of spur gears. *Cambridge University*, 1962.

[80] A. Seireg and D.R. Houser. Evaluation of dynamic factors for spur and helical gears. *Journal of Eng. Ind. , Trans. ASME*, 192(2):504–514, 1970.

[81] K. Ichimaya and I. Hirano. Dynamic behavior of heavy-loaded spur gears. *ASME Trans. J. Eng. for Ind.*, May:373, 1974.

[82] R.W. Cornell. Compliance and stress sensitivity of spur gear teeth. *Journal of Mechanical Design Vol. 103(2)*, 1981.

[83] W.J. O'Donnell. Stresses and deflections in built-in beams. *Journal of Engineering for Industry*, 1963.

[84] I.R. Delgado F.B. Oswald, H.H. Lin. Dynamic analysis of spur gear transmissions (DANST) pc version. *NASA TR 1189*, 1996.

[85] R.G. Parker J. Lin. Analytical characterization of the unique properties of planetary gear free vibration. *Journal of Vibrations and Acoustics*, 121(3):316–321, 1999.

[86] R.G. Parker and X. Wu. Vibration modes of planetary gears with unequally spaced planets and an elastic ring gear. *Journal of Sound and Vibration*, 329:2265–2275, 2010.

[87] D.G. Lewicki, Robert Handschuh, Zachary Henry, and Faydor Litvin. Improvements in spiral-bevel gears to reduce noise and increase strength. *NASA TM106613 / ARL-TR-459*, Sept. 1994.

[88] Faydor L. Litvin. *Theory of Gearing (NASA)*. NASA TR 88-C-035, 1989.

[89] Dennis Townsend. Common problems and pitfalls in gear design. *NASA TM 88858*, TM 88858:1–19, 1986.

[90] H.H. Lin, C. Liou, F. Oswald, and D. Townsend. Balancing dynamic strength of spur gears operated at extended center distance. *NASA TM 107222*, 1996.

[91] J.J. Coy, D.P. Townsend, and E.V. Zaretsky. Gearing. *NASA / AVSCOM Tech Report*, NASA 1152 AVSCOM 84-C-15:1–69, 1985.

[92] Sameer Hameer Jarrer Hameer. *PhD Dissertation: A comparative study and application of continuously variable transmission to a single main rotor heavy lift helicopter*. PhD thesis, Georgia Institute of Technology, 2009.

[93] C. H. Liou H. H. Lin. A parametric study of spur gear dynamics. *NASA CR 419*, 1998.

[94] H.H.Lin, R. Huston, and J. Coy. On dynamic loads in parallel shaft transmissions i - modeling and analysis. *NASA TM 100180*, 1987.

[95] H.H. Lin and R. Huston. Dynamic loading on parallel shaft gears. *NASA CR 179473*, pages 1–80, 1986.

[96] H.H Mabie R.W.Furrow. The measurement of static deflection in spur gear teeth. *Journal of Mechanisms*, 5:147–168, 1970.

[97] M. Savage, R. Caldwell, and D. Lewicki. Gear mesh compliance modeling. *NASA TM 88843*, 1986.

[98] A.Y. Attia. Deflection of spur gear teeth cut in thin rims. *Trans. of ASME: Journal of Engineering for Industry*, pages 333–342, 1964.

[99] F. Chaari, W. Baccar, M. Abbes, and M. Haddar. Effect of spalling or tooth breakage on gearmesh stiffness and dynamic response of a one-stage spur gear transmission. *European Journal of Mechanics A/Solids*, 27:691–705, 2008.

[100] R.G. Parker J. Lin. Structured vibration characteristics of planetary gears with unequally spaced planets. *Journal of Sound and Vibration*, 233(5):921–928, 2000.

[101] M.S. Murat Inalpolat. *A Theoretical and Experimental Investigation of Modulation Sidebands of Planetary Gear Sets PH.D Dissertation.* PhD thesis, Ohio State University, Ohio, 2009.

[102] A. Kahraman. Planetary gear train dynamics. *Journal of Mechanical Design*, 116:713–720, 1994.

[103] Timothy L. Krantz. Gear tooth stress measurement of two helicopter planetary stages. *NASA TM 105651*, 1992.

[104] S.M. Vijayakar. A combined surface integral and finite contact problem element solution for a three-dimensional. *International Journal for Numerical Methods in Engineering*, 31:525–545, 1991.

[105] R.G. Parker, V. Agashe, and Sandeep Vijayakar. Dynamic response of a planetary gear system using finite element/contact mechanics model. *Transactions of the ASME*, 122:304–310, 2000.

[106] R.G. Parker, S.M. Vijayakar, and T. Imajo. Non-linear dynamic response of a spur gear pair: Modelling and experimental comparisons. *Journal of Sound and Vibration*, 237(3):435–455, 2000.

[107] R.G.Parker V.K. Ambarish. Nonlinear dynamics of planetary gears using analytical and finite element models. *Journal of Sound and Vibration*, pages 577–595, 2007.

[108] D. G. Lewicki and J.J. Coy. Vibration characteristics of oh-58a helicopter main rotor transmission. *NASA TP 2705 / AVSCOM TR 86-C-42*, NASA 2705, 11987.

[109] Chris Baldwin, Jason Kiddy, Paul Samuel, Joseph Coker, and Darry Pines. Fiber optic sensors monitoring transmission rign gears. *SPIE: Photonics in the Transportation Industry: Auto to Aerospace*, 2007.

[110] J. Zakrajsek, R. Handschuh, D. Lewicki, and H. Decker. Detecting gear tooth fracture in a high contact ratio face gear mesh. *NASA/TM-106822*, ARL-TR-600, 1995.

[111] Irem Tumer and E. Huff. Using triaxial accelerometer data for vibration monitoring of helicopter gearboxes. *2001 ASME Design Engineering Technical Conferences*, September 2001.